THÈSE

Pour obtenir le grade de

DOCTEUR DE L'UNIVERSITÉ GRENOBLE ALPES

École doctorale : I-MEP2 - Ingénierie - Matériaux, Mécanique, Environnement, Energétique, Procédés, Production
Spécialité : 2MGE : Matériaux, Mécanique, Génie civil, Electrochimie
Unité de recherche : Science et Ingénierie des Matériaux et Procédés

Étude de la sorption de gaz dans des matériaux poreux à transition de spin par DFT et diffusion de neutrons

Probing gas adsorption in spin-crossover porous materials by DFT and neutron scattering

Présentée par :

Angel FERNANDEZ BLANCO

Direction de thèse :

Roberta POLONI Chargé de Recherche HDR, Université Grenoble Alpes	Directrice de thèse
Alberto RODRIGUEZ VELAMAZAN Institut Laue Langevin	Co-encadrant de thèse

Rapporteurs :

Takafumi KITAZAWA
FULL PROFESSOR, Toho University, Faculty of Science, Department of Chemistry
Miguel CASTRO CORELLA
ASSOCIATE PROFESSOR, Universidad de Zaragoza / Departamento de Ciencia y Tecnología de Materiales y Fluidos

Thèse soutenue publiquement le **15 décembre 2022**, devant le jury composé de :

Roberta POLONI CHARGE DE RECHERCHE, SIMaP / Université Grenoble Alpes	Directrice de thèse
Takafumi KITAZAWA FULL PROFESSOR, Toho University, Faculty of Science, Department of Chemistry	Rapporteur
Miguel CASTRO CORELLA ASSOCIATE PROFESSOR, Universidad de Zaragoza / Departamento de Ciencia y Tecnología de Materiales y Fluidos	Rapporteur
José ANTONIO REAL FULL PROFESSOR, Universitat de Valencia, Department of Inorganic Chemistry	Examinateur
Marie PLAZANET CHARGE DE RECHERCHE, LIPHY / CNRS	Examinatrice
Noel JAKSE PROFESSEUR DES UNIVERSITES, SIMaP / Grenoble	Président
Christian SERRE DIRECTEUR DE RECHERCHE, ENS - Département de chimie / CNRS	Examinateur

Invités :

Jose Alberto RODRIGUEZ VELAMAZAN
CHERCHEUR, Institut Laue Langevin (ILL)

Acknowledgements

First and foremost I would like to express my deepest appreciation to my supervisors, Roberta Poloni and J. Alberto Rodríguez Velamazán, who guided me during these years. Their invaluable advice, continuous support, patience and immense knowledge have encouraged me in all the time of my academic research.

I would also like to extend my sincere thanks to Jose Sanchez Costa and Lucía Piñeiro who have colaborated closely on this project and allowed me to spend some time in their laboratory at IMDEA.

I very much appreciate the assistance and guidance of Mónica Jiménez Ruiz and Stéphane Rols during the neutron experiments at the ILL as well as to all those who have made possible the realization of the same.

I would like to thank my friends, lab mates and colleagues at the ILL and SIMaP, specially Marta, Peter, Palmerina, Carmen, Irina, Stas, Mohammed, Joao, Imad, Ali and Aseem. A special thank to Lorenzo Mariano for his help and advices since the beginning of my Ph.D.

I would also like to thank my very good fiends Marion, Quentin Mermillod, Yassine, Amadeo, Asier, Alberto Cuquejo, Javier Costa, Sara and Irene, for their support and all the good times we have spent together.

My sincere thanks to Ambrine for her support and with whom I shared a very special time these years.

Finally, I would like to express my gratitude to my mother and brother as well as to the rest of my family for their unconditional love and support.

Résumé en français

Les mécanismes d'adsorption de gaz nocifs (CO, CO_2 et SO_2) dans les clathrates de type Hofmann de formule générale $Fe(pz)[M(CN)_4]$ (M = Ni, Pd ou Pt; pz = pyrazine) ont été étudiés par des techniques de diffusion neutroniques (diffusion inélastique et diffraction) et par des calculs de la théorie de la fonctionnelle de la densité (DFT). Ces clathrates de Hofmann sont un type de réseaux métallo-organiques ou *metal-organic frameworks* (MOFs) caractérisés par la présence de centres métalliques, M, présentant une coordination insaturée, lequels agissent comme des sites de liaison potentiels pour les molécules de gaz. Ces sites métalliques ouverts sont liés via des ligands cyanure (CN) à un centre Fe(II) avec coordination octaédrique. Les plans de métal-cyanure $Fe[Pt(CN)_4]_\infty$ sont connectés par des ligands pyrazine agissant comme des piliers entre eux, résultant en un réseau nanoporeux 3D qui, en plus, présente une bistabilité, *i.e.* les centres de Fe(II) peuvent subir une transition d'état de spin sous l'effet de stimuli externes tels que la température, la lumière ou l'incorporation de molécules invitées. La combinaison de sites métalliques ouverts et de centres Fe(II) bistables fait de ces matériaux des candidats intéressants pour les applications d'adsorption de gaz. À basse température, lorsque les centres de Fe(II) sont dans un état de bas spin, la diffraction de neutrons et les calculs DFT suggèrent un arrangement ordonné des ligands pyrazine dont la configuration dépend de la quantité de gaz adsorbé. Cette structure ordonnée a des implications directes dans la transition de spin. Les expériences de diffusion inélastique de neutrons fournissent des signatures spectroscopiques du processus d'adsorption qui peuvent être interprétées à l'aide de la densité d'états de phonons généralisée obtenue par les calculs. Combinés, les résultats de diffusion inélastique, la diffraction de neutrons et les calculs DFT permettent de fournir une caractérisation détaillée du processus d'adsorption. Enfin, nous utilisons une approche DFT corrigée en densité pour étudier un éventuel processus inédit d'adsorption et de désorption de gaz basé sur l'utilisation d'une transition de spin se produisant sur le site métallique ouvert. Nous montrons que dans certains cas, une désorption de gaz assistée par une transition de spin induite par la température impliquant un changement important de l'affinité entre le gaz et le métal peut être thermodynamiquement réalisable.

Summary

The adsorption mechanism of harmful gases (SO_2, CO and CO_2) in the Hofmann-like clathrates with general formula $Fe(pz)[M(CN)_4]$ (M = Ni, Pd and Pt; pz = pyrazine) is studied by neutron scattering techniques (inelastic neutron scattering and neutron diffraction) and density-functional theory calculations (DFT). These Hofmann clathrates are a type of metal-organic frameworks (MOFs) characterized by the presence of metallic centers, M, exhibiting an unsaturated coordination which can act as potential bonding sites for the gas molecules. These open-metal sites are linked via cyanide (CN) ligands to an octahedrally coordinated Fe(II) center. The metallo-cyanide planes $Fe[Pt(CN)_4]_\infty$ are pillared by bridging pyrazines resulting in a 3D nanoporous network exhibiting bistability, *i.e.* the Fe(II) centers can undergo a spin-state transition under the influence of external stimuli such as temperature, light or the incorporation of guest molecules. The combination of open-metal sites and bistable Fe(II) centers makes these materials interesting candidates for gas adsorption applications. At low temperature when the Fe(II) centers are in low-spin state, neutron diffraction and DFT calculations suggest an ordered arrangement of the bridging pyrazines whose configuration depends on the amount of gas adsorbed. This ordered structure has direct implications on the spin-crossover transition. Inelastic neutron scattering experiments provide spectroscopic signatures of the adsorption process that can be interpreted using the computed generalized phonon density of states. If combined together, the inelastic scattering data, neutron diffraction and the DFT calculations allow to provide a detailed characterization of the adsorption process. Finally, we employ a density-corrected DFT scheme to study a possible novel gas adsorption-and-desorption process based on the use of a spin-crossover transition occurring on the open-metal site. We show that in certain cases, an efficient temperature-driven spin crossover-assisted gas desorption implying a large change in the affinity between the gas and the metal may be thermodynamically feasible.

Contents

Chapter 1

Introduction

1.1 Motivation

Most of human activities such as manufacturing, transportation or power generation produce greenhouse gases from burning fossil fuels. These greenhouse gases trap the sun's radiation in the Earth's atmosphere increasing the average temperature of the planet resulting in drastic consequences for life. Common pollutants produced during these processes are carbon dioxide (CO_2), nitrogen oxides (NO_x), sulfur dioxide (SO_2) and volatile organic compounds (VOCs). Carbon dioxide is the most important anthropogenic greenhouse gas [1] and its emission has continued to grow since the industrial revolution in response to a growing population that is increasingly dependent on fossil fuels. Coal, oil and gas often contain sulfur which is emitted as toxic sulfur dioxide and sulfur trioxide during the burning process. In the atmosphere, these sulfur oxides can mix with droplets suspended in the air causing the oxidation of sulfur dioxide into sulfuric acid, which is the main component of acid rain and smog [2, 3]. Another important and very toxic gas generated when burning fossil fuels is the carbon monoxide (CO) which, upon its release into the atmosphere, can affect several processes that contribute to climate change [4].

The sustainable development goals of the agenda 2030 stablished by the United Nations [5] urges to take action to combat climate change and its impacts. However, achiving a zero-emission goal is complicated and it could take years before we are able to switch completely to green energy sources. A mid-term contribution to mitigate this problem is to implement carbon capture reutilization or storage technologies (CCS), *i.e* CO_2 capture and storage in deep geological formations where it is not harmful anymore for the environment [6]. Development of capture technologies for gases like CO is important not just for environmental protection but also for the possibility of reusing them in other industrial chemical processes [4]. This idea is the underlying motivation to this thesis where several adsorption and desorption mechanims of toxic gases (CO, CO_2 and SO_2) by metal-organic frameworks (MOFs) are studied.

Metal-organic frameworks have emerged as potential porous materials in the last 50 years. The number of research studies focused on the use MOFs for adsorption applications have grown exponentially in the last decade resulting in some industrial and pre-industrial projects. For instance, the European project MOF4AIR [7], which intends to develop and demonstrate the performances of MOF-based CO_2 capture technologies in power plants and energy industries.

MOFs are 3D nanoporous materials composed of metal centres connected by organic ligands. An important feature of MOFs over other porous materials such as zeolites or porous carbons is their extraordinary tunability that allows the design of the physicochemical inner surface properties for specific applications. The presence of open-metal sites (OMS) in their structure is a very important feature that allows to increase the selectivity and gas uptake [8]. A high adsorption capacity and selectivity is important for post-combusting gas capture strategies where, generally, the target gas is produced as a mixture of different gases. For instance, carbon capture and storage strategies where the CO_2 is separated from a mixture of CH_4 or N_2 in different concentrations require high CO_2 uptake and selectivity [9]. Also the purification of CO from streams containing H_2, CO_2, N_2 and H_2O originated from power plants requires a very selective CO adsorption in order to obtain pure CO that can be reused in other industrial processes. [4, 10]

Our work focuses on the study of the gas adsorption mechanisms of three toxic gases, CO, CO_2 and SO_2 using the family of Hofmann clathrates with general formula $Fe(pz)[M(CN)_4]$, where M is a square-planar coordinated open-metal site (Ni, Pd and Pt). This family of MOFs is interesting because of the bistable Fe(II) centers that exhibit spin-crossover transition. The spin-crossover transition occurs when a metal center switches between low-spin and high-spin state as a response to an external stimulus such as temperature, pressure or light excitation. This bistability combined with the presence of open-metal sites makes them good candidates for gas adsorption or sensing applications. For example, significant higher SO_2 uptake capacities have been reported for $Fe(pz)[Pt(CN)_4]$ compared to other good performer porous materials [11]. Also CO_2 and CO kinetic and isothermal experiments showed a considerably higher uptake with respect to other MOFs with much larger surface areas such as NOTT-401 for CO_2 or MOF-74(Mg) for CO [12]. The CO_2 adsorption capacity was compared for ten different MOFs, all of them with larger surface areas, finding the highest adsorption capacity for the Hofmann-like clathrate $Fe(pz)[Pt(CN)_4]$, only surpassed by HKUST-1, which has a surface area *ca.* four times larger. These results show the importance of studying the adsorption mechanisms in these materials to assist the design of better performers.

It is important to develop effective adsorption and desorption processes with minimal energy consumption in order to motivate the use of this technology at large scale in industry. In this context, the design of MOFs which are able to undergo an adsorption/desorption process minimizing the energy penalty is of crucial interest. This idea motivates the last part of this thesis where an ab initio study of different transition metal cations for the open-metal site of Fe(pz)[M(CN)$_4$] is presented. The idea is to find a potential transition metal cation that, replaced in the open-metal site of the clathrate, can udergo a spin-crossover transition upon temperature yielding a change in uptake of gas and consequently to an efficient desorption.

The work presented in this manuscript results from a combined experimental (neutron scattering experiments) and computational study (density functional theory calculations). The use of neutron diffraction allows, together with DFT, the characterization of the MOF structure and the bonding sites of the gas molecules, which is crucial for understanding the adsorption mechanism. Inelastic neutron scattering is suitable for studying materials with high hydrogen content, present in the organic linkers of the MOF framework. The use of these techniques has the advantage that no-selection rules apply. The interpretation of these modes is done by the computed generalized phonon density of states obtained by DFT calculations, which allows a direct proof of the adsorption. Furthermore, we employ density-corrected DFT calculations to study the electronic structure of the potential open-metal sites for efficient adsorption/desorption processes.

1.2 Thesis outline

The **Chapter 1** of this thesis is dedicated to an introduction and motivation of the project. **Chapter 2** presents an introduction and overview of metal-organic frameworks for gas adsorption applications. The main properties that make MOFs good candidates for such applications are presented and special emphasis is paid to the use of open-metal sites as potential bonding sites and the study of their interaction with gas molecules by means of molecular orbital analysis. The spin-crossover phenomenon is explained by ligand field theory and thermodynamic considerations. Finally, the last section is dedicated to the family of spin-crossover Hofmann-clathrates with general formula Fe(pz)[M(CN)$_4$] (pz = pyrazine; M= Ni, Pd or Pt).

Chapter 3 includes a summary of the theory and main experimental methods used in this thesis. The first five sections are focused on neutron techniques and the last five on density functional theory.

After a brief introduction to neutron techniques, three sections are dedicated to the theoretical background of neutron scattering. Neutron diffraction, a brief overview of the diffractometer D20, and the Rietveld method for data analysis are also discussed. Finally, the main inelastic neutron techniques and the instruments IN1 and PANTHER are presented.

A brief introduction to density functional theory and density functional perturbation theory used for phonon calculations are presented.

The subsequent chapters are published studies (chapters 4 and 5) or ready for publication (chapters 6 and 7).

Chapter 4 is dedicated to the analysis of an ordered structure of the pyrazine ligands of $Fe(pz)[Pt(CN)_4]$ found by means of neutron diffraction experiments. The ordered structure is observed at low temperature with the pyrazines alternately oriented in two orthogonal positions perpendicular to each other. The ordering is retained until the spin-crossover transition is reached, which causes the pyrazine ligands to adopt a disordered configuration. The implications of the ordered structure on the spin-crossover transition are evaluated by density functional theory calculations and thermodynamical considerations. A change of the spin-transition temperature of *ca.* 30 K is estimated if the configuration of the pyrazine rings in the low-spin state was disordered and not ordered.

In **Chapter 5** the SO_2 adsorption mechanism in the $Fe(pz)[Pt(CN)_4]$ is probed by combining inelastic neutron scattering experiments and DFT calculations. An extensive analysis of the INS spectra for the empty MOF and upon SO_2 adsorption is reported with special emphasis in the spectral region between 100 and 140 cm^{-1}, where the main signature of the gas adsorption is observed. The analysis of the computed vibrational modes allow us to attribute this signature to the hampered rotation of the pyrazine and the out-of-plane movement of cyanide ligands. The results are consistent with an adsorption mechanism being a physisorption type of binding resulting from the combination of charge transfer, electrostatic, and dispersion interactions.

In **Chapter 6** a complete analysis of the CO and CO_2 adsorption mechanism in $Fe(pz)[Pt(CN)_4]$ by neutron diffraction, inelastic neutron scattering and density functional theory is presented. This chapter includes the study of the binding mechanism and the analysis of the main signatures on the INS spectra upon adsorption. Upon CO and CO_2 adsorption, the peak located at *ca.* 100 cm^{-1} undergoes a blue-shift, similar to the SO_2 adsorption.

Additionally, a second signature is observed when two CO molecules per f.u. are adsorbed: the intense peak at 400 cm^{-1} undergoes a red-shift. A study of the changes induced in the computed generalized phonon density of states when different amounts of adsorbed gas are considered is also presented.

The experimental signatures when saturation points are reached show clear differences between CO and CO_2. We concluded that the signatures are attributed to the hindered rotation or torsion of the pyrazines rings and the out-of-plane vibrations of the cyanide ligands. Only a few vibrational modes involved in the signatures present a dependency on the nature of the gas. For both, CO and CO_2, the adsorption mechanism is consistent with a physisorption type of binding.

In **Chapter 7** the computational desing of MOFs that employ a spin-crossover transition to efficiently desorb the gas is explored. This is done by computing the adiabatic energy differences between different spin states in presence of gas molecules, and the associated change in binding energy. A screening study is performed on $M(CN)_4$ fragments (M = Fe(II), Fe(III), Ni(II) and Co(II)) and the Hofmann-clathrates $Fe(L)[M(CN)_4]$ (L = pyrazine or bpac; M = Fe(II), Mn(II) and Ni(II)) with adsorbate CO, CO_2, N_2 and H_2 molecules. Promising values of adiabatic energy difference and change in binding energy upon spin-transition for M = Fe(II) and Mn(II) are found upon H_2 adsorption and for M= Fe(II) and N_2.

Finally, **Chapter 8** is a compilation of the conclusions of this thesis.

Chapter 2

Metal-organic frameworks for gas adsorption

2.1 Introduction

Metal Organic Frameworks (MOFs) [13], also Porous Coordination Networks (PCNs), are 3D nanoporous materials composed of metal ions or clusters linked by organic ligands, called *linkers*. The large variety of possible metal-ligand combinations allows a facile optimization of the structures and properties for specific applications. Since their discovery in the 90s, MOFs have been extensively studied and a great variety of interesting physical properties, such as luminiscence [14, 15, 16], magnetism [17, 18], resistance [19], electrical conductivity [20, 21] or ferroelectricity [22] were reported. Due to these diverse properties, MOFs have demonstrated great potential in different application fields including catalysis [23, 24, 25, 26], drug delivery [27], gas adsorption [28, 29], separation [30, 31], sensing [32, 33, 26, 16] and storage [34, 30]. In this thesis, we are interested in the gas adsorption applications for which MOFs are ideal candidates because of their large internal surface areas, ultrahigh porosity, tunability, acceptable thermal stability and crystallographically well-defined frameworks that allow them to retain the porosocity after several adsorption/desorption cycles. We also pay special interest to the presence of unsaturated coordination metal centres in their framework, which can potentially enhance their adsorption capacity, selectivity and sensitivity by interaction with the gas molecules.

2.2 MOFs for gas capture and storage

In the past 50 years, MOFs have been extensively studied as potential porous materials for gas adsorption and separation applications. Their Brunauer-Emmett-Teller (BET) surface areas can go up to thousands of square meters per gram (e.g 2320 m^2 g^{-1} for MOF-5) [35] allowing large uptake capacities. Additionally, they can exhibit coordinatively unsaturated metal centers along that surface, which, potentially, can increase the interaction with the gas, resulting in good adsorption capacities and selectivity [8]. The multiple choices of metal centres and organic ligands allow to conceptually desing their structure and properties. This remarkable tunability enables to control the pore size and surface functional groups to increase the selectivity of the adsorption process or other properties for specific applications. A prove of the great diversity can be found in the Cambridge Structural Database (CSD) [36] where, up to now, more than 80000 different MOFs have been reported. The regenerability is another important requirement for a good adsorbent if an efficiency in the adsorption/desorption process is sought. In the case of MOFs, the building blocks are linked by coordination bonds resulting in robust framework structures that are able to retain porosity after several adsorption/desorption cycles. Their high crystallinity is advantageous for structural determination using x-ray or neutron diffraction techniques which provide important structural information about the gas adsorption. All of this properties make MOFs ideal candidates for gas adsorption applications.

In gas adsorption studies, the adsorption isotherms (or equillibrium isotherms) allow us to characterize the adsorption process [31]. Experimentally, the amount of adsorbed gas per unit mass of the solid can be measured at a fixed temperature as a function of the applied gas pressure. During the adsorption, the interaction between the gas (adsorbate) and the MOF (adsorbant) can occur *via* weak electrostatic interactions, such as van der Waals interactions, London forces and dipole-dipole forces (physisorption), or by formation of covalent bonds (chemisorption), or a combination of both. The nature of the adsorbate and adsorbant determine the interactions, which directly influences the adsorption equilibrium. Therefore, various types of adsorption isotherms exist depending on the strength of the interaction and other properties such as the porosity of the adsorbant. Over the years, several models were proposed to interpret the different types of adsorption [37]. The Langmuir model is, probably, the most used due to its simplicity and accurate description of certain practical systems. The simplicity of the model arises from the consideration of a monolayer adsorption in which the potential bonding sites are identical and equivalent and no interactions between the adsorbed molecules are considered.

For an efficient adsorption-desorption process, it is important to design MOFs in order to obtain high uptake values at room temperature and low pressure to avoid the use of expensive cryogenic or high-pressure techniques [38]. Once the gas has been adsorbed, the desorption process must also be considered so the material can be reactivated [39] and the costs kept to a minimun. The capability of a material to be used in succesive adsorption/desorption cycles is called regenerability and, as mentioned before, MOFs exhibit good regenerability due to their highly crystalline structures that allow them to maintain their porosity upon desorption (see for example ref. [12]). Generally, the desorption is carried out by a temperature or pressure swing that will modify the resulting gas uptake, $Q(P)$, due to a change in the adsorption enthalpy ΔH.

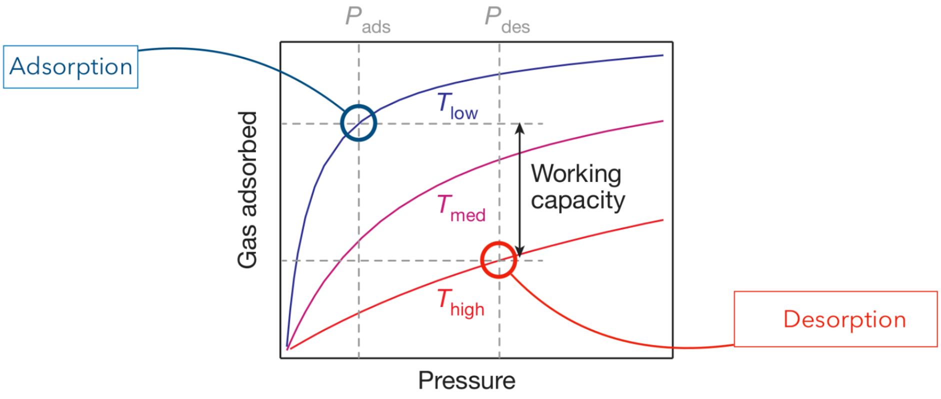

Figure 2.1: Idealized gas adsorption isotherms at different temperatures: (blue) low, T_{low}, (purple) medium, T_{med} and (red) high, T_{high}). Blue and red circles represent the adsorption and desorption points, respectively, at the corresponding adsorption, P_{ads}, and desorption pressures, P_{des}. The figure was reproduced and modified from ref. [40]

In adsorption/desorption processes, considering we work at a fixed volume, the gas is first adsorbed at low temperature and pressure (see blue circle in Fig. 2.1) reaching high uptake rates, and then, an increase of temperature will trigger the decrease in uptake with the consequent gas desorption and increase of pressure (see red circle in Fig. 2.1). The amount of gas that can be released from the adsorbent by a temperature or pressure swing is called the *working capacity* (see Fig. 2.1). Porous materials with good regenerabilities and *working capacities* are important for industrial processes. In applications like carbon capture and storage (CCS) [6] where the CO_2 is captured directly from industrial processes, *e.g.* coal power plants, and injected into suitable geological formations where its not harmful anymore for the environment [41], the efficiency of the process is of paramount importance to reduce costs and promote its use. In most of the cases, the concentration of CO_2 is about the 14-16% of the flue gas and the rest is mainly N_2 (73-77 %) [42]. Therefore, high uptake, working capacities and good selectivity of CO_2 over N_2 is required [43]. The same requirements are necessary, for example, for CO purification processes where the carbon monoxide has to be separated from H_2, CO_2, N_2 and hydrocarbons [10].

At the beginning of this chapter, I mentioned the possibility of using unsaturated coordination metal centers to enhance the adsorption mechanism. In the next section, I present an overview of the role of open-metal sites on gas adsorption mechanism.

2.3 Open metal sites (OMS) in metal-organic frameworks: gas adsorption

A metal complex with a free coordination site is called open metal site (OMS). Square-planar complexes, for example, have inherently two free coordination sites in the axial positions. These unsaturated metal centers can act as potential binding sites for gas molecules. Their presence in metal-organic frameworks can enhance the adsorption capacity and selectivity compared to MOFs where metal sites are fully occupied. Therefore, an OMS-MOF is a good candidate for gas adsorption applications like gas separation, sensing or catalysis [8]. Initially, the coordinatively unsaturated sites can be occupied by a solvent molecule as a result of the reaction in solution. These labile molecules can be removed in a process called *activation*, which may be thermic, chemical or photothermal [44]. After activation, gaseous adsorbates can strongly interact with the open coordination site by mainly electrostatic interactions and covalent bonds. The analysis of the molecular orbitals (MOs) [45] resulting from the hybridization of the metal and the gas can help to understand the interaction and establish a connection between the electronic configuration of the metal and the binding energy.

Molecular orbitals are usually expressed as linear combination of atomic orbitals of the different atoms or molecules that constitute the studied system. The shape of these orbitals depends on the relative magnitude and signs of the different coefficients. The interaction between two atomic orbitals, χ_1 and χ_2, produces a bonding (ϕ_+) and an antibonding (ϕ_-) MO. The first is stabilized with respect to the initial atomic orbitals (AOs) as a result of an in-phase combination with coefficients of the same sign while the later is destabilized due to an out-of-phase combination with coefficients of opposite sign. If the AOs have different energies, the bonding MO (ϕ_+) will be more localized on the fragment that has the lowest-energy orbital (χ_1), whereas the antibonding (ϕ_-) will be more localized in the highest-energy MO (χ_2) (see Fig. 2.2). The stabilization and destabilization is proportional to $S^2/\Delta\epsilon$ where S represents the overlap between the two initial atomic orbitals and $\Delta\epsilon$ the energy difference [45]. An important requirement for the interaction to take place is that the orbitals must have the same symmetry, otherwise, the overlap S, which is equal to the integral over all space of the product of the functions χ_1^* and χ_2, is zero and no interaction is stablished. We can distinguish between two types of interactions: σ interactions that take place with an *axial* orbital overlap, and π interactions with *lateral* overlap. The *axial* is more efficient than the *lateral* overlap, thus, σ bonds are, in general, stronger than π bonds.

In this PhD we worked mainly with the adsorption of CO, CO_2 and SO_2. I present here a brief overview of the frontier MOs of these three gases and an example of the interaction with OMS-MOFs for each of them:

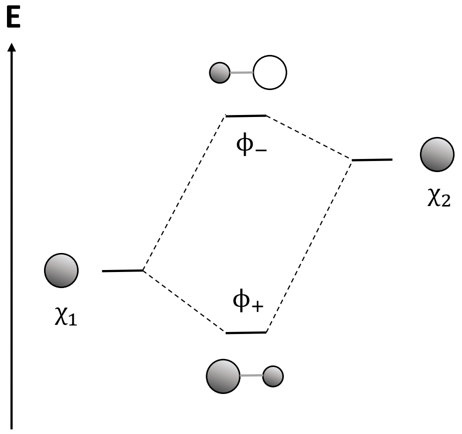

Figure 2.2: Interaction diagram for two orbitals with different energies.

Carbon monoxide, CO. Carbon monoxide is a strong σ-donor and a good π-acceptor ligand. Therefore, the strongest M-CO (M = metal) bonds are expected to occur with electron rich metals that are able to back-donate charge density to the CO ligand, *i.e.* metals in negative or low oxidation state. The frontier orbitals, HOMO (Highest Occupied Molecular Orbital) and LUMO (Lowest Unoccupied Molecular Orbital), of carbon monoxide are shown in Fig. 2.3. The HOMO is a bonding σ orbital which, in general, is responsible for the formation of σ_{M-CO} bonds. It is mainly localized on the carbon atom making it the preferential bonding site. The LUMO orbitals are two degenerated π^* antibonding orbitals mainly localized on the carbon atoms. These two orbitals can be used to establish π-type interactions with metal orbitals of adequate energy and symmetry. The π^*-orbitals are empty so they can receive electron density from the metal stablishing a backbonding interaction. In some cases, two additional π orbitals located below the HOMO orbital, mainly located on the oxygen atoms, can also interact with an empty nd-orbital from the metal resulting in a ligand-to-metal charge transfer. [45] It has to be noted that CO has a dipole moment of 0.1 Debye [46] and a quadrupole moment of 2.8 Debye Å [47], thus, electrostatic contributions have to be considered when evaluating the OMS-CO interaction.

An example on how molecular orbital analysis can help understand the CO interaction with OMS-MOFs was published in 2019 by H. Kim et *al.* [48]. They reported DFT calculations for adsorbed CO in the M-MOF-74 (M = Mg^{2+}, Co^{2+} and Ni^{2+}) confirming a π-backbonding from the Ni^{2+} and Co^{2+} to a π-orbital of the CO. For the Mg^{2+} this interaction was not observed due to the absence of d-valence electrons. Figure 2.3 shows the isosurface representation of the total charge density for CO-Co^{2+} and CO-Ni^{2+}.

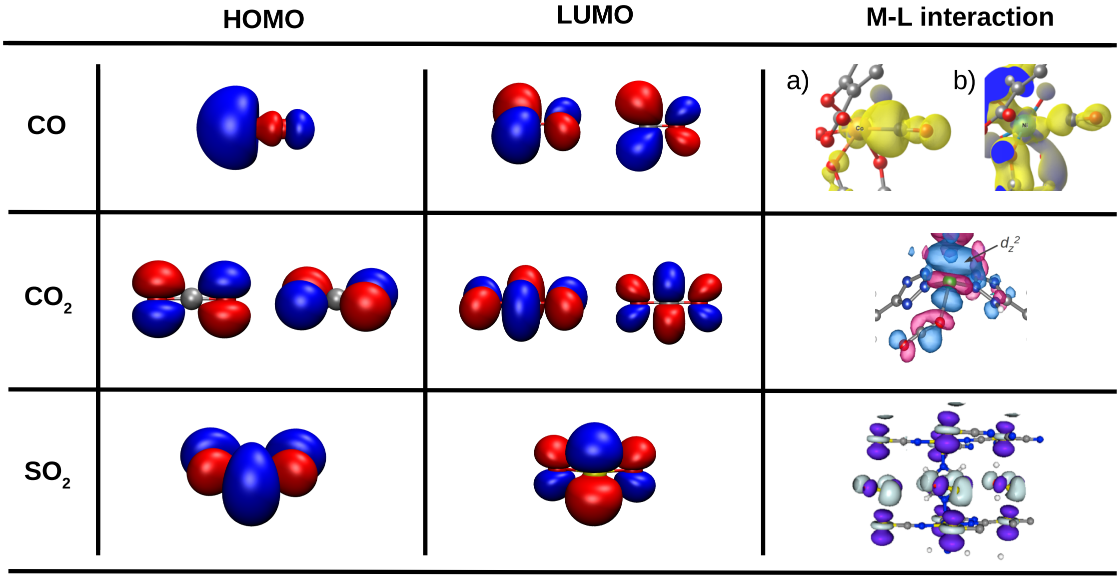

Figure 2.3: Molecular orbital representation of HOMO and LUMO orbitals for CO (upper row), CO_2 (middle row) and SO_2 (lower row). A published example of the interaction between an OMS and the HOMO orbital of the corresponding gas is also shown in the last colummn: (upper row) CO-[M_2(DOBDC)] for M= (a) Co^{2+} and (b) Ni^{2+} (middle row) interaction between V-d_{z2} orbital and CO_2-HOMO orbital (lower row) mixing between the SO_2 σ-HOMO orbital and the Pt-d_{z2} orbital. The figures of metal-ligand interactions were reproduced from ref. [48] (for CO), [49] (for CO_2) and [11] (for SO_2).

Sulfur dioxide, SO_2. The LUMO orbital of the SO_2 has π character resulting from the antibonding combination of *p* orbitals from the S and O. The HOMO orbital is characterized by an antibonding interaction between the *s*-orbital of the S atom and *p*-orbitals from the O (see Fig. 2.3) [50]. Similar to CO, sulfur dioxide can donate electron charge from the σ-HOMO orbital to an empty nd-orbital of the metal, σ-interaction, or receive it from an occupied nd-orbital into the empty π^*-LUMO orbital, π-interaction. Both orbitals are more localized in the sulphur atom, thus, the interaction occurs preferentially through that site. In comparison to CO, the SO_2 has a higher dipole moment of 1.6 Debye [46], thus, the electrostatic and van der Waals contributions are also expected to play an important role in the interaction.

Arcis-Castillo et *al*. [11] studied the molecular orbital interaction of SO_2 with the Hofmann clathrate Fe(pz)[Pt(CN)$_4$] using X-ray diffraction and DFT calculations. They reported two main interactions: first, a σ-interaction between the σ-HOMO orbital of the SO_2 and the Pt-d$_{z^2}$ orbital and second, a back-donation from an hybridized $\mathrm{Pt}_{d_{z^2}-p_z}$ orbital to the π^* LUMO of the SO_2 molecule (see figure 2.3). They suggested by DFT calculations that the interaction of the SO_2 with the open-metal site (Pt(II)) takes place through the S atom, with the SO_2 tilted with respect to the metal-cyanide layers (see pyramidal configuration in Fig. 2.4). This result was in contrast with the inferred from X-ray data, where the iron, sulfur and oxygen atoms are part of the same plane perpendicular to the Fe[Pt(CN)$_4$]$_\infty$ sheets (see planar configuration in Fig. 2.4). They concluded that the X-ray structure corresponds to an average or disordered structure of the possible orientations of the SO_2. A third coordination mode was also considered where the oxygen atoms act as bridges between Pt(II) from different Fe[Pt(CN)$_4$]$_\infty$ layers (see O,O-bridging configuration in Fig. 2.4). However, this configuration was found to be less stable than the other two configurations.

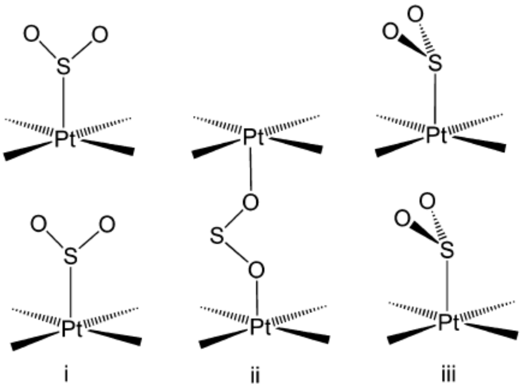

Figure 2.4: Coordination bonds considered for DFT analysis by Arcís-Castillo et *al.*: Planar (i), O,O-Bridging (ii), and pyramidal (iii). Figure reproduced from ref. [11]

Carbon dioxide, CO_2. The HOMO orbital of CO_2 is a π-orbital localized on the two O atoms (lone pair) while the LUMO is a π^* orbital resulting from the antibonding combination of p carbon and oxygen atomic orbitals [51, 52] (see Fig. 2.3). The CO_2 is a linear and symmetric molecule, thus, it has no dipole moment. However, it exhibits a high quadrupole moment of 4.4 Debye Å [47] which can establish important van der Waals interactions.

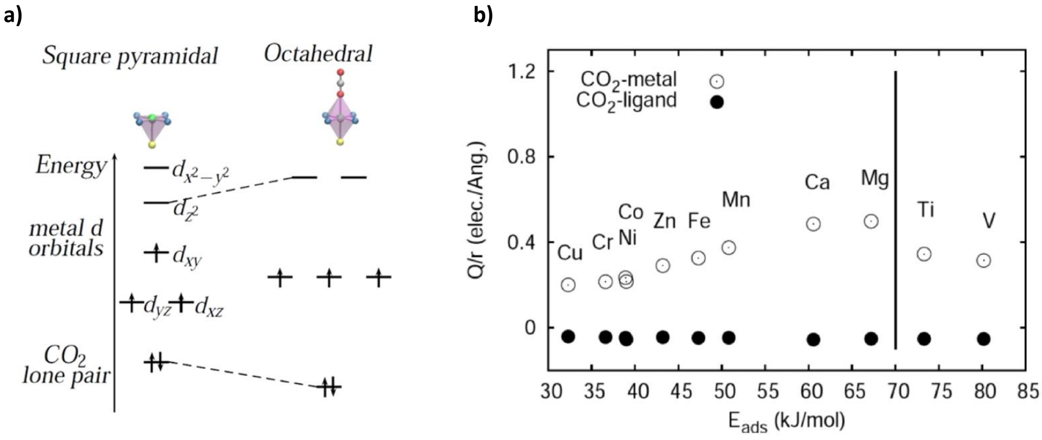

Figure 2.5: a) Change of the Crystal field splitting for a V^{2+} (d^3) from square pyramidal (open-metal site) to octahedral coordination (CO_2 adsorbed). b) Plot of CO_2 adsorption energy versus the computed electrostatic contribution (Q/r) for different metal cations for the M-BTT MOF. Figure reproduced from ref. [49].

In 2014, Poloni et *al.* [49] published a study on the binding energy trend of CO_2 in MOFs considering different metal cations for the open-metal sites of the sodalite-type framework M-BTT ($H_3[(M_4Cl)_3(BTT)_8]$, $M = M^{2+}$ metal, BTT = 1,3,5-benzenetristetrazole). A three-site interaction was previously reported [53], where the oxygen atoms of the CO_2 interact with the unsaturated metal site and the hydrogens of the framework, leading to a second attraction between the CO_2 carbon atom and a negatively charged nitrogen located on the tetrazol ligand. They computed the binding energies for the first-row of transition metal cations in HS (except Sc) and Mg^{2+} and Ca^{2+}, reporting binding energies from 32.2 kJ/mol, for the weakest interaction with Cu, to 73.2 and 80.2 kJ/mol, for the strongest with Ti and V, respectively. The general trend showed a correlation between the binding energies and the electrostatic contributions, Q/r, where Q is the computed Mulliken charge of the cation atom and r the metal-oxygen distance (see Fig. 2.5). However, the binding energies for Ti and V were significantly larger compared to other metallic atoms with the same Q/r, such as Fe (47.3 kJ/mol), suggesting that another contribution, apart from the electrostatic, was playing an important role in the interaction. When the CO_2 binds on top of the open-metal site, a molecular orbital analysis revealed the formation of a coordination bond between the CO_2-HOMO orbital and the d_{z^2} orbital of the metal (Fig. 2.3). For electron counts of d^2 (Ti) and d^3 (V), the antibonding d_{z^2} orbital is empty (see Fig. 2.5) and no energy penalty resulting from the interaction is expected, while for larger electron counts the occupation of d_{z^2} decreases the binding energy, increasing the bond distances. For Mg and Ca, the lower binding, even though they do not have d-valence electrons, is justified by a more effective screening of the nucleus by 3s and 4s electrons in comparison to the partially filled 3d electrons of the transition metal cations.

This work demonstrated that the interaction of the gas and the OMS can be modulated by controlling the occupation of the antibonding orbital d_{z^2}. This motivates the last part of this thesis (chapter 6) where we explore the use of spin-crossover transition in the open-metal sites of MOFs for efficient gas adsorption and desorption process. The next section is dedicated to the concept of spin-crossover transition explained within the Crystal Field Theory (CFT) and thermodynamic approaches.

2.4 Spin-crossover and ligand field theory

In the previous section we made use of the molecular orbital theory to explain the bonding in transition metal complexes. The same concepts can be explained, with certain limitations, with a simplified theory, the Crystal Field Theory (CFT). Despite its simplicity, this theory provides useful results and, generally, it is used to describe qualitatively the spin-crossover electronic structure and spin transition phenomena [54]. The CFT was first introduced by H. Bethe in 1929 and its first assumption is to consider the metal ions (M) as positive point charges subjected to a purely electrostatic interaction by its ligands (L), treated as negative point charges or point dipoles. Initially, in the absence of ligands (see Fig. 2.6 left), the free metal ion presents a 5-fold degeneracy of its *d*-orbitals (d_{zx}, d_{yz}, d_{xy}, d_{z^2} and $d_{x^2-y^2}$) with the electrons distributed following the Hund's rule (or rule of maximun multiplicity). If we suppose that the metal atom is surrounded by negative charges uniformly distributed over the surface of a sphere (see spherical field in Fig. 2.6 middle), the five *d* orbitals will remain degenerated but their energy will increase due to electrostatic repulsions. If this charge is then placed, in equal portions (representing the ligands), at the vertices of an octahedron (Fig. 2.6 right), the degeneracy will break, resulting in different sets of orbitals of different energies. The orbital distribution will depend on the symmetry of the ligand arrangement. For an octahedral coordination, the

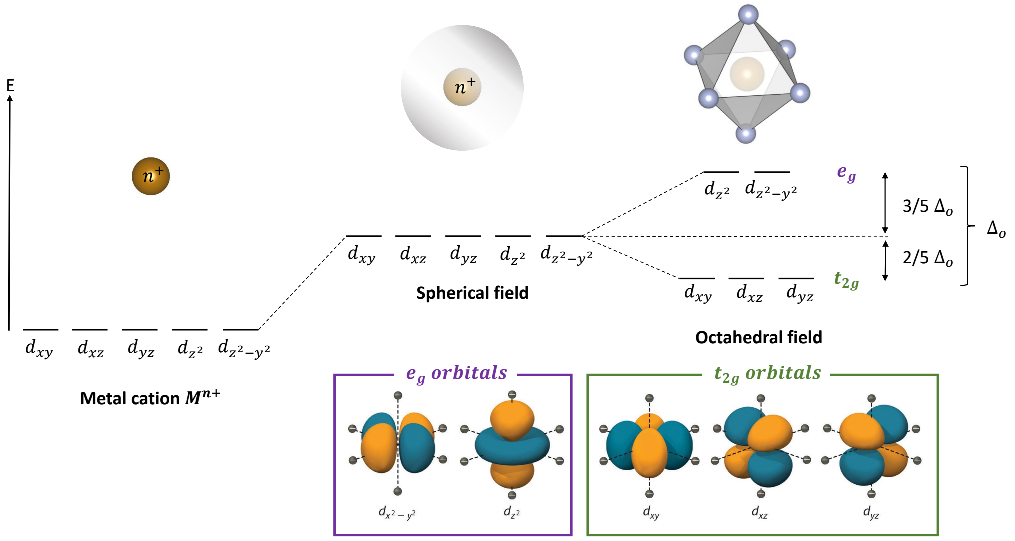

Figure 2.6: Representation of the *d*-orbital distribution of a (left) transition metal cation, M^{n+}, (middle) metal cation surrounded by a spherical surface of negative charges and (right) metal cation in a octahedral coordination. In the lower part the representation of the molecular *d*-orbitals in octahedral coordination is shown.

d-orbitals with electron density pointing towards the ligands (d_{z^2} and $d_{x^2-y^2}$), suffer a destabilization, whereas the orbitals with electron density lying between the M-L axes are stabilized (d_{zx}, d_{yz}, d_{xy}) with respect to the spherical field case. Consequently, the *d*-orbitals are splitted into two sets, a 3-fold degenerated (t_{2g}) and 2-fold degenerated (e_g), with an energy difference between them called the ligand-field splitting, Δ_0 (*o* refers to octahedral field) (see Fig. 2.6). The splitting depends on the nature of the ligands, the metal ion, the metal-ligand interaction and the M-L bond distance, r, and the magnitude of stabilization and destabilization is inversely proportional to the degeneracies, $2/5\Delta_0$ and $3/5\Delta_0$, respectively ([55] p.629-656).

Lets consider as case study Fe(II), with an electron count of 6 *d*-electrons, in octahedral coordination (see Fig. 2.7). The distribution of the 6 *d*-electrons along the two sets of orbitals for the ground state depends on wether Δ_0 is greater or less than the electron pairing energy, P. In the case of a strong ligand field, $\Delta_0 > P$, electrons will occupy the low lying orbitals and the total spin momentum takes a minimal value ($2S{+}1 = 1$ for Fe(II)). Conversely, for a weak ligand field $\Delta_0 < P$, the electrons will enter the five *d*-orbitals according to Hund's rule, with maximum spin multiplicity ($2S{+}1 = 5$ for Fe(II)). The first situation is known as the low spin (LS) state, while the second is the high spin (HS) state (see Fig. 2.7). If the low- and high-spin states are close enough, an external

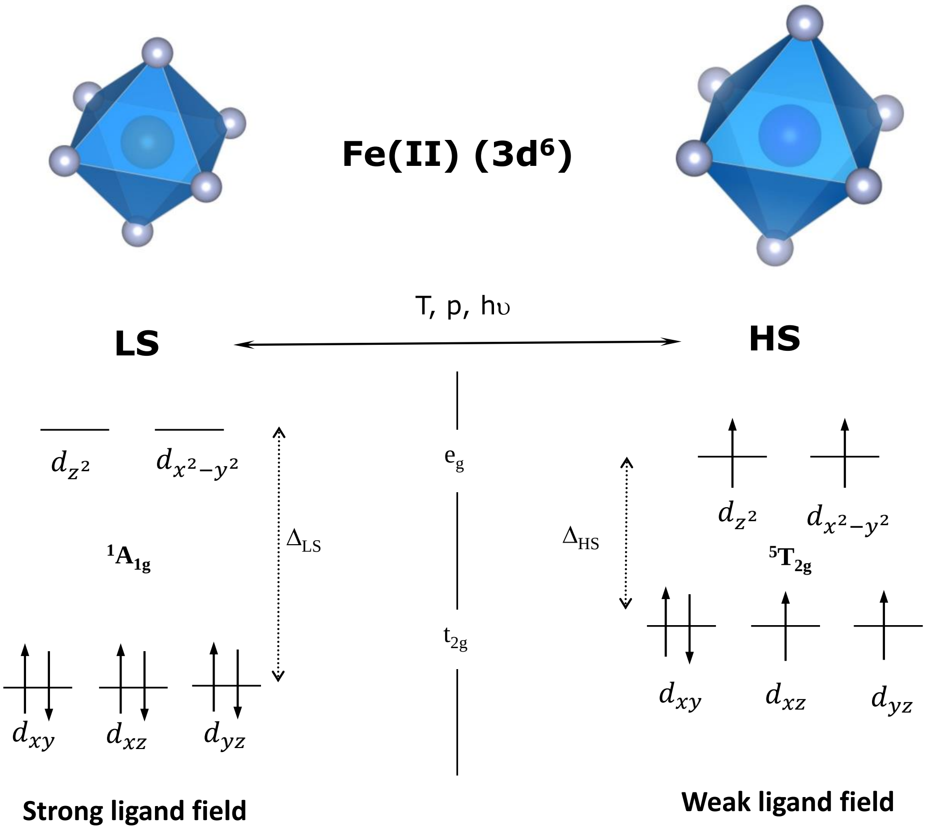

Figure 2.7: Schematic representation of the spin-crossover transition in octahedrically coordinated Fe(II). (left) LS state ($^1\mathrm{A}_{1g}$) in presence of a strong ligand field and (right) HS state ($^5\mathrm{T}_{2g}$) in presence of a weak ligand field. In HS, the longer metal-ligand bond distances than in LS, due to occupation of the antibonding orbitals d_{z^2} and $\mathrm{d}_{x^2-y^2}$, is ilustrated with a bigger octahedra. The ligand field splitting is Δ_{LS} for LS and Δ_{HS} for HS state. T, p and $h\nu$ denote an external stimulus of temperature, pressure or light excitation, respectively.

stimulus, such as temperature [56, 57], pressure [58], light excitation [59] or a magnetic field [60], can induce a reversible spin state change, resulting in a spin-crossover transition. A temperature-induced SCO is possible when the zero-point energy difference between the two spin states is of the same order of the thermal energy, $\Delta E = E_0^{HS} - E_0^{LS} \approx k_b T$, otherwise the thermal population of the excited state would be negligible. A consequence of the SCO transition from LS to HS is the occupation of the antibonding e_g orbitals that decreases the metal-ligand bond order and consequently, an increase of the bond distances, changing the vibrational properties. This implies that the potential energy surfaces, E_p, of the two spin states, are displaced relative to each other. Generally, the ground state is the LS state at zero temperature (see Fig. 2.8) and as temperature increases, an entropy-

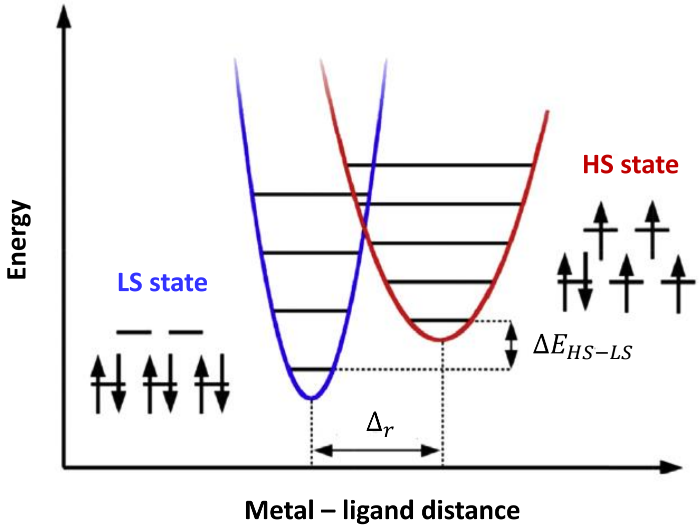

Figure 2.8: Schematic representation of potential energy curves within the adiabatic approximation (T =0) for low- and high- spin state of an Fe(II) complex. Figure reproduced from ref [61]

driven population of the HS may be observed, becoming the thermodynamically stable state. There are two main contributions to the entropy difference between the two spin states, the first is an electronic contribution due to the spin degeneracy of the HS state, and the second is a vibrational contribution due to the generally lower vibrational frequencies of the HS state which results in higher density of vibrational states. Therefore, the SCO occurs as an entropy-driven transition. [54] At the crossing point of the two potential curves, the M-L distance r is the same for both states, representing an energetically unstable configuration where the system undergoes a SCO transition from LS to HS.

So far in this chapter, the use of MOFs with good working capacities (2.2), open-metal sites (2.3) and spin-crossover transition (2.3 and 2.4) for gas adsorption applications has been exposed. I present now an example of a material combining these characteristics that was published by Jeffrey R. Long and coworkers in 2017 [40]. They reported two metal-organic frameworks with square pyramidal iron (II) centers, Fe_2Cl_2(bbta) (H_2bbta=1*H*,5*H*-benzo(1,2-*d*:4,5-*d′*)bistetrazole) and Fe_2Cl_2(btdd) (H_2btdd=bis(1*H*-1,2,3-triazolo[4,5-*b*],[4’,5]-*i*]dibenzo[1,4] dioxin), for selective adsorption of CO based on cooperative binding (see Fig. 2.9). These materials exhibit high working capacities with temperature swings of *ca.* 40 °C, a much lower temperature in comparison to other non-cooperative adsorbents for the same removal capacity. Initially, the Fe(II) centers are in HS state and the affinity for CO is low, resulting in low gas adsorption. In this situation, the CO is not able to induce a spin-transition to LS on a single iron centre since the neighbouring metal

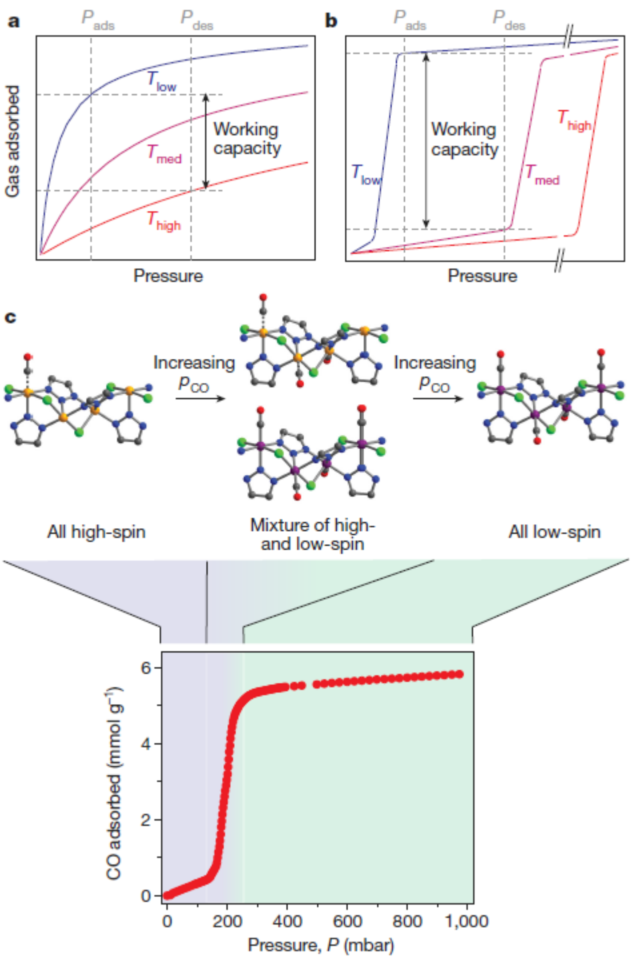

Figure 2.9: Comparison of working capacities for idealized adsorption isotherms of classical (a) and cooperative (b) adsorbents at different temperatures (low, T_{low}, medium, T_{med} and high, T_{high}). The greater working capacity for cooperative adsorbents is highlighted when passing from T_{low} to T_{med} instead of T_{low} to T_{high} for classical adsorbents. (c) Schematic representation of the cooperative spin transition mechanism for CO-Fe_2Cl_2(bbta) interaction. At low CO pressure all the Fe(II) atoms are in HS (yellow spheres) and the gas uptake is low. As the pressure increases the spin-crossover transition from HS to LS (purple spheres) is induced and the gas adsorption increases rapidly. At high CO pressures all the Fe(II) are in LS reaching the maximum adsorption capacity. Color code: C, Cl, high-spin Fe(II), low-spin Fe(II), N and O atoms are grey, green, orange, purple, blue and red spheres, respectively. H atoms are omitted for clarity. The figure was reproduced from ref. [40]

centers are also in HS preventing the rearrangement of the structural parameters induced when going from HS to LS. However, when a pressure threshold of CO is reached, a large number of Fe(II) centers are interacting with CO and the transition becomes thermodynamically favorable, causing all the iron centers to undergo a simultaneous spin-crossover transition (SCO) to LS. In LS, the affinity for CO is higher resulting in a sharp rise of adsorption in a narrow pressure window. For a fixed CO pressure, as the temperature increases, the transition pressure also increases, causing the metal centers to return to HS where the affinity is low, leading to the gas desorption. This cooperative adsorption is characterized by a steep adsorption isotherm with higher working capacities than the non-cooperative Langmuir-type isotherms (see Fig. 2.9).

2.5 Thermodynamics of Spin-crossover

The spin-crossover phenomenon of a system interacting with an external environment can be understood by thermodynamic aspects [61]. For a set of N non-interacting SCO molecules at constant temperature, T, and pressure, P, the SCO transition can be considered as a thermal equilibrium between the HS and LS state. The state function for such sytem corresponds to Gibbs energy $G = H - TS$ and the thermodynamic properties are described by the Gibbs energy difference between the two states:

$$\Delta G = \Delta H - T\Delta S \tag{2.1}$$

where $\Delta H = H_{HS} - H_{LS}$ is the enthalpy variation and $\Delta S = S_{HS} - S_{LS}$ is the entropy variation of the system. The spin transition temperature, $T_{1/2}$, corresponds to the temperature at which the number of centres in HS equals the centres in LS. In such equilibrium conditions $\Delta G = 0$, thus

$$T_{1/2} = \frac{\Delta H}{\Delta S} \tag{2.2}$$

When $T < T_{1/2}$, the enthalpic term dominates and the LS state is thermodinamically stable, whereas for $T > T_{1/2}$ the entropic term becomes dominant and the HS is favored. The enthalpy and entropy variations can be further subdivided in temperature-independent electronic and temperature-dependent contributions

$$\Delta H = \Delta H_{el} + \Delta H_{vib}(T) \tag{2.3}$$

$$\Delta S = \Delta S_{el} + \Delta S_{vib}(T) + \Delta S_{rot}(T) + \Delta S_{trans}(T) \tag{2.4}$$

where the subscripts *el*, *vib*, *rot* and *trans* denoted electronic, vibrational, rotational and translational contributions. For solids, the translation contributions are usually neglected. The electronic entropy variation takes into account the difference in the spin multiplicity between the LS and HS states, *i.e.*

$$\Delta S_{el} = Rln\left(\frac{2S_{HS}+1}{2S_{LS}+1}\right) \tag{2.5}$$

where R is the ideal gas constant and the term S is the total spin momenta of the corresponding state. Continuing with the Fe(II) in octahedral coordination as case study, the eq. 2.5 becomes $\Delta S_{spin} = Rln(5) = 13.38\ Jmol^{-1}K^{-1}$.

The vibrational terms in eq. 2.3 and eq. 2.4 can be derived using the vibrational contribution, q_{vib}, of the total partition function. The derivation of these equations can be found in most of the standard books on thermodynamics (see for example ref [62]). For the entropy, the vibrational contribution can be calculated using the following relation (ref [62], Chapter 7-6, Eq.7.27):

$$S = Nk_B + Nk_Bln\left(\frac{q_{vib}}{N}\right) + Nk_BT\left(\frac{\partial lnq_{vib}}{\partial T}\right) \tag{2.6}$$

where k_B is the Boltzmann constant. If molar values are considered we can divide by $n = N/N_A$, and subsitute $N_Ak_B = R$, thus:

$$S = R\left(ln(q_{vib}) + T\left[\frac{\partial lnq_{vib}}{\partial T}\right]_V\right) \tag{2.7}$$

And for the enthalpy, the relation takes the form (ref [62], Chapter 3-8, Eq.3.41):

$$H = Nk_BT^2\left(\frac{\partial lnq_{vib}}{\partial T}\right)_V \tag{2.8}$$

Where the vibrational contribution to the partition function, q_{vib}, considering the zero energy to be at the bottom of the internuclear potential energy well, is given by (ref [62], Chapter 4-7, Eq.4.46):

$$q_{vib} = \sum_{\nu_i}\frac{e^{-\Theta_{\nu_i}/2T}}{1-e^{-\Theta_{\nu_i}/T}} \tag{2.9}$$

where $\Theta_{\nu_i} = h\nu_i/k_B$ stands for the characteristic vibrational temperature of the vibrational mode, i. Combining eq. 2.7 and eq. 2.9 we can obtain the vibrational entropy contribution:

$$S_{vib} = R\sum_{\nu_i}\left(\frac{\Theta_{\nu_i}/T}{e^{\Theta_{\nu_i}/T}-1} - ln(1-e^{-\Theta_{\nu_i}/T})\right) \tag{2.10}$$

Analogously, combining eq. 2.8 and eq. 2.9, we obtain the vibrational enthalpy contribution:

$$H_{vib} = R\sum_{\nu_i}\Theta_{\nu_i}\left(\frac{1}{2}+\frac{1}{e^{\Theta_{\nu_i}/T}-1}\right) \tag{2.11}$$

A similar procedure where q_{vib} is substituted by q_{rot} (ref [62], Chapter 4-8, Eq.4.56) in eq. 2.7 can be followed to calculate the rotational entropy contribution, S_{rot}. However, Ando et *al*. [63] proposed another method, particularly adapted to the structure of Fe(pz)[Pt(CN)$_4$], to calculate S_{rot}. Considering that most of the results presented in this thesis are for the same MOF, it is convinient to use the approach of Ando et *al*.. The rotational entropy, S_{rot}, is evaluated following three steps:

(1) The potential energy curves (PECs) of the pyrazine rotation in the LS and HS are calculated for a structural model with two square-planar [Fe(NC)$_4$]$^{2-}$ and three pyrazine ligands where only the middle pyrazine rotates around the Fe-Fe axis.

(2) The quantized rotational energy levels (E$_j$) are calculated by solving the rotational Schrödinger equation

$$\left(-\frac{\hbar^2}{2I_\theta}\frac{\partial^2}{\partial\theta^2}+\hat{V}(\theta)\right)\Psi_j(\theta) = E_j\Psi_j(\theta) \tag{2.12}$$

using the Fourier grid Hamiltonian method [64]. The term $\hat{V}$ represents the PECs calculated in the first point, I_θ the moment of inertia of the N-N principal axis of the pyrazine rings calculated by diagonalization of the inertia tensors for the experimental structures (276.50 amu Bohr^2 for LS and 285.68 amu Bohr^2 for HS) and θ the rotational angle for the pyrazine.

(3) Finally, the rotational entropy S_{rot} is obtained within the canonical ensemble formalism:

$$S_{rot} = \frac{\partial(\beta^{-1}lnq_{rot})}{\partial T} \tag{2.13}$$

where T, β and q_{rot} are the temperature, inverse temperature and partition function, respectively. If the pyrazines are considered to rotate independently, the partition function takes the form:

$$q_{rot} = \left(\sum_{j=1}^{N_{basis}} e^{-\beta E_j} \right)^{N_A} \tag{2.14}$$

where N$_A$ is the Avogadro constant and N$_{basis}$ the number of basis functions for the Fourier grid Hamiltonian method [64].

The calculation of the remaining term, the adiabatic electronic energy difference, (ΔH_{el}), is the most challenging one for any modern *ab initio* methods [65, 66, 67], and yet it was estimated to be the dominant term in the expression of the ΔH_{HS-LS}. The complexity of the calculation arises from the different correlation energies between the two spin states that results in a lack of error cancellation when computing the energy differences. An accurate calculation of ΔH_{el} requires methods that can capture correctly these interactions. Density functional theory (DFT) within the local-density approximation (LDA) tends to strongly underestimate electron pairing energies stabilizing the LS over the HS [65]. This is because LDA understimates by *ca.* 10% the electron exchange between parallel-spin electron pairs [68], which is responsible of keeping the electrons apart, reducing electron repulsion. Therefore, an underestimation of electron exchange implies an overestimation of electron repulsion leading to a destabilization of the HS state where the number of parallel-electron pairs is higher than in LS. Generalized gradient approximations (GGAs) reduce the pairing energy problem but they do not eliminate it completely. Hybrid functionals are able to describe it correctly by adding a fraction of exact Hartree-Fock exchange to GGA functionals which stabilizes the HS relative to the LS state [69], however, the amount of exact exchange that has to be added for a correct description of ΔH_{el} is system-dependent, thus, other methods or corrections should be considered for a more general description. The method used in this thesis to evaluate the adiabatic energy difference between HS and LS state is the Hubbard U-corrected approach scheme [70]. This method allows to improve the description of localized *d*-orbitals, strongly affected by the energy interaction error, by using the Hubbard U-correction method in DFT.

2.6 Spin-crossover Hofmann clathrates Fe(pz)[M(CN)$_4$] (M = Ni, Pd or Pt)

A well-known family of MOFs with OMS that can undergo spin-crossover transition near room temperature is the family of Hofmann clathrates with general formula Fe(pz)[M(CN)$_4$] (M = Ni, Pd or Pt). This family of metal-organic frameworks was synthesized for the first time in 2001 by J.A. Real and coworkers [71] as an attemp to develop new 3D-compounds exhibiting spin-crossover transitions. The synthesis was inspired by the 2D-pyridine complexes reported 5 years before by Kitazawa et *al.* [72], $Fe(C_5H_5N)_2Ni(CN)_4$, resulting from the substitution of NH_3 by pyridine ligands in the series of 2D-compounds previously synthesized, $M(NH_3)_2M'(CN)_4$ (M = Mn^{2+}, Fe^{2+}, Co^{2+}, Ni^{2+}, Cu^{2+}, Zn^{2+} or Cd^{2+}; M' = Ni^{2+}, Pd^{2+}, Pt^{2+}) [73, 74]. All of these compounds belong to the well-known family of Hofmann-type inclusion compounds reported for the first time 125 years ago when the propotype $[Ni(CN)_2(NH)_3]{\cdot}C_6H_6$ was synthesized by Hofmann itself and Küspert [75], and the structure resolved by Powell and Rayner in 1949 [76, 77]. The structure of $Fe(pz)[M(CN)_4]$ shows two diferent crystallographic metal centres, the first are octahedrally coordinated Fe(II) atoms conected by cyanide *linkers*, CN^-, to the second metal centre, a square-planar open-metal site, M(II). The open-coordination sites are usually transition metals from the tenth group of the periodic table (Pd, Pt or Ni), known for their great stability in square-planar coordinations. The sheets $Fe[M^{II}(CN)_4]_\infty$ are then held together by bridging pyrazine ligands bonded to the apical positions of Fe(II). Longer ligands such as bpac (bis(4-pyridyl)acetylene) can be used to increase the pore size or tune the flexibility and cooperativity of the framework [78, 79] (see Fig. 2.10). The resulting 3D-framework structure exhibits the desired characteristics for a potential gas adsorbent (vide supra): high porosity and surface area (431 m^2/g), retention of crystallinity and surface area after several cycles of gas adsorption/desorption (good regenerability) [12], water and thermal stability (thermal decomposition starts at *ca.* 520 K) [71] and the presence of open-metal sites to enhance adsorption and separation. Additionally, $Fe(pz)[M(CN)_4]$ displays cooperative spin-crossover (SCO) transition near room temperature ($T_{1/2} \downarrow =$ 280 K and $T_{1/2} \uparrow =$ 305 K for M = Ni; $T_{1/2} \downarrow =$ 233 K and $T_{1/2} \uparrow =$ 366 K for M = Pd; $T_{1/2} \downarrow =$ 220 K and $T_{1/2} \uparrow =$ 240 K for M = Pt) in the closed Fe(II) centres with hysteresis loops of 25, 33 and 20 K, respectively [71, 80]. The combination of their porosity and spin-crossover properties, attracted great attention for applications like gas adsorption or sensing where the SCO can modulate or be modulated by the presence of adsorbates [71, 11, 81, 82, 83, 84, 85, 86].

These compounds are the focus of the experimental and computational work of this thesis, which is devoted to the study of the gas sorption in these materials by means of neutron scattering and DFT calculations.

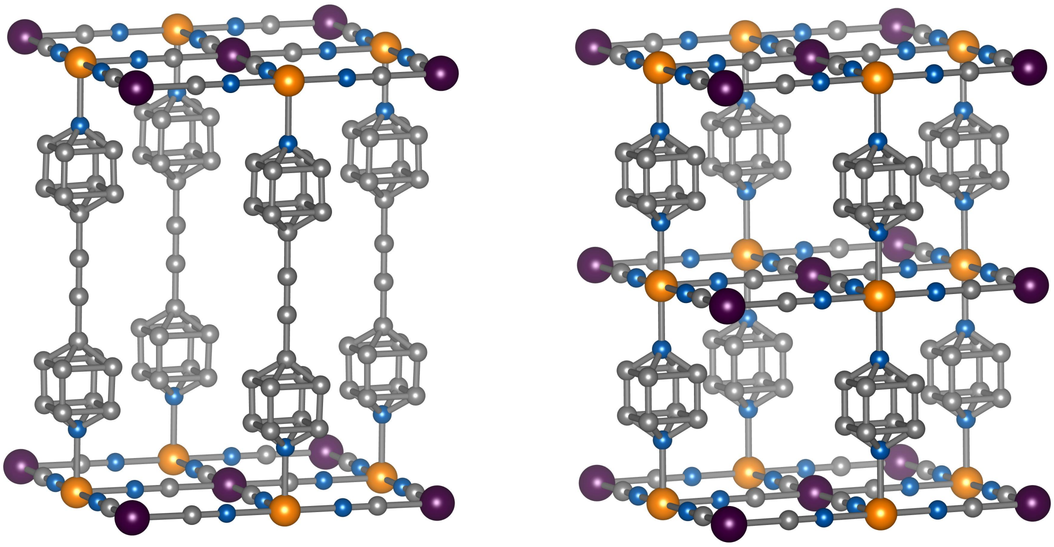

Figure 2.10: Schematic representation of $Fe(bpac)[Pt(CN)_4]$ (left) and $Fe(pz)[Pt(CN)_4]$ (right). The c parameter is doubled for $Fe(pz)[Pt(CN)_4]$. Colour code: Fe, Pt, N and C are orange, purple, blue and grey spheres, H atoms are omitted for clarity.

Chapter 3

Methodology

3.1 Introduction to neutron techniques

Neutrons are produced in nuclear reactions. The three possible ways to generate them are by fusion, fission or spallation. However, the current available technology does not allow to control fusion reactions, limiting neutron production to fission or spallation sources. The neutrons emerging from those sources have energies of a few MeV but for most neutron-scattering studies, one needs neutrons with energies around 25 meV. Therefore, they are slowed down by a moderator, where they are brought into thermal equilibrium through inelastic collisions with light atoms. The temperature of the moderator determines the energy of the neutrons. Cold neutrons have energies below 10 meV, thermal neutrons around 25 meV and hot neutrons more than 100 meV [87].

Due to their basic properties, neutrons are useful to investigate the structure and motion of atoms. The most important properties of thermal neutrons are [88, 87, 89]:

-A wavelength of the order of Ångstrom (10^{-8} cm) comparable to the interatomic distances in many solids and liquids. Therefore, scattering processes are possible and the resulting interference patterns allow the structure determination.

-A neutral charge that allows them to deeply penetrate the sample and interact with the nuclei via the very short-range nuclear force. The radius of the nucleus and the interaction range of the strong force for a neutron-nucleus interaction is of the order of fm (10^{-13} cm). Since the wavelength of the neutron is too long, it cannot resolve the structure of the nucleus, hence the scattering is isotropic (independent of the angle). This short-range interaction is characterized by a scattering length b that depends on the particular nucleus and the spin state of the nucleus-neutron system. The combination of the neutron (1/2) and nucleus (I) spin gives two possible states ($I + 1/2$ and $I - 1/2$), each of them characterized by the scattering length b^+ or b^-, respectively. The values of b can only be determined experimentally.

-An energy range that corresponds to typical excitation energies in many solids and liquids. Inelastic scattering processes can create or annihilate an excitation, thus, the measurement of the energy of the scattered neutrons contains important information about those excitations.

- A magnetic dipole moment that can interact with the magnetic moments of the sample giving information about the magnetic properties. If the scattering is elastic, the interaction can provide information about the arrangement of electron spins and the density distribution of unpaired electrons, whereas for an inelastic magnetic scattering, information about the energy of magnetic excitations can be obtained.

A compilation of the basic properties of neutrons is shown in table 3.1.

mass	$m_n = 1.675\text{x}10^{-27}$ kg
spin	s = 1/2
magnetic moment	μ_n=1.913 μ_N
electric charge	0
electric dipole moment	d_n = (-0.7+-0.4)$\cdot 10^{-21}$ e cm
polarizability	$\alpha = (1.2\pm1.0)\cdot 10^{-3}$ fm^3
life time	$\tau = 888\pm3$ s

Table 3.1: Properties of the neutron

Unpolarized neutrons are characterized by their wavevector $\boldsymbol{k}$ with magnitude

$$k = \frac{2\pi}{\lambda} \tag{3.1}$$

where λ is the wavelength of the neutron. From $\boldsymbol{k}$ we can calculate their momentum $\boldsymbol{p}$ and velocity $\boldsymbol{v}$ by

$$\boldsymbol{p} = \hbar\boldsymbol{k} = m_n\boldsymbol{v} \tag{3.2}$$

where m_n is the neutron mass and $\hbar$ the reduced Planck constant, $\hbar = h/2\pi$, and h the Planck constant. The relation between the momentum p, velocity v and kinetic energy E of a neutron is

$$E = \frac{1}{2}mv^2 = \frac{h^2}{2m_n\lambda^2} = \frac{\hbar^2k^2}{2m_n} \tag{3.3}$$

The interaction of neutrons with matter can be *inelastic* or *elastic*. The first implies an energy $\hbar\omega$ and momentum transfer, whereas the second implies only a change in the direction of $\boldsymbol{k}$. An inelastic process is then controlled by the energy and momentum conservation

$$\hbar\omega = E_i - E_f = \frac{\hbar^2}{2m_n}(k_i^2 - k_f^2) \tag{3.4}$$

and

$$\mathbf{Q} = \boldsymbol{k}_i - \boldsymbol{k}_f \tag{3.5}$$

respectively. The parameters $\boldsymbol{k}_i$ and $\boldsymbol{k}_f$ represent the initial and final wavevector, respectively.

3.2 Introduction to scattering cross-sections

The quantities measured in a scattering experiment are called cross-sections. To define these quantities, we should consider an incident flux, Φ_{inc}, of thermal neutrons with energy E_i interacting with a scattering system. We can define Φ_{sc} as the number of scattered neutrons counted in a given direction, given by the polar coordinates θ and ϕ, with a final energy between E_f and E_f+dE_f into a small angle, dΩ, subtended by the counter at the scattering system. If we do not take into account the initial and final spin of the neutron, the $partial\ differential\ cross-section$ can then be defined as

$$\frac{d^2\sigma}{d\Omega dE_f} = \frac{\Phi_{sc}}{\Phi_{inc} d\Omega dE_f} \tag{3.6}$$

If we simply count the number of neutrons scattered into the solid angle dΩ in the direction θ and ϕ, and we call it Φ'_{sc}, we can define the $differential\ cross-section$ by

$$\frac{d\sigma}{d\Omega} = \frac{\Phi'_{sc}}{\Phi_{inc} d\Omega} \tag{3.7}$$

Finally, considering only the total number of scattered neutrons per second, Φ''_{sc}, the $total\ scattering\ cross-section$ can be defined by

$$\sigma_{tot} = \frac{\Phi''_{sc}}{\Phi_{inc}} \tag{3.8}$$

Based on their definitions, the three scattering cross-sections are related by the following equations

$$\frac{d\sigma}{d\Omega} = \int_0^\infty \left(\frac{d^2\sigma}{d\Omega dE_f}\right) dE_f \tag{3.9}$$

$$\sigma_{tot} = \int_{all\ directions} \left(\frac{\sigma}{\Omega}\right) d\Omega \tag{3.10}$$

The $differential\ cross - section$ can also be related to the scattering length by

$$\frac{d\sigma}{d\Omega} = b^2 \tag{3.11}$$

and with the total cross-section by

$$\sigma_{tot} = 4\pi b^2 \tag{3.12}$$

It is convenient to derive theoretical expressions for these quantities in order to interpret and also model by computational methods the collected data. In the next section, I present an overview of the main theoretical equations for the scattering cross-sections for elastic and inelastic scattering processes.

3.3 Evaluation of scattering cross-sections

The derivation of theoretical expressions for the cross-sections can be found in standard text books (*e.g.* refs. [88] and [90]). In this section, all the equations and mathematical derivations were taken from ref [88] unless otherwise indicated.

Consider a beam of incident neutrons with wavevector $\boldsymbol{k}_i$ interacting with a scattering system of N nuclei in a state characterised by an index λ. Suppose the neutron interacts with the system via a potential V, resulting in scattered neutrons with wavevector $\boldsymbol{k}_f$ and a final state λ_f for the system. In a coordinate system with the origin at some arbitrary point of the scattering system, $\boldsymbol{R}_j$ $(j = 1, ...N)$ is the position vector of the jth nucleus, and $\boldsymbol{r}$ that of the neutron.

The differential scattering cross-section for all the processes in which the state of the system changes from an initial state λ_i to a final state λ_f and the wavevector of the neutrons changes from $\boldsymbol{k}_i$ to $\boldsymbol{k}_f$, can be derived using the Fermi's golden rule, obtaining

$$\left(\frac{d\sigma}{d\Omega}\right)_{\lambda_i \to \lambda_f} = \frac{k_f}{k_i} \left(\frac{m_n}{2\pi\hbar^2}\right)^2 |\langle \boldsymbol{k}_f \lambda_f | V | \boldsymbol{k}_i \lambda_i \rangle|^2 \tag{3.13}$$

Adding the energy distribution of the scattered neutrons in the form of a δ-function, we obtain the partial differential scattering cross-section

$$\left(\frac{d^2\sigma}{d\Omega dE_f}\right)_{\lambda_i\to\lambda_f} = \frac{k_f}{k_i}\left(\frac{m_n}{2\pi\hbar^2}\right)^2 |\langle \boldsymbol{k}_f\lambda_f|V|\boldsymbol{k}_i\lambda_i\rangle|^2\delta\left(E_{\lambda_i}-E_{\lambda_f}+E_i-E_f\right) \tag{3.14}$$

For nuclear scattering, the neutron-nucleus potential interaction, V, can be written in terms of the Fermi pseudopotential

$$V_l(\boldsymbol{x}_l) = \frac{2\pi\hbar^2}{m_n}b_l\delta(\boldsymbol{x}_l) \tag{3.15}$$

where b_l is the scattering length of the lth nucleus and $\boldsymbol{x}_l$=$\boldsymbol{r}$-$\boldsymbol{R}_l$.

To continue with the expansion of eq. 3.14 one has to use some algebra involving $|\boldsymbol{k}_i\rangle = e^{i\boldsymbol{k}_i r}$ and δ-functions and introduce quantum mechanical Heisenberg operators. A summation over all the states λ_f and the average over λ_i is also required. This is done due to the fact that in real experiments we do not measure the cross-section of a process going from a specific state λ_i to another state λ_f. Instead, we measure the full partial differential cross-section ($\mathrm{d}^2\sigma/\mathrm{d}\Omega\mathrm{dE}_f$). Additionally, in a real scattering case we have a large number of scattering systems with different distributions of the scattering lengths, b_l, due to the presence of isotopes or the randomly oriented nuclear spins. Therefore, it is necessary to average over b_l. This can be done easily if we consider that they are not correlated, which in principal is a valid assumption except at ultra-low temperatures (T≤1 mK), where nuclear spins may be correlated [89]. The final expression after all this considerations is given by

$$\left(\frac{d^2\sigma}{d\Omega dE_f}\right) = \frac{k_f}{k_i}\frac{1}{2\pi\hbar}(\bar{b})^2\sum_{ll'}\int\langle l',l\rangle e^{(-i\omega t)}dt + \frac{k_f}{k_i}\frac{1}{2\pi\hbar}\{\overline{b^2}-(\bar{b})^2\}\sum_{l}\int\langle l,l\rangle e^{(i\omega t)}dt \tag{3.16}$$

where

$$\langle l',l\rangle = \langle e^{\{-i\mathbf{Q}\boldsymbol{R}_{l'}(0)\}}e^{\{-i\mathbf{Q}\boldsymbol{R}_l(t)\}}\rangle \tag{3.17}$$

$$\overline{b_{l'}b_l} = (\bar{b})^2 \qquad if \quad l' \neq l \tag{3.18}$$

$$\overline{b_{l'}b_l} = \overline{b^2} \qquad if \quad l' = l \tag{3.19}$$

where $\mathbf{Q}$ is the scattering vector (eq.3.5), ω is defined by eq. 3.4 and $\boldsymbol{R}_l(t)$ and $\boldsymbol{R}_l(0)$ are the position vectors of the lth atom at a certain time t and $t=0$, respectively. The first term of eq. 3.16 is known as the *coherent* scattering cross-section and the second as the *incoherent* scattering cross-section. Thus, we can write:

$$\left(\frac{d^2\sigma}{d\Omega dE_f}\right)_{coh} = \frac{\sigma_{coh}}{4\pi}\frac{k_f}{k_i}\frac{1}{2\pi\hbar}\sum_{ll'}\int_{-\infty}^{\infty}\langle e^{\{-i\mathbf{Q}\boldsymbol{R}_{l'}(0)\}}e^{\{i\mathbf{Q}\boldsymbol{R}_l(t)\}}\rangle e^{(-i\omega t)}dt \tag{3.20}$$

and

$$\left(\frac{d^2\sigma}{d\Omega dE_f}\right)_{inc} = \frac{\sigma_{inc}}{4\pi}\frac{k_f}{k_i}\frac{1}{2\pi\hbar}\sum_{l}\int_{-\infty}^{\infty}\langle e^{\{-i\mathbf{Q}\boldsymbol{R}_{l'}(0)\}}e^{\{i\mathbf{Q}\boldsymbol{R}_l(t)\}}e^{(-i\omega t)}dt. \tag{3.21}$$

The terms $\sigma_{coh} = 4\pi(\bar{b})^2$ and $\sigma_{inc} = 4\pi\{\overline{b^2} - (\bar{b})^2\}$ are called the coherent and incoherent scattering cross-sections, respectively. The *coherent* scattering takes into account the correlation between the positions of the same nucleus at different times, and the correlation between the positions of different nuclei at different times. Thus, it gives interference effects resulting in diffraction patterns. Whereas the *incoherent*, depends only on the correlation betweeen the position of the same nucleus at different times. Therefore, it does not give interference effects. This type of scattering is characterised by an even distribution of intensity appearing in all directions [87].

The next step to develop the expressions for the cross-section is the evaluation of the coherent and incoherent contributions for a specific physical system. Considering a crystal acting as scattering system, the instantaneous position of the nucleus l displaced from its equilibrium position $\boldsymbol{L}$ due to thermal contributions is given by

$$\boldsymbol{R}_l = \boldsymbol{L} + \boldsymbol{u}_l \tag{3.22}$$

where $\boldsymbol{u}_l$ is the displacement from the equilibrium position. For simplicity, the scattering system is considered to be a Bravais crystal *i.e.* a crystal with one atom per unit cell, unless otherwise specified. Equivalent equations can be obtain for a non-Bravais crystal *i.e.* a crystal with more than one atom per unit cell.

For a Bravais crystal we can consider that $l' = 0$ in eq. 3.20 and the coherent differential cross-section can be expresed as:

$$\left(\frac{d^2\sigma}{d\Omega dE_f}\right)_{coh} = \frac{\sigma_{coh}}{4\pi}\frac{k_f}{k_i}\frac{N}{2\pi\hbar}e^{\langle U^2\rangle}\sum_{l}e^{(i\mathbf{Q}\boldsymbol{L})}\int_{-\infty}^{\infty}e^{\langle UV\rangle}e^{(-i\omega t)}dt. \tag{3.23}$$

where $U = -i\mathbf{Q}\boldsymbol{u}_0(0)$, $V = i\mathbf{Q}\boldsymbol{u}_l(t)$ and $\langle e^U e^V\rangle = e^{\langle U^2\rangle}e^{\langle UV\rangle}$. Then, the term $e^{\langle UV\rangle}$ can be expanded by

$$e^{\langle UV\rangle} = 1 + \langle UV\rangle + \frac{1}{2!}\langle UV\rangle^2 + ... + \frac{1}{p!}\langle UV\rangle^p. \tag{3.24}$$

This is called the *phonon expansion* and each pth term represents a scattering process when substituted into eq. 3.23 by the exponential $e^{\langle UV \rangle}$. This means that the first term $e^{\langle UV \rangle} = 1$ represents the 0-phonon process, or the elastic process, the second term $e^{\langle UV \rangle} = \langle UV \rangle$ is the one-phonon process, the third term $e^{\langle UV \rangle} = (1/2!)\langle UV \rangle^2$ is the two-phonon process and so on. This conclusion is justified during the derivation of the expressions of the partial differential cross-sections, due to appearance of δ-functions that establish the conditions that have to be satisfied for the scattering process to take place (see ref. [88] for the demonstration). In the next four subsections, the expressions for the different cross-sections obtained by applying the phonon expansion are shown.

Coherent elastic scattering (Bragg's law).

Therefore, to obtain the coherent elastic scattering cross-section the term $e^{\langle UV \rangle}$ is substituted by 1 in eq 3.23 and some algebra is applied. The final expression for a non-Bravais crystal is

$$\left(\frac{d\sigma}{d\Omega}\right)_{coh\ elas} = N\frac{(2\pi)^3}{\nu_0}\sum_{\boldsymbol{\tau}}\delta(\mathbf{Q}-\boldsymbol{\tau})|F_N(\mathbf{Q})|^2, \tag{3.25}$$

where ν_0 is the volume of the unit cell, $\boldsymbol{\tau}$ is a reciprocal lattice vector and $F_N(\mathbf{Q})$ is the nuclear structural factor expressed by

$$F_N(\mathbf{Q}) = \sum_{d}\overline{b_d}e^{(i\mathbf{Q}\boldsymbol{d})}e^{(-2W_d)}, \tag{3.26}$$

where the index $\boldsymbol{d}$ stands for the reciprocal coordinates of the l-atom inside the dth-unit cell. The equivalent expression in terms of the position vectors $\boldsymbol{x}_l$, $\boldsymbol{y}_l$ and $\boldsymbol{z}_l$ and Miller indices (hkl) is

$$F_{hkl} = \sum_{l}\overline{b_l}e^{(2\pi i(h\boldsymbol{x}_l+k\boldsymbol{y}_l+l\boldsymbol{z}_l))}e^{(-2W_l)} \tag{3.27}$$

From the expression of F_{hkl}, it can be seen that the structure factor contains the information about the atom distribution within the unit cell. In a neutron diffraction experiment, the observed intensity can be related to the structure factor, allowing to connect the experimental observable with the atomic arrangement. More details about this relation are provided in the next section (**Neutron diffraction experiments**).

The exponential term in eqs. 3.26 and 3.27 is the Debye-Waller factor that takes into account the attenuation of the scattered intensity due to thermal contributions. In general, it can be expressed by

$$2W = \frac{\mathbf{Q}\langle\overline{u^2}\rangle}{3}, \tag{3.28}$$

where $\langle\overline{u^2}\rangle$ is the average of the mean square displacements over all the atoms and is expressed by (ref. [88] p.34-35).

$$\langle\overline{u^2}\rangle = \frac{\hbar}{2\overline{M}N}\sum\frac{1}{\omega_j}coth\left(\frac{1}{2}\hbar\omega_j\beta\right). \tag{3.29}$$

where $\overline{M} = \sum_l M_l/N$, n is the thermal equilibrium occupation number of the vibrational state, $\langle n+1\rangle = exp(\hbar\omega\beta)/(exp(\hbar\omega\beta)-1)$ with $\beta = 1/k_BT$ and ω_j is the phonon frequency of the jth normal mode.
In eq. 3.25, the δ-function indicates that the scattering occurs only when $\boldsymbol{Q} = \boldsymbol{k}_i$ - $\boldsymbol{k}_f = \boldsymbol{\tau}$. This is the equivalent condition to the Bragg's law and it is called the *Laue condition.* It can be graphically represented by a reciprocal lattice with origin at O (see Fig. 3.1). If $\boldsymbol{k}_i$=AO is the wavevector of the incident neutrons, and $\boldsymbol{k}_f$=AB that of the scattered neutrons, AO must be equal to AB since the scattering is elastic and there is no energy or momentum transfer between the neutron and the scattering system. Since $\boldsymbol{k}_i$ and $\boldsymbol{k}_f$ have the same length, the scattering vector $\mathbf{Q}$ must lie on the surface of a sphere of radius $2\pi/\lambda$ (eq.3.1), called the *Ewald* sphere (see also Fig. 3.2 (b)). Only for special orientations of $\boldsymbol{k}$ and the scattering angle θ, the point B coincides with a reciprocal lattice point with wavevector $\boldsymbol{\tau} = BO$, originating the coherent scattering.

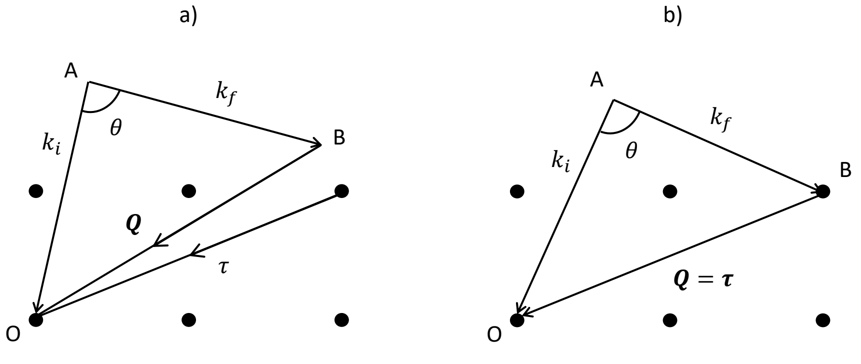

Figure 3.1: Representation of the Laue condition in reciprocal space. (a) $\mathbf{Q} \neq \boldsymbol{\tau}$; no coherent elastic scattering and (b) $\mathbf{Q} = \boldsymbol{\tau}$; coherent elastic scattering occurs.

Due to $\boldsymbol{k}_i$=$\boldsymbol{k}_f$, OAB is an isosceles triangle where

$$\tau = 2ksin\frac{1}{2}\theta. \tag{3.30}$$

and from eq.3.1 $k = 2\pi/\lambda$. By definition, the reciprocal lattice vector $\boldsymbol{\tau}$ is perpendicular to a set of crystal planes and it is expressed as

$$\tau = n\frac{2\pi}{d}. \tag{3.31}$$

where n is an integer and d is the space between reciprocal planes. Substituting eqs. 3.1 and 3.31 into eq. 3.30 the Bragg's law is obtained:

$$n\lambda = 2dsin\frac{1}{2}\theta \tag{3.32}$$

For this reason, sometimes the coherent elastic scattering is named Bragg scattering [88]. Experimentally, the elastic scattering can be measured by three different methods: the Laue method, the crystal rotation or the powder method. The first two are used for single crystals while the last one is for powder samples.

In the **Laue method**, the incident neutrons have a continuous range of wavelengths, DO, and the single crystal is fixed in a certain orientation (see Fig. 3.2). The angle between the scattered neutrons and the incident direction is set to a value $\theta = \pi - 2\psi$. For certain values of $\boldsymbol{k'}_i$=AO the scattered wavevector is $\boldsymbol{k'}_f$ and the Bragg condition is not satisfied because $\mathbf{Q} = BO$ does not equal $\boldsymbol{\tau} = TO$. Conversely, for other certain values of $\boldsymbol{k}_i$, with the correspondent scattered wavevector $\boldsymbol{k}_f$, the condition $\mathbf{Q} = TO = \boldsymbol{\tau}$ is satisfied and the bragg scattering occurs. The values of $\boldsymbol{k}$ that produce elastic scattering are given by

$$k = \frac{\tau}{2cos\psi} \tag{3.33}$$

In the **single crystal rotation method** a monochromatic beam of neutrons with wavevector $\boldsymbol{k}$ is incident on a crystal that can be rotated. As the crystal rotates, so does the reciprocal space and the reciprocal lattice point $T = \boldsymbol{\tau}$ (see Fig. 3.2 (b)) traces a circle. When the point T passes through the scattering vector $B = \mathbf{Q}$, the scattering angle θ satisfies the relation from eq 3.25, and the scattering occurs.

In the **powder method** a monochromatic beam of neutrons with fixed wavevector $\boldsymbol{k}$ is incident on a powder sample. A powder sample is made of a large number of small single crystals randomly oriented. A large number of those small crystals will have the same orientation, thus the same diffraction conditions. Consequently, only the microcrystals whose $\boldsymbol{\tau}$ lies on a cone, known as the Debye-Scherrer cone (see Fig. 3.2 (c)), with axis along $\boldsymbol{k}$ and semi-angle

$$\psi = \frac{1}{2}\pi - \frac{1}{2}\theta \tag{3.34}$$

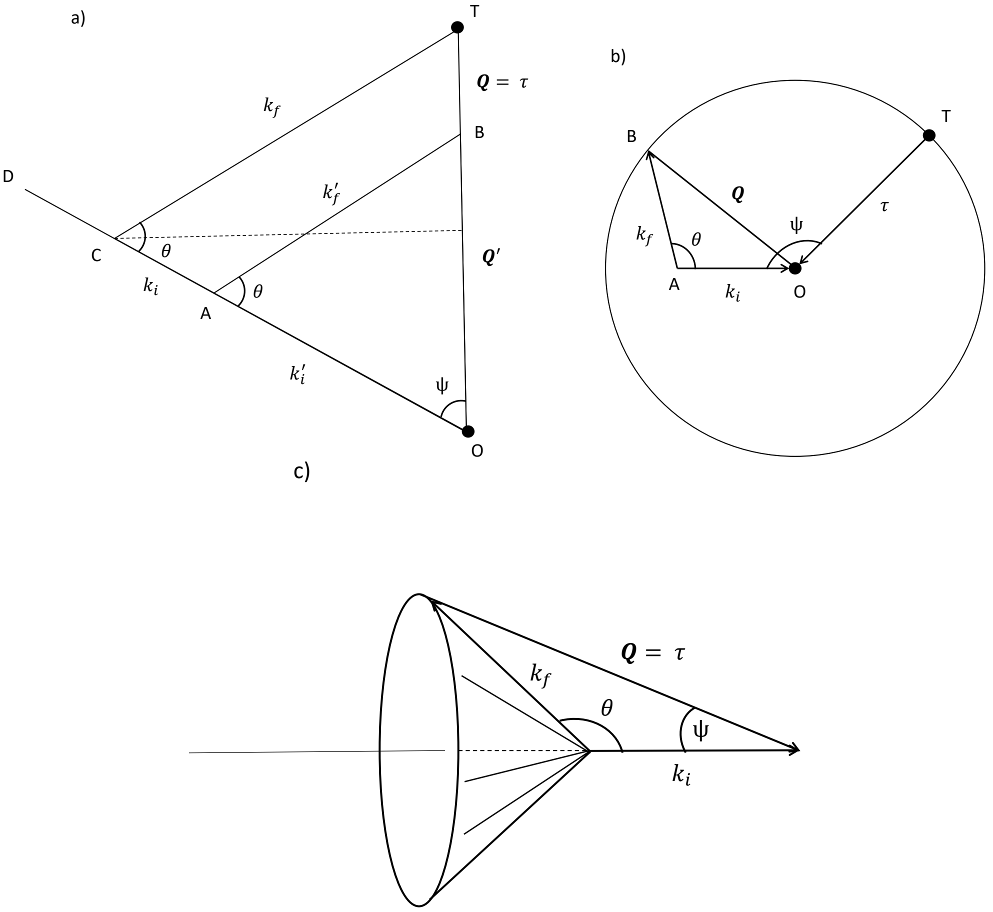

Figure 3.2: Graphical representation of (a) the Laue method (b) the single crystal rotation method and (c) the powder method.

contribute to the scattering.

Coherent one-phonon scattering cross-section.

The coherent one-phonon cross-section is obtained by substituting in eq. 3.23 the exponential term by $\langle UV\rangle$ from the expansion of $e^{\langle UV\rangle}$(see eq. 3.24). The final expression for non-Bravais crystals is given by

$$\left(\frac{d^2\sigma}{d\Omega dE_f}\right)_{coh\ 1\ ph} = \frac{k_f}{k_i}\frac{(2\pi)^3}{2\nu_0}\sum_j\sum_{\boldsymbol{\tau}}\frac{1}{\omega_j}|\sum_d\frac{\overline{b_d}}{(M_d)^{1/2}}e^{-W_d}e^{i\mathbf{Q}\boldsymbol{d}}(\mathbf{Q}\boldsymbol{e}_{ds})|^2\langle n{+}1\rangle\delta(\omega{-}\omega_j)\delta(\mathbf{Q}{-}\boldsymbol{q}{-}\boldsymbol{\tau}) \tag{3.35}$$

where $\boldsymbol{q}$ is the wavevector of the mode j. This expression contains the factors $\delta(\omega-\omega_j)$ and $\delta(\mathbf{Q}-\boldsymbol{q}-\boldsymbol{\tau})$. Therefore, two conditions must be satisfied for scattering to occur:

$$(1)\ \ \omega = \omega_j \qquad\qquad (2)\ \ \mathbf{Q} = \boldsymbol{k}_i - \boldsymbol{k}_f = \boldsymbol{\tau} + \mathbf{q} \tag{3.36}$$

From the condition (1), which is equivalent to eq.3.4, it can be concluded that the energy of the neutron must decrease by an amount equal to the energy of a phonon for the jth normal mode. This process is known as a *phonon emission* because the neutron creates a phonon.

The condition (2) can be seen as a conservation of momentum. Multiplying by $\hbar$ in both sides of the equation, the quantity $\hbar(\boldsymbol{k}_i - \boldsymbol{k}_f)$ is the change in the momentum of the neutron and $\hbar(\boldsymbol{\tau} + \mathbf{q})$ is the momentum donated to the crystal. A similar expression of eq. 3.35 can be obtained for a *phonon absorption* process where the neutron anhilates a phonon in the jth normal mode. The energy and momentum conditions for this case are $(\hbar^2/2m_n)(k_f^2 - k_i^2) = \hbar\omega_j$ and $\mathbf{Q} = \boldsymbol{k}_i$ - $\boldsymbol{k}_f = \boldsymbol{\tau}$ - $\boldsymbol{q}$. One of the most important applications of the coherent one-phonon scattering process is the measurement of phonon dispersion relations, *i.e.* the measurement of the frequency ω_j as a function of the wavevector $\boldsymbol{q}$.

Incoherent elastic scattering cross-section.

The incoherent scattering cross-section obtained from eq. 3.21 for a Bravais crystal is given by

$$\left(\frac{d^2\sigma}{d\Omega dE_f}\right)_{inc} = \frac{\sigma_{inc}}{4\pi}\frac{k_f}{k_i}\frac{N}{2\pi\hbar}e^{\langle U^2\rangle}\int e^{\langle UV_0\rangle}e^{-i\omega t}dt \tag{3.37}$$

where $U = -i\mathbf{Q}\boldsymbol{u}_0(0)$, $V_0 = i\mathbf{Q}\boldsymbol{u}_0(t)$ and $\langle e^U e^{V_0}\rangle = e^{\langle U^2\rangle}e^{\langle UV_0\rangle}$. Analogously to the coherent case, the exponential term $e^{\langle UV_0\rangle}$ can be expanded in powers of $\langle UV_0\rangle$ (see eq. 3.24) and the pth will correspond to a p-phonon process. For the incoherent elastic cross-section, the exponential term in eq. 3.37 $e^{\langle UV_0\rangle}$ is equal to unity, and the expression takes the form

$$\left(\frac{d\sigma}{d\Omega}\right)_{inc\ elas} = N\sum_d \overline{b_d^2} - (\overline{b_d})^2 e^{-2W_d} \tag{3.38}$$

for a non-Bravais crystal. At low temperatures, the Debye-Waller factor e^{-2W_d} is close to unity, and the scattering is almost isotropic. Therefore, experimentally, the main contribution of the incoherent elastic cross-section is to the background.

Incoherent one-phonon scattering cross-section.

The incoherent one-phonon cross-section is obtained by replacing $e^{\langle UV_0\rangle}$ for $\langle UV_0\rangle$ (see phonon expansion in eq. 3.24) in eq. 3.37, obtaining

$$\left(\frac{d^2\sigma}{d\Omega dE_f}\right)_{inc\ 1\ ph} = \frac{k_f}{k_i}\sum_d \frac{1}{2M_d}\{\overline{b_d^2} - (\overline{b_d})^2\}e^{-2W_d}\sum_j \frac{|\mathbf{Q}\boldsymbol{e}_{dj}|^2}{\omega_j}\langle n+1\rangle\delta(\omega-\omega_j) \quad (3.39)$$

where $\boldsymbol{e}_{dj}$ is the polarization vector of the normal mode j. The δ-function establishes $\omega = \omega_j$ or eq. 3.4 as the energy condition to observe incoherent inelastic scattering. In the expression 3.39 there is no interference condition like for the coherent one-phonon scattering cross-section (eq. 3.36 (2)). Therefore, for a given $\boldsymbol{k}_f$, the scattering takes place for all normal modes whose ω_j satisfies this condition $\omega = \omega_j$. This implies that the cross-section depends only on the number of modes that have the correct frequency, thus, it can be expressed in terms of the generalized phonon density of states G(ω) [88] by

$$\left(\frac{d^2\sigma}{d\Omega dE_f}\right)_{inc\ 1\ ph} = \frac{k_f}{k_i}\sum_d \frac{N}{2M_d}\{\overline{b_d^2} - (\overline{b_d})^2\}\mathbf{Q}^2 e^{-2W}\frac{G(\omega)}{\omega}\langle n+1\rangle \quad (3.40)$$

for a non-Bravais crystal. For inelastic neutron scattering it is common to express the scattering cross-sections in terms of a function, S, called the *scattering function* or *scattering law*. This function is related to the observed intensities by

$$\frac{d^2\sigma}{d\Omega dE_f} = \frac{k_f}{k_i}\frac{\sigma}{4\pi}S(\mathbf{Q},\omega) \quad (3.41)$$

This equation separates the interaction of the neutrons with the sample, given by $(k_f/k_i)(\sigma/4\pi)$, from $S(\mathbf{Q},\omega)$ which describes the properties of the sample. The final expression for $S(\mathbf{Q},\omega)$ is

$$S(\mathbf{Q},\omega) = e^{-2W}\frac{Q^2\hbar}{2\overline{M}\omega}\langle n+1\rangle G(\omega) \quad (3.42)$$

In this section the scattering cross-sections for the four principal scattering processes have been presented. From coherent elastic scattering the bragg peaks can be measured and the atomic arrangement elucidated by relating the structure factor ($F_N(\mathbf{Q})$) to the observed intensities. The incoherent elastic scattering contributes mainly to the background. From coherent one-phonon scattering the dispersion relations can be obtained and from incoherent one-phonon scattering the phonon density of states may be determined. The multiphonon processes, which can be obtained by evaluating the successive terms in the phonon expansion (eq. 3.24), do not, in general, give useful information. They just add contributions to the background scattering, thus, they were not considered here.

In the next two sections, the principal advantages and experimental techniques of neutron diffraction and inelastic neutron scattering experiments are presented together with a brief description of the instruments used during this PhD.

3.4 Neutron powder diffraction experiments

All the samples measured during this project were powder samples. In this section, I will discuss the advantages of powder diffraction, the two main methods for carrying out this type of measurements together with a brief description of the instrument D20 used for data collection and the Rietveld method used for data analysis.
Since its development in 1913, powder diffraction has become one of the most important techniques for structure determination. Its success is due to essentially three features:

(i) Its well-defined physics, both conceptually and technically, of the diffraction process that allows an easy interpretation of the data, making it an accessible technique for non-crystallographers.

(ii) It provides information not only about the structure, but also about the microstructure, texture, morphology and phase composition of crystalline solid materials.

(iii) A large number of interesting materials cannot easily be synthesized as single crystals (*e.g.* zeolites, catalysts etc.) and powder diffraction is the only method available to obtain structural information.

The two alternative methods to make a diffraction experiment are time-of-flight (TOF) or energy-dispersive procedure and constant wavelength (CW) or angle-dispersive procedure. In the TOF technique, a white neutron beam ,*i.e.* neutrons with a wide range of wavelengths, is incident on a sample, keeping the detector at a fixed angle θ_0. As the neutron pulse travels toward the sample, the faster neutrons, *i.e.* with shorter wavelength, disperse from the slower neutrons, *i.e* with longer wavelength, arriving at different times to the detector. The time of flight from the source to the detector can be related to the wavelength by

$$t = 252.78 L \lambda \tag{3.43}$$

where L is the total length of the flight path measured in meters and t the time of flight in μsec. The different wavelengths of the scattered neutrons are related to different d-spacings by the Bragg's condition

$$\lambda' = 2 d_{hkl} sin\theta_0. \tag{3.44}$$

The final diffraction pattern is a measurement of the intensity with respect to the time-of-flight.

In the CW method, neutrons of a fixed wavelength, λ_0, are scattered by the sample and the intensity of the scattered beam is measured as a function of the scattering angle, 2θ. At each 2θ different d-spacings are measured following the Bragg's law

$$\lambda_0 = 2d_{hkl} sin\theta_{hkl}. \tag{3.45}$$

This is the most common way of perform a powder diffraction experiment and it was the technique used during this PhD. The instrument selected for this purpose was the diffractometer D20 located at the Institut Laue Langevin (ILL).

Instrument D20

D20 (see Fig. 3.3) is a high intensity two-axis diffractometer with variable resolution located in the thermal beam of the reactor hall in the ILL. It has a set of four monochromators (pyrolitic graphite PG (002), two Cu (200) monochromators and Germanium (113)) that allow to select the desired initial wavevector $\boldsymbol{k}_i$ from a white thermal neutron beam. Then, the monochromatic neutron beam leaves the monochromator shielding by one of its five take-off ports, each offering a different resolution. It then reaches the sample which diffracts it in many directions. Finally, the diffracted neutrons are simultaneously counted by a large microstrip multidetector during a certain time until a powder diffraction pattern with suitable intensity is obtained.

Rietveld refinement

Once the diffraction pattern is recorded, the data analysis aims at extracting the crystallographic information. Nowadays, the Rietveld refinement is the most common technique for this purpose.
The principle of the Rietveld method, proposed by Hugo Rietveld in 1969, is to minimize a function M which analyzes the difference between a calculated profile, y_{ci}, and the observed data y_i. More specifically, the refinement routine minimizes, by non-linear least squares approach, the function

$$M = \sum_i w_i(y_i - y_{ci})^2 \tag{3.46}$$

where $w_i = 1/\sigma_i^2$ is the weight assigned to the individual step intensity y_i (the parameter σ_i is the variance assigned to the observation y_i), y_i is the observed intensity at the ith step of the pattern, y_{ci} is the calcualted intensity at the ith step of the pattern and the

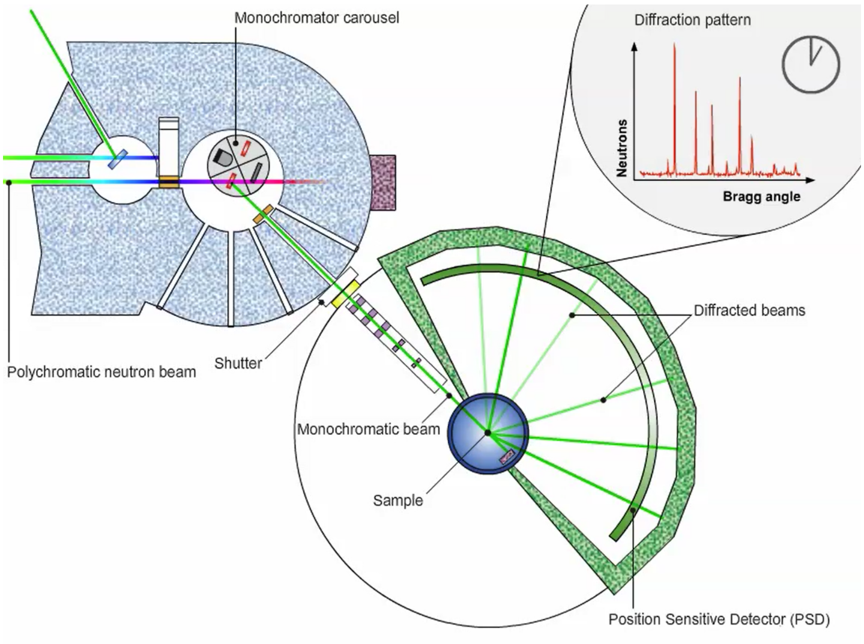

Figure 3.3: Schematic representation of the instrument D20 located at the ILL. Figure reproduced from [91]

sum runs over all data points i. The calculated intensity is given by

$$y_{ci} = \sum_{\phi=1}^{Phases} S \sum_{hkl} \Big(m_k L_k O_k |F_{hkl}|^2 \Omega(2\theta_k) + y_{bi} \Big) \tag{3.47}$$

where S is a scale factor, m_k is the multiplicity of the kth reflection, which accounts for symmetrically equivalent points in the reciprocal lattice, L_k is the Lorentz factor, defined by diffraction geometry and O_k is a factor intended to describe the effects of preferred orientation. The first summation runs over all contributing phases ϕ and the second one over all reflections contributing to a given step i. The background intensity, b_{bi}, can be estimated by linear extrapolation of points where peaks do not contribute or by a polynomial. The profile shape function (PSF) $\Omega(2\theta_k)$, describes the powder diffraction line shape. It takes into account intrumental resolution and sample broadening. Normally, the PSF's are pseudo-Voigt functions of the form

$$\Omega(2\theta) = \eta L(2\theta, H_L) + (1-\eta) G(2\theta, H_G) \tag{3.48}$$

where η is the mixing parameter ($\eta = 0$ for Gaussian and $\eta = 1$ for Lorentzian forms) and L and G denote a Lorentzian and Gaussian components, respectively. Rietveld refinement requires a good structural model, at least approximately *e.g.* the atomic positions and cell parameters, to start with. Therefore, it solves the problem of structure analysis but is not a method for structural determination.

3.5 Inelastic neutron scattering experiments

The advantages of using INS with respect to other well stablished optical techniques, *e.g.* infrared and Raman spectroscopy, can be summarized in the following points [87]:

(i) INS spectra can be accurately modelled. The measured INS intensities are related to the atomic displacements of the scattering atoms, which can often be obtained from simple classical dynamics. Indeed, the intensity and band positions can be accurately calculated using *ab initio* computational methods.

(ii) INS spectra, and in general neutron techniques, are highly sensitive to light atoms such as hydrogen, which has an uniquely high scattering cross-section (82.0 barn) in comparison to other atoms. Whereas optical techniques are more sensitive to heavy atoms.

(iii) INS techniques are not subject to the rules of optical selection. All vibrational modes are active and, in principle, measurable.

(iv) INS techniques can acces a wider spectral range (16-4000 cm^{-1}) in comparison to Raman or IR spectroscopy, for which access to low energy regions (below 400 cm^{-1}) is experimentally more complicated.

In a typical INS experiment the aim is to measure the scattering intensity $S(\mathbf{Q}, \omega)$ as a function of $(\mathbf{Q}, \omega)$. Therefore, it requires the knowledge of the energy transfer $\hbar\omega$ (eq.3.4) and momentum transfer $\mathbf{Q}$ (eq.3.5). There are two main techniques to perform an INS experiment: triple axis (TAS) and time-of-flight (TOF). For the latter, the instruments can be divided into *direct* and *indirect* geometry. Direct geometry instruments fix the initial energy of the neutrons, whereas the indirect geometry fix the final energy [87].

In a **TAS instrument**, a monochromatic neutron beam of wavevector $\boldsymbol{k_i}$ is selected from a white incident beam, using Bragg reflections from a single crystal, the monochromator. After being scattered by the sample, the neutron beam is reflected by a second monochromator, called the analyser, which is oriented such that only a given final wavevector, $\boldsymbol{k_f}$, is reflected onto a single detector.

A given configuration of the instrument corresponds to a single point in $(\mathbf{Q}, \omega)$ space. Due to the three axis of rotation (monochromator, sample and analyser), either $\boldsymbol{k_i}$ or $\boldsymbol{k_f}$ can be changed stepwise and the scattering angle varied and, in principle, any point in $(\mathbf{Q}, \omega)$ space can be measured. The main drawback of these intruments comes, in fact, from their ability to scan step-by-step any point of the $S(\mathbf{Q}, \omega)$ which makes the data accumulation very slow [87].

The instrument IN1-LAGRANGE [92, 93], located in the hot beam H8 of the reactor hall at the ILL, is a variant of a classical TAS spectrometer. In this instrument, the initial white neutron beam is reflected by one of its three monochromators (Cu(220), Si(311) or Si(111)). After selecting the desired initial wavevector, $\boldsymbol{k}_i$, the monochromatic neutron beam enters in a secondary spectrometer where the sample chamber is located (see Fig. 3.4). After being scattered by the sample, the scattered neutrons interact with a barrel-like analyser of pyrolitic graphite (PG) that reflects the neutrons with a fixed final energy of 4.5 meV into a single detector. Finally, the whole secondary spectrometer (sample, analyser and detector) moves along the vertical axis of the first monochromator varying the initial scattering angle, θ, to change the energy of the incident neutrons, recording, step-by-step, the whole inelastic spectra. The major difference with respect to a normal TAS instrument is the change in the trajectory of the scattered neutrons: while the incident beam is kept in the horizontal plane, the scattered neutrons propagate in the directions out of this plane, all around the vertical axis sample-detector, where the analyser is located.

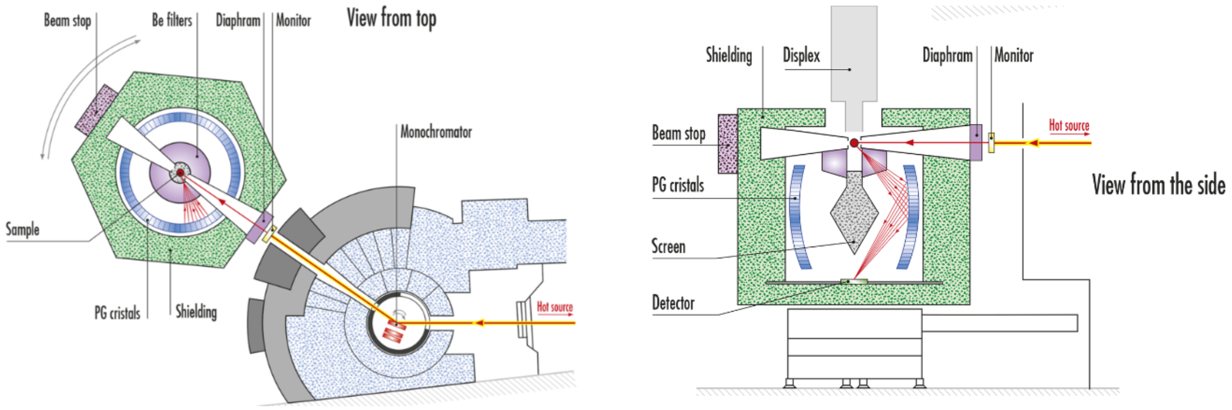

Figure 3.4: Schematic representation of the (left) top view and (right) side view of the instrument IN1 located at the ILL. Figure reproduced from [92]

The accesible range of $(\mathbf{Q}, \omega)$ space for IN1 is given by

$$\frac{\hbar^2 \mathbf{Q}^2}{2m_n} = 16.7\mathbf{Q}^2 = 2E_f + \hbar\omega - 2\{E_f(E_f + \hbar\omega)\}^{1/2} cos\theta. \tag{3.49}$$

This expression can be obtained considering $\hbar/(2m_n) = 16.7cm^{-1}\AA^{-2}$ and combining eqs. (3.5) and (3.3). The eq. 3.49 gives rise to a parabola (see Fig. 3.5) with an almost fixed trajectory along $(\mathbf{Q}, \omega)$ space. This is due to the fact that the final energy (hence

$\boldsymbol{k}_f$) is too small in comparison to the incident energies (and hence $\boldsymbol{k}_i$), so the momentum transfer $\mathbf{Q}$ is almost equal to $\boldsymbol{k}_i$ and almost independent of the scattering angle [87, 94]. Therefore, eq. 3.49 can be approximated to:

$$\mathbf{Q}^2 \approx E/16.7 \tag{3.50}$$

where energy is in cm^{-1} and $\mathbf{Q}$ in $\mathring{A}^{-1}$.

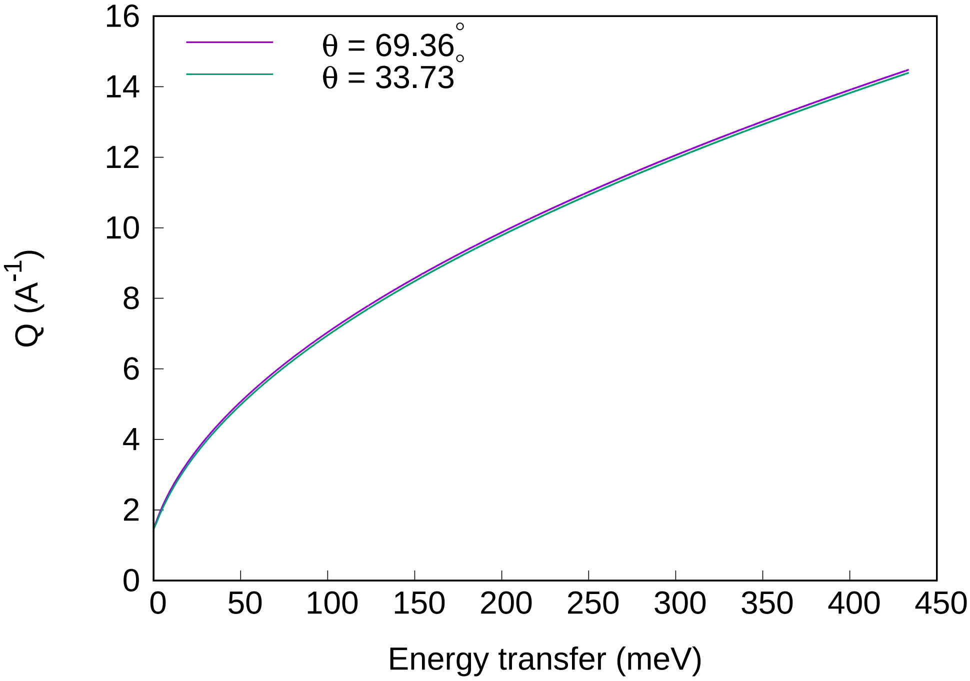

Figure 3.5: Kinematic range of IN1-LAGRANGE. The final energy is set to 4.5 meV (36.3 cm^{-1}) and the scattering angle goes from 33.73° to 69.36°

Direct geometry instruments use a monochromator or chopper to fix the initial energy. These spectrometers are able to measure the $\mathbf{Q}$ and ω independently. Neutrons with the same final energy, or $\boldsymbol{k}_f$, can be scattered in different directions, or scattering angle θ. The momentum transfer, $\mathbf{Q}$, is different for each scattering angle, therefore, detectors located at different angles allow to measure $\mathbf{Q}$ at a given energy transfer (see Fig. 3.6 (a)). On the other hand, neutrons scattered with the same angle θ, can have different energy transfer, or $\boldsymbol{k}_f$, thus, the energy transfer can be measured at a given $\mathbf{Q}$ (see Fig. 3.6 (b)). In these instruments, a detector located at a scattering angle θ performs a scan in time resulting in a parabola in $(\mathbf{Q}, \omega)$ space (see Fig. 3.7), given by the relation:

$$\frac{\hbar^2\mathbf{Q}^2}{2m_n} = 16.7\mathbf{Q}^2 = 2E_i - \hbar\omega - 2\{E_i(Ei - \hbar\omega)\}^{1/2}cos\theta \tag{3.51}$$

This expression can be obtained in a similar way than eq. 3.49 but expressing it in terms of incident energy, E_i, which is fixed. From Fig. 3.6, it can be seen that the trajectory along $(\mathbf{Q}, \omega)$ strongly depends on the scattering angle, θ.

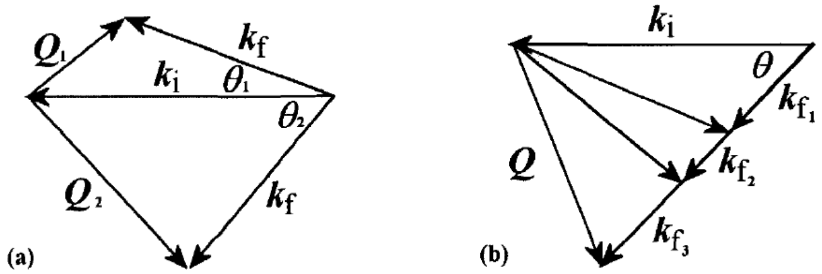

Figure 3.6: Scattering triangles for a direct geometry instrument. a) Neutrons at constant energy transfer are detected at different scattering angles θ and (b) Neutrons at constant $\mathbf{Q}$ are detected at different energy transfer. Figure reproduced from [87]

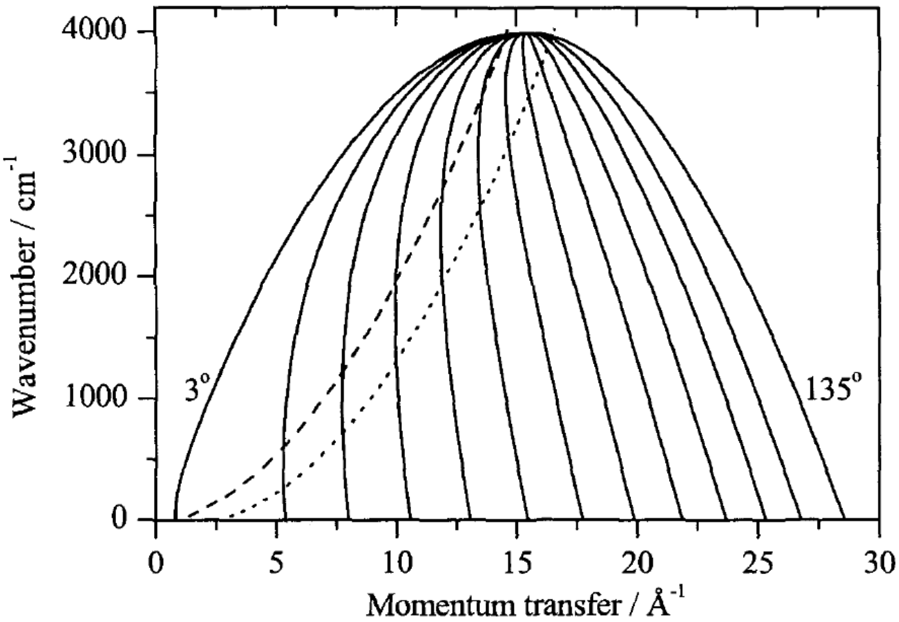

Figure 3.7: Trajectories in $(\mathbf{Q}, \omega)$ space for a direct geometry instrument at angles 3, 20, 30, 40, 50, 60, 70, 80, 90, 100, 110, ,120 and 135° and with incident energy of 4000 cm^{-1}. The dashed lines are the trajectories for an indirect geometry instrument at two different angles, 45 (long dashes) and 135° (short dashes) and final energy of 28 cm^{-1}. Figure reproduced from [87]

The instrument PANTHER [95] is an example of a direct geometry TOF instrument located at the thermal beam H12 in the reactor hall of the ILL. It is optimized for energy transfers in the range 2-60 meV. In this instrument, the initial neutron energy is fixed by a monochromator of pyrolytic graphite or Cu(220) (see Fig. 3.8). The monochromatic neutron beam passes through a slit Fermi chopper which produces short neutron pulses before they enter in the sample chamber. Finally, after passing through a radial collimator, the scattered neutron beam is detected by position-sensitive detectors (PSD) and the spectra are recorded. Other components like a saphire filter, background choppers or a diaphragm are also distributed along the instrument to reduce the background or to shape the neutron beam.

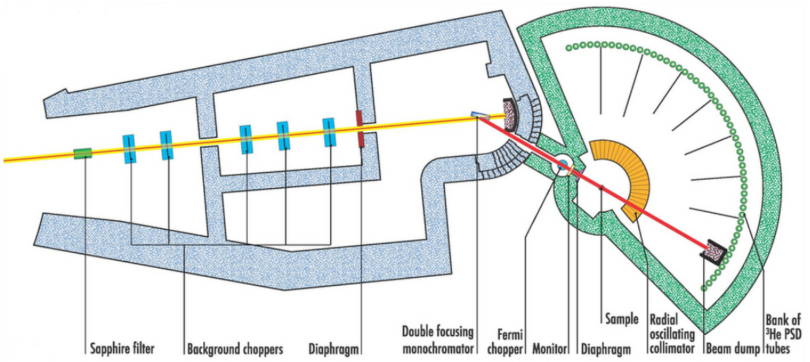

Figure 3.8: Schematic representation of PANTHER instrument located at the ILL. Figure reproduced from [95]

Another example of a direct geometry instrument is IN5 [96], located at the ILL.

The **indirect geometry** instruments work with a fixed final energy. Unlike the direct geometry instruments, the indirect spectrometers with low final energy work with a fixed trajectory through $(\mathbf{Q}, \omega)$ space, similar to the IN1 trajectories (see Fig. 3.5). The trajectories can be plotted with eq 3.49 or 3.50, if the low final energies are considered. An example of the trajectories in $(\mathbf{Q}, \omega)$ space can be seen in Fig. 3.7. An example of an indirect geometry spectrometer is the TOSCA isntrument located at ISIS [97].

This section closes the topic on neutron scattering. The next four sections are dedicated to a brief description of the theoretical fundaments of density functional theory and density perturbation theory used during this PhD.

3.6 Variational principle

In quantum mechanics, the main objective is to solve the time-independent Schrödinger equation,

$$\hat{H}\psi = E\psi. \tag{3.52}$$

where ψ is the eigenfunction of the Hamiltonian operator $\hat{H}$ representing the wavefunction of the system. However, the Schödinger equation can be solved exactly for a few simple systems (particle in a box, harmonic oscilator, rigid rotor and hydrogen atom). For systems with more than one electron, the Schrödinger equation cannot be analytically solved and the wavefunction ψ may be approximated by a trial wavefunction , ϕ. The trial function ϕ will no longer be an eigenfunction of the Hamiltonian operator and the accuracy of the approximation is assesed based on how close the expectation value of $\hat{H}$ for ϕ given by

$$\tilde{E} = \frac{\langle\phi|\hat{H}|\phi\rangle}{\langle\phi|\phi\rangle}, \tag{3.53}$$

is to the actual energy eigenvalue, E_0. In general, we are more interested in the ground state of the system, ψ_0, and, E_0 represents the associated ground state energy. The variational principle establishes that the expectation value of the Hamiltonian, $\hat{H}$, obtained with any approximated ground trial wavefunction is greater or equal to the real ground state energy:

$$\tilde{E} \geq E_0 \tag{3.54}$$

The equality symbol is only satified if the trial wavefunction is the actual wavefunction that describes the system. In practice, the variational problem can be solved adopting two different strategies:

(1) Assume a single wavefunction written in terms of one or more p_N parameters

$$\phi = \phi(p_1, p_2, ..., p_N) \tag{3.55}$$

and minimize over the parameters. Then, it is possible to find a good approximation of the total ground state energy, E_0, by looking for the values of p_N that gives the lowest values of $\tilde{E}$.

(2) Assume a linear combination of wavefunctions without any parameters and minimize over the coefficients of the expansion. This is called the linear variational method.

3.7 The electronic Hamiltonian

The properties of atoms, molecules and solids can be studied by determining the many-body Hamiltonian. For a system of electrons and nuclei it is convenient to adopt the Born-Oppenheimer or adiabatic approximation [98]. This approximation is based on the fact that the mass of the electron is much smaller compared to the nuclei, causing the time scale of the motion of electrons to be much larger than that of the nuclei. The response time of the electrons to any change in the positions of the nuclei is considered to be immediate, thus the different terms of the Hamiltonian depend only on electronic variables and only parametrically on the nuclei positions.

The electronic Hamiltonian for a system with N_e electrons can be written as

$$H = T_e + V_{ext} + V_{ee}, \tag{3.56}$$

where T is the electron kinetic energy operator that represents the sum of the kinetic energy over N_e. The potential terms V_{ext} and V_{ee} are the potential acting on the electrons due to nuclei and the electron-electron interaction, respectively. The external potential V_{ext} is a Coulombic interaction involving one electron at a time. Most of the efforts to solve the many-body problem are focussed on trying to find good approximations to simplify the electron-electron interaction.

The extended expression of eq. 3.56 in Hartree atomic units ($\hbar = m_e = e = 4\pi/\epsilon = 1$) is given by

$$H = -\frac{1}{2}\sum_{i}^{N_e} \nabla_i^2 - \sum_{i}^{N_e}\sum_{I}^{N_n} \frac{Z_I}{|\boldsymbol{r}_i - \boldsymbol{R}_I|} + \frac{1}{2}\sum_{i}^{N_e}\sum_{j\neq i}^{N_e} \frac{1}{|\boldsymbol{r}_i - \boldsymbol{r}_j|} \tag{3.57}$$

where $\boldsymbol{r}_i$ ($\boldsymbol{r}_j$) and $\boldsymbol{R}_I$ are the position vectors of the ith (jth) electron and Ith nucleus, respectively, and Z_I is the charge of the Ith nucleus.

It is imposible to solve the Schrödinger equation for a many-electron wavefunction due to the exponential growth in degrees of freedom with increasing number of particles. There are two type of approximate methods that can be use to solve eq. 3.57. These are, $wavefunction - based$ or $density - based$ methods and each of them can be further subdivided into different approaches. The $wavefunction - based$ methods calculate observables using a explicit form for the wavefunction. They can be perturbational methods (*e.g.* Moller-Plesset) or variational methods (*e.g* Hartree-Fock or configuration interaction (CI)). In the $density - based$ methods the wavefunction is not written explicity, instead, the total energy is expressed as a functional of the electronic density of the system, $\rho(\mathbf{r})$. Examples of this method are the Thomas-Fermi approximation or the Density-Functional

Theory (DFT) which is the one used during this PhD project. In the next subsection an overview of the DFT theory is presented.

3.8 Density Functional Theory

The central core of DFT is that any property of a many interacting particle system can be viewed as a functional of the ground state density, $\rho_0(\mathbf{r})$. The existence proofs of such functionals are given by the Hohenberg and Kohn theorems [99]. The approach of Hohenberg and Kohn can be applied to any sytem of interacting particles in an external potential $V_{ext}(\mathbf{r})$ for which the hamiltonian is expressed (using atomic units $\hbar = m_e = e = 4\pi/\epsilon_0 = 1$) by

$$H = -\frac{1}{2}\sum_i \nabla_i^2 + \sum_i V_{ext}(\mathbf{r}_i) + \frac{1}{2}\sum_{i\neq j} \frac{1}{|\mathbf{r}_i - \mathbf{r}_j|}. \tag{3.58}$$

In the case of a many-electron system, the external potential $V_{ext}(\mathbf{r})$ is generated by the nuclei. The first theorem by Hohenberg and Kohn states that for any system of interacting particles, the external potential, $V_{ext}(\mathbf{r})$, acting on those particles is a unique functional of the ground-state electronic charge density, $\rho_0(\mathbf{r})$. Therefore, all the properties of the system are determined by the ground state density $\rho_0(\mathbf{r})$. The second theorem establishes that, for any external potential $V_{ext}(\mathbf{r})$, a universal functional for the energy $F[\rho(\mathbf{r})]$ can be defined in terms of the density $\rho(\mathbf{r})$, *i.e.*

$$F[\rho(\mathbf{r})] = T[\rho(\mathbf{r})] + \frac{1}{2}\int \frac{\rho(\mathbf{r})\rho(\mathbf{r}')}{|\mathbf{r} - \mathbf{r}'|} dr dr' \tag{3.59}$$

where $T[\rho(\mathbf{r})]$ is the kinetic functional and the integral represents the classical Coulomb interaction energy of the electron density $\rho(\mathbf{r})$ interacting with itself, also known as Hartree energy. The minimization of the functional $F[\rho(\mathbf{r})]$ for a given $V_{ext}(\mathbf{r})$ corresponds to the ground state energy of the system, E_0, and the density $\rho(\mathbf{r})$ that minimizes the functional is the exact ground state density $\rho_0(\mathbf{r})$. Since all properties of the system are uniquely determined and expressed as a functional of $\rho(\mathbf{r})$, one can write the total energy as a functional of the density

$$E = F[\rho(\mathbf{r})] + \int V_{ext}(\mathbf{r})\rho(\mathbf{r}) dr \tag{3.60}$$

The Hohenberg-Kohn theorems allowed to reformulate the many-body problem in terms of the charge density $\rho(\mathbf{r})$ instead of the wavefunctions Ψ, making it a more tractable problem. However, they provide no guidance for constructing the functionals and no exact functionals are known for many-particle systems. Nowadays, density functional theory is a useful tool thanks to the approach proposed by Kohn and Sham [100]. This approach replaces the original many-body problem by an auxiliary independent-particle problem so that the exact ground state density can be expressed by the ground state density of the auxiliary non-interacting system. The Kohn-Sham Hamiltonian, H_{KS}, has the usual kinetic operator and an effective local potential $V_{eff}(\mathbf{r})$ acting on an electron at point $\mathbf{r}$ and it is given by

$$H_{KS} = -\frac{1}{2}\nabla^2 + V_{eff}(\mathbf{r}). \tag{3.61}$$

The density of the auxiliary system, composed of N independent electrons, is given by a sum of norm squares of single-particle orbitals, called Kohn-Sham orbitals, expressed by

$$\rho(\mathbf{r}) = \sum_{i=1}^{N} |\phi_i^{KS}(\mathbf{r})|^2 \tag{3.62}$$

and the independent-particle kinetic energy T_s by

$$T_s = -\frac{1}{2}\sum_{n=1}^{N}\langle\phi_i^{KS}|\nabla^2|\phi_i^{KS}\rangle = -\frac{1}{2}\sum_{n=1}^{N}\int dr\phi_i^{KS} * (\mathbf{r})\nabla^2\phi_i^{KS}(\mathbf{r})dr. \tag{3.63}$$

The Kohn-Sham approach replaces the Hohenberg-Kohn expression for the ground state energy functional (eq. 3.60) in the form of an energy functional for a non-interacting many-body system given by

$$E_{KS} = T_s[\rho(\mathbf{r})] + \int V_{ext}(\mathbf{r})\rho(\mathbf{r})dr + \frac{1}{2}\int \frac{\rho(\mathbf{r})\rho(\mathbf{r}')}{|\mathbf{r}-\mathbf{r}'|}drdr' + E_{xc}[\rho(\mathbf{r})]. \tag{3.64}$$

All many-body effects due to exchange and correlation are grouped into the exchange and correlation energy, E_{xc}.

The single-particle Kohn-Sham wavefunctions, $\phi^{KS}(\mathbf{r})$, can be obtained by solving the Kohn-Sham system of equations

$$H_{KS}\phi_i^{KS}(\mathbf{r}) = -\frac{1}{2}\nabla^2\phi_i^{KS}(\mathbf{r}) + \left[V_{ext}(\mathbf{r}) + \frac{1}{2}\int \frac{\rho(\mathbf{r})\rho(\mathbf{r}')}{|\mathbf{r}-\mathbf{r}'|}drdr' + V_{xc}(\mathbf{r})\right]\phi_i^{KS}(\mathbf{r}) = \varepsilon_i\phi_i^{KS}(\mathbf{r}) \tag{3.65}$$

self-consistently, where the ε_i are the eigenvalues and the terms inside the braquets represent the effective potential $V_{eff}(\mathbf{r})$:

$$V_{eff} = V_{ext}(\mathbf{r}) + \frac{1}{2}\int \frac{\rho(\mathbf{r}')}{|\mathbf{r}-\mathbf{r}'|}dr' + V_{xc}(\mathbf{r}) \tag{3.66}$$

The exchange-correlation potential, $V_{xc}(\mathbf{r})$, is the functional derivative of E_{xc}, which can be expressed as

$$V_{xc} = \epsilon_{xc}[\rho(\mathbf{r})] + \rho(\mathbf{r})\frac{\delta\epsilon_{xc}[\rho(\mathbf{r})]}{\delta\rho(\mathbf{r})} \tag{3.67}$$

where $\epsilon_{xc}[\rho(\mathbf{r})]$ is defined by

$$E_{xc} = \int dr\rho(\mathbf{r})\epsilon_{xc}[\rho(\mathbf{r})] \tag{3.68}$$

The Kohn-Sham equations allow to separate the independent-particle kinetic energy and the long-range Hartree terms. The remaining term, the exchange-correlation functional, $E_{xc}[\rho(\mathbf{r})]$, can be reasonably approximated as a local, semi-local or non-local functional of the density. Even though the exact functional $E_{xc}[\rho(\mathbf{r})]$ is unknown, several approximations exist:

- **Local Density Approximation (LDA):** It is the oldest and simplest approximation to the exchange-correlation functional, it assumes a local functional of the density at each point of the space r, *i.e.*:

  $$E_{xc}^{LDA} = \int \rho(\mathbf{r})\epsilon_{xc}^{hom}[\rho(\mathbf{r})]dr \tag{3.69}$$

  where ϵ_{xc}^{hom} is the exchange correlation energy density of an interacting homogeneous electron gas at the density $\rho(\mathbf{r})$. The exchange part of ϵ_{xc}^{hom} can be calculated exactly using the Hartree-Fock approach [101, 102] and the correlation part has been calculated with accurate Monte Carlo methods [103]. Although LDA is a very simple approach, it has proven to be a successful approximation, especially for systems where the charge density varies smoothly in the space. The reason is, in part, due to the cancellation of errors where LDA typically overestimates E_x, while it underestimates E_c.

- **Generalized Gradient Approximation (GGA):** The main assumption of LDA is to consider all systems as homogeneous, however, real systems are clearly inhomogeneous. GGA functionals include not only the information about the density at a particular point r, like LDA does, but also density gradients, $\nabla\rho(\mathbf{r})$, in order to account fo the non-homogeneity of the electron density, *i.e.*:

  $$E_{xc}^{GGA} = \int \rho(\mathbf{r})f\left[\rho(\mathbf{r}), \nabla\rho(\mathbf{r})\right]dr \tag{3.70}$$

where different parametrizations of the function f have been proposed *e.g* PW91 [104], PBE [105], PBEsol [106] and rev-vdW-DF2 [107] among others. In general, GGA functionals give better results than LDA for, almost, the same computational cost. Further approximations are available, *e.g.* by adding the Laplacian of the density $\nabla^2\rho(\mathbf{r})$ and/or the kinetic energy density $\tau(\mathbf{r})$, *i.e.*:

$$E_{xc}^{mGGA} = \int \rho(\mathbf{r}) f \left[\rho(\mathbf{r}), \nabla\rho(\mathbf{r}), \nabla^2(\rho(\mathbf{r}), \tau(\mathbf{r}))\right] dr. \tag{3.71}$$

The functionals that follow this approximation are called meta-gradient approximation (meta-GGA) functionals. Examples of this functionals are the TPSS [108] and M06-L [109].

- **Hybrid functionals:** These functionals result from the combination of the above-mentioned exchange-correlation functionals (LDA, GGA and meta-GGA) with a portion of the Hartree-Fock exchange [101]. An example of a hybrid functional is the well-known B3LYP [110, 111].

3.9 Density Functional Perturbation Theory: Phonon calculation

In section 3.3 we have seen how the INS intensity is related to the scattering function $S(\mathbf{Q}, \omega)$ (eq. 3.42), which depends on the generalized phonon density of states, $G(\omega)$

$$G(\omega) = \sum_{I=1} \sum_{q,j} |u_I(j, \mathbf{q})|^2 \delta(\omega - \omega_I(\mathbf{q})) \frac{\sigma_I}{M_I} \tag{3.72}$$

where σ_I and M_I are the incoherent neutron scattering cross-section and mass of the Ith atom, $\omega_I(\mathbf{q})$ is the phonon frequency of the j-branch at $\mathbf{q}$ wavevector and $u_I(j, \mathbf{q})$ is the corresponding atomic displacement.

From the Born-Oppenheimer approximation (section 3.7) we can decouple the electronic and vibrational degrees of freedom, and the lattice dynamics properties can be computed by solving the Schrödinguer equation (eq. 3.65). The equilibrium geometry of a system is given by the condition that the forces acting on individual nuclei vanish:

$$\boldsymbol{F}_I = -\frac{\delta E(\boldsymbol{R})}{\delta \boldsymbol{R}_I} = 0 \tag{3.73}$$

where $E(\boldsymbol{R})$ is the ground state energy of the system of interacting electrons moving in the field of fixed nuclei, which depend on the nuclei positions $\boldsymbol{R}$. The vibrational frequencies

ω are determined by the eigenvalues of the Hessian of the energy, scaled by the nuclear masses:

$$det \left| \frac{1}{\sqrt{M_I M_J}} \frac{\partial^2 E(\boldsymbol{R})}{\partial \boldsymbol{R}_I \partial \boldsymbol{R}_J} - \omega^2 \right| = 0 \tag{3.74}$$

Therefore, from eqs. 3.73 and 3.74, to compute the equilibrium geometry and ω of a sytem we have to compute the first and second derivative of the energy. The theorem of Hellmann-Feynman states that the first derivative of the eigenvalues, $\frac{\delta E(\boldsymbol{R})}{\delta \mathbf{R}_I}$, is given by the expectation value of the derivative of the Hamiltonian, therefore, the force acting on the Ith nucleus in the electronic ground state can be expressed as

$$\boldsymbol{F}_I = -\frac{\partial E(\boldsymbol{R})}{\partial \boldsymbol{R}_I} = \left\langle \phi_{\boldsymbol{R}} \left| \frac{\partial H_{\boldsymbol{R}}}{\partial \boldsymbol{R}_I} \right| \phi_{\boldsymbol{R}} \right\rangle \tag{3.75}$$

where $\phi_{\boldsymbol{R}}$ is the eigenfunction of $H_{\boldsymbol{R}}$ corresponding to the $E_{\boldsymbol{R}}$ eigenvalue given by $H_{\boldsymbol{R}}\phi_{\boldsymbol{R}} = E_{\boldsymbol{R}}\phi_{\boldsymbol{R}}$. The Hamiltonian $H_{\boldsymbol{R}}$ depends on $\boldsymbol{R}$ via the electron-ion interaction. Thus, the Hellmann-Feynman theorem states that:

$$\boldsymbol{F}_I = -\int \rho_{\boldsymbol{R}}(\mathbf{r}) \frac{\partial V_{ext}(\mathbf{r})}{\partial \boldsymbol{R}_I} dr - \frac{\partial E_N(\boldsymbol{R})}{\partial \boldsymbol{R}_I} \tag{3.76}$$

where E_N is the electrostatic interaction between different nuclei and $V_{ext}(\mathbf{r})$ is the electron-nucleus interaction given by

$$V_{ext} = -\sum_{iI} \frac{Z_I}{|\boldsymbol{r}_i - \boldsymbol{R}_I|} \tag{3.77}$$

and $\rho_{\boldsymbol{R}}(\mathbf{r})$ is the ground-state electron charge density corresponding to the nuclear configuration $\boldsymbol{R}$.

The Hessian of the energy (eq. 3.74) is obtained by differentiating the Hellmann-Feynman forces (eq. 3.76) with respect to nuclear coordinates:

$$\frac{\partial^2 E(\boldsymbol{R})}{\partial \boldsymbol{R}_I \partial \boldsymbol{R}_J} = -\frac{\partial \boldsymbol{F}_I}{\partial \boldsymbol{R}_J} = \int \frac{\partial \rho_{\boldsymbol{R}}(\mathbf{r})}{\partial \boldsymbol{R}_J} \frac{\partial V_{ext}(\mathbf{r})}{\partial \boldsymbol{R}_I} dr + \int \rho_{\boldsymbol{R}}(\mathbf{r}) \frac{\partial^2 V_{ext}(\mathbf{r})}{\partial \boldsymbol{R}_I \partial \boldsymbol{R}_J \boldsymbol{R}} dr + \frac{\partial^2 E_N(\boldsymbol{R})}{\partial \boldsymbol{R}_I \partial \boldsymbol{R}_J} \tag{3.78}$$

Equation 3.78 establishes that the calculation of the energy requires the calculation of the ground-state electron density $\rho_{\boldsymbol{R}}(\mathbf{r})$ and its linear response to a distorsion of the geometry, $\partial \rho_{\boldsymbol{R}}(\mathbf{r})/\partial \boldsymbol{R}_I$. The second derivative of the energy, $\frac{\partial^2 E(\boldsymbol{R})}{\partial \boldsymbol{R}_I \partial \boldsymbol{R}_J}$, is called the interatomic force constant (IFC). The linear response is calculated by density functional perturbation theory by linearizing eqs. 3.62, 3.65 and 3.66 with respect to wavefunction, density and potential variations. Linearization of eq. 3.62 is

$$\Delta\rho(\mathbf{r}) = 4Re\sum_{n=1}^{N/2}\phi_i^{KS*}(\mathbf{r})\Delta^{\boldsymbol{R}}\phi_i^{KS}(\mathbf{r}) \tag{3.79}$$

where the finite-difference operator $\Delta^{\boldsymbol{R}}$ is defined by

$$\Delta^{\boldsymbol{R}}F = \sum_I \frac{\partial F_I}{\partial \boldsymbol{R}_I}\Delta\boldsymbol{R}_I \tag{3.80}$$

The variation of the Kohn-Sham oritals $\Delta^{\boldsymbol{R}}\phi_i^{KS}(\mathbf{r})$ is obtained by first order perturbation theory:

$$(H_{KS} - \epsilon_i)|\Delta\phi_i^{KS}\rangle = -(\Delta V_{eff} - \Delta\epsilon_i)|\phi_i^{KS}\rangle \tag{3.81}$$

where H_{KS} is the unperturbed Kohn-Sham Hamiltonian defined in eq. 3.65,

$$\Delta V_{eff} = \Delta V_{ext}(\mathbf{r}) + \frac{1}{2}\int\frac{\Delta\rho(\mathbf{r}')}{|\mathbf{r}-\mathbf{r}'|}dr' + \frac{dV_{xc}[\rho(\mathbf{r})]}{d\rho(\mathbf{r})}\Delta\rho(\mathbf{r}) \tag{3.82}$$

is the first order correction to the effective potential (eq. 3.66) and $\Delta\epsilon_i = \langle\phi_i^{KS}|\Delta V_{eff}|\phi_i^{KS}\rangle$ is the first order variation of the Kohn-Sham eigenvalue ϵ_i.

The equations 3.79, 3.80, 3.81, 3.82 and the H_{KS} from eq. 3.65 form a set of self-consistent equations for the perturbed system. By solving the system of equations self-consistently, one obtains the second derivatives of eq. 3.78.

In crystalline solids, the position of a nucleus Ith is given by

$$\boldsymbol{R}_I = \boldsymbol{R}_a + \boldsymbol{\tau_l} + \boldsymbol{u}_l(a) \tag{3.83}$$

where $\boldsymbol{R}_a$ is the position of the ath unit cell in the Bravais lattice, $\boldsymbol{\tau_l}$ is the equilibrium position of the atom in the unit cell, and $\boldsymbol{u}_l$ indicates the deviation from the equilibrium position. Due to translational invariance, the matrix of interatomic force constants depends on the positions of the unit cells a and b only through the difference $\boldsymbol{R} = \boldsymbol{R}_a$ - $\boldsymbol{R}_b$ and it can be expressed as

$$C_{I\alpha,J\beta}(a,b) = \frac{1}{\sqrt{M_I M_J}}\frac{\partial^2 E}{\partial u_{I\alpha}^a \partial u_{J\beta}^b} \tag{3.84}$$

where $u_{I\alpha}^a$ is the displacement of atom I in the cartesian direction α in the unit cell a and M_I is the atomic mass of atom I. The IFC matrix is related to the dynamical matrix by

$$\tilde{D}_{I\alpha,J\beta}(\mathbf{q}) = \frac{\tilde{C}_{I\alpha,J\beta}(\mathbf{q})}{\sqrt{M_I M_J}} = \frac{1}{\sqrt{M_I M_J}} \sum_b C_{I\alpha,J\beta}(a,b) e^{-i\mathbf{q}\vec{R}_b} \tag{3.85}$$

where $\tilde{C}_{I\alpha,J\beta}(\mathbf{q})$ is the discrete Fourier transform of the interatomic force constants (IFC) in real space.

Finally, the phonon frequencies ω, and eigenvectors, $\boldsymbol{u}$, are determined by diagonalization of the dynamical matrix obtained from the secular equation (eq. 3.74)

$$\sum_{J\beta} \tilde{D}_{I\alpha,J\beta}(\mathbf{q}) u_{J\beta}(\mathbf{q}) = \omega_q^2(\mathbf{q}) u_{I\alpha}(\mathbf{q}) \tag{3.86}$$

where $u_{I\beta}(\mathbf{q})$ is the atomic displacement of atom I*th* along the cartesian direction β at $\mathbf{q}$ wavevector.

The density functional perturbation theory [112, 113], also called linear response method, provides an analytical way of constructing the dynamical matrix and hence the phonon structure. Other methods can be used to calculate the second derivatives of the energy, such as the *frozen phonon* (FP) method [114] (also called *finite displacement* (FD) method) which uses a finite different approach of the form

$$C_{I\alpha,J\beta}(0,b) \approx \frac{1}{\sqrt{M_I M_J}} \frac{\partial^2 E}{\partial u^0_{I\alpha} \partial u^b_{J\beta}} = \frac{1}{\sqrt{M_I M_J}} \frac{\partial}{\partial u^0_{I\alpha}} \left(\frac{\partial E}{\partial u^b_{J\beta}} \right) = -\frac{1}{\sqrt{M_I M_J}} \frac{\partial F^a_{J\beta}}{\partial u^0_{I\alpha}}. \tag{3.87}$$

This equation tells us that if we displace the atom I in the unit cell along the cartesian direction α, $\partial u^0_{I\alpha}$, and compute how the forces change on atom J in the unit cell a along the direction β, $\partial F^a_{J\beta}$, we can obtain the force constant matrix in real space, $C_{I\alpha,J\beta}(0,b)$. The finite difference approach only requires solving the Kohn-Sham equations self-consistently for the original system and several perturbed systems. The DFPT differs from the *frozen phonon* method in the fact that DFPT uses perturbation theory to compute the change in the Hamiltonian under a given perturbation of charge density or wavefunction, while the finite difference method computes the derivative numerically.

An example of a software package that runs with FD approach is SIESTA [115, 116] and with DFPT is QuantumEspresso package [117, 118, 119]. The latter is the one used during this PhD.

Chapter 4

Hidden ordered structure in the archetypical Fe(pyrazine)[Pt(CN)$_4$] spin-crossover porous coordination compound

Ángel Fernández-Blanco[1,2], Lorenzo A. Mariano[2], Lucía Piñeiro-López[3], José Antonio Real[4], Jose Sanchez Costa[3], Roberta Poloni[2], J. Alberto Rodríguez-Velamazán[1]

[1] *Institut Laue Langevin, 71 Avenue des Martyrs, CS 20156-38042, Grenoble, France*

[2] *SIMaP, Grenoble-INP, University of Grenoble-Alpes, CNRS, 38042 Grenoble, France*

[3] *IMDEA Nanociencia, Faraday 9, Ciudad Universitaria de Cantoblanco, 28049 Madrid, Spain*

[4] *Departamento de Química Inorgánica, Insituto de Ciencia Molecular (ICMol), Universidad de Valencia, 46980, Paterna, Spain*

Ángel Fernández-Blanco, Lorenzo A. Mariano, Lucía Piñeiro-López, José Antonio Real, Jose Sanchez Costa, Roberta Poloni, J. Alberto Rodríguez-Velamazán, “Hidden ordered structure in the archetypical Fe(pyrazine)[Pt(CN)$_4$] spin-crossover porous coordination compound”, *CrystEngComm*, vol. 24, p. 6349-6356, 2022.

4.1 Abstract

Despite the fact that Fe(pyrazine)[M^{II}(CN)$_4$] (where M^{II} is a metal in open square-planar configuration, namely Pt, Pd, Ni) is one of the most thoroughly studied families of spin-crossover compounds, its actual structure has remained imprecisely known up to now. Using neutron diffraction and density-functional theory calculations, we demonstrate that the pyrazine rings, instead of being disordered in two orthogonal positions in the low-spin phase, adopt an ordered arrangement with the rings alternatively oriented in these two positions. This finding has a direct implication on the most characteristic property of these systems, the spin-crossover transition, which is notably affected by this arrangement. This is because the energy difference between both spin states depends on the pyrazine configuration and the ordering of the rings changes the balance of entropy contributions to the entropy-driven spin-crossover phenomenon.

4.2 Introduction

Coordination chemistry has experienced a remarkable surge in the last years largely due to the burgeoning of metal-organic frameworks (MOFs), a topic where the structure-property correlation plays a crucial role. Evidently, X-ray diffraction is an essential tool in this research field, but it has some limitations that may be overcome with other techniques. In this line, neutron diffraction is a powerful complement, in particular for cases where hydrogen positioning is important, since it gives information that can be essential, as we illustrate in this work.

A new field opened for spin-crossover (SCO) materials [120] when the bistability provided by the SCO phenomenon was combined with porosity in a porous coordination polymer (PCP) or a MOF [121]. This combination opened a vast playground of possibilities for applications in fields like gas capture [40] or chemical sensing [122], since SCO can both modulate the interaction with the guest molecule and be modulated by the interaction with an adsorbed molecule [85, 123, 80, 124, 125]. An archetypical example of this class of compounds is the family Fe(pyrazine)[M^{II}(CN)$_4$] (where M^{II} is a metal in open square-planar configuration, namely Pt, Pd, Ni) [71, 126]. Based on the classical Hofmann clathrate compounds [75], these three-dimensional frameworks present, together with the mentioned combination of porosity and SCO [83, 127], an extremely rich display of functional properties. These include, for example, chemo-[81, 128, 129] and photo-switching [130, 59, 131] molecular rotation correlated with the change of spin

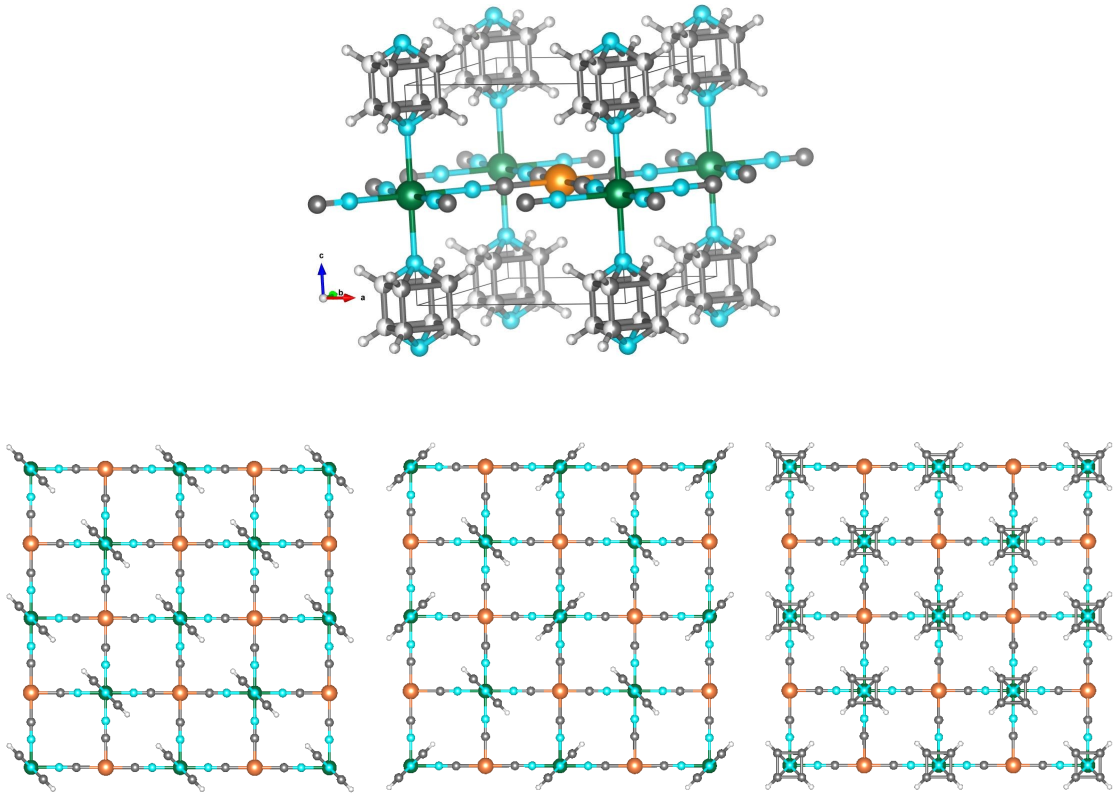

Figure 4.1: (Top) Scheme of the crystal structure of Fe(pyrazine)[$M^{II}(CN)_4$] with the pyrazine rings in disordered configuration: Fe (green), M^{II} (orange), N (light blue), C (dark grey), H (light grey). The unit cell is represented as black lines. (Bottom) Representations of the three possible configurations of the pyrazine bridges: in parallel configuration, in perpendicular configuration and in disordered configuration. Details of the structural parameters used for depicting these structures are given in the Supporting Information.

state [132], or pressure-tunable bistability [133]. Inspired by this approach, many other examples have followed, aiming at enhancing the porosity [78], the cooperativity and loading capacity [134], as well as the interplay between the host-guest function and the SCO [135]. The structure of Fe(pyrazine)[$M^{II}(CN)_4$] adopts a general topology consisting of 2D $\{Fe[M^{II}(CN)_4]\}_\infty$ layers, with the pyrazine ligands occupying the apical positions of the Fe octahedra and connecting the layers along the perpendicular direction (Fig. 4.1). Three possible configurations can be contemplated for the orientation of the pyrazine rings in a layer (Fig. 4.1): the molecules in parallel configuration, in perpendicular configuration in two positions at 90° one from each other, or orientationally disordered in these two positions (disordered configuration). It is generally assumed that the pyrazine rings are orientationally disordered, this disorder being dynamic in the high-spin (HS) state and nearly static in the low spin (LS) state [132]. Initially, a tetragonal space group $P4/m$, which implies a disordered configuration due to the 4-fold axis passing through the N atoms of the pyrazine, was proposed from the structural determination based on PXRD data [71]. Later, single-crystal x-ray diffraction studies allowed the assignation of the $P4/mmm$ space group (also implying a disordered configuration) [83, 81, 128, 129, 59], which has been thoroughly assumed in subsequent studies for these compounds in both spin states in absence of host molecules. Interestingly, Southon et *al*. [83] pointed to a parallel configuration upon incorporation of two water molecules per unit cell. They found a twinned structure with orthorhombic space group $Pmmm$, with the pyrazines parallel within each twin, but with 50:50 occupation of both possible orthogonal orientations. In the same work, the authors reported also an intermediate partially dehydrated phase, with one water molecule in the cavities presenting a perpendicular configuration of the pyrazine rings characterized by the appearance of superstructure peaks. The disordered configuration was nevertheless retained for the apohost.

In this work, we use neutron diffraction to demonstrate that the pyrazine rings adopt the perpendicular configuration in the LS state in the guest-free Fe(pyrazine)[Pt$^{\mathrm{II}}$(CN)$_4$] compound, contrarily to what has been generally assumed before. This observation is fully confirmed by density-functional theory calculations performed on the two configurations. Finally, the consequences of the pyrazine ordering on the spin crossover transition temperature are discussed based on the effect on the computed energy and entropy contributions. These findings have important implications because the number of studies dedicated to this family is huge owing to the vast panoply of remarkable properties these compounds present.

4.3 Results and discussion

4.3.1 Neutron diffraction

The structure of the generally accepted disordered configuration is described in the $P4/mmm$ tetragonal space group with cell parameters $a = b = 7.33(3)$ Å, $c = 6.94(2)$ Å for the low-spin state [81]. The perpendicular configuration implies instead a structural transformation to a tetragonal supercell with $\mathbf{a''} = \mathbf{a} - \mathbf{b}$, $\mathbf{b''} = \mathbf{a} + \mathbf{b}$, and $\mathbf{c''} = \mathbf{c}$, giving $a'' = b'' \approx \sqrt{2}a$ and $c'' \approx c$ [83]. This transformation may therefore involve the emergence of superstructure diffraction peaks. However, when working with x-rays, these peaks are weak and can be overlooked, in particular in powder diffraction. Additionally, these superstructure reflections can be diffuse, because the orientation of the rings may be uncorrelated between layers along c [83]. The contrast provided by neutrons for light atoms (like the hydrogen in the pyrazine molecule) allows distinguishing between the possible configurations of the rings, in particular if hydrogen is replaced by the more coherent scatterer deuterium (Fig. 4.2). We note that the parallel configuration, with the same cell parameters as the disordered configuration, but space group *Pmmm* [81] is also clearly distinguishable when using neutron diffraction on the deuterated compound (Fig. 4.2).

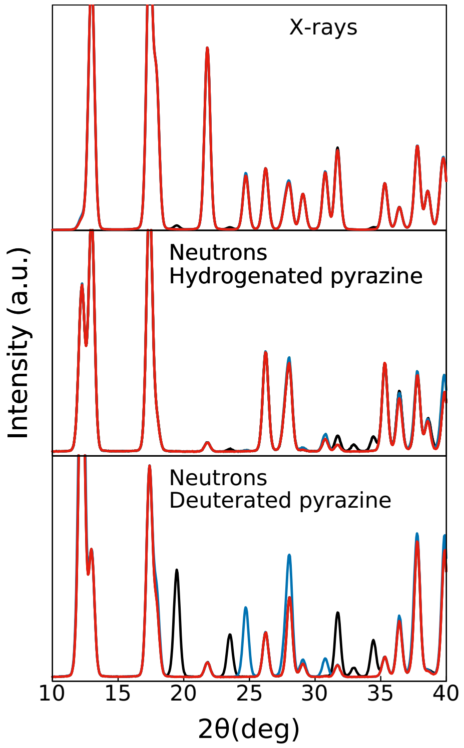

Figure 4.2: Simulated powder diffraction patterns (wavelength 1.54 Å) of Fe(pyrazine)[Pt(CN)$_4$] in low-spin state with the pyrazine rings in disordered configuration (red lines), in ordered perpendicular (black lines) and parallel (blue lines) configurations: (top) X-rays and hydrogenated pyrazine; (middle) neutrons and hydrogenated pyrazine; (bottom) neutrons and deuterated pyrazine. Details of the parameters used in the simulation are given in the Supporting Information.

Dehydrated microcrystalline Fe(pyrazine)[Pt^{II}(CN)$_4$] and its d$_4$-pyrazine homologue Fe(d$_4$-pyrazine)[Pt^{II}(CN)$_4$] were prepared as described elsewhere [71, 81, 128, 129]. Neutron diffraction experiments were performed on powder samples of ca. 0.25 g using the D20 instrument [136] at Institut Laue-Langevin, Grenoble, France, equipped with a cryofurnace and using a wavelength of 1.54 Å coming from a germanium monochromator. Rietveld refinements and calculations of the structures were performed using the FullProf suite of programs [137, 138] and the tools from the Bilbao Crystallographic Server [139].

The neutron diffraction results are shown in Fig. 4.3 and Table 4.1. Fig. 4.3a shows the

Compound	Fe(d$_4$-pyrazine)[Pt(CN)$_4$]		Fe(pyrazine)[Pt(CN)$_4$]	
T(K)	100	320	130	320
Spin state	Low-spin	High-spin	Low-spin	High-spin
Space group	$P4/mbm$	$P4/mmm$	$P4/mbm$	$P4/mmm$
a, b (Å)	10.1568(4)	7.4285(8)	10.1576(5)	7.4299(3)
c (Å)	6.7632(5)	7.2316(7)	6.7668(4)	7.2369(5)
$d_{Fe-N(C)}$ (Å)	1.903(5)	2.1599(3)	1.941(5)	2.1583(2)
$d_{Fe-N(pz)}$ (Å)	1.983(7)	2.2273(3)	1.978(7)	2.2291(3)
R$_{Bragg}$	5.69	7.70	5.03	8.81

Table 4.1: Results of the refinement of the powder neutron diffraction patterns of Fe(d$_4$-pyrazine)[Pt(CN)$_4$] and Fe(pyrazine)[Pt(CN)$_4$]: space group, cell parameters, selected distances and agreement factors are reported in each case.

neutron diffraction pattern of Fe(d$_4$-pyrazine)[M^{II}(CN)$_4$] at 100K (low-spin state). At 2θ = 19.5, 23.7 and 34.7 degrees, the superstructure reflections appearing due to the pyrazine ordering in perpendicular configuration can be clearly observed. The experimental pattern agrees well with a model with the pyrazine rings in perpendicular configuration, described in the supercell defined above, with a tetragonal space group $P4/mbm$ [83] presenting a 4-fold axis passing through the Pt atom. We note that the real symmetry is probably lower, but the tetragonal pseudosymmetry avoids overparametrization. The fit is slightly improved if some disorder is allowed between both perpendicular positions of the pyrazine - with a refined value of 17.4 (3) %. This is consistent with some degree of orientational disorder and with defects in the correlation of the layers along c.

The ordering in perpendicular configuration of the pyrazine bridges is concomitant with the spin transition. The recorded diffraction patterns on cooling from 320 K to 245 K (Fig. 4.3b) show the appearance of the superstructure reflections at the same temperature (ca. 285 K) of the abrupt change in the whole pattern occurring at the transition. The perpendicular configuration is the most stable at low temperatures (see below) and in fact it has been observed in similar compounds not displaying spin-crossover [140]. However, in the present case, it sets up concurrently with the abrupt structural changes produced at the spin transition. It deserves to be noted that the perpendicular configuration is also the one found compatible with the experimental results and calculations when certain types (and quantities) of molecules are adsorbed [83, 141]. In the high-spin state, the diffractogram does not show any signal of superstructure reflections and can be sat-

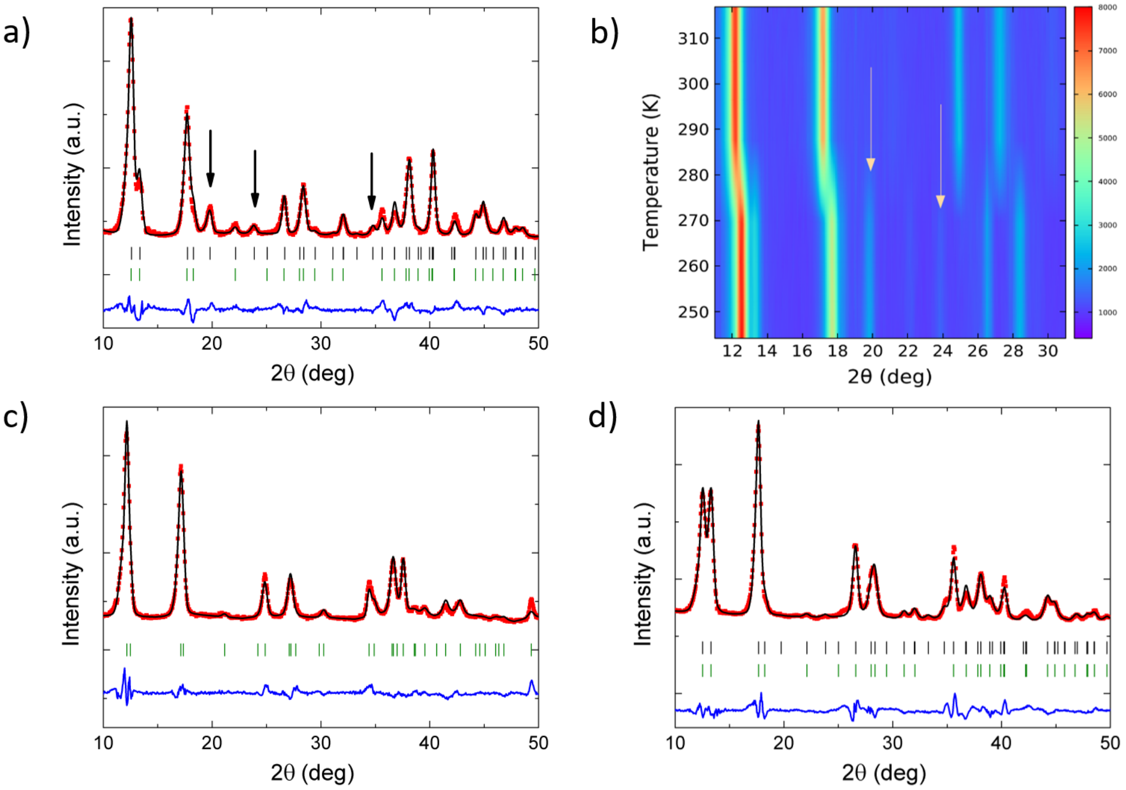

Figure 4.3: Detail of the most relevant part of the powder neutron diffraction patterns (wavelength 1.54 Å) of Fe(d_4-pyrazine)[Pt(CN)$_4$] (a,c) and Fe(pyrazine)[Pt(CN)$_4$] (d). Experimental patterns (red), calculated (black), and difference patterns (blue lines). Position of the Bragg reflections for the disordered configuration (green marks) and the ordered arrangement of the pyrazine bridges in perpendicular configuration (black marks). The arrows indicate the observed superstructure reflections related with the ordering of the pyrazine bridges in perpendicular configuration. Panel a) Fe(d_4-pyrazine)[Pt(CN)$_4$] in the low-spin state (100 K). Panel b) Neutron thermodiffractograms collected on cooling from 320 K to 245 K (cooling rate ca. 1.5 K/min, acquisition every 5 minutes) for Fe(d_4-pyrazine)[Pt(CN)$_4$]. Panel c) Fe(d_4-pyrazine)[Pt(CN)$_4$] in the high-spin state (320 K). Panel d) Fe(pyrazine)[Pt(CN)$_4$] in the low-spin state (130 K).

isfactorily fitted with the disordered model with space group $P4/mmm$ (Fig. 4.3c). It is worthy of note that the ordering of the pyrazine molecules in the low-spin state is not an effect of the deuteration. Indeed, although less visible than in the deuterated compound, the diffraction patterns measured for the hydrogenated compound in the low-spin state (Fig. 4.3d) also show evidence of pyrazine ordering (see the superstructure reflections at $2\theta = 34.6$ degrees).

4.3.2 Pyrazine interaction

In order to understand the greater stability of the perpendicular configuration we have performed DFT calculations using the Quantum ESPRESSO package [117, 118]. The PBE+D2 functional [142, 143] was used to compute the binding energy of three different pyrazine dimers that represent the possible configurations present in the system: i) perpendicular, ii) top-on and iii) side-to-side dimers for the parallel arrangement (see inset of Fig. 4.4). See computational details in the Supporting Information for more details.

Taking the positions and structures of the pyrazine rings from the corresponding relaxed compound as starting point, one of the monomers was moved along the axis that connects the centers of mass of the two molecules until a local minimum was reached. The potential energy curves obtained for the three configurations are represented in Fig. 4.4. The three minima were found at center-to-center distances ($R_{centers}$) between pyrazines of 4.8 Å, 3.8 Å, and 6.4 Å for the perpendicular, top-on, and side-to-side dimers, respectively. We note that the distance between complexed pyrazines in the framework is 7.1 Å, which is significantly larger than any of these $R_{centers}$ and falls almost at the end of the potential energy curves (see circles on the curves of Fig. 4.4). An attractive interaction is predicted nonetheless for every configuration at $R_{centers}$=7.1 Å, being E_{int} = -11.1 meV and E_{int} = -6.7 meV for the perpendicular and side-to-side configurations, respectively, and negligible (E_{int} =-0.2 meV) for the top-on dimer. By adding up the side-to-side and the top-on energy contributions we obtain a lower value than the interaction predicted for the perpendicular configuration. This simple dimer model therefore suggests a perpendicular configuration of pyrazines for molecules located at the same distance found in the clathrate.

We note the unusual shape of the potential energy curve of the side-to-side configuration where two different regions can be found: a stabilization region between 6.1 Å and 7.6 Å and a destabilization region for $R_{centers} > 7.6$ Å. The first corresponds to d(H-H) between [2.1 - 3.4] Å which correlates with the typical formation distances of H-H bond [144, 145]. This weak bond of dispersive nature exhibits energies of the order of 0.017 eV, comparable to the maximum stabilization of 0.020 eV predicted at the equilibrium position in Fig. 4.4. For $R_{centers} > 7.6$ Å, the H-H distance is too large for a typical H-H bond and the electrostatic repulsion between the pyrazines may dominate. Finally, this analysis is consistent with the (PBE+D2) computed total energy difference between the parallel and perpendicular configurations in the supercell which gives a more stable perpendicular case by 35 meV per pyrazine.

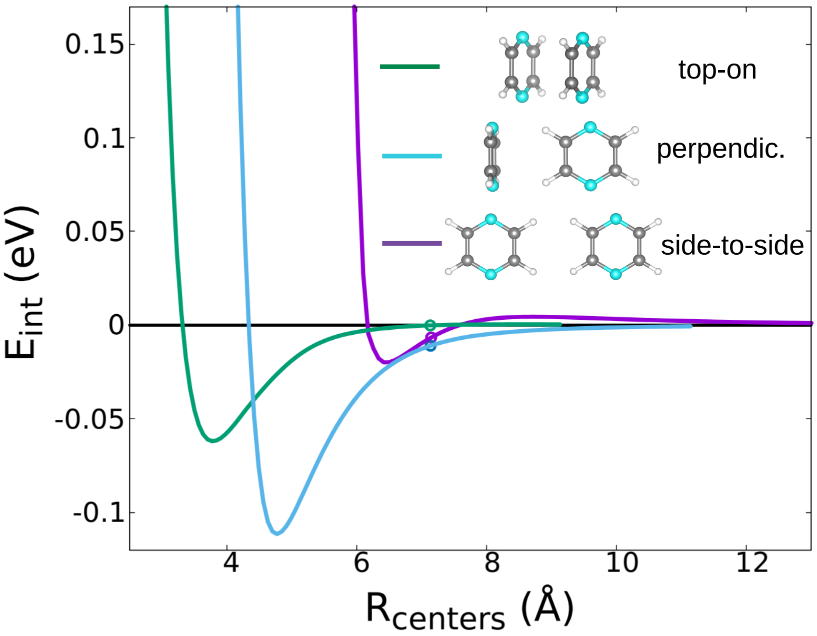

Figure 4.4: Interaction energy, E_{int}, computed for the three pyrazine dimers: top-on (green), perpendicular (light blue), and side-to-side (purple). The x-axis ($R_{centers}$) gives the center-to-center distance between pyrazine moieties. The circles indicate the distance at which pyrazines are found in the Hofmann clathrate, i.e. $R_{centers} = 7.1$ Å.

4.3.3 Influence of the pyrazine arrangement on the spin transition

The configuration of the pyrazine rings has important consequences for the most characteristic feature of this material: the spin-crossover transition.

It is not unusual to observe order-disorder processes coupled to SCO [146, 147], in most cases related to counterions or solvent molecules present in the structure [148, 149], and more rarely to ligands [150, 151]. An order-disorder process can affect the spin transition in several ways, including the temperature of the transition and its abruptness (and hysteresis), and this has been taken into account in theoretical models of the spin transition [152]. When a coupling exists between the spin-active part of the system and the moieties susceptible of undergoing order-disorder, the presence of order-disorder processes tends to increase the abruptness of the transition, as has been observed in different examples [153, 154, 155]. The wide hysteresis observed in Fe(pyrazine)[Pt(CN)$_4$] may be therefore related with the order-disorder process undergone by the pyrazine rings.

Particularly relevant is how the pyrazine arrangement significantly affects the transition temperature. The spin transition temperature, $T_{1/2}$, from LS to HS is defined as the temperature at which the thermodynamic equilibrium between the two phases is reached, i.e.

when the difference of Gibbs free energy is zero. The transition temperature is then given by $T_{1/2} = \Delta H_{\text{HS-LS}}/\Delta S_{\text{HS-LS}}$, being $\Delta H_{\text{HS-LS}}$ ($\Delta S_{\text{HS-LS}}$) the enthalpy (entropy) difference between both spin states. The experimental values for these quantities are $\Delta H_{\text{exp}} = 25$ kJ mol^{-1} and $\Delta S_{\text{exp}} = 84$ J mol^{-1} K^{-1} (giving $T_{1/2} = 297$ K) [126]. Both the energy and the entropy differences depend on the configuration of the pyrazine rings, and therefore the transition temperature would be substantially modified if the pyrazine arrangement were different. The different terms contributing to $\Delta H_{\text{HS-LS}}$ and $\Delta S_{\text{HS-LS}}$, and thus to $T_{1/2}$ are written in eq. 4.1

$$T_{1/2} = \frac{\Delta H_{HS-LS}}{\Delta S_{HS-LS}} = \frac{\Delta E_{ad} + \Delta E_{vib}}{\Delta S_{vib} + \Delta S_{rot} + \Delta S_{el}} \tag{4.1}$$

The enthalpy difference, $\Delta H_{\text{HS-LS}}$, contains two terms, the adiabatic energy difference, ΔE_{ad}, and the vibrational contribution, ΔE_{vib}. The entropy variation, $\Delta S_{\text{HS-LS}}$, contains the vibrational contribution, ΔS_{vib}, a rotational term, ΔS_{rot}, which accounts for the degrees of freedom associated with the rotational motion of the pyrazine rings [132], plus an electronic contribution, ΔS_{el}, that takes into account the different spin multiplicity between the two spin states. In the case of a LS-HS transition in Fe(II) complexes between a LS state with $S = 0$ and a HS state with $S = 2$, $\Delta S_{el} = 13.38$ J mol^{-1} K^{-1}. This term, which represents ca. 16% of the entropy variation at the transition, is independent from the arrangement of the pyrazine rings.

ΔS_{rot} is instead significantly affected by the pyrazine configuration. In 2012, a study of the dynamics of this system by some of us demonstrated, by means of quasielastic neutron scattering - a technique particularly adapted to probe the movement of hydrogen atoms - that the pyrazine rings are rotating in HS, while in LS the movement is virtually deactivated [132]. The rotational term ΔS_{rot} was thereby calculated to amount to 7.95 J mol^{-1} K^{-1}[132] (ca. 9.4% of the total entropy gain at the transition) assuming a LS state with the pyrazine rings disordered in two perpendicular positions. Because the pyrazine molecules are ordered in LS, as demonstrated in the present neutron diffraction study, the number of accessible positions is divided by two, and so does the entropy. This leads to a change in ΔS_{rot} of at least a factor of two (under the approximation used of a harmonic oscillator around its equilibrium position, which is the case with less entropy, and therefore less favorable to produce big differences when applying a factor two to it). A difference of this magnitude in ΔS_{rot} between the LS-ordered case and the LS-disordered one implies a decrease of ca. 10% of the total experimental entropy obtained for the title compound. We performed DFT calculations to compute how the pyrazine configuration affects the other terms such as E_{ad}, E_{vib} and S_{vib}. For this we computed total energy and normal modes for the compound with the pyrazine rings in perpendicular and in parallel configuration in both the HS and LS states. We take the average of the perpendicular and parallel cases as an approximation for the disordered case (see the full set of values in Table 4.3 of the Supporting Information). The expression for the vibrational contributions E_{vib} and S_{vib} can be derived within the statistical thermodynamic theory from the partition function of a harmonic oscillator. For a given normal modes vibrational spectrum $\{\nu_i\}$, the vibrational contributions are:

$$E_{vib} = R \sum_{\nu_i} \frac{h\nu_i}{k_B} \left(\frac{1}{2} + \frac{1}{e^{h\nu_i/k_BT} - 1} \right) \tag{4.2}$$

and

$$S_{vib} = R \sum_{\nu_i} \left(\frac{h\nu_i}{k_BT} \frac{1}{e^{(h\nu_i/k_BT)} - 1} - \ln\left(1 - e^{-h\nu_i/k_BT}\right) \right) \tag{4.3}$$

The DFT results show a difference of 0.83 J mol^{-1} K^{-1} in ΔS_{vib} (ca. 1% of the total experimental entropy gain at the transition) between a LS-ordered case and a fully disordered scenario. The LS-ordered case consists of the difference between a disordered HS state and an ordered LS state with a perpendicular arrangement. The fully disordered case consists of disordered configuration both in the HS and LS states. Regarding ΔE_{vib}, a negligible difference of 0.02 kJ mol^{-1} (less than 0.1% of the total enthalpy variation at the transition) is computed.

Finally, the adiabatic energy difference, ΔE_{ad}, is computed as the total energy difference between the two spin states each taken at its corresponding geometry. We note that the calculation of adiabatic energy differences in transition metal complexes represents a significant challenge for modern electronic structure methods [66, 156, 157, 158, 159]. Within DFT, different exchange and correlation functionals including semilocal, meta-GGAs, and global hybrids have been tested in this respect and variations by up to 3 eV can be found depending on the specific choice of the functional and the chosen molecular complex [67]. Here, to evaluate ΔE_{ad}, we use the non-self consistent Hubbard U-corrected density approach scheme which employs linear response U [70] values computed separately for high spin and low spin (see Supporting Information for more details). Recently, this method has been shown to provide accurate results of spin splitting energies for a serie of Fe(II) molecules and periodic compounds when compared with higher level calculations and experimentally extracted results [159]. The adiabatic energy difference computed with this method is 36.64 kJ mol^{-1} when both spin states are disordered and 36.91 kJ mol^{-1} when the LS state is in perpendicular arrangement. This gives, as expected, a marginal energy difference of 0.27 kJ mol^{-1} between the two pyrazine configurations.

Adding together all the contributions (see Eq. 4.1), we obtain that the change in the configuration of pyrazine moieties in the LS state from an ordered perpendicular arrangement to a disordered case implies a decrease of 0.29 kJ mol^{-1} in ΔH and of 8.78 J mol^{-1} K^{-1} in ΔS at the spin transition, which translates in a variation of $T_{1/2}$ of the order of 30 K. Thus, if the configuration of the pyrazine rings in the LS state were disordered and not ordered, the transition temperature would have been *ca.* 30 K higher, mostly due to the change in rotational entropy.

4.4 Conclusion

Herein we have demonstrated, by means of neutron diffraction experiments, that the pyrazine rings in Fe(pyrazine)[Pt(CN)$_4$] adopt an ordered arrangement in the low-spin state with the rings alternatively oriented in the two positions perpendicular to each other. Our DFT calculations have shown that this configuration stems from the interaction between the pyrazine molecules and have allowed us to estimate the effect of this arrangement in the spin transition temperature. The implications of the actual configuration of the pyrazine moieties in the energy and entropy balance between the high-spin and low-spin states are substantial, and thus the spin transition temperature is significantly dependent on this configuration. The fact that Fe(pyrazine)[M^{II}(CN)$_4$] (M^{II} = Pt, Pd, Ni) are prototypical examples of the growing class of porous spin-crossover compounds, with a relevant potential for applications, and the great number of studies concerning this family and many other compounds based on it, underlines the significance of the accurate structural knowledge, which may be of crucial importance for the understanding of the properties of such materials.

Acknowledgements

We thank the ILL for the PhD contract of A.F.B. and for the beamtime allocation under experiment numbers 5-22-795 (doi.ill.fr/10.5291/ILL-DATA.5-22-795) and DIR-274 (doi.ill.fr/10.5291/ILL-DATA.DIR-214). J.S.C. acknowledges funds from the MICINN through the National Research Project (PID2019-111479GB-100), the Ramon y Cajal Research Program (RYC-2014-16866). IMDEA Nanociencia acknowledges support from the Severo Ochoa Program for Centres of Excellence in R&D (MICINN, Grant CEX2020-001039-S). J.A.R. thanks Grant PID2019-106147GB-I00 funded by MCIN/AEI/10.13039/501100011033. Calculations were performed using resources granted by GENCI under the CINES and TGCC grant numbers A0020907211 and A0110907211. Additionally, the

froggy and Dahu platform of the CIMENT infrastructure, which is supported by the Rhone-Alpes region (GRANT CPER07_13 CIRA) and the Equip@Meso project, was employed for the calculations.

4.5 Supplementary information

Computational details The DFT calculations were performed with the QuantumESPRESSO (QE) package [119, 117, 118] (v.6.4) within the generalized gradient approximation of Perdew, Burke and Ernzerhof (PBE) [160] and long-range interactions described with the semiempirical approach proposed by Grimme (PBE+D2) [142, 143]. We employ the pseudopotentials from Garrity-Bennet-Rabe-Vanderbilt library (GBRV) [161]. The convergence threshold on forces is 0.0001 Ry/Bohr and the wavefunctions and charge density cutoffs are set to 100 Ry and 1000 Ry, respectively. These are carefully chosen to obtain converged phonon frequencies. To describe both the perpendicular and parallel orientation a supercell with lattice parameter $a''=\sqrt{2}a$ and $b''=\sqrt{2}b$ was used, with a, b and c the lattice parameters of the primitive cell. The PBE+D2 lattice parameters are $a''= b''$ = 10.1 Å and c'' = 6.7 Å. The Brillouin zone is sampled using 3×3×3 Monkhorst-Pack k-points grid.

The vibrational contributions to the enthalpy and entropy are computed using eqs. 4.2 and 4.3 of the main text. The phonon frequencies $\{\nu_i\}$ for perpendicular and parallel configuration in LS and HS are obtained by diagonalizing the dynamical matrix by employing the ph.x package implemented in Quantum Espresso. The harmonic interactomic force constants are computed using density functional perturbation theory [112, 113]. The values of ΔE_{vib} and ΔS_{vib} that we present in the main text are obtained using the corresponding E_{vib} and S_{vib}. In the case of the disordered configuration, the average of E_{vib} and S_{vib} computed between the parallel and perpendicular configuration of the corresponding spin state is taken.

We note that we obtain one negative frequency for the LS parallel case and for the HS perpendicular configuration, at -8.9 cm^{-1} and -27.8 cm^{-1}, respectively. Because the negative frequency is not counted in the summation of eqs. 4.2 and 4.3, one expects an underestimation of the vibrational entropy and enthalpy in these cases. Thus, in the two cases mentioned above we add one frequency in the low and one the intermediate energy range in two separate calculations and then compute the average. The corresponding values are indicated with an asterisk in Table 4.3. We add one frequency at 10 cm^{-1} (right after the three translational modes) and then one at 500 cm^{-1} (right before the internal modes associated with the pyrazine). We stress here that if we take the values of vibrational energy and entropy computed as they are, i.e. without adding any new frequency, the final results on the value of $T_{1/2}$ reported in the main article negligibly changes (by less that one 1 K).

To evaluate ΔE_{ad}, we use DFT within the Hubbard U-corrected density approach scheme, which has been recently proposed and tested by some of us [159]. This method exploits the capabilities of the Hubbard U-correction method in DFT in improving the description of localized d electrons (more strongly affected by the self-interaction error in standard PBE and at the same time removes the systematic bias toward high spin observed in Fe(II) complexes when the fully self-consistent PBE+U approach is used [67]. In this work we adopt the linear-response approach proposed by Cococcioni et *al*. [70] to compute the Hubbard parameter U for the iron site in the unit cell and we obtain 7.29 eV for HS and 8.87 eV for LS. The values of adiabatic energy differences reported in Table 4.3 and in the main paper are computed on the relaxed PBE+D2-geometries by employing the Hubbard U-density corrected approach that we name PBE[U], i.e. by taking the PBE+U total energy contribution and removing the Hubbard term as explained in detail in ref. [159] (we stress that no D2 term is used for this set of calculations).

Configuration	Disordered	Perpendicular	Parallel
λ (Å)	1.54		
Crystal system	Tetragonal	Tetragonal	Orthorhombic
Space Group (No.)	$P4/mmm$ (123)	$P4/mbm$ (127)	$Pmmm$ (47)
a (Å)	7.1786	10.1520	7.1786
b (Å)	7.1786	10.1520	7.1786
c (Å)	6.7741	6.7741	6.7741
V (Å^3)	349.08	698.16	349.08
Pt: x	0.5	0.5	0.5
y	0.5	0.5	0.5
z	0.5	0.5	0.5
Fe: x	0	0	0
y	0	0.5	0
z	0.5	0.5	0.5
N(1): x	0	0	0
y	0	0.5	0
z	0.79800	0.79800	0.79800
N(2): x	0.19400	0.19400	0.19400
y	0.19400	0.5	0.19400
z	0.5	0.5	0.5
C(1): x	0.31200	0.31200	0.31200
y	0.31200	0.5	0.31200
z	0.5	0.5	0.5
C(2): x	0	0.08250	0
y	0.16500	0.58250	0.16500
z	0.89000	0.89000	0.89000
H / D: x	0	0.13745	0
y	0.27490	0.63745	0.27490
z	0.81780	0.81780	0.81780

Table 4.2: Structural parameters used for depicting the structures (Fig. 1) and for the simulation of the expected powder diffraction patterns (Fig. 2) of Fe(pyrazine)[Pt(CN)$_4$] in low-spin state with the pyrazine rings in disordered, perpendicular and parallel configurations.

		Perpendicular	Parallel	Disordered (average)
HS	E_{ad} (kJ mol^{-1})	-890367.87373	-890364.31075	-890366.09224
	E_{vib} (kJ mol^{-1})	*339.02486 ±0.285385	338.61891	338.82188
	S_{vib} (J mol^{-1} K^{-1})	*285.41634 ±7.655215	286.28380	285.85007
LS	E_{ad} (kJ mol^{-1})	-890403.00375	-890402.46490	-890402.73433
	E_{vib} (kJ mol^{-1})	346.87958	*346.92117 ±0.285385	346.90038
	S_{vib} (J mol^{-1} K^{-1})	222.21025	*223.87080 ±7.655215	223.04053
diff HS (diso) - LS (perp/para/diso)	ΔE_{ad} (kJ mol^{-1})	36.91151	36.37266	36.64209
	ΔE_{vib} (kJ mol^{-1})	-8.05770	-8.09929	-8.07850
	ΔS_{vib} (J mol^{-1} K^{-1})	63.63982	61.97927	62.80954

Table 4.3: Adiabatic energy and vibrational energy and entropy for the three configurations (parallel, perpendicular and disordered) in HS and LS. *Average value between one frequencye added at low and one at high energy. The error is also reported. The label diso (*disordered*) referes to the average between parallel and perpendicular.

Chapter 5

Probing the SO_2 Adsorption Mechanism in Hofmann Clathrates via Inelastic Neutron Scattering and Density Functional Theory calculations

Ángel Fernández-Blanco[1,2], Lucía Piñeiro-López[3], Mónica Jiménez-Ruiz[1], Stephane Rols[1], José Antonio Real[4], J. Alberto Rodríguez-Velamazán[1] and Roberta Poloni[2]

[1] *Institut Laue Langevin, 71 Avenue des Martyrs, CS 20156-38042, Grenoble, France*

[2] *SIMaP, Grenoble-INP, University of Grenoble-Alpes, CNRS, 38042 Grenoble, France*

[3] *IMDEA Nanociencia, Faraday 9, Ciudad Universitaria de Cantoblanco, 28049 Madrid, Spain*

[4] *Departamento de Química Inorgánica, Insituto de Ciencia Molecular (ICMol), Universidad de Valencia, 46980, Paterna, Spain*

Ángel Fernández-Blanco, Lucía Piñeiro-López, Mónica Jiménez-Ruiz, Stephane Rols, José Antonio Real, J. Alberto Rodríguez-Velamazán and Roberta Poloni, "Probing the SO_2 Adsorption Mechanism in Hofmann Clathrates via Inelastic Neutron Scattering and Density Functional Theory calculations", *The Journal of Physical Chemistry C*, vol. 126, p. 8090-8099, 2022.

5.1 Abstract

The adsorption mechanism of SO_2 in the Hofmann-like coordination polymer Fe(pz)[Pt(CN)$_4$] is studied using inelastic neutron scattering and density functional theory calculations. We find that the most important spectral change upon gas adsorption is the blueshift of the low energy peak found at 100 cm^{-1}, a feature that is fully confirmed by the computed neutron-weighted phonon density of states. Our calculations suggest that the origin of this change is two fold: i) an increase in the force constant of the cyanide out-of-plane movement due to the binding of the gas onto the Pt(CN)$_4$ plane, and ii) the hampered rotation of the pyrazine due to steric hindrance. The high energy region of the neutron scattering data whose spectral weight is dominated by the internal vibrations of the pyrazine is negligibly affected by the presence of the gas as expected from a physisorption type of binding.

5.2 Introduction

Metal-organic frameworks (MOFs) are 3D nanoporous materials formed through coordination bonds between metal cations and organic ligands. The great variety of metal ions, organic linkers, combined with the structural topology, allow to achieve an almost infinite number of possible combinations. Owing to this exceptional tunability, combined with the larger surface area and nanoscale porosity, the past 10-15 years have seen a rapid development in the field of MOFs for efficient gas adsorption and separation [162, 29]. In recent years, adsorption and chemical sensing of toxic gas molecules using MOFs has become a very active field of research [32, 33, 16]. Among these, iron (II) spin-crossover Hofmann-type clathrates represent an interesting class of MOFs with sensing capabilities due to their bistability, meaning that they can be *switched* between two different spin states [72, 127, 80]. These complexes undergo a spin-state change under the influence of external stimuli such as light, temperature, pressure or the incorporation of guest molecules. A relevant feature is the presence of metallic centers with an “open” metal coordination, i.e. metal centers exhibiting an unsaturated coordination. Interestingly, these open-metal sites have been shown to exhibit a high affinity for many gases, such as CO_2[28], CH_4 [163], and CO[40]. Based on the well known Hofmann clathrate compounds [75], these materials are built via cyanide (CN) bridging ligands forming metallo-cyanide planes with different linkers acting as bridges between the planes. The most representative example of this class of compounds is the family Fe(pz)[M(CN)$_4$], with M = Ni, Pd, Pt, and pz = pyrazine [71]. The Fe(II) centers undergo a transition (spin crossover) from low spin to high spin, yielding a change in the magnetic, optical, dielectric, and structural properties of the material. This bistability coupled with the presence of potentially high-affinity open metal sites makes them excellent candidate materials for MOF-based gas sensing switches [33]. In 2013, Arcís-Castillo et *al.* [11] studied the adsorption of SO_2 in the Fe(pz)[Pt(CN)$_4$] Hofmann-type clathrate by measuring the adsorption isotherms and the x-ray diffraction patterns. The experimental results, combined with the DFT calculations established that the SO_2 binds strongly via chemisorption. The authors demonstrated a higher SO_2 uptake capacity for these compounds with respect to other materials such as BPL-activated carbon, mixed metallic oxides and other MOFs. This high adsorption capacity together with the reversibility of the process, previously reported for square-planar organoplatinum molecules[164, 165, 166], make Hofmann clathrates a promising class of materials for efficient adsorption/desorption processes.

In this work, we combine inelastic neutron scattering data with DFT calculations to further understand and clarify the SO_2 adsorption mechanism in Fe(pz)[Pt(CN)$_4$]. The most relevant signature of the binding occurs in the spectral region between 100 cm^{-1} and 140 cm^{-1}. The intense low energy peak at around 100 cm^{-1} blueshitfs upon adsorption, a signature that we attribute to both the hampered rotation of the pyrazine and the out-of-plane movement of the cyanide. The well defined peaks in the high-energy region of the spectra are associated with the internal vibrations of the pyrazine and are negligibly affected by the adsorbed gas. These findings are well reproduced by the computed generalized-phonon density of states and are consistent with the analysis of a strong physisorption occurring via the Pt(CN)$_4$ plane and the pyrazine molecules. This work shows that INS measurements provide a powerful tool to probe the gas adsorption mechanism in this class of materials thus allowing to unambiguosly characterize the nature of the interaction when supported by DFT calculations.

5.3 Methods

Sample preparation. [Fe(pz)Pt(CN)$_4$]·nH_2O precipitates when a solution of K_2[Pt(CN)$_4$] in H_2O is added with constant stirring to a solution which contains stoichiometric amounts of pz and Fe(BF$_4$)$_2$·6H_2O in MeOH/H_2O (1:1) under nitrogen at room temperature. A small amount of ascorbic acid was added to prevent the oxidation of Fe(II). After stirring for 1h, the yellow precipitate was collected by suction filtration, washed with water and methanol and dried under ambient pressure [71]. The sample was then heated in a drying oven at a temperature of 100 °C.

Gas adsorption. The sample (722.9 mg, 1.6 mmol) was placed inside a cylindrical aluminium sample holder allowing the gas injection, connected with a capilar to a manifold gas pumping system. Temperature control was achieved using either a closed cycle cryostat (IN1-LAGRANGE) or an Orange cryostat (IN5 and PANTHER). The empty MOF was measured at 30 K. The adsorption of SO_2 was performed near room temperature in two injection steps until reaching a total of 1.6 mmol of SO_2 adsorbed, that is, one molecule of SO_2 per formula unit of the host. The amount of gas adsorbed by the MOF was calculated from the pressure drop measured (reaching equilibrium) 30 minutes after the sample holder was put in contact with the gas reservoir. Finally, the temperature of the sample was decreased to 30 K to perform the measurements.

IN1-LAGRANGE. The INS experiment was performed in the indirect geometry-type spectrometer IN1-LAGRANGE [93] installed on the hot neutron source of the high flux reactor at the Institut Laue-Langevin (ILL) in Grenoble, France. The incident neutron energy was determined using a combination of Cu and Si monochromators for the intermediate and lower energy range respectively. Upon scattering by the sample, neutrons enter a secondary spectrometer where a beryllium filter is installed to remove higher-order harmonics in the analyser reflections. Neutrons are then reflected to a He3 gas detector at fixed final energy of 4.5 meV. This is done by using a focussing analyzer built around the vertical sample-detector axis. The scattering angle, θ, varies from 33.7° to 69.4° and the accesible kinematical range of the instrument, Q, is defined as

$$Q^2 = k_i^2 + k_f^2 - 2k_i k_f cos(\theta) \tag{5.1}$$

Where k_i ad k_f are the initial and final scattering wave vectors that can be related to neutron energy by $E=\frac{\hbar^2 k^2}{2m_n}$, m_n being the neutron mass. To collect the data, the incident neutron energy was scanned step-by-step by rotating the whole secondary spectrometer around the monochromator allowing the measurement of a neutron energy loss spectra. The monochromators were selected to provide the best relation between energy transfer range and resolution: we employed Cu(220), Si(311), and Si(111), respectively, for energy transfers of [44 - 161] cm^{-1}, [130 - 286] cm^{-1}, and [209 - 1500] cm^{-1}. Data were collected at 30 K for both the empty and loaded material. The data treatment was done using LAMP[167] and it consists in a normalization of the data to the monitor counts and a posteriori subtraction of the empty sample holder.

IN5. INS data for the bare material were collected in the low energy region, i.e. $<$ 100 cm^{-1}, as a function of momentum transfer on the direct geometry disk chopper time-of-flight spectrometer at the ILL (Grenoble, France). The cold neutron flux from the neutron guide H16 is scattered by the sample after being turned into a pulsed monochromatic beam by a set of 6 choppers. The scattered neutrons are collected by a large cylindrical array of pixelated position-sensitive detectors (PSD) mounted inside a vacuum time-of-flight chamber, giving access to the dynamic structure factor $S(Q, \omega)$. Data were collected at 295 K (at low-spin state) using the standard configuration with a wavelength of 5 Å ($E_i \approx 29.8$ cm^{-1}) and a Q range of $\backsim$ 0.2 - 4.1 Å^{-1} for the angular detector coverage.

PANTHER. Complementary measurements for the low energy region were performed in the high-flux direct-geometry time-of-flight spectrometer PANTHER installed on the H12 thermal beam tube at the ILL. A double focusing pyrolytic graphite monochromator determines the incoming energy in the range 7.5 - 112 meV. Short neutron pulses produced by a slit Fermi chopper are scattered by the sample and collected by PSD. Data were collected at 10 K using an initial energy of 50 meV.

Computational details The DFT calculations were performed with the Quantum Espresso package [119, 117, 118] (v. 6.4) within the generalized gradient approximation (GGA) of Perdew, Burke and Ernzerhof (PBE)[160] and long-range interactions described with the semiempirical approach proposed by Grimme (PBE+D2)[142, 143]. We use the Rappe-Rabe-Kaxiras-Joannopoulos ultrasoft (rrkjus) pseudopotentials [168] without semicore states in valence. The convergence threshold on forces is 0.0001 Ry/Bohr and the wavefunctions and charge density cutoffs are set to 100 Ry and 1000 Ry, respectively. These are carefully chosen to obtain converged phonon frequencies. The low temperature (low spin) structure of the Hofmann clathrate was described by many authors as a disordered orientation of the pyrazines [132, 71, 83, 81, 59]. Recently, the present authors employed neutron diffraction data collected at D20@ILL to show an ordered configuration with the pyrazines perpendicular to each other [169], a configuration that has already been observed in certain conditions [83, 81, 140, 82]. To describe this perpendicular orientation, a supercell with lattice parameters $a'=\sqrt{2}a$ and $b'=\sqrt{2}b$ was used, with a and b lattice parameters of the primitive cell. The PBE+D2 lattice parameters of the bare MOF are a = 10.096 Å, b = 10.097 Å and c = 6.711 Å. The Brillouin zone is sampled using 3×3×3 Monkhorst-Pack k-points grid. A revised PBE approximation for densely packed solids by Perdew et. al [106] (PBEsol+D2) and the nonlocal functional rev-vdW-DF2

[107] were used to study the effect of the functional choice on the computed density of states (vide infra). For rev-vdW-DF2, we employ PBE-generated pseudopotentials while for PBEsol+D2, since the convergence of the electronic structure with the rrkjus was not reached, we employed pseudopotentials from Garrity-Bennet-Rabe-Vanderbilt library [161]. Wavefunctions and charge density cutoffs used for PBEsol+D2 and rev-vdW-DF2 are 70 Ry and 700 Ry. Calculations are performed using the low spin (S=0) electronic configuration.

Generalized-phonon density of states. The phonon frequencies were obtained by diagonalizing the dynamical matrix by employing the ph.x package in Quantum Espresso[119]. The harmonic interatomic force constants are computed using density functional perturbation theory [112, 113]. The inelastic scattering data collected at IN1-LAGRANGE are compared with the computed generalized-, or neutron-weighted, phonon density of states. The l-atom contribution to the total one-phonon density of states is given by

$$g_l(\omega) = \sum_{q,j} |u_l(j, \mathbf{q})|^2 \delta(\omega - \omega_j(\mathbf{q})) \tag{5.2}$$

where $\omega_j(\mathbf{q})$ is the phonon frequency of the j-branch at $\mathbf{q}$ wavevector and $u_l(j, \mathbf{q})$ is the corresponding atomic displacement. Thus, $g(\omega)d\omega$ gives the number of eigenstates in the frequency interval (ω, $\omega+d\omega$). The total generalized-phonon density of states, G(ω), is then defined as the phonon density of states weighted by the neutron scattering power of each atom l and it is given by

$$G(\omega) = \sum_{l=1} g_l(\omega) \frac{\sigma_l}{M_l} \tag{5.3}$$

where σ_l is the incoherent neutron scattering cross section and M_l is the mass. In the harmonic and incoherent approximation, this density of vibrational states is related to the scattering function $S(Q, \omega)$ by the following relation[88, 170, 171]

$$S(Q, \omega) = e^{-2\overline{W}} \frac{Q^2 \hbar}{2\overline{M}\omega} < n + 1 > G(\omega) \tag{5.4}$$

where $\overline{M}=\sum_l$ M$_l$/N, n is the thermal-equilibrium occupation number of the vibrational state and $< n + 1 >= \frac{exp(\hbar\omega\beta)}{exp(\hbar\omega\beta)-1}$ with $\beta = \frac{1}{K_B T}$. We drop the vector symbol from the scattering function because for powders we measure the average over momentum transfer. The exponential term is the Debye-Waller factor for neutron attenuation by thermal motion and 2W=$\frac{Q^2 <\overline{u^2}>}{3}$. The average of the mean-square displacements over all the atoms is $< \overline{u^2} >$ and it is computed as

$$< \overline{u^2} >= \frac{\hbar}{2\overline{M}N} \sum \frac{1}{\omega_j} coth(\frac{1}{2}\hbar\omega_j\beta) \tag{5.5}$$

where Q is the kinematical range of IN1-LAGRANGE (eq. 5.1). Because of the small Q range measured at each energy transfer, we compute phonons only at Γ (center of the Brillouin zone) to compare with experimental INS data. We drop the sum over the phonon wavevector in eq. 5.2 and eq. 5.4 becomes $S(\omega)$. This should be a fair approximation since we are measuring small Q at low energy while at high energy optical modes show small dispersion. Finally, the phonon density of states is convoluted with a Gaussian function to account for the resolution of the monochromators. We set the standard deviation of the Gaussian to 3.0 cm^{-1} for the range [0 - 478] cm^{-1} and 0.009ω for [478 - 4033] cm^{-1}, close to the experimental resolution of IN1-LAGRANGE [93].

5.4 Results and discussion

The INS spectra collected at IN1-LAGRANGE are shown in the upper panel of Fig. 5.1 for the empty and loaded MOF. The scattering function computed using eq. 5.4 is shown in the lower panel of Fig. 5.1. The full spectra including experimental errors are reported in Fig. 5.6. We note the need to rescale the computed $< \overline{u^2} >$ by a factor of 10 in order

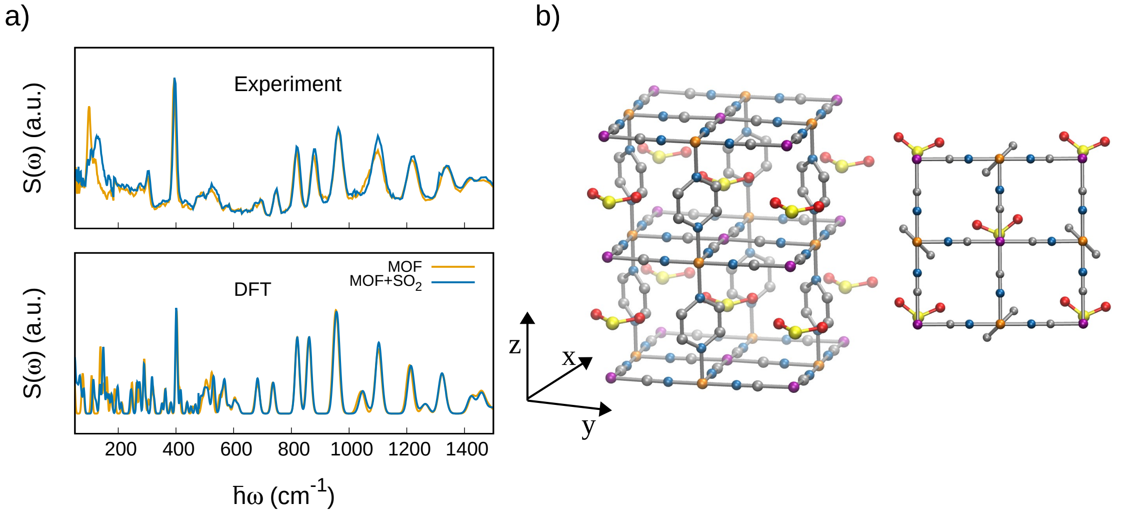

Figure 5.1: Experimental inelastic neutron scattering data, S(ω), collected at 30 K at IN1-LAGRANGE for the bare compound and upon SO_2 uptake, upper panel (a). The S(ω) computed using the PBE+D2 functional is reported in the lower panel (a). Side and top view illustrations of unit cell employed for the calculations containing neighboring pyrazine molecules oriented perpendicularly. Color code: purple, orange, blue, silver, red, and yellow are Pt, Fe, N, C, O, and S, respectively. H atoms are omitted for clarity.

to predict the experimental energy-decay of the intensity. This deviation may derive from the fact that only the normal modes are employed to compute eq. 5.5 which is a rough approximation to the full density of vibrational states, especially in the low energy region which dominates $< \overline{u^2} >$.

Since the IN1 measurement is not optimized below 100 cm^{-1} (see Fig. 5.6), we studied this energy region for the bare material by using the time-of-flight spectrometer IN5. The data are reported in Fig. 5.7. These low-energy vibrational modes are associated with the vibrations of the whole lattice and with out-of-plane and in-plane vibrations of the Pt atom. Because of the difference between the computed normal modes at Γ and the experimental data, the assignement of the modes within this region is somehow problematic.

Between 75 and 450 cm^{-1} of the measured INS data, two main peaks are observed for the bare material, at 100 cm^{-1} and 393 cm^{-1}, and in between these two a less resolved region appears. Upon adsorption of SO_2, the peak at 100 cm^{-1} becomes broader and shifts to higher energy, the maximum being found at 129 cm^{-1}. The remaining part of the spectrum is negligibly affected by the presence of the gas, even the strong excitation at 393 cm^{-1}. This behavior is in excellent agreement with the computational results.

The high energy region between 700 and 1500 cm^{-1} reveals several well defined excitations which are very well reproduced by the simulations and whose nature will be discussed later. The negligible change upon gas adsorption measured in this region is also confirmed by the calculations.

5.4.1 Partial G(ω)

To better analyze the nature of the measured excitations we report in Fig. 5.2 the partial G(ω), i.e. the $g_l(\omega)\frac{\sigma_l}{M_l}$, where l represents the different atoms or molecules in the MOF, for the Hofmann clathrate with adsorbed SO_2 molecules.

In the low energy region, between 20 and 100 cm^{-1}, the G(ω) is dominated by the vibrations of the heavy atoms, Fe and Pt, and to a minor extent by vibrations of the pyrazines and the CN groups. A few librational modes of SO_2 also appear between 20 and 120 cm^{-1} (see Fig. 5.8). Concerning the SO_2 molecule, the normal modes in the gas phase are predicted at 484 cm^{-1}, 1107.7 cm^{-1} and 1303.5 cm^{-1} (see Fig. 5.8). These are respectively the scissoring (i.e. the symmetric bending), and the symmetric and asymmetric stretches. All these modes are IR active and are found to change negligibly upon SO_2 adsorption (see Fig. 5.8). When the molecule is adsorbed in the MOF, these are computed at 484.5 and 485.6 cm^{-1}, 1042.2 and 1072.4 cm^{-1}, and 1248.9 and 1250.4 cm^{-1}.

Between 100 and 500 cm^{-1}, all atoms contribute to the generalized density of states

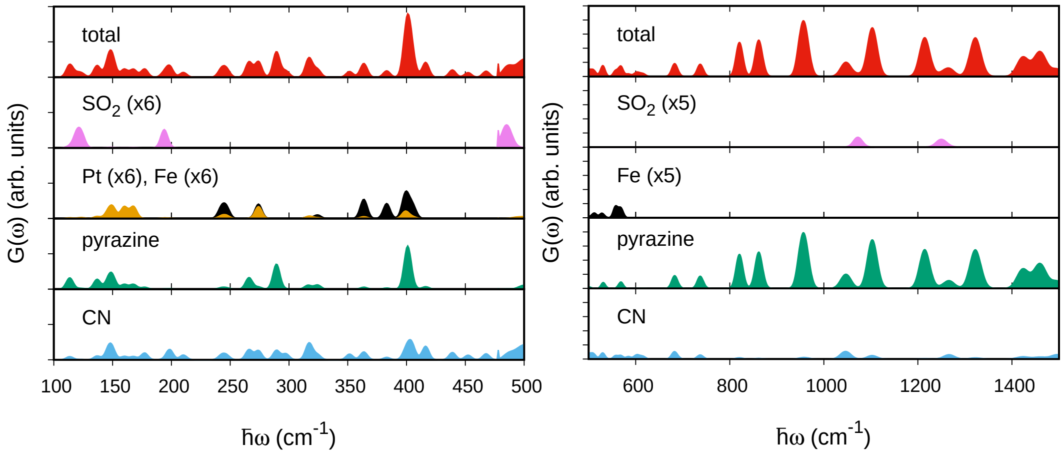

Figure 5.2: Total and partial (atom-specific) generalized phonon density of states computed for the Hofmann clathrate with adsorbed SO_2 molecules. Pt and Fe are depicted in yellow and black respectively. A negligible contribution from Fe is found around 150 cm^{-1}. The low energy part and the high energy part are plotted separately in upper and lower panels, respectively. The partial g(ω) of SO_2, Pt, and Fe is multiplied by a factor of 6 in order to be visualized in the same scale of the y axis.

as shown in the upper panel of Fig. 5.2. The contribution from Fe in this region was previously reported by Félix et *al.*[172] in Fe(pz)[Ni(CN)$_4$] using Raman and nuclear inelastic scattering. The authors found several Fe-ligand vibrations in the region [160-560] cm^{-1} in very good agreement with our computed-G(ω). The Raman spectra allowed to identify Fe-N$_{pz}$ and Fe-N$_{CN}$ stretchings modes at 306 and 381 cm^{-1}, respectively. Our calculations give 324.3 cm^{-1} and 315.9 cm^{-1} for the Fe-N$_{pz}$ stretching and 364.3 cm^{-1} and 363.0 cm^{-1} for the Fe-N$_{CN}$. Some additional modes could be assigned as arising from Fe-N$_{CN}$ stretching around 400 cm^{-1}. The peaks predicted at *ca.* 140 cm^{-1} and 400 cm^{-1} have contributions mainly from the pyrazine and the CN groups as explained in more detail below, while the peak computed at 107 cm^{-1} is mainly due to a vibration of the pyrazine. At high energy, between 600 and 1500 cm^{-1}, the heavy atoms do not contribute any longer and the CN contribution is almost negligible. Here the well defined peaks are associated with vibrations of the pyrazine and their assignment is reported later. These bands exhibit a strong spectral weight due to the contribution from H atoms. Our analysis of the nature of the vibrational modes is in full agreement with previous IR measurements performed on the same compound[173, 174]: internal vibrations of the pyrazine between 600 and 1700 cm^{-1}, metal-ligand vibrations below 600 cm^{-1} and external modes below 100 cm^{-1}.

5.4.2 Low-energy region

The main change upon adsorption is found in the peak at 100 cm^{-1} (see Fig. 5.1). The intensity of this peak decreases and a new broad feature appears centered at about 129 cm^{-1}. This result is confirmed by the INS data collected on PANTHER which are shown in Fig. 5.9. The peak measured on PANTHER at 96.7 cm^{-1} for the bare material should correspond to the intense band measured at 94.4 cm^{-1} on IN1 (see Fig. 5.6).

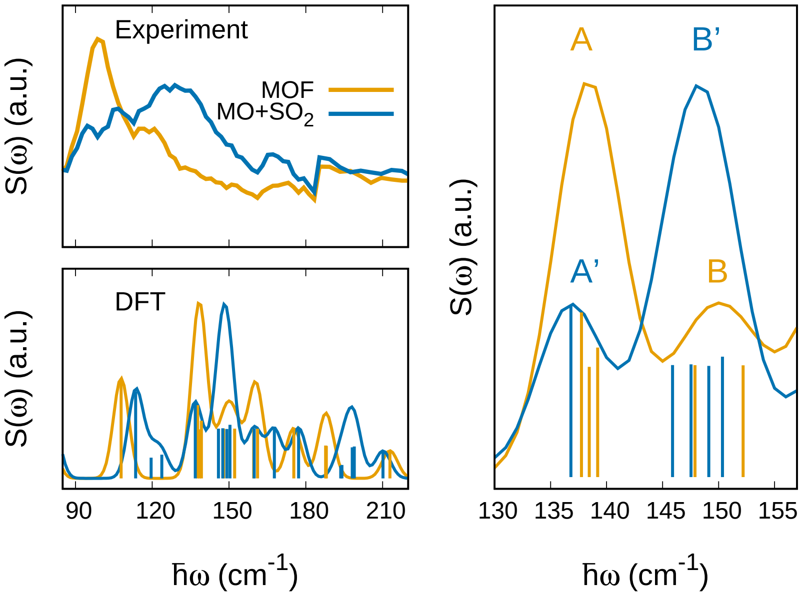

Figure 5.3: Left panels: INS spectra measured at IN1 at 30 K for the empty Fe(pz)[Pt(CN)$_4$] (orange) and after SO_2 adsorption (blue) in the upper figure. The lower figure reports the computed S(ω). Rigth panel: zoom in the region [130 - 160] cm^{-1} where the main change upon gas adsorption occurs.

In this region, the most intense bands predicted by the calculations for the bare material appear at 107.9 cm^{-1} and at 139 cm^{-1}, as shown in Fig. 5.3. The first one corresponds to the rotation of the pyrazine around the z axis, in agreement with calculations by Hochdörffer et al. [175] on a 3D molecular cluster composed of several repetitions of the clathrate unit cell. The second band includes 3 vibrational modes at energies 137.8, 138.5, and 139.2 cm^{-1}. We name this second intense peak A in Fig. 5.3 to assist the analysis. The first peak at 137.8 cm^{-1} is a collective mode involving a movement of the CN group with contributions from in-plane and out-of-plane, together with a rotation of the pyrazine around the z axis. The second at 138.5 cm^{-1} involves a rigid out-of-plane twisting of the $Fe(CN_4)N_2$ octahedra yielding a rigid twisting of the pyrazine about the y axis. This vibrational mode corresponds to the one computed at 140 cm^{-1} in ref. 175. The vibration at 139.2 cm^{-1} involves a large out-of-plane vibration of the cyanide together with a small libration of the pyrazine. The change in the eigenvectors is illustrated in Fig. 5.10. Upon gas uptake, the vibration at 107.9 cm^{-1} blueshifts to 113.5 cm^{-1} possibly due to steric hindrance by the SO_2 molecule and it becomes coupled with a libration of SO_2. Two new modes consisting of pure SO_2 librations appear at 119.5 and 123.7 cm^{-1}. Under peak A, the first mode barely changes (i.e. 137.8 $\rightarrow$ 136.8 cm^{-1}) while the second and third blueshift by 9 and 10 cm^{-1}, respectively (i.e. 138.5 $\rightarrow$ 147.5 cm^{-1}, and 139.2 $\rightarrow$ 149.1 cm^{-1}). The Pt atom does not participate in these vibrations for the bare MOF, but upon gas adsorption the heavy atom contributes to the out-of-plane bending of the cyanide for the mode at 149.1 cm^{-1}. For the bare MOF the peak named B in Fig. 5.3 includes two vibrations at 147.9 cm^{-1} and 152.2 cm^{-1}. These correspond to an in-plane movement of the Pt atoms together with a rigid in-plane displacement of the pyrazines. Upon adsorption, these slightly redshift to 145.9 cm^{-1} and 150.4 cm^{-1}, respectively. All of the vibrations found in peaks A' and B' exhibit a negligible contribution from SO_2. Because the scattering cross section of hydrogen, $\sigma_H = 82.0$ barn, is significantly larger than any other atom (Fe and Pt for example have 11.62 and 11.71 barn, respectively), the gas adsorption mechanism is here probed mainly through changes in the riding modes of H, i.e. those modes that involve vibrations of the hydrogens [87]. As described above, in this region, the vibrations that imply the rotation of the pyrazine around the z axis and the cyanide out-of-plane movement shift to higher energy while those exhibiting in-plane bendings of cyanides show a negligible shift. We attribute the blueshift of this peak predicted at *ca.* 139 cm^{-1} to an increase of the cyanide out-of-plane bending force constant due to steric hindrance, similarly to the hindered rotation of the pyrazine predicted at 107 cm^{-1}.

While the assignment of the experimental peak at 400 cm^{-1} can be performed without ambiguity based on the good agreement with the calculations, the intense band at 100 cm^{-1} may be assigned either to the group of bands predicted at 137.8, 138.5, and 139.2 cm^{-1}, or to these bands together with the peak at 107 cm^{-1}. The intensity of the well defined peak predicted by DFT at *ca.* 400 cm^{-1} includes two normal modes at 403.5 and 405 cm^{-1} which are associated with the torsion of the pyrazine. It undergoes a blueshift upon gas adsorption of 0.8 cm^{-1} and a redshift of 2.06 cm^{-1} for the duplicated mode. The predicted negligible change in the energy of this vibration by the DFT calculations is in agreement with the small change found experimentally (see Fig. 5.1).

5.4.3 The SO_2 binding mechanism

The molecular orbital interaction of SO_2 with this MOF was previously studied by Arcís-Castillo et *al.* [11] using DFT calculations and it was reported before by many authors for other metal complexes [176, 177, 178, 179]. The results of our calculations agree with those of ref. 11 except for the interpretation: we do not identify the mixing between the hybridized Pt d_{z^2}-p_z orbital [45] and the π^* LUMO (lowest unoccupied molecular orbital) of the SO_2 as a π-backbonding because of the absence of π symmetry in this interaction [45]. Below we discuss in more detail the molecular orbital interaction between SO_2 and the metal center.

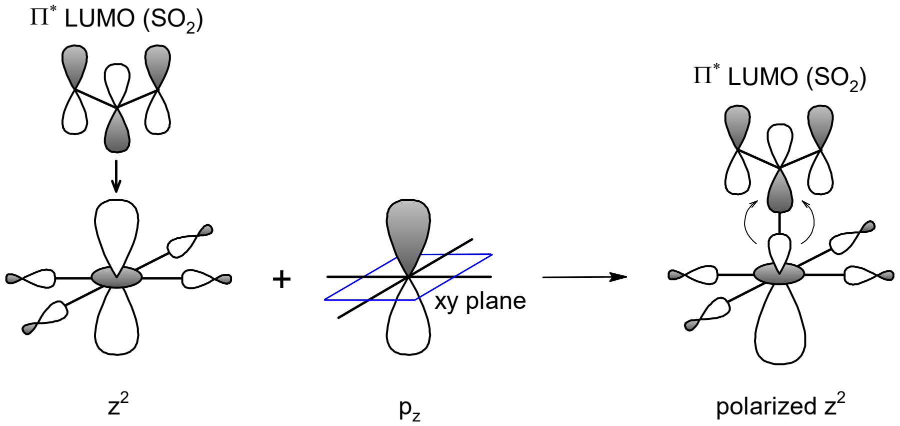

Figure 5.4: Molecular orbital picture of the interaction between the SO_2 LUMO and the polarized hybridized d_{z^2}-p_z orbital of Pt. Because this unoccupied electronic state involves a contribution from the Pt-d_{z^2} that is fully occupied in the bare material, such interaction results in a metal→molecule charge transfer.

When SO_2 binds on top of a metal with square planar coordination, a strong electron donor interaction may be achieved when the σ HOMO (highest occupied molecular orbital) of the molecule can donate electron density to the empty d_{z^2} of the metal. In this case, the expected binding configuration is the η^1-planar [177] as illustrated and discussed in ref. 11. Because for a d^8 electron count the d_{z^2} is doubly occupied, the molecule can act only as an electron acceptor [179]. Since the d_{z^2} is fully occupied, the molecule orients in such a way to decrease the antibonding σ interaction between the HOMO of the molecule and the Pt d_z^2, thus adopting an η^1-pyramidal configuration [177] with the angle between the Pt and the molecular plane of the SO_2 being θ=101.2° (PBE+D2). In this bent configuration, the LUMO of the molecule interacts with a polarized molecular

orbital of Pt (see Fig. 5.11 and 5.4) which is a hybridized Pt d_{z^2}-p_z orbital, the polarized character resulting from the addition (bigger lobe) and cancellation (smaller lobe) of the two d_{z^2} and p_z amplitudes [45]. Such polarized character reduces the antibonding interaction. Possibly because of the bent configuration that would reduce the π type overlap, the interaction of the π^* LUMO does not occur with the d_{xz} or d_{yz} orbitals of Pt.
On the basis of the discussed binding mechanism, SO_2 is thus expected to act as an electron acceptor. The Bader charge analysis peformed in this work using PAW pseudopotentials reveals a rather small charge transfer from the MOF to the molecule of 0.12 electrons, suggesting that other effects possibly related to the MOF skeleton may contribute to the large value of the computed binding energy per SO_2 molecule, i.e. 0.769 eV (with PBE+D2). This value decreases to 0.239 eV upon full geometrical optimization after the D2 correction is removed. We note the stronger binding computed by Arcís-Castillo et *al.* [11] using PBEsol+D2. They predict a binding energy of 0.977 eV, in agreement with the value that we compute when using the same functional, i.e. 0.911 eV. To corroborate this, we computed the binding energy of SO_2 only with the two $[Pt(CN)_4]$ planes, respectively below and above the molecule, by fixing all the atomic coordinates to the relaxed geometry in the MOF. The lattice parameters are set to a=b=c=20 Åin order to reduce interaction between the images. The binding energy is 0.274 eV. This large energy difference between the two cases points to a binding mechanism originating from a combined charge transfer mechanism with the $[Pt(CN)_4]$ planes via the SO_2-Pt interaction, together with a strong interaction with the rest of the MOF skeleton.

	E_{bind}(eV)	d(S-Pt) (Å)	∠(Pt-S-O) (°)	∠(O-S-O) (°)
PBE	0.239	2.895	102.4	116.8
PBE+D2	0.769	2.933	101.2	117.2
PBE+D2+U	0.683	3.470	95.2	118.2
PBE+D2[U]	0.730	2.933	101.2	117.2
PBEsol+D2	0.911	2.786	102.1	116.8

Table 5.1: Comparison of the binding energy, bond distance and bond angles computed using the different functionals. The PBE+D2 computed SO_2 bond angle for the isolated molecule is 119.4°.

An efficient way to improve the treatment of electronic correlations in DFT is to adopt the DFT+U approach where the Hubbard U correction is computed in terms of some localized Hubbard states. We employ the simplified rotationally invariant formulation[180] as implemented in Quantum Espresso. To study how the change in hybridization [159] of the localized d states of Pt upon U correction affects the binding mechanism[181], we employ ortho-atomic projectors to compute self-consistently the linear-response U parameters associated to the d states of Pt (5.2 eV) and Fe (7.5 eV), using density functional perturbation theory [182]. By setting the atomic coordinates to the optimized PBE+D2, we compute a DFT+U binding energy of 0.617 eV. When the geometry is allowed to fully relax using PBE+D2+U, we predict a SO_2 binding energy of 0.683 eV. The full optimization with Hubbard U gives a significantly different SO_2 binding geometry with respect to PBE+D2 case. Tab. 5.1 reports the binding energy, bond distance and bond angles computed with the different computational schemes. The S-Pt bond distance changes from 2.933 Å (PBE+D2) to 3.470 Å (PBE+D2+U) and the Pt-S-O angle from 101.2° to 95.2°. The SO_2 bond angle, O-S-O, slighlty increases upon U correction (see Tab. 5.1). The projected density of states shown in Fig. 5.12 reveals a lower contribution from the polarized Pt atoms (see Fig. 5.4) to the states associated with the LUMO of the molecule, consistent with a reduced charge transfer mechanism and larger SO_2 bending angle. We note that the reported experimental Pt-S bond distance at 120 K is 2.585 Å [11], significantly shorter than the PBE+D2+U one. This elongation of bond lengths upon U correction has already been reported and discussed by some of us [159] and is the reason behind the choice of the PBE+D2 geometry in the calculation of the vibrational modes. Because of this bond elongation and because the use of DFT+U may lead to a bias when computing total energy differences[67], we also report the binding energy computed using a DFT+U density-corrected approach by employing the DFT+D2 geometry. This consists in using the PBE+D2 total energy evaluated on the PBE+D2+U electronic density, an approach that we have named PBE+D2[U] [159]. Here it gives a binding energy of 0.730 eV.

This result together with the above analysis of the binding mechanism indicate that the SO_2 adsorption occurs via a physisorption mechanism, the high value of the computed binding energy arising from a combination of stabilizing electrostatic and van der Waals forces.

5.4.4 High-energy region

The high energy region, which is dominated by the vibrations of the pyrazine, negligibly changes upon gas adsorption. We have computed the $G(\omega)$ of the pyrazine in gas phase and we report the comparison with the partial $G(\omega)$ of the pyrazine in the compound in Fig. 5.13. The complexation of the pyrazine in the MOF slightly modifies the position of the vibrational modes with respect to the gas phase. A comparison and a brief description of the modes is reported in Table 5.2. These were studied by various authors by employing

IR and Raman spectroscopies [183, 184, 185, 186, 187, 188, 189] and INS [190]. Three different spectral regions can be identified for the free and complexed pyrazine: (i) in-plane CH bendings and ring stretching motions in [990 - 1600] cm^{-1}, (ii) intense bands associated with the CH out-of-plane deformation vibrations at [700 - 990] cm^{-1}, and (iii) CH stretching near 3000 cm^{-1}. The vibrations with predominant CC and CN character can be further divided into C-C and C-N stretching modes at 1058 - 1551 cm^{-1}, in-plane bending modes at 580 cm^{-1} and 690 cm^{-1} and out-of-plane bending in the region 750 - 990 cm^{-1} and bellow 500 cm^{-1} like 413 cm^{-1} and 312 cm^{-1}. The characteristic breathing mode of the pyrazine appears at 1009 cm^{-1}. As a general trend, the complexation with Fe(II) blueshifts by [0 - 55] cm^{-1} the vibrational modes of the free pyrazine, in some cases reaching larger shifts [90 - 100] cm^{-1} for certain low-frequency modes. Molnár et

Experiment (INS)	DFT - pz@MOF	DFT - gas phase pz	Assignment
-	3168 3167 3165 3164	3059 3067	CH stretching
-	3155 3153 3152 3150	3088 3092	CH stretching
1601	1597 1596	1551	CH in-plane bending, CC stretch
1482	1487 1486	1525	CN and CC stretch
1472	1459 1458	1472	CH in-plane bending, CN stretch
1430	1426.8 1426.3	1389	CH in-plane bending, CN and CC stretch
1338	1323 1322	1324	CH in-plane bending, CN stretch
1220	1263.9 1263.6	1225	CN and CC stretch
1220	1211 1208	1209	CH in-plane bending, CN and CC stretch
1105	1105 1104	1058	CH in-plane bending, CN and CC stretch
1105	1099 1093	1128	CH in-plane bending, CN stretch
1105	1047 1045	996	CN in-plane bending
1105	1032 1031	1009	Breathing mode
959	960 959	967	CH out-of-plane bending, CNC twisting
959	949.9 949.4	959	CH out-of-plane bending, CNC wagging
876	862 857	913	CH out-of-plane bending, CNC twisting
817	820 819	725	CH out-of-plane bending, CNC wagging
749	735.6 735.5	757	CH out-of-plane bending, CNC wagging
696	687 685	690	CNC in-plane bending
674	680 676	580	CNC in-plane bending
394	403 404	312	CH out-of-plane bending, CNC twisting
-	566 525	413	CH out-of-plane bending, CNC wagging

Table 5.2: Energy position of the peaks measured from the INS data for the bare MOF, the calculated values in the bare MOF and for pyrazine in gas phase, and their assignment. We could not find a correspondence between theory and experiment for the modes at 566 and 525 cm^{-1} due to the low signal and resolution intensity.

al.[173] observed the same tendency upon complexation. This effect is possibly driven by an electron-acceptor effect of the pyrazine from the occupied d orbitals of the metal [191] that increases the π cloud of the ring (and the strength of the double bonds) thus yielding to larger vibrational frequencies [192]. We note that the CH out-of-plane bending mode at 913 cm^{-1} undergoes the opposite effect and redshifts to *ca.* 859 cm^{-1} thus appearing in the gap between [760 - 910] cm^{-1} of the free pyrazine (see Fig. 5.2).

5.4.5 Choice of the supercell

Several authors have reported a specific long range ordering of the pyrazine ligands within these materials as a consequence of gas adsorption [81, 83, 82]. In the absence of diffraction data, we assessed the ordering of the pyrazine upon SO_2 adsorption using DFT calculations. We performed two supercell calculations where we impose that the pyrazines are oriented either perpendicularly with neighboring ones or parallel. We find negligible energy differences between these two configurations when the material is loaded with one SO_2 molecule per Pt atom. We recall that for the bare material such energy difference becomes 39 meV/f.u. [169]. The comparison between the corresponding generalized phonon density of states and that of the bare material, however, shows that the configuration with all pyrazines oriented parallel with one another results in a predicted $G(\omega)$ exhibiting some deviations from the bare material that are not observed experimentally. The comparison between the empty (pyrazine perpendicular) and the loaded material is reported in Fig. 5.5.

The configuration with parallel pyrazines upon SO_2 adsorption results in a noticeable change in the intense peak at 400 cm^{-1} with respect to the bare material, a feature that is not observed in the experiment. Similarly, the high energy features between 800 and 1000 cm^{-1} redshift in the configuration with parallel pyrazines, suggesting that the INS data may correspond to a configuration with pyrazines oriented perpendicularly with each other both before and after gas adsorption.

We tested a few functional choices on the computed $G(\omega)$ for the bare material. For this we employed the primitive cell (thus imposing parallel pyrazines) and the exchange and correlation functionals PBEsol+D2, rev-vdW-DF2, and PBE+D2. The three functionals give very similar results. At high energy, the spectra negligibly depend on the specific choice while at low energy, as expected, they are more strongly affected by the approximation to the exchange and correlation energy [193], as shown in Fig. 5.14. Specifically, we see a tendency to predict higher frequencies in this region using PBEsol+D2, as compared with PBE+D2, consistent with shorter bond distances and smaller lattice

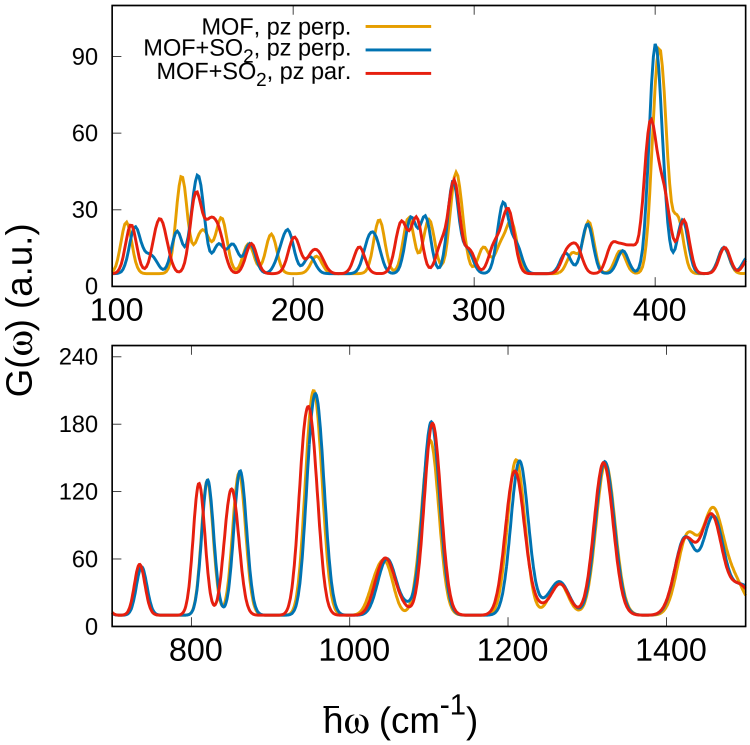

Figure 5.5: Total G(ω) in the low (upper panel) energy and high energy (lower panel) computed for the bare material with perpendicularly oriented pyrazines (yellow), and for the material loaded with one SO$_2$ per Pt site computed by employing perpendicular (blue) or parallel (red) pyrazines.

parameters.

5.5 Conclusion

The SO$_2$ adsorption mechanism in the Fe(pz)[Pt(CN)$_4$] Hofmann clathrate is here probed by combining inelastic neutron scattering experiments and DFT calculations. The most noticeable change upon adsorption is the blueshift of the peak measured at *ca.* 100 cm^{-1} which we attribute to an increase of the cyanide out-of-plane bending force constant due to steric hindrance and to the hindered rotation of the pyrazine around the z axis. The experimental observations are consistent with an adsorption mechanism being a combined charge transfer, electrostatic and dispersion interactions, as predicted by the DFT calculations. The high-energy peaks which are associated with the internal vibrations of the pyrazine molecule are negligibly affected by the presence of the physisorbed gas molecule. We note that, upon heating, this material undergoes a spin crossover transition from S=0 to S=2. In this respect, we expect a lower sensitivity to this gas in the high-spin state phase due to the larger lattice parameters[71] and therefore smaller steric effects. Finally, because the change in the vibrational properties upon gas adsorption strongly depends on the nature of the adsorption mechanism, we expect different gas molecules to yield distinctive modifications of the spectral features of the INS data, possibly allowing to differenciate, for example, steric effects from chemical modifications. We are confident that the present joint computational and experimental scheme will help future efforts towards the characterization of other gas adsorption in these families of materials.

5.6 Acknowledgement

This work benefited from the support of the project ANR-15-CE06-0003-01 funded by the French National Agency for Research. Calculations were performed using resources granted by GENCI under the CINES and TGCC grant numbers A0020907211 and A0110907211. Additionally, the froggy and Dahu platform of the CIMENT infrastructure, which is supported by the Rhone-Alpes region (GRANT CPER07_13 CIRA) and the Equip@Meso project, was employed for the calculations. We thank the ILL for the PhD contract of A.F.B. and for the beamtime allocation under experiment numbers 7-02-108, 7-05-513, and 7-05-430 (doi.ill.fr/10.5291/ILL-DATA.7-05-430). J.A.R. acknowledges resources from Grant PID2019-106147GB-I00 funded by MCIN/AEI/10.13039/501100011033.

5.7 Supporting Information

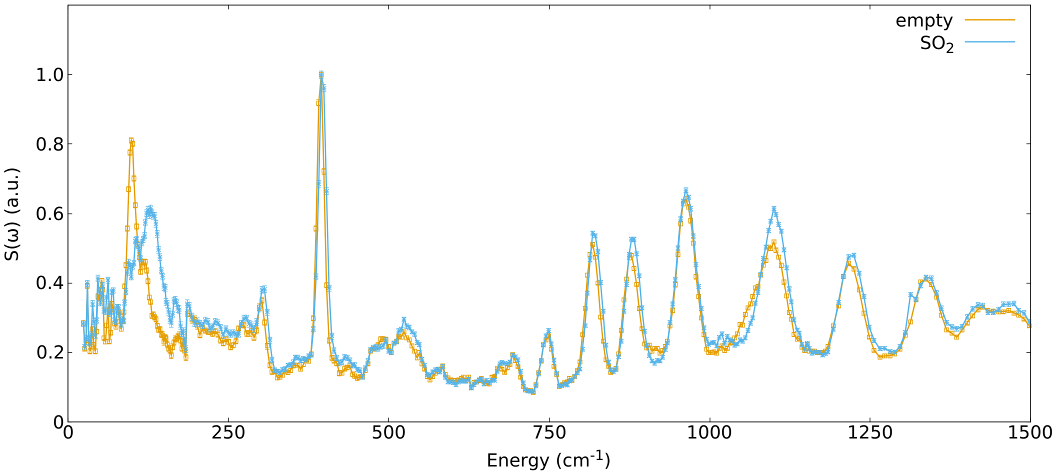

Figure 5.6: INS spectra (and errors) measured at IN1-LAGRANGE at 30 K for the empty Fe(pz)[Pt(CN)$_4$] (orange) and after SO_2 adsorption (blue).

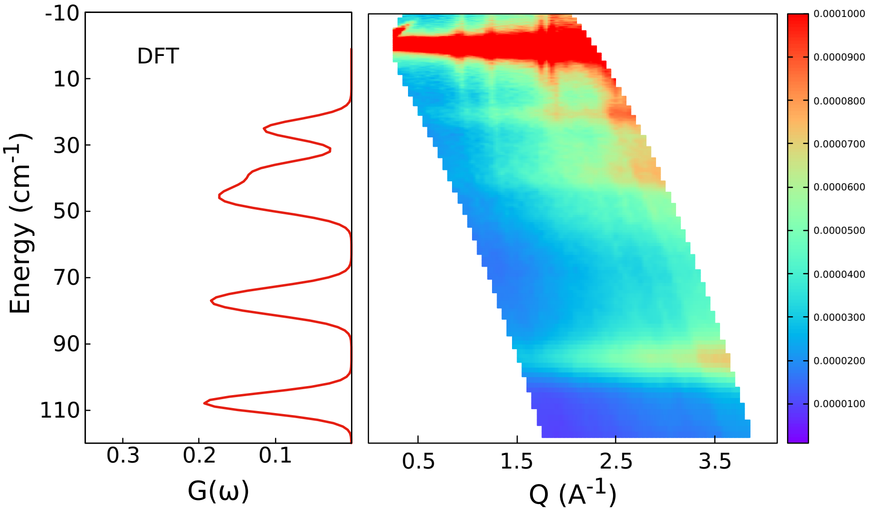

Figure 5.7: Right: INS data collected at IN5 at 295 K for the empty material. Left: low-energy vDOS computed using PBE+D2 also for the empty material. The IN5 data show 3 peaks at 94.4 cm^{-1}, 37.9 cm^{-1} and 20.2 cm^{-1}. The peak at 94.4 cm^{-1} corresponds to the peak observed in the IN1 data at around 100 cm^{-1}. See Figure 5.1 of the manuscript.

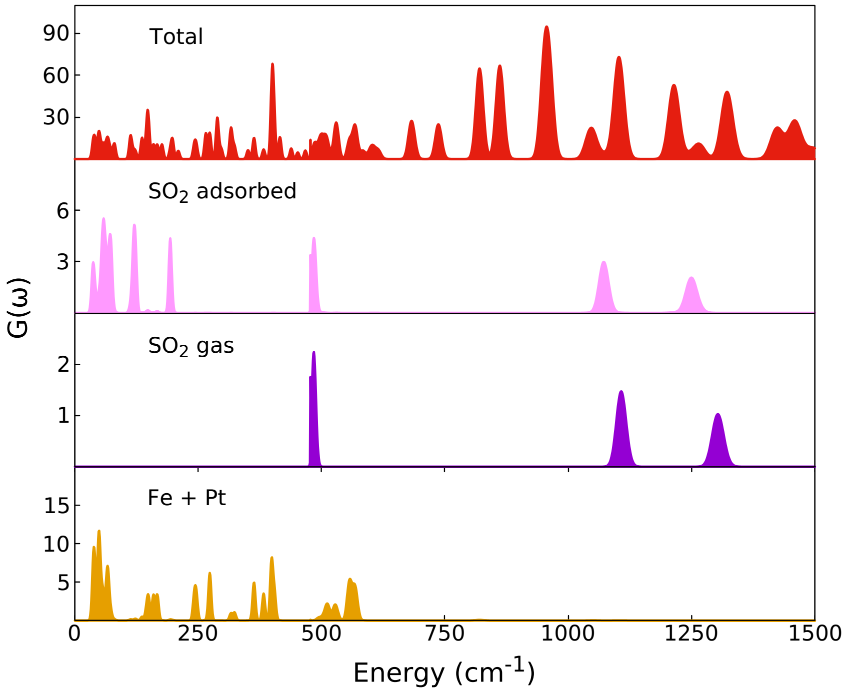

Figure 5.8: Total and partial G(ω). The G(ω) of gas phase SO_2 is also reported for comparison.

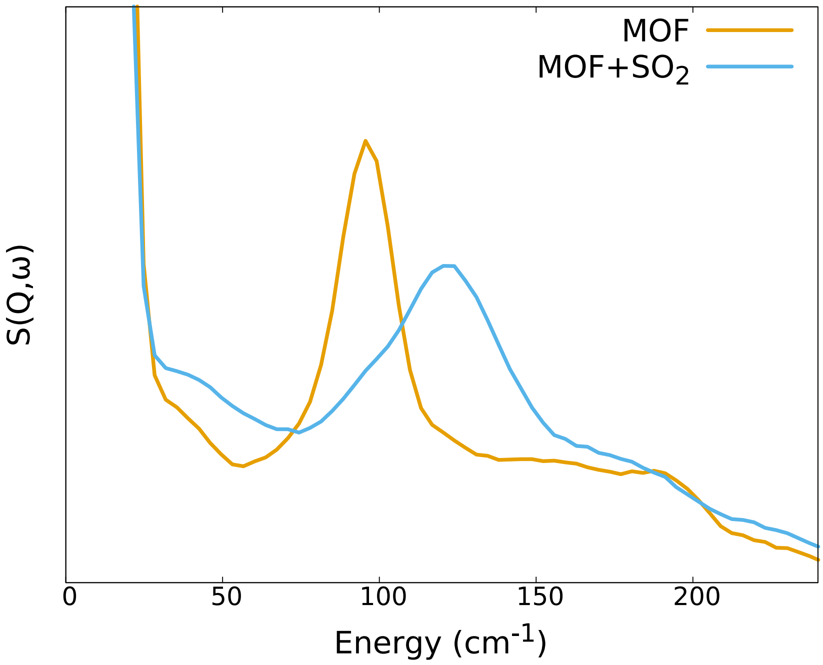

Figure 5.9: INS data collected at 10 K on PANTHER for the bare and loaded material.

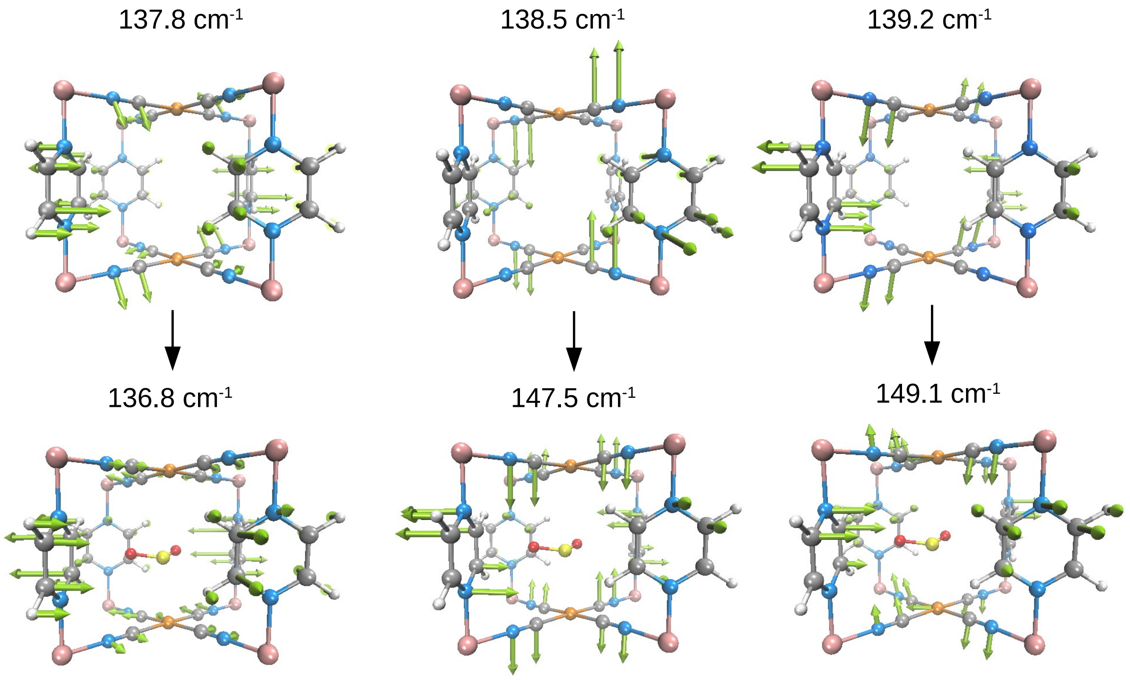

Figure 5.10: Change in the eigenvalue and eigenvectors of the three normal modes predicted below the intense peak at *ca.* 139 cm^{-1} (peak A in Fig. 5.3 of the manuscript).

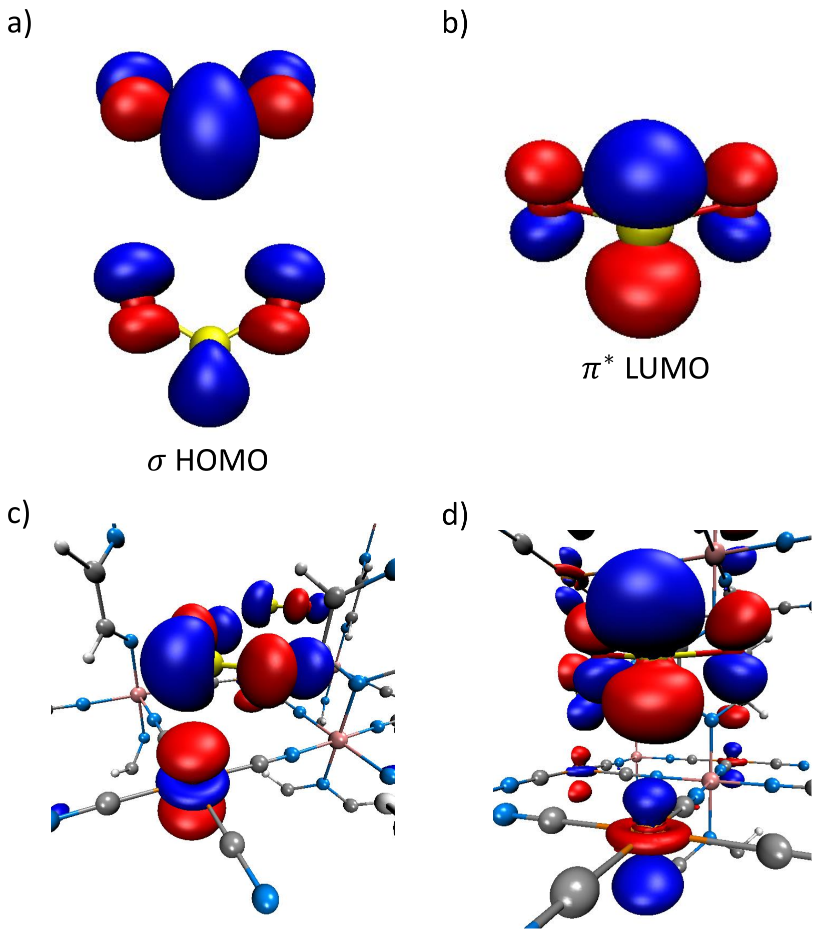

Figure 5.11: DFT+D2 wavefunctions of a) σ HOMO and b) π^* LUMO of free SO_2 and molecular orbital interaction of c) Pt-d_{z^2} and SO_2 HOMO predicted at -1.75 eV and d) Pt d_{z^2}-p_z and SO_2 LUMO at 0.69 eV (see PDOS in Figure 5.12, upper panel).

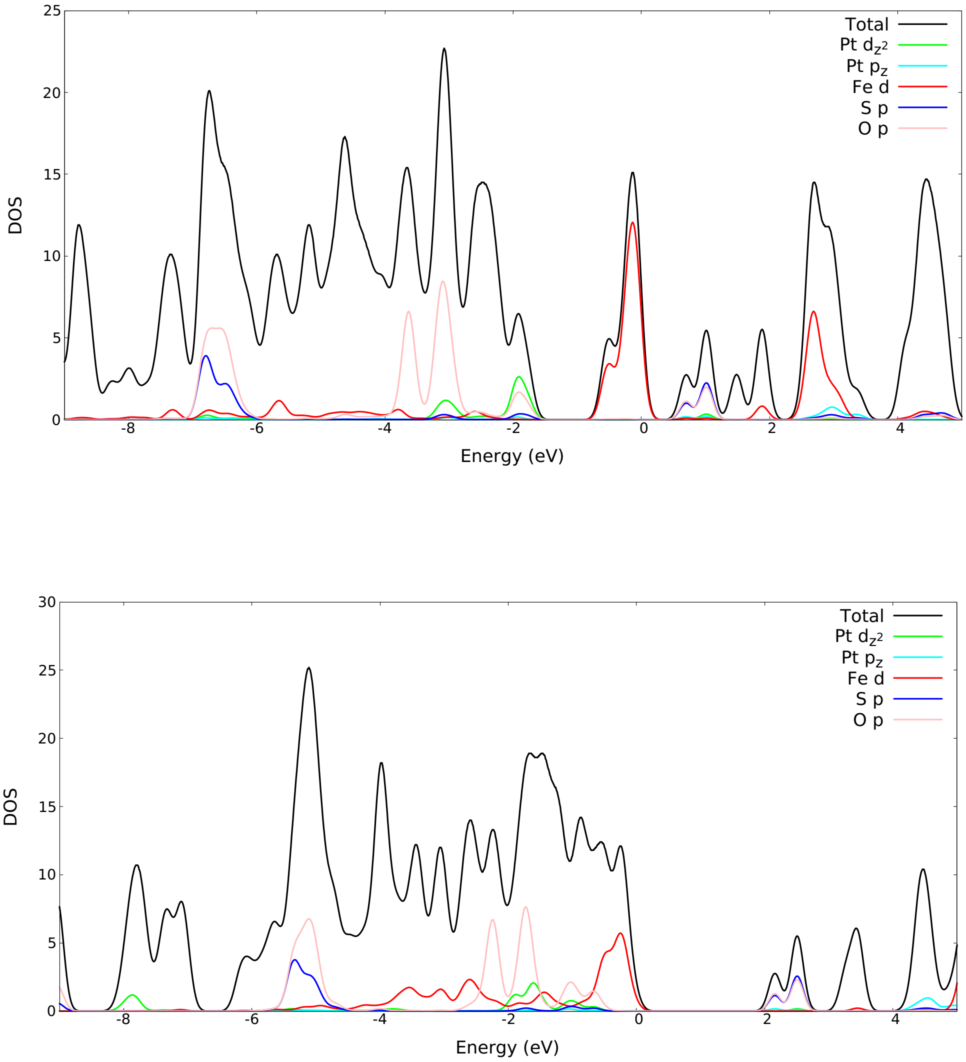

Figure 5.12: Upper panel: Total and partial (Pt d_{z^2} and p_z orbital specific) DOS computed for the MOF+SO_2 using PBE+D2. Lower panel: the same computed using DFT+D2+U. The DOS is shifted in energy by -1.90 eV (upper panel) and 0.17 eV (lower panel) to align the HOMO to zero.

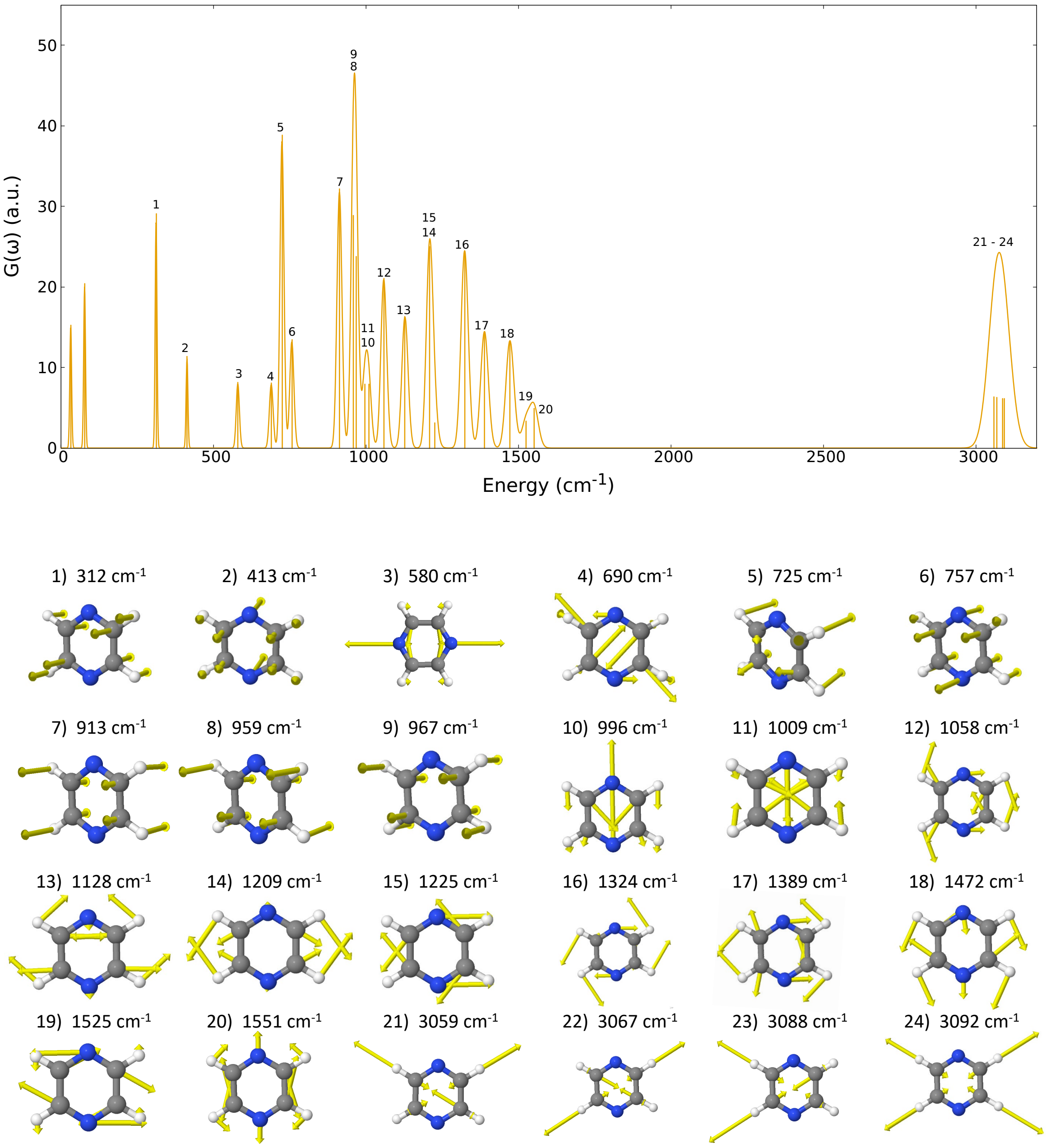

Figure 5.13: Total G(ω) computed for the gas phase pyrazine in the upper panel and the corresponding visualization of the eigenvectors in the lower figure.

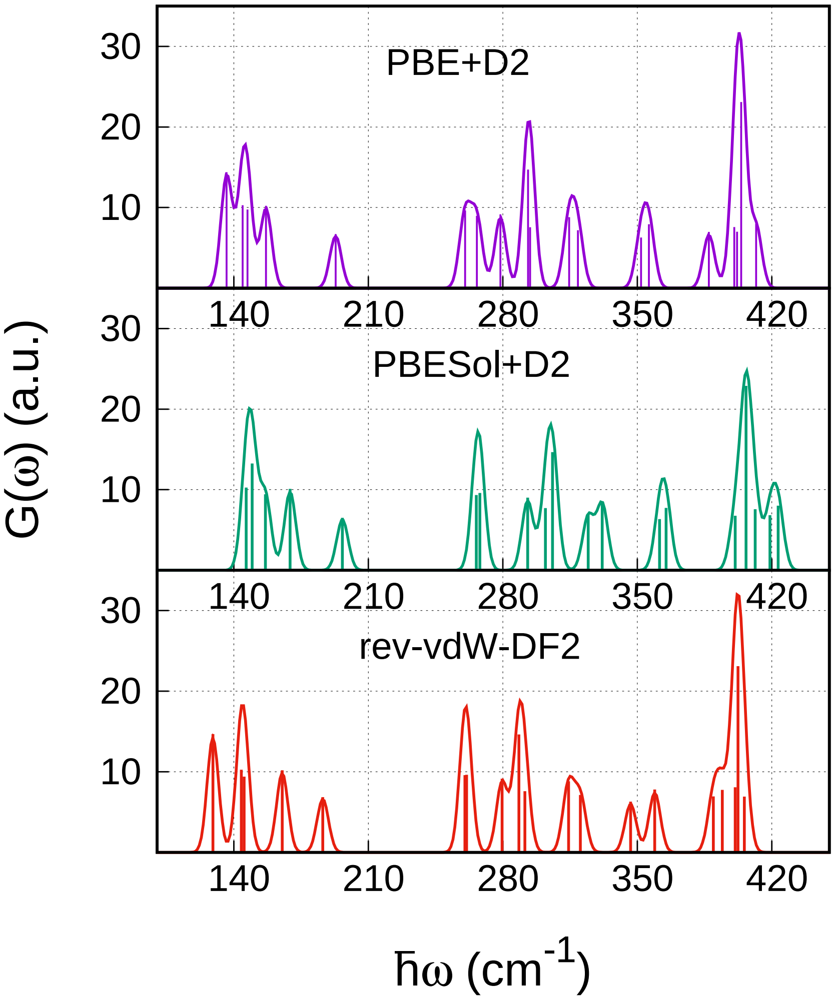

Figure 5.14: Comparison of the total G(ω) computed with the primitive cell using three different functionals. We predict a=7.13 Å, b=7.14 Å, c=6.71 Å, using PBE+D2, while for PBEsol+D2, a=7.02 Å, b=7.08 Å, and c=6.62 Å. rev-vdW-DF2 gives values of a=7.16 Å, b=7.10 Å, and c=6.70 Å.

Chapter 6

CO and CO_2 Adsorption Mechanism in Fe(pz)[Pt(CN)$_4$] Probed by Neutron Scattering and Density-Functional Theory Calculations

Ángel Fernández-Blanco[1,2], Lucía Piñeiro-López[3], Mónica Jiménez-Ruiz[1], José Antonio Real[4], Jose Sanchez Costa[3], Roberta Poloni[2] and J. Alberto Rodríguez-Velamazán[1]

[1] *Institut Laue Langevin, 71 Avenue des Martyrs, CS 20156-38042, Grenoble, France*

[2] *SIMaP, Grenoble-INP, University of Grenoble-Alpes, CNRS, 38042 Grenoble, France*

[3] *IMDEA Nanociencia, Faraday 9, Ciudad Universitaria de Cantoblanco, 28049 Madrid, Spain*

[4] *Departamento de Química Inorgánica, Insituto de Ciencia Molecular (ICMol), Universidad de Valencia, 46980, Paterna, Spain*

Ángel Fernández-Blanco, Lucía Piñeiro-López, Mónica Jiménez-Ruiz, José Antonio Real, Jose Sanchez Costa, Roberta Poloni and J. Alberto Rodríguez-Velamazán, "CO and CO_2 Adsorption Mechanism in Fe(pz)[Pt(CN)$_4$] Probed by Neutron Scattering and Density-Functional Theory Calculations".

6.1 Abstract

By combining neutron diffraction (ND), inelastic neutron scattering (INS) and density-functional theory (DFT) calculations we study the binding mechanism of CO and CO_2 in the porous spin-crossover compound Fe(pz)[Pt(CN)$_4$]. Two main interaction sites are identified for the guest molecules, above the open-metal site, and between the pyrazine rings. For CO, the most stable orientation implies the CO molecules located parallel to the neighboring gas molecules and perpendicular to the pyrazine planes. For CO_2, the molecules located on-top of the open-metal site are perpendicular to the pyrazine rings while those between the pyrazines are almost parallel. These configurations are consistent with the INS experiment, well-reproduced by the computed generalized phonon density of states. The most relevant signatures of the binding occur in the spectral region around 100 cm^{-1} and around 400 cm^{-1}. The first one blue-shifts for both CO and CO_2 adsorption, while the higher energy one red-shifts for CO and remains nearly unchanged for CO_2. The interpretation of these results together with the computed binding energy and a molecular orbital analysis are consistent with a physisorption mechanism for both gases. This work shows the strength of the combination of neutron techniques and DFT calculations to characterize in detail the gas adsorption mechanism in this type of materials.

6.2 Introduction

Metal organic frameworks (MOFs) are hybrid and crystalline materials composed of metal centers connected by organic ligands. The resulting 3D frameworks exhibit ultrahigh porosity and large surface areas that can be modulated for specific applications due to the wide availability of metal-ligand combinations. For this reason, MOFs have been extensively studied for applications in many different fields of science such as catalysis [23, 24, 25, 26], drug delivery [27] or gas adsorption [28, 29], separation [30, 31], sensing [32, 33, 26, 16] and storage [34, 30], among others. One of the applications that has attracted the most attention in recent years is the $in-situ$ capture of polluting gases emitted from anthropogenic sources. Special attention has been paid to carbon dioxide due to its strong impact on the greenhouse effect [41, 1, 42]. Other gases, like carbon monoxide, can also play an important role in climate change and the development of capture strategies is interesting not just for environmental concerns but also for the possibility of reusing them in other industrial chemical processes [4].

Hofmann-like clathrates with general formula Fe(pz)[M(CN)$_4$] (pz = pyrazine, M = Ni, Pd, Pt) [71] are a versatile class of MOFs with octahedrally coordinated Fe(II) centers connected by cyanide ligands, CN^-, to a square-planar open-metal site, M(II). The resulting Fe[$M^{II}(CN)_4]_\infty$ layers are pillared by bidentated aromatic ligands resulting in three-dimensional networks. These materials are interesting for gas capture applications due to the combination of open-metal sites and bistable Fe(II) spin-crossover centers. These can undergo a spin-state *switch* under the influence of external stimuli such as temperature, pressure, light or incorporation of guest molecules. The presence of unsaturated metal centers can, potentially, enhance the adsorption capacity [8], whereas their bistability can be used for sensing applications. Recently, the member of the series Fe(pz)[$M(CN)_4$] with M = Pt(II) has shown a significant higher CO_2 and CO uptake capacities compared to other MOFs with larger surface areas [12] and several studies of gas adsorption have been published [83, 81, 11, 194, 195, 196] since they discovery in 2001 [71]. In this work, we focus our interest in the CO and CO_2 capture properties of these Hofmann-like clathrates. We report a detailed study of gas adsorption mechanism of CO and CO_2 in Fe(pz)[$Pt(CN)_4$] by means of neutron scattering techniques and density-functional theory calculations. We identified two adsorption sites, over the open-metal site and between the pyrazine rings, and the most stable orientational configuration of the guest molecules and the pyrazine ligands of the framework was determined. The inelastic neutron scattering results assisted by DFT calculations, show signatures of a hindrance of the pyrazine libration and the out-of-plane movement of cyanide ligands when the gas is adsorbed. Together with the computed binding energy and a molecular orbital analysis, these results agree with a physisorption mechanism for both gases.

6.3 Methods

Sample preparation Dehydrated powder samples of Fe(pz)[$Pt(CN)_4$] and its deuterated homologue Fe(d_4-pz)[$Pt(CN)_4$] were prepared as described elsewhere.[71, 81, 128, 129] The samples were activated by heating them overnight at 100°C.

Neutron diffraction. Neutron experiments were performed in the high-intensity two-axis diffractometer D20 installed on the hot neutron source of the high-flux reactor at the Institut-Laue Langevin (ILL) in Grenoble, France. A wavelength of 1.54 Å was used. The empty and gas-loaded samples were measured at 100 K. Rietveld refinements and calculations of the structures were performed using the FullProf suite of programs.[137, 138] The schematic illustrations of the crystal structures and magnetic arrangements were obtained with the VESTA program [197].

Inelastic Neutron Scattering. Inelastic neutron scattering experiments were performed in the indirect geometry-type spectrometer IN1-LAGRANGE installed on the hot neutron source of the high-flux reactor at the Institut Laue Langevin (ILL) in Grenoble, France. Monochromators of Si(111), Si(311) and Cu(220) were selected to collect the data for energy transfers of [8-129], [92-215] and [173-427] cm^{-1}, respectively. The measurements were done at 30 K for both the empty and loaded materials. A post-processing treatment of normalization to monitor counts and subtraction of the empty sample holder was done using LAMP. [190]

Gas adsorption The powder samples were placed inside a cylindrical aluminium sample holder connected to a sample stick adapted for gas adsorption. A manifold gas pumping system was attached to the stick through a capillary and the temperature control was achieved using either a closed-cycle cryostat (IN1-LAGRANGE) or an Orange cryostat (D20). The samples were loaded to saturation by initially injecting the gas doses at room temperature and then lowering the temperature of the sample holder (to 100 K for CO and 200 K for CO_2), creating a cold point to force the gas to move towards the sample and facilitate the adsorption. For CO_2, the saturation loading is about 1.5 mol of CO_2 per Fe mol, as determined experimentally from adsorption isotherms [81, 195]. In the absence, to the best of our knowledge, of published absorption isotherms for CO, we estimate the saturation loading at about 2 CO mol / Fe mol from the kinetic uptake experiments reported by Ibarra et *al.*[12]. Our ND, DFT and INS results are consistent with these saturation loading values (vide infra).

Computational details. The DFT calculations were performed with the Quantum Espresso package[119, 117, 118] (v 6.4) within the generalized gradient approximation (GGA) of Perdew, Burke and Ernzerhof (PBE)[160] and long-range interactions described with the semiempirical approach proposed by Grimme (PBE+D2)[142, 143]. We use the Rappe-Rabe-Kaxiras-Joannopoulos ultrasoft (rrkjus) pseudopotentials[168] without semicore states in valence. The convergence threshold on forces is 0.0001 Ry/Bohr and the wavefunctions and charge density cutoffs are set to 100 and 1000 Ry, respectively. All the calculations are performed using the low-spin (S = 0) electronic configuration for the Fe(II) atoms. The Brillouin zone is sampled using a 3 × 3 × 3 Monkhorst-Pack *k*-point grid. The Becke-Johnson (BJ) damping scheme[198, 199] together with the D3 Grimme approach (PBE+D3+BJ) was also used to perform a Barder charge analysis in the loaded

MOFs. The same pseudopotentials, force thresholds, Monkhorst-Pack k-point grid, wavefunctions and charge density cutoffs than for PBE+D2 were used for this functional. The inelastic scattering data collected on IN1-LAGRANGE are compared with the computed scattering function $S(Q,\omega)$ given by[88, 170, 171]

$$S(Q,\omega) = e^{-2\overline{W}}\frac{Q^2\hbar}{2\overline{M}\omega} < n+1 > G(\omega) \tag{6.1}$$

where G(ω) is the generalized phonon density of states defined elsewhere[141], $\overline{M}$=$\sum_l$ M$_l$/N, n is the thermal-equilibrium occupation number of the vibrational state and $< n+1 >= \frac{exp(\hbar\omega\beta)}{exp(\hbar\omega\beta)-1}$ with $\beta = \frac{1}{K_BT}$. The exponential term is the Debye-Waller factor for neutron attenuation by thermal motion and ω the phonon frequencies obtained by employing the ph.x package in Quantum Espresso.[119] Q corresponds to kinematical range of IN1-LAGRANGE. A convolution with a Gaussian function is also applied to account for the resolution of the monochromators with a standard deviation of 3.0 cm^{-1} for the range [0 - 478] cm^{-1} and 0.009ω for [478 - 4033] cm^{-1}, close to the experimental resolution of IN1-LAGRANGE.[93]

Supercell geometry The orientational configuration of the pyrazine rings depends on the nature and amount of the guest molecules incorporated in the material. Recently, the present authors reported an ordered structure for the empty Hofmann clathrate Fe(pz)[Pt(CN)$_4$] with the pyrazine ligands oriented in a perpendicular configuration [169]. The ordered structure is found below the spin-transition temperature (*ca.* 285 K), whereas at higher temperature the Fe(II) atoms switch to HS and the pyrazines display a dynamic disorder [132]. To account for a possible perpendicular configuration, a supercell with lattice parameters a'=$\sqrt{2}a$ and b'=$\sqrt{2}b$ is used, where a and b are the lattice parameters of the primitive cell. The PBE+D2 lattice parameters of the bare MOF are a = 10.096 Å, b = 10.097 Å, and c = 6.711 Å[141]. In presence of adsorbed molecules, the orientation of the pyrazines can remain perpendicular[141] or change to a parallel configuration as reported for water[83], depending on the type and amount of adsorbed gas. To address this problem, we collected neutron diffraction data of the deuterated homologue, taking advantage of the sensitivity of this technique to the deuterium position and consequently to the pyrazine orientation. The different configurations were also explored by DFT calculations by studying an increasing number of adsorbed CO and CO$_2$ molecules: 1, 1.5, and 2 molecules per formula unit (f.u.) both in the parallel and the perpendicular configuration of the pyrazines.

6.4 Results and discussion

6.4.1 Neutron diffraction.

We used neutron diffraction data collected on gas-loaded Fe(d_4-pz)[Pt(CN)$_4$] to get insight into the configuration of the pyrazine moieties. The absence of the peaks characteristic of a perpendicular configuration (Fig. 6.10 in SI) is a strong indication to discard this possibility. Additionally, some peaks related to the parallel configuration show an increase (although this could be also in part correlated with the presence of gas molecules in the structure). Therefore we used the parallel configuration as starting model, which is consistent with DFT calculations (see below). In subsequent refinements, some disorder was allowed between the possible positions of the pyrazine.

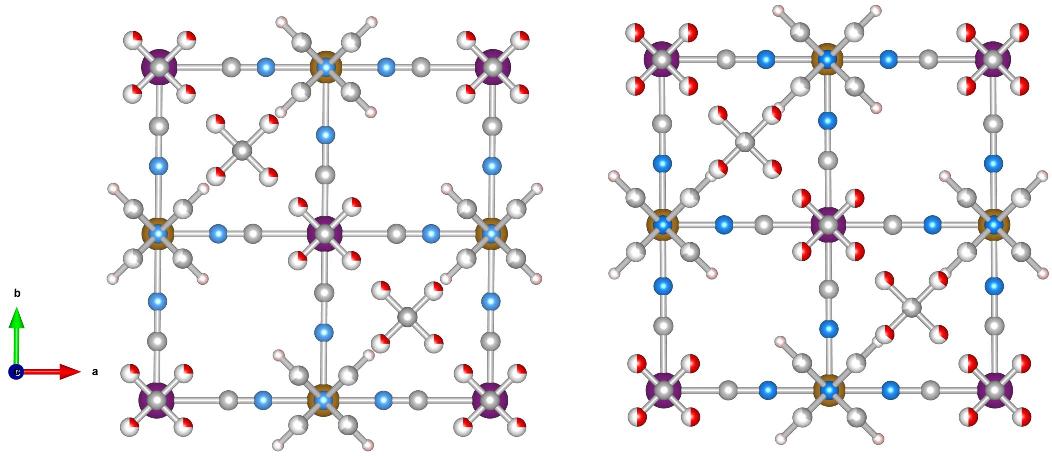

Figure 6.1: Top-view illustrations of the structure of gas-loaded Fe(pz)[Pt(CN)$_4$] obtained by neutron diffraction. Left: Fe(pz)[Pt(CN)$_4$] loaded with two CO molecules per f.u. Right: Fe(pz)[Pt(CN)$_4$] loaded with 1.7 CO_2 molecules per f.u. Color code: purple, orange, blue, silver, red and pink are Pt, Fe, N, C, O and H, respectively.

The residual scattering density obtained when the initial model of the bare Fe(pyrazine)[Pt(CN)$_4$] with parallel pyrazines is compared to the experimental neutron diffraction pattern of the gas-loaded compounds (see Fig. 6.11 in SI for the case of CO) allows us to distinguish two bonding sites for the guest molecules: (i) On top of the open-metal site (site A) and (ii) between the pyrazine rings (site B). The higher density is found in site A, which is an indication of a preference for this site. The residual density observed, located mainly in the $z = 0$ plane, is indicative of a position of the gas molecules in parallel to the Pt[CN]$_4$ plane. The guest molecules were then incorporated to the model. Initially, these molecules were placed disordered in two perpendicular positions (see Fig. 6.1), and 2 and

1.5 molecules per f.u. were considered for CO and CO_2, respectively (with site A always fully occupied, since it shows a significantly higher residual density). With this model, the disorder of the pyrazine rings between their two possible positions was estimated by a fit to the gas-loaded Fe(d_4-pz)[Pt$(CN)_4$] patterns, with refined values of 35(2) and 30(3) % for CO and CO_2, respectively. This disorder was then fixed in the ensuing refinements. Finally, constrained fits (due to the quality of the data and the number of parameters) of the gas-loaded Fe(pyrazine)[Pt$(CN)_4$] patterns (see details in the SI) yielded the structural models presented in Figure 6.1.

The structures present a slight monoclinic distorsion (of ca. 0.5° in γ for both CO and CO_2) , in agreement with DFT results (vide infra). The ordering of the pyrazine rings in a preferentially parallel configuration implies the existence of two non-equivalent B sites, one with more space available than the other. Attempts to introduce gas molecules in the site with less available space produced worse fits. A total occupancy of 2 CO molecules per f.u. gave the best agreement for the CO-loaded material, with both A and B sites fully occupied. For CO_2, the best fits are obtained with a total occupancy of 1.69(6) CO_2 molecules per f.u. (the A site was considered fully occupied while the occupancy of guest molecules in the B site was allowed to vary). The refinement of the disorder among the possible orientations of the guest molecules allowed by the proposed model did not give significant improvement of the fits, thus the disordered configurations were retained.

6.4.2 Calculated configuration

DFT calculations are used to resolve the most stable configuration in the ground state. For CO, we find a perpendicular orientation of the pyrazines upon adsorption of 1 molecule per f.u. while for 1.5 and 2 CO per f.u. a parallel orientation is predicted. The energy differences between the two configurations are -0.029 eV, 0.007 eV, and 0.119 eV, respectively, per formula unit. Therefore, for the predicted saturation loading of 2 CO per f.u., the parallel orientation of the pyrazine ring is the most stable. This is consistent with the observations made on the neutron diffraction patterns of CO-loaded Fe(d_4-pz)[Pt$(CN)_4$]. For 1.5 and 2 CO per f.u., the two binding sites obtained in our calculations are in agreement with the observed by neutron diffraction: on-top of the open-metal site (site A), and between the pyrazine rings (site B). The occupancy of site B is 0.5 for 1.5 CO per f.u. and 1.0 for 2 CO per f.u. The A site is always fully occupied. The CO molecules are oriented perpendicular to the pyrazine planes and parallel to the Pt$[CN]_4$ plane (see Fig. 6.2), regardless of the amount of gas. The unit cell presents a monoclinic distortion ($\gamma = 89.55°$), in agreement with the neutron diffraction results.

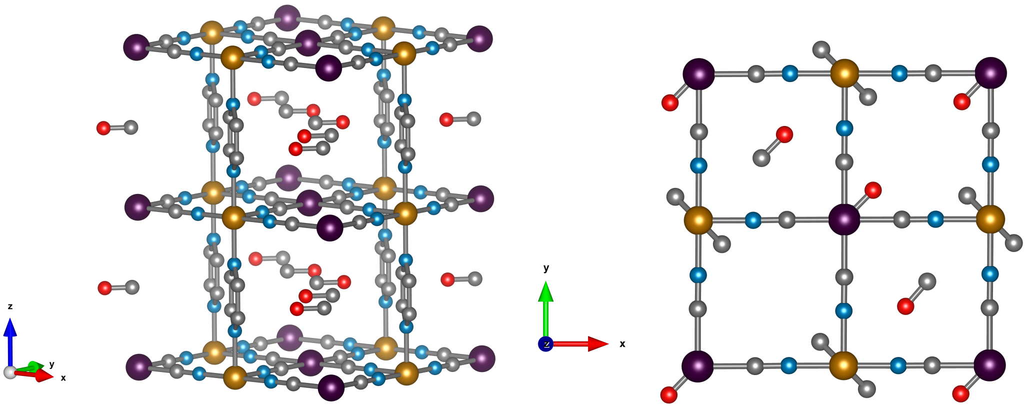

Figure 6.2: Side- and top-view illustrations of Fe(pz)[Pt(CN)$_4$] loaded with two CO per open-metal-site. Color code: purple, orange, blue, silver and red are Pt, Fe, N, C and O, respectively. For clarity, hydrogen atoms are omitted.

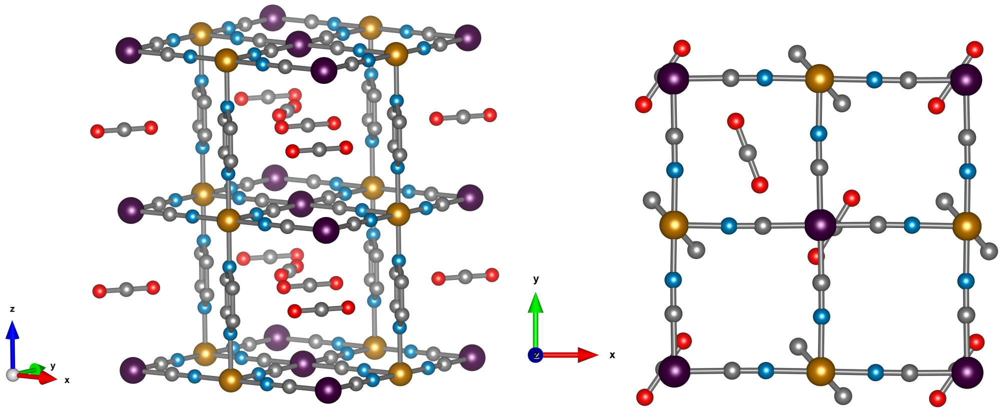

Figure 6.3: Side- and top-view illustrations of Fe(pz)[Pt(CN)$_4$] loaded with 1.5 CO$_2$ per open-metal-site. Color code: purple, orange, blue, silver and red are Pt, Fe, N, C and O, respectively. For clarity, hydrogen atoms are omitted.

In the case of CO$_2$, the orientation of the pyrazines is parallel for 1 and 1.5 CO$_2$ per f.u. with a corresponding energy difference between parallel and perpendicular of 0.016 and 0.036 eV per f.u., respectively. Only the parallel configuration could be converged for 2 molecules suggesting that large interatomic forces could prevent a perpendicular configuration in this case. For a loading of 1 CO$_2$ per f.u. the molecules are located only on site A and are perpendicular to the pyrazine planes. When 1.5 and 2 molecules per f.u. are considered, CO$_2$ locates in both sites A and B. The molecules in site A are again perpendicular to the pyrazine planes, while the molecules in site B are almost parallel to the pyrazine planes and perpendicular to the neighbouring CO_2 (Fig. 6.3), possibly owing to repulsive interactions. While molecules in site B are parallel to the $Pt(CN)_4$ plane for a loading of 1.5 CO_2, for a 2 molecule-loading, the CO_2 are tilted off-plane. In the first case, the molecules on-top of the platinum in site A move slightly off the metal position (see top-view in Fig.6.3). Also in this case, the structure is monoclinically distorted ($\gamma = 89.51°$), consistent with the neutron diffraction results.

6.4.3 Amount of gas adsorbed.

Neutron diffraction on the deuterated compound suggests that most of the pyrazines are in parallel orientation for both the CO- and CO_2-loaded materials. DFT confirms that this configuration only occurs when 1.5 or 2 molecules of CO are adsorbed per open-metal-site. Therefore, we can deduce that more than one molecule has been adsorbed. Since no reported absorption isotherms for CO are available, the saturation loading can be estimated at about 2 CO mol / Fe mol from kinetic uptake experiments [12], in agreement with our neutron diffraction results. The combination of INS and DFT calculations is consistent with this loading value. In the case of CO_2, a parallel configuration is predicted by DFT for all the loading values considered. We have retained the value of 1.5 molecules per f.u. in our calculations, which is consistent with the saturation loading for CO_2 determined experimentally from adsorption isotherms (about 1.5 mol of CO_2 per Fe mol [81, 195]), and with the refined value of ca. 1.7 obtained by neutron diffraction. The INS results are also consistent with these loading values (vide infra).

6.4.4 Inelastic Neutron Scattering

The experimental spectra for the empty MOF and upon CO and CO_2 adsorption are shown in Fig. 6.4 (upper panel) together with the scattering function computed using eq. 6.1 (lower panel). For the bare material the pyrazines are considered perpendicular in agreement with previous calculations and experimental findings [141, 169]. The scattering function upon CO adsorption in Fig. 6.4 is computed by adopting the configuration described in the previous section with 2 molecules per f.u. and pyrazines in a parallel orientation. For CO_2, we consider 1.5 molecules per f.u. , which is consistent with neutron diffraction analysis, and a parallel orientation of the pyrazines.

The experimental errors are reported in Fig. 6.13 and Fig. 6.14 in the SI upon CO and CO_2 adsorption, respectively. Data were collected up to 427 cm^{-1}. The measurements below 100 cm^{-1} are not optimized at IN1 making it difficult to assign the vibrational modes from the calculations; while at high energy a reasonable good agreement between experiment and DFT is found[200, 141], low energy modes may present larger relative errors due to the underlying approximations (specifically basis set and functional choice may affect this part of the spectra).

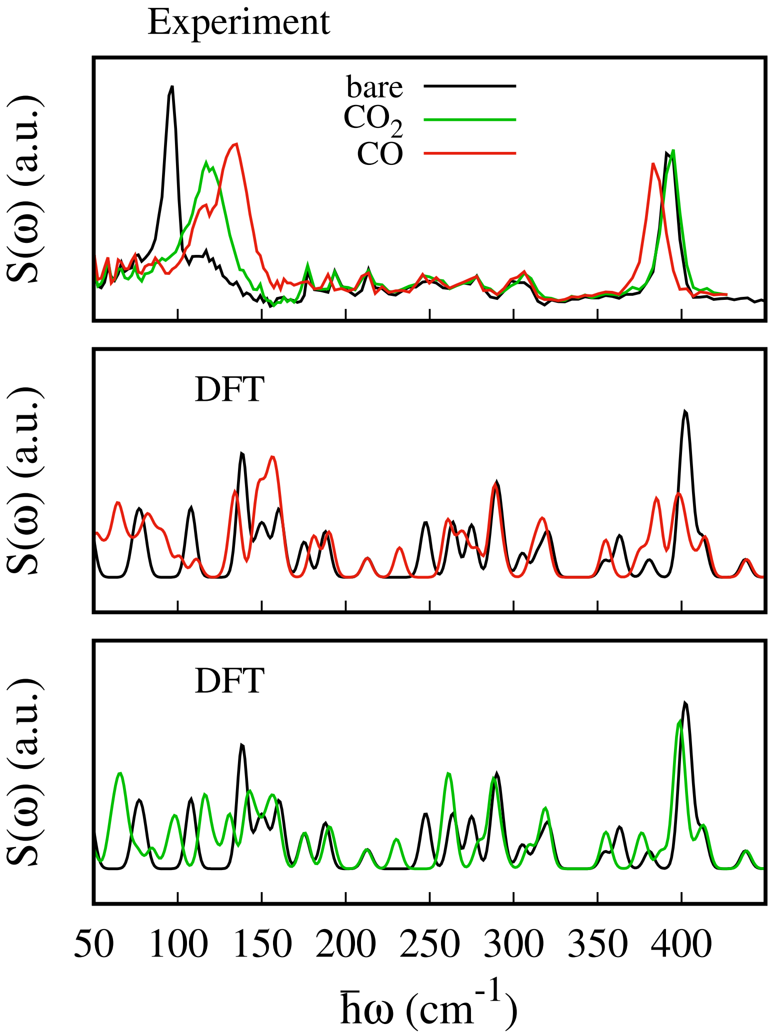

Figure 6.4: Experimental inelastic neutron scattering data, S(ω), collected at 30 K at IN1-LAGRANGE for the bare compound (black) and upon CO (red) and CO_2 (green) uptake (upper panel). Computed S(ω) for the bare material and upon CO (middle panel) and CO_2 adsorption (lower panel).

At higher energies, the vibrational modes of the pyrazine [700-1500] cm^{-1} and cyanide stretching modes [2100-2200] cm^{-1}, which appear with intense and well-defined peaks, were found to undergo negligible changes upon SO_2 adsorption[141]. The experimental data show two well defined peaks for the bare MOF centered at *ca.* 96 and 396 cm^{-1} and less resolved peaks between them. The first peak at 96 cm^{-1} blueshifts and becomes broader and less intense upon CO and CO_2 adsorption. It blueshifts to 133 cm^{-1} for CO and to *ca.* 116 cm^{-1} for CO_2. The second peak at 396 cm^{-1} redshifts upon CO adsorption while it is negligibly affected by the CO_2 uptake.

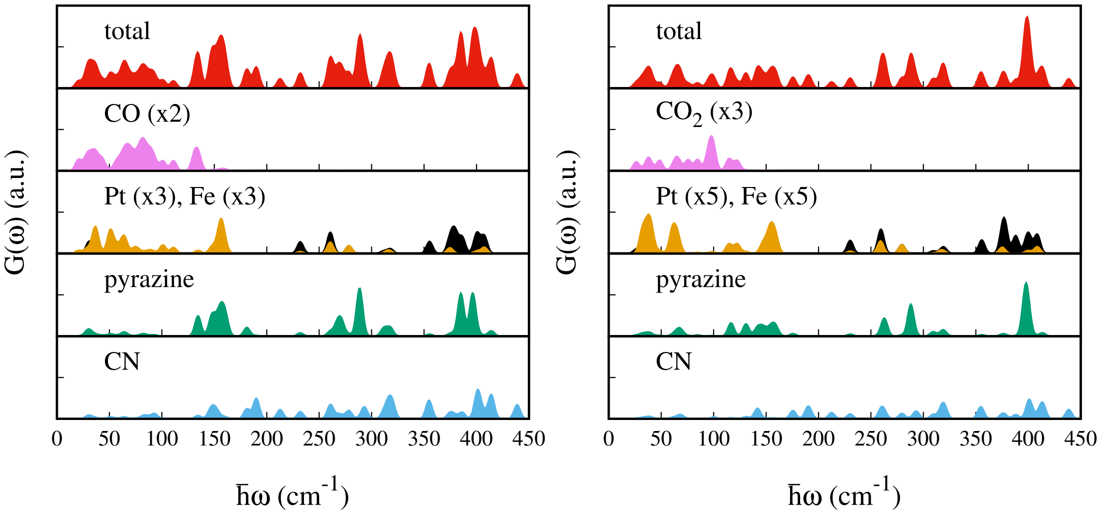

Figure 6.5: Total and partial generalized phonon density of states for Fe(pz)[Pt(CN)$_4$] with adsorbed CO (left) and CO_2 (right). Pt and Fe are depicted in yellow and black, respectively. For a better visualization the PDOS of Pt and Fe were multiply by a factor of 3 and the one of CO by a factor of 2 in the case of CO and by 5 and 3 for CO_2, respectively. The scale of the y axis is the same for all of them.

To assist the analysis of the inelastic scattering data, we compute the partial G(ω) for each atom or group of atoms in the case of CO and CO_2 adsorption (see Fig. 6.5). The distribution of the specific contributions to the total G(ω) is similar in the two cases, and to the case of SO_2 [141]. Below 100 cm^{-1} the spectra are dominated by vibrations of the heavy atoms, Fe and Pt, with the Pt being the dominant one. A minor contribution from the pyrazines and cyanides can be observed as well, together with the vibrational modes of CO or CO_2 (mainly rotational or translational modes). For the intense peak which is found in the experiment at *ca.* 96 cm^{-1} and predicted around 150 cm^{-1}, the main contributions arise from the pyrazine, cyanides and the Pt atoms. In the region [100-400] cm^{-1} we find vibrations from all the atoms. In this region, Felix et *al.*[172] identified the characteristic Fe-N_{pz} and Fe-N_{CN} stretching modes using Raman and nuclear inelastic scattering for Fe(pz)[Ni(CN)$_4$] at 306 and 381 cm^{-1}, respectively. We identified these modes upon CO adsorption at 311.3 and 318.0 cm^{-1} for Fe-N$_{pz}$ stretching and at 374.7 and 386.4 cm^{-1} for Fe-N$_{CN}$. For CO_2, Fe-N$_{pz}$ stretchings appear at 309.25 and 320.11 cm^{-1} and Fe-N$_{CN}$ stretchings at 387.97 and 375.16 cm^{-1}. Finally, the peaks at 400 cm^{-1} have a strong contribution from the pyrazines and a smaller contribution from CN and Pt.

Signature at 100 cm^{-1}. Upon CO and CO_2 adsorption, the peak at 96 cm^{-1} blue-shifts giving rise to a broader and less intense peak. The gas adsorption results in a larger shift for CO (37 cm^{-1}) than for CO_2 (20 cm^{-1}) and the previously studied SO_2 molecule (29 cm^{-1}, see ref. 141). This is well reproduced by the computed S(ω) (see Fig 6.6). In this region, the calculations predict two peaks centered at *ca.* 107 cm^{-1} and 138 cm^{-1} for the bare MOF. The first one corresponds to a libration of the pyrazine ligand around the z-axis, while the second, named A in Fig. 6.6, contains three vibrational modes: (i) a collective mode involving in-plane and out-of-plane movements of the CN groups and a libration of the pyrazine around the z-axis at 137.8 cm^{-1}, (ii) a rigid out-of-plane twisting of the Fe(CN)$_4$N$_2$ octahedra at 138.5 cm^{-1} and (iii) an out-of-plane vibration of the cyanide together with a small libration of the pyrazine at 139.2 cm^{-1} [141].

The first peak at 107.9 cm^{-1} blue-shifts to 134.3 cm^{-1} (under peak A') upon CO adsorption and to 116.6 cm^{-1} (under peak A") upon CO_2 adsorption. In the new mode, the initial pyrazine libration is coupled with a libration of the CO and with a small translation of the CO_2, respectively. The shift is substantially larger for CO. We attribute the blue-shift to the hindered rotation of the pyrazines. As shown in more detail in the next section, this mode is the most sensitive to both the amount of adsorbed gas and the type of molecule. The band A' that arises upon CO adsorption includes two additional modes at 131.0 and 135.1 cm^{-1}. The first one results from a pure libration of the CO. The second one is the result of the red-shift of the mode located at 137.8 cm^{-1} in peak A, i.e. mode (i) described above. A similar situation is found for CO_2: the mode at 137.8 cm^{-1} under peak A red-shifts to 130.9 cm^{-1}, under peak A"'. Because the shift of the mode at 107 cm^{-1} is significantly smaller for CO_2 (9.6 cm^{-1}) than for CO (27.4 cm^{-1}), two separate peaks (A" and A"') are observed for CO_2 and one for CO (peak A'). The peak A" includes as well two additional translational modes of CO_2 at 122.5 and 114.4 cm^{-1}.

The other two vibrational modes under peak A, i.e. (ii) 138.5 and (iii) 139.2 cm^{-1}, undergo a blueshift to 146.6 (142.3) and 151.5 cm^{-1} (141.3), upon CO adsorption (CO_2), respectively, resulting in peak B' (B"). For these modes, a larger blueshift is found for CO (8 and 12.3 cm^{-1}) than CO_2 (3.8 and 2.1 cm^{-1}). This blue-shift can be attributed to the increase in the cyanide out-of-plane bending force constant due to steric hindrance.

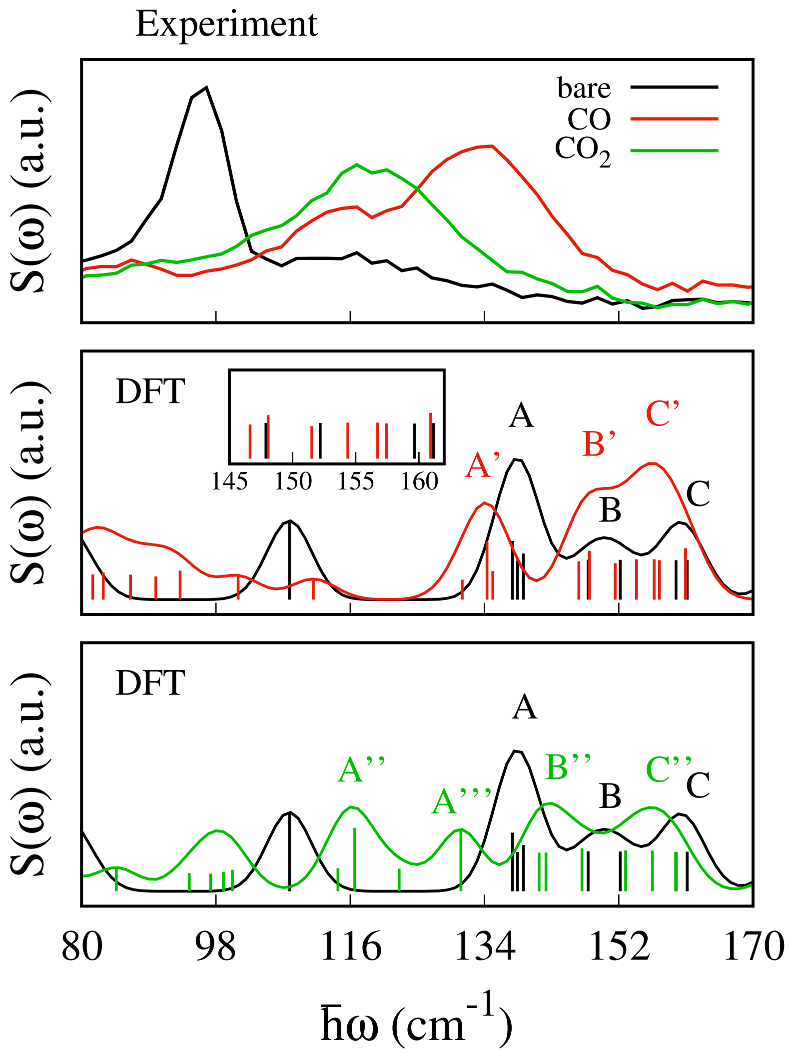

Figure 6.6: Upper panel: zoom of the INS spectra measured at IN1 at 30 K in the low energy region between 80 and 170 cm^{-1}. The spectra or the empty Fe(pz)[Pt(CN)$_4$] (black) and after CO (red) and CO$_2$ (green) adsorption are reported. The computed S(ω) is reported in the middle and lower panels. For a better visualization, the vertical lines represent the normal mode frequencies ω with intensity $S(\omega)$ and no convolution with the Gaussian function.

For the bare MOF, the two vibrational modes under peak B, at 147.9 and 152.2 cm^{-1}, correspond to an in-plane movement of the Pt atoms together with a rigid back-and-forth movement of the pyrazines and Fe atom. Upon CO adsorption, we observe a small blueshift to 148.1 and 154.4 cm^{-1}, respectively, (peaks B' and C'). In the case of CO$_2$, the first red-shifts by 0.8 cm^{-1} (peak B") and the second blue-shifts by 0.7 cm^{-1} (beginning of peak C"). Finally, under peak C, two vibrational modes are found at 159.7 and 161.2 cm^{-1} for the bare MOF. These are similar to the modes of peak B but in this case the rigid displacement of the pyrazine together with the Fe atoms occurs in-plane. A shift to lower energies is found upon CO (CO_2) adsorption from 159.7 to 156.7 (156.5) cm^{-1} and from 161.2 to 157.5 (159.6) cm^{-1} under peak C'(C"). In the case of CO adsorption, a new vibrational mode located at 160.9 is found under peak C'. This corresponds to a collective mode consisting of a libration of the pyrazines and the CO and an in-plane movement of the Pt.

Signature at 400 cm^{-1}. The intense peak centered at 396 cm^{-1} in the experiment undergoes a red-shift to 383 cm^{-1} and a small decrease in intensity upon CO adsorption, while no significant change is found upon CO_2 adsorption. In this region, the computed S(ω) for the bare MOF predicts an intense peak at *ca.* 400 cm^{-1}, named D, and a smaller peak at *ca.* 411 cm^{-1}. Upon CO adsorption, peak D shifts to lower energy and splits into peak D' at 385 cm^{-1} and D" at 396 cm^{-1} (see Fig. 6.7). For CO_2, the computed S(ω) exhibits a single peak, named D"', located almost at the same position as D (*ca.* 399 cm^{-1}). For both molecules, we see a small peak centered at around 413 cm^{-1} which moves negligibly with respect to the bare material.

For the bare MOF, peak D is a combination of seven vibrational modes (400.0, 400.3, 400.4, 400.4, 400.9, 403.6 and 405.0 cm^{-1}). Two of these at 403.6 and 405.0 cm^{-1} dominate the intensity of the S(ω) and are associated with a torsion of the pyrazines. With CO, they undergo a red-shift by 18.4 and 8.7 cm^{-1}, giving rise to peak D' at 385.1 cm^{-1} and peak D" at 396.3 cm^{-1}, respectively. For CO_2 the associated red-shift is smaller (7.0 and 6.4 cm^{-1}) and gives rise to peak D"' (two modes at at 396.6 and 398.6 cm^{-1}). This result differs from the case of SO_2 adsorption where the two modes are almost unchanged [141]. The intensity of the other five modes under peak D is more than a factor of two lower and only two of them (400.0 and 400.3 cm^{-1}) undergo a noticeable shift upon gas adsorption. These involve large displacements of the two Fe atoms and result in tilting and distortion of the octahedra together with an in-plane movement of the Pt atoms. Upon CO (CO_2) adsorption, the first blue-shifts by 7.5 (8.6) cm^{-1} from 400.0 to 407.5 (408.5) cm^{-1} and falls under peak D" (D"'). The second one red-shifts by 13.6 (12.3) cm^{-1} from 400.3 to 386.4 (388.0) under peak D' (D"'). The two remaining modes at 400.4 cm^{-1} under peak D are out-of-plane movements of CN groups which are anti-symmetric with respect to the Fe atom and result in a rigid movement of the Fe(N)$_4$ planar complex. They undergo a small blue-shift to 401.1 and 401.8 cm^{-1} for CO and 401.1 and 401.4 cm^{-1} for CO$_2$, respectively. Finally, the vibrational mode at 400.9 cm^{-1} consists of distortions of the two octahedra resulting primarily from the movement of the Fe atoms which are almost unchanged after adsorption (400.1 cm^{-1} for CO and 399.9 cm^{-1} for CO$_2$).

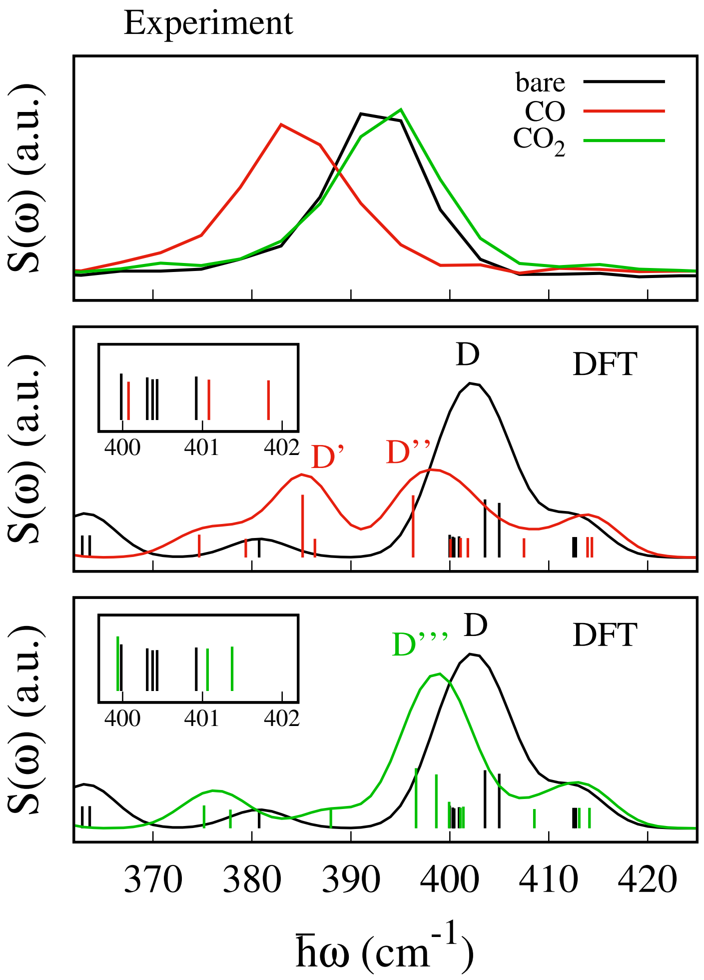

Figure 6.7: Upper panel: INS spectra measured at IN1 at 30 K between 362 and 425 cm^{-1}. The spectra of the empty Fe(pz)[Pt(CN)$_4$] (black) and after CO (red) and CO$_2$ (green) adsorption are reported. The computed S(ω) is reported in the lower panels. The insets show zoom around 400 cm^{-1}. For a better visualization, the vertical lines represent the normal mode frequencies ω with intensity $S(\omega)$ and no convolution with the Gaussian function.

6.4.5 Effect of amount of adsorbed gas on the spectral features

In Fig. 6.8 we show a comparison of the computed G(ω) for 1, 1.5 and 2 CO adsorbed molecules with the experimental INS data. In the presence of a single molecule, it can be observed that neither of the two characteristic signatures of adsorption occurs. The peaks at around 108, 138 and 400 cm^{-1} do not undergo any displacement, whereas in the other two cases, both peaks are shifted upon adsorption. We performed a similar comparison for 1 and 1.5 CO_2 molecules adsorbed per f.u. (see Fig. 6.15 in SI).

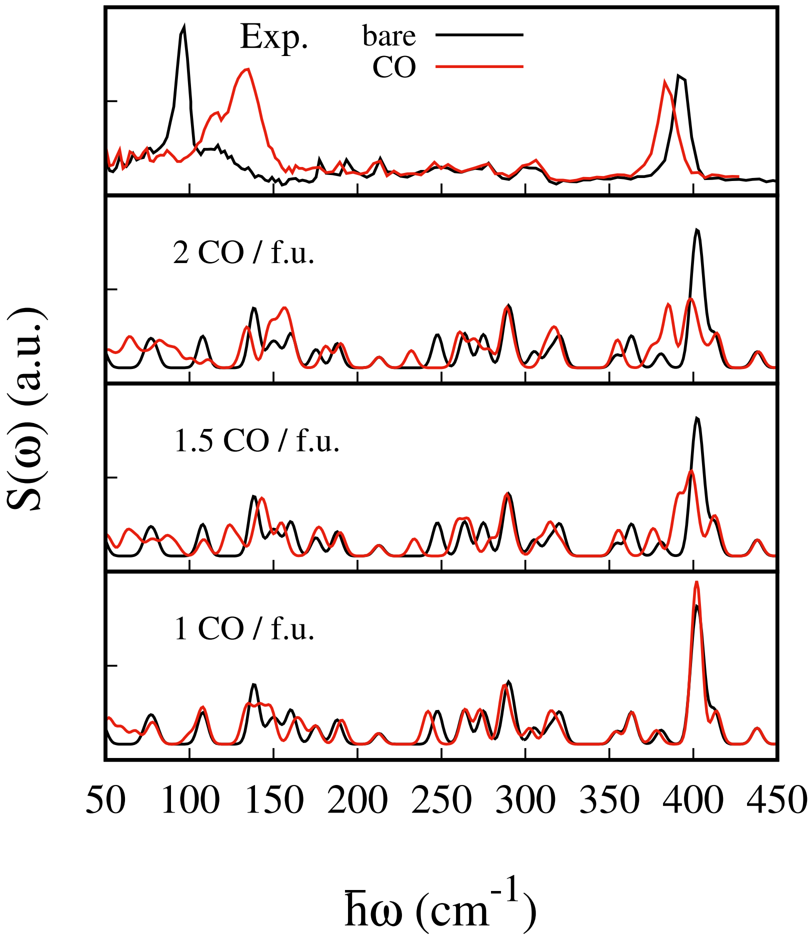

Figure 6.8: INS spectra measured at IN1 at 30 K for the empty Fe(pz)[Pt(CN)$_4$] (black) and after CO adsorption (red) in the upper panel. Total S(ω) computed for 2, 1.5 and 1 CO molecules per f.u., respectively, in the lower panels.

In an attempt to separate the steric effect from the nature of the binding, in what follows we report the shift of the 6 most characteristic and intense modes as a function of the volume occupied by the adsorbed molecules. The van der Waals volume is considered in each case. Specifically, we report the shift upon adsorption for the mode at 107.9 cm^{-1},

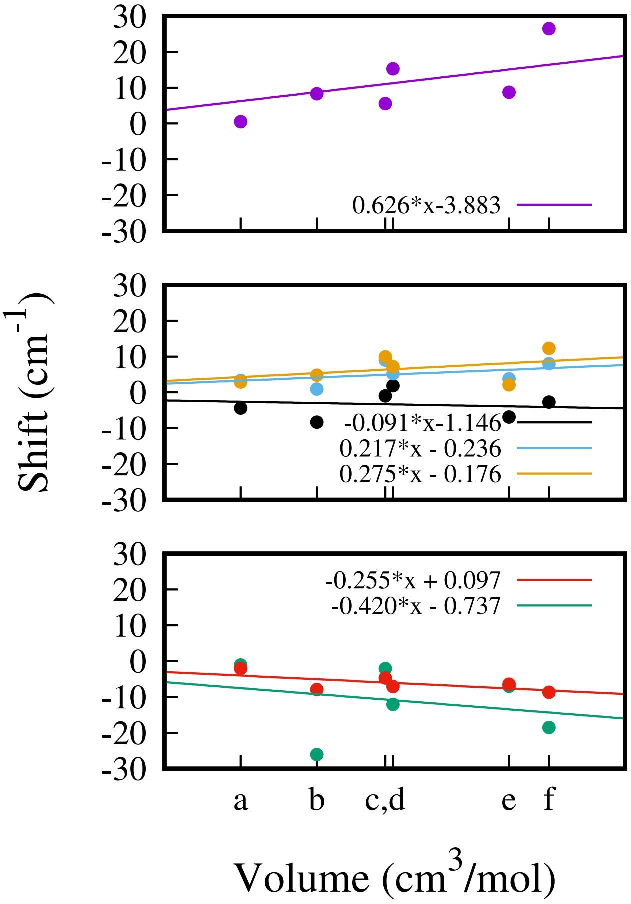

Figure 6.9: Energy shift with respect to the bare material of the 5 most characteristic modes versus the van der Waals volume occupied by the different gases. The van der Waals volumes are calculated by Monte Carlo integration considering the isolated gas molecules. We report the mode at 107.9 cm−1 (purple data, upper panel), 137.8 (black), 138.5 (light blue), and 139.2 cm^{-1} (orange, middle panel), 403.6 (green) and 405.0 cm^{-1} (red, lower panel). Points in the abscissa correspond to a=16.2 (1 CO/f.u.), b=20.2 (1 CO_2/f.u.), c=23.8 (1 SO_2/ f.u.), d=24.2 (1.5 CO/f.u.), e=30.3 (1.5 CO_2/ f.u.), and f=32.4 (2 CO/f.u.) cm^3/mol.

for peak A and for peak D in Fig. 6.9. For peak D only the two modes giving the most intense contribution to the G(ω) are considered (403.6 and 405.0 cm^{-1}). The energy of mode at 107.9 cm^{-1} exhibits the strongest dependence on the occupied volume upon adsorption, reaching a maximum displacement of 27 cm^{-1} when 2 CO per f.u. are adsorbed. Interestingly, when 1 SO_2 (point c, 23.8 cm^3/mol) and 1.5 CO per f.u. (point d, 24.2 cm^3/mol) are considered, the displacement of this mode differs considerably by 9.7 cm^{-1} even though the occupied volume is similar in the two cases. This indicates a dependence not only on the volume but also on the nature of the gas and the associated interactions established within the cavity. For the three modes under peak A (137.8, 138.5 and 139.2 cm^{-1}) we find overall a smaller shift upon adsorption and the correlation between energy shift and occupied volume is weaker, in particular for the mode at 137.8 $^{-1}$ (black data) which exhibits the weakest correlation with the gas volume. The two modes under peak D (403.6 and 405.0 cm^{-1}) overall red-shift upon adsorption. The mode at 403.6 cm^{-1} shows a strong dependence on volume and on the molecule choice, whereas the mode at 405.0 has a weak correlation between energy shift and occupied volume.

6.4.6 Binding Mechanism.

Carbon monoxide is a strong σ-donor and a good π-acceptor [201]. It can donate electron charge from the σ-HOMO (highest occupied molecular orbital) orbital, mostly localized in the carbon atom (see Fig. 6.16 in SI), to an empty d-orbital of the metal and receive back electron charge from an occupied d orbital of the metal into the empty π*-LUMO (lowest unoccupied molecular orbital) orbitals (see Fig. 6.16 in SI) via a mechanism called back-donation. When it binds on top of an open-metal site with a square-planar coordination, a strong electron-donor σ-bonding can occur when the σ-HOMO orbital of the molecule can donate to the d_{z^2} orbital. In this case, the metal cation is Pt(II) which exhibits a doubly occupied d_{z^2} and therefore cannot act as an electron acceptor. In order to decrease the repulsion, the CO tilts down in a configuration almost parallel to the Pt(CN)$_4$ plane with the Pt-C-O bond angle being $\theta = 94.7°$ (PBE+D2) (see Fig. 6.2). In the case of CO_2 on top of the metal site, we find no mixing of the metal-molecule orbitals, as expected from an electrostatic/dispersion interaction (see PDOS in Fig. 6.17 in SI). The strength of the π-acceptor interaction was computed by performing a Bader charge analysis using PAW pseudopotentials and the PBE+D3+BJ functional. For the CO located in site A, the analysis revealed a small charge transfer from the MOF to the molecule of 0.06 electrons, confirming a weak backbonding interaction. A negligible charge transfer is predicted for CO_2. For CO, the metal-ligand charge transfer causes a decrease of the C-O bond order due to the antibonding character of the π*-LUMO orbitals. This is confirmed by the C-O bond distances being always larger for the CO adsorbed on site A (1.142 Å) than in site B (1.139 Å). The longer C-O bond distances can cause a red-shift of the stretching CO frequency with respect to the free CO. The stronger the backbonding, the weaker the C-O bond and the lower the stretching frequency. The computed CO stretching frequency for the free CO appears at approx. 2123 cm^{-1} while for the adsorbed CO in site A is around 2092 cm^{-1}. The typical red-shift for a strong backbonding interaction is normally more than 100 cm^{-1} (e.g. the experimental shift for $Cr(CO)_6$ is of *ca.* 143 cm^{-1}) [201]. As expected, the stretching frequencies of the CO located between the pyrazines remain unchanged upon adsorption consistent with the absence of backbonding.

In the case of CO_2, a backbonding interaction would increase the O-C-O bond distances due to the antibonding character of the π*-LUMO orbitals, resulting in lower stretching frequencies. Here, the O-C-O distances remain almost unchanged with respect to the free CO_2 (1.172 Å versus 1.174 Å) and the symmetric and antisymmetric stretching frequencies shift by less than 10 cm^{-1}.

The predicted binding energies for CO and CO_2 using PBE+D2 are 0.277 and 0.435 eV, respectively. These decrease to 0.029 and 0.002 eV when the PBE functional is used without the Grimme correction, indicating that van der Waals interactions are dominating the binding in both cases. In order to further assess the role of the open metal site in the binding mechanism, we computed the binding energy of CO and CO_2 adsorbed between two $[Pt(CN)_4]$ planes (representing site A) and between two pyrazines (representing site B) and removing the rest of the framework. This is done by fixing the atomic coordinates to the relaxed geometry in the MOF and by removing the pyrazine ligands and the planes, respectively. We imposed cell parameters of a=b=c= 20 Å in both cases to avoid interactions between periodic images. We employed PBE+D2 for this comparison. For CO, the computed binding energies are 0.190 and 0.088 eV for the molecule adsorbed respectively on pseudo-site A and B. For CO_2 these are 0.256 and 0.142 eV, respectively. This comparison indicates a stronger contribution of the $[Pt(CN)_4]$ plane to the binding energy. This is different for SO_2, where a larger decrease in binding energy (by 64.4 %) was predicted (see table 6.1) than for CO (31.4 %) and CO_2 (41.1 %) when comparing the full MOF and the $[Pt(CN)_4]$ fragments.

	MOF (PBE+D2)	MOF (PBE)	Pseudo-site A (PBE+D2)	Pseudo-site B (PBE+D2)
CO	0.277	0.029	0.190	0.088
CO_2	0.435	0.002	0.256	0.142
SO_2[141]	0.769	0.210	0.274	-

Table 6.1: Computed binding energies in eV for the MOF with PBE+D2 and PBE and for pseudo-site A and pseudo-site B for CO, CO_2 and SO_2.

6.5 Conclusion

For the experimental uptake of 2 CO per f.u. the molecules orient perpendicular to the pyrazine ligands and parallel to the $Fe[Pt(CN)_4]_\infty$ for both sites, A and B. For 1.5 CO_2, the molecules on site A are perpendicular to the pyrazines, while on site B they are parallel resulting in 'T' shape interactions with the neighbouring CO_2. In both cases they are parallel to $Fe[Pt(CN)_4]_\infty$ planes. The main signatures of the INS spectra upon 2 CO and 1.5 CO_2 adsorbed molecules per f.u. occur in the peaks located at *ca.* 100 cm^{-1} and 400 cm^{-1}. The first blue-shifts upon CO and CO_2 adsorption, with a larger shift for CO, while the second red-shifts only in the presence of CO. DFT calculations confirm these signatures and allow us to characterize the blue-shift as due to a hindered pyrazine libration and the out-of-plane movement of cyanide ligands when the gas is adsorbed. The red-shift of the peak at 400 cm^{-1} is caused by the steric effect of the guest when the pyrazines display a torsion movement. The DFT-predicted energy of the modes yielding the most intense INS features is studied with respect to the volume occupied upon adsorption by different amount and type of gases. The predicted shift of these modes show that those at *ca.* 107.9 and 403.6 cm^{-1} are the most sensitive upon volume and the nature of the gas. Consistent with a fully occupied d_z^2 orbital Pt that prevents a molecule/metal σ-donor/-acceptor interaction, the adsorption mechanism in both cases is of electrostatic and van der Waals nature (physisorption) with the latter dominating the binding. A weak backbonding metal-to-ligand charge transfer is predicted for the CO located on site A while no charge transfer was computed for CO_2. In conclusion, this work reports the gas adsorption mechanism of CO and CO_2 in the Hofmann-like clathrate Fe(pz)[Pt(CN)$_4$] for which large adsorption capacities were previously reported when compared to other MOFs with larger surface areas [12]. We have made use of the information coming from neutron diffraction, inelastic neutron scattering and density-functional theory calculations in a complementary way. The results suggest that only a few modes depend on the nature of the adsorbed gas and, although the use of these modes as a reference to selectively detect between CO and CO_2 seems complicated, the experimental signatures are clearly different when saturation points are reached.

6.6 Supplementary information

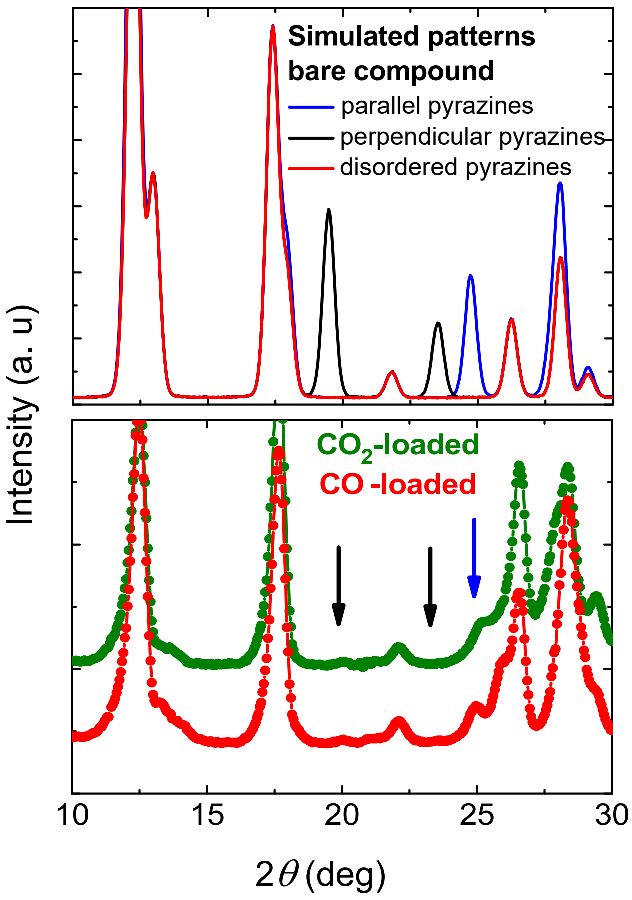

Figure 6.10: Top: Detail of the low Q part of the simulated neutron powder diffraction patterns (wavelength 1.54 Å) of Fe(d_4-pyrazine)[Pt(CN)$_4$] in the low-spin state with the pyrazine rings in disordered (red lines), perpendicular (black lines) and parallel (blue lines) configurations. Bottom: Experimental neutron diffraction patterns of CO (red) and CO_2-loaded (green) Fe(d_4-pyrazine)[Pt(CN)$_4$]. The arrows indicate the position of the reflections related to the different configurations of the pyrazine moieties: perpendicular (black lines) and parallel (blue lines)

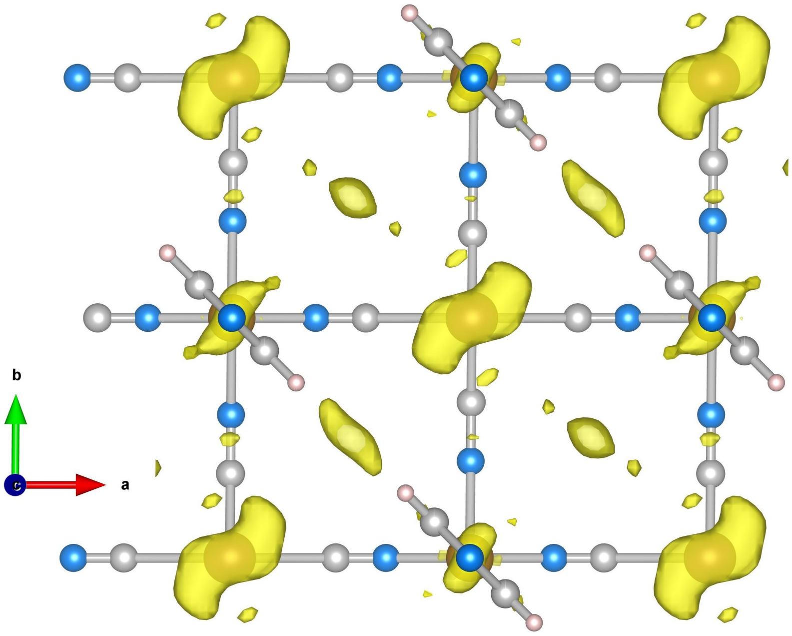

Figure 6.11: Residual scattering density in the ab plane when a model of the bare Fe(pyrazine)[Pt(CN)$_4$] with parallel pyrazines is compared to the experimental neutron diffraction pattern of the CO-loaded compound. Two bonding sites for the CO are distinguished: (i) On top of the open-metal site (platinum site) and (ii) in-between the pyrazine rings (pyrazine site). The residual density on the pyrazine molecules is an indication of orientational disorder of the rings

Compound	CO-loaded	CO_2-loaded
T(K)	100	100
Spin state	Low-spin	Low-spin
Space group	$P-1$	$P-1$
a (Å)	10.166(1)	10.164(1)
b (Å)	10.138(1)	10.136(1)
c (Å)	6.756(1)	6.753(1)
γ (°)	89.56(1)	89.68(2)
R_{Bragg}	13.95	17.33

Table 6.2: Metric parameters obtained from the refinement of the powder neutron diffraction patterns of CO- and CO_2-loaded Fe(pyrazine)[Pt(CN)$_4$].

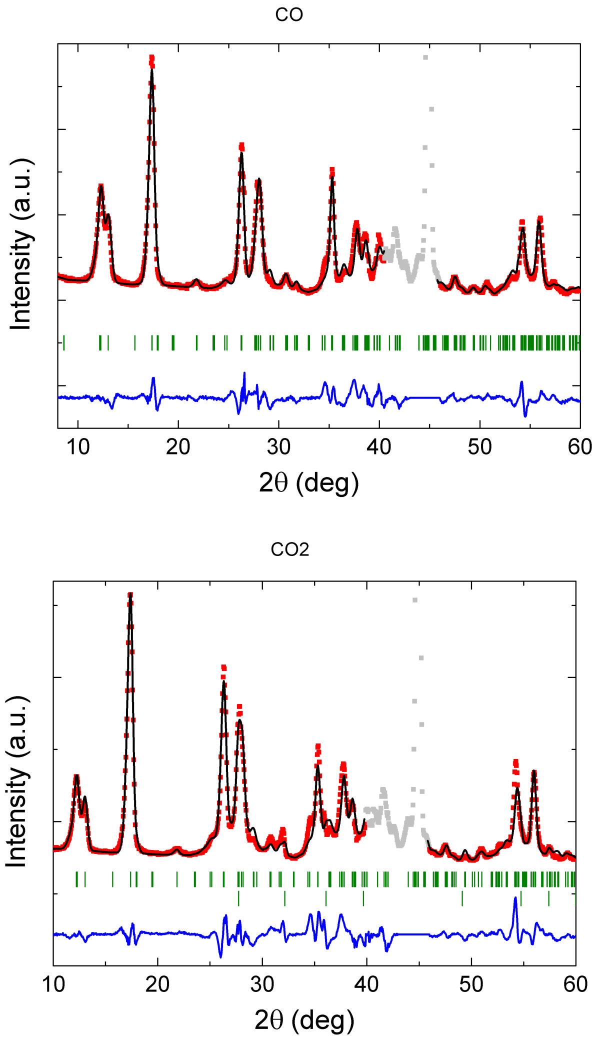

Figure 6.12: Details of the most relevant part of the powder neutron diffraction patterns (wavelength 1.54 Å) of Fe(pyrazine)[Pt(CN)4] loaded with CO (upper panel) and CO_2 lower panel. Experimental patterns (red), calculated patterns (black), difference patterns (blue lines), and position of the Bragg reflections (green marks). The parts in gray are regions with spurious scattering from the sample environment. A minor fase of solid CO_2 is also included in the case of the CO_2-loaded material (green marks in the lower line). The structural models were built in $P-1$ space group, allowing distortion of the unit cell, but the atomic displacements were constrained to maintain a pseudo-tetragonal symmetry. The configuration of the pyrazine rings was fixed from the results obtained in the deuterated compound. For the CO-loaded material, full occupation of both A and B sites gave the best fits. For CO_2 the A site was considered fully occupied while the occupancy of guest molecules in the B site was allowed to vary. The refinement of the disorder among the possible orientations of the guest molecules did not give significant improvement of the fits, thus the disordered configurations were retained.

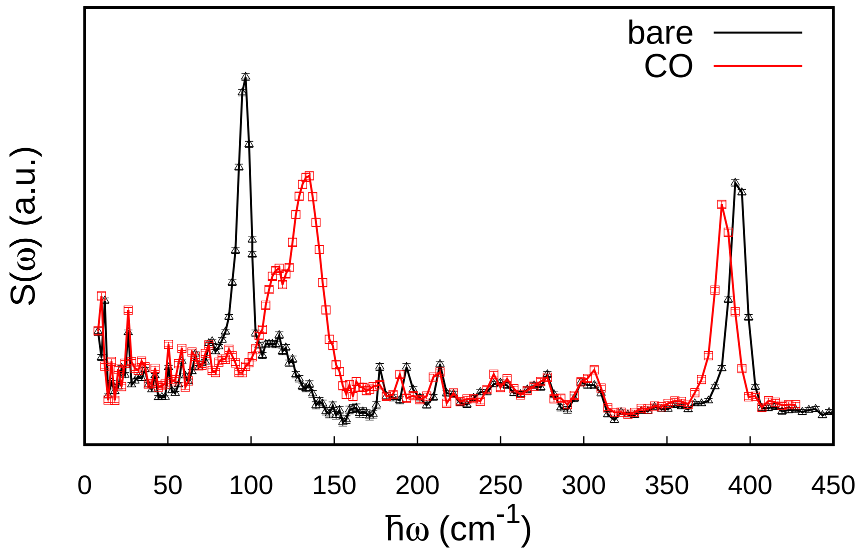

Figure 6.13: INS spectra (and errors) measured at IN1-LAGRANGE at 30 K for the empty Fe(pz)[Pt(CN)$_4$] (orange) and after CO adsorption (blue).

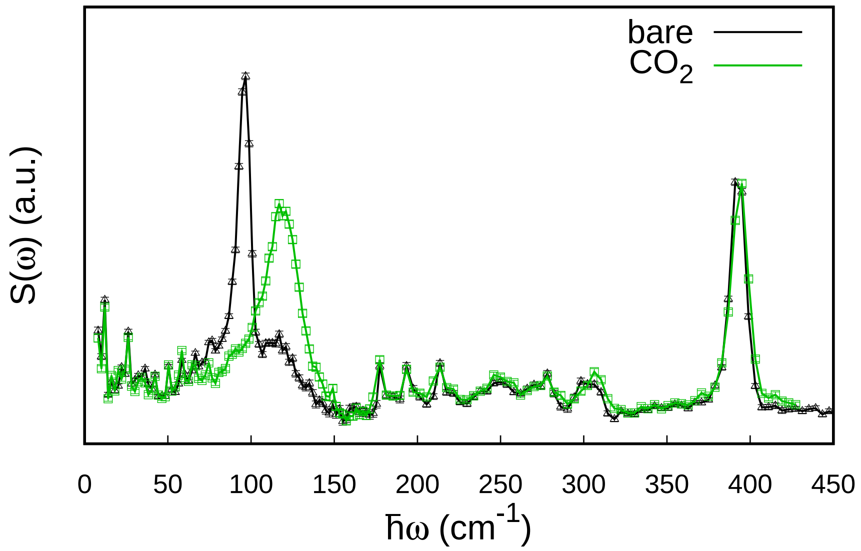

Figure 6.14: INS spectra (and errors) measured at IN1-LAGRANGE at 30 K for the empty Fe(pz)[Pt(CN)$_4$] (orange) and after CO_2 adsorption (blue).

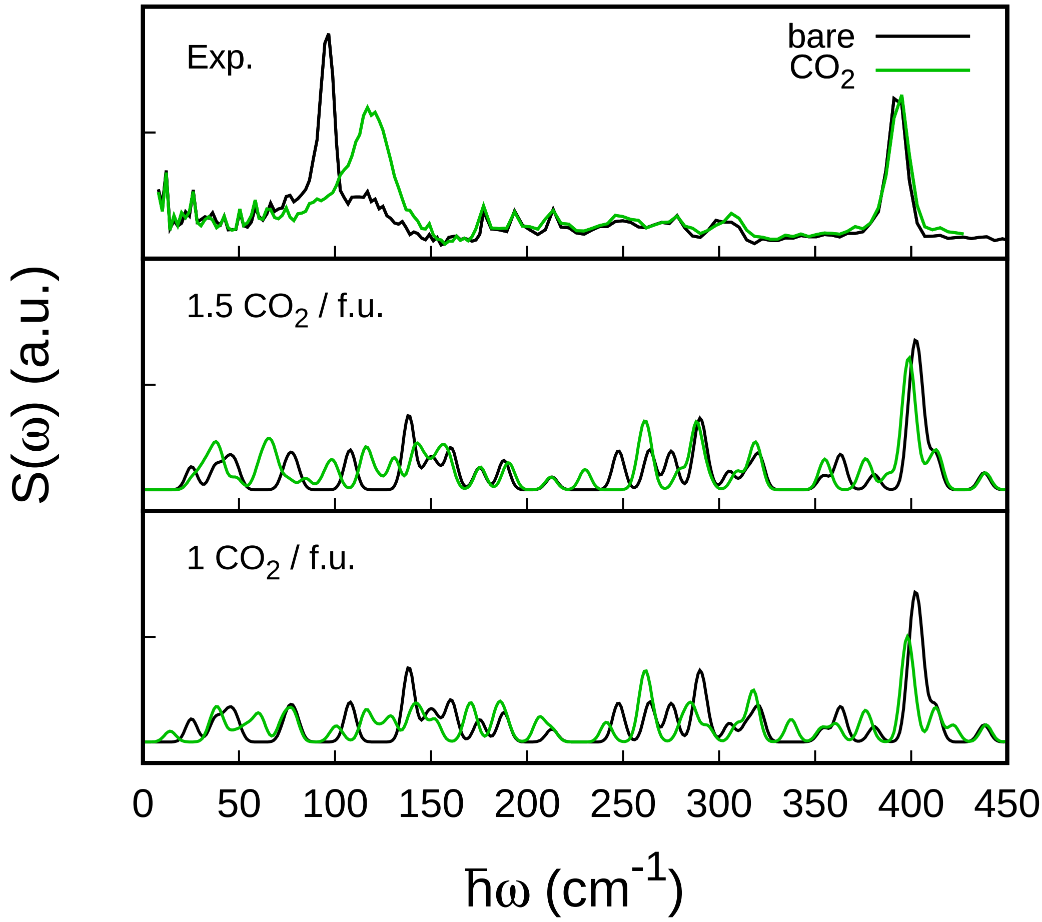

Figure 6.15: INS spectra measured at IN1 at 30 K for the empty Fe(pz)[Pt$(CN)_4$] (black) and after CO_2 adsorption (green) in the upper panel. Total S(ω) computed for 1.5 and 1 CO_2 per f.u., respectively, in the lower panels. The displacement of the most intense modes at 107.9, 17.8, 138.5 and 139.2 cm $^{-1}$ are approximately similar for both cases. The peak around 400 cm^{-1} does not undergo any displacement in any case.

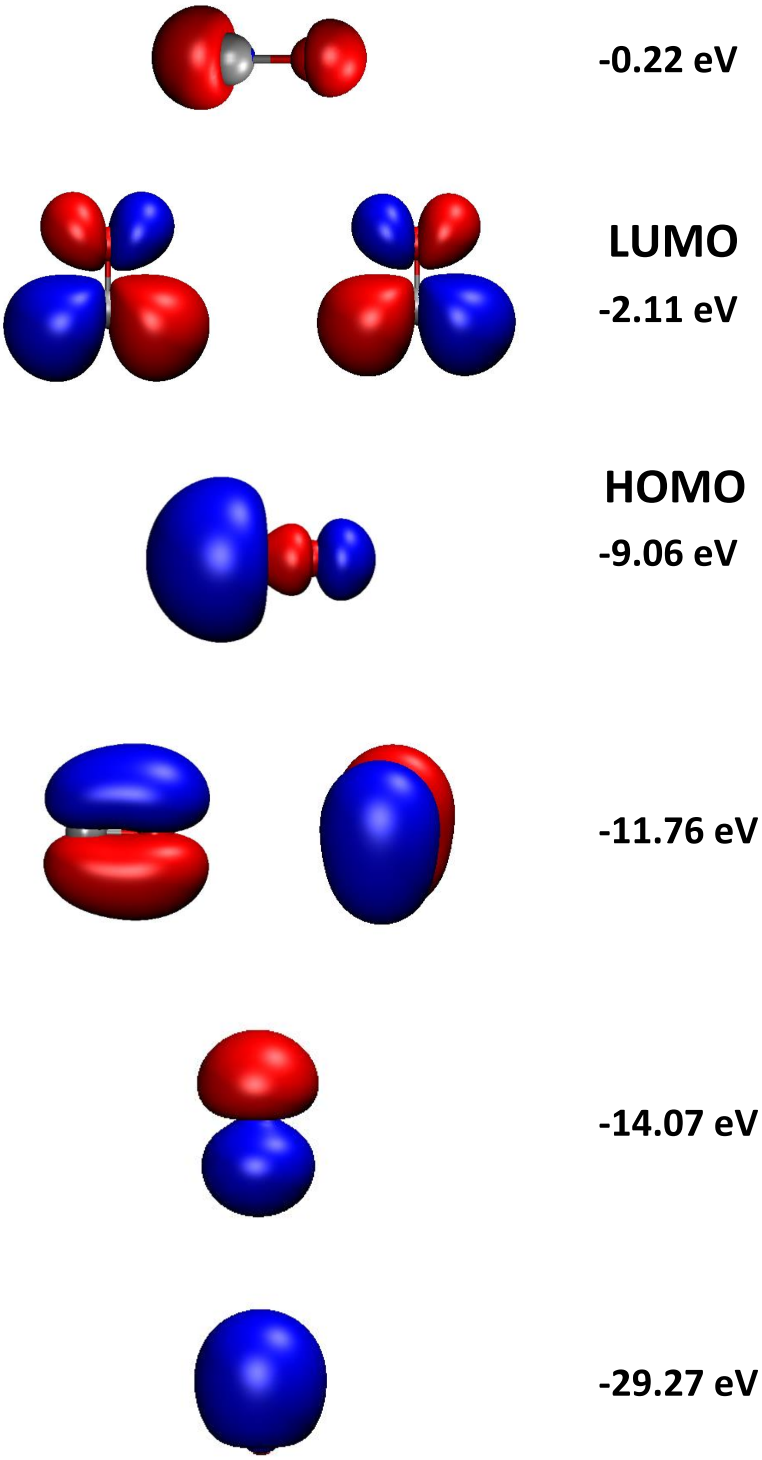

Figure 6.16: DFT+D2 wavefunctions of free CO.

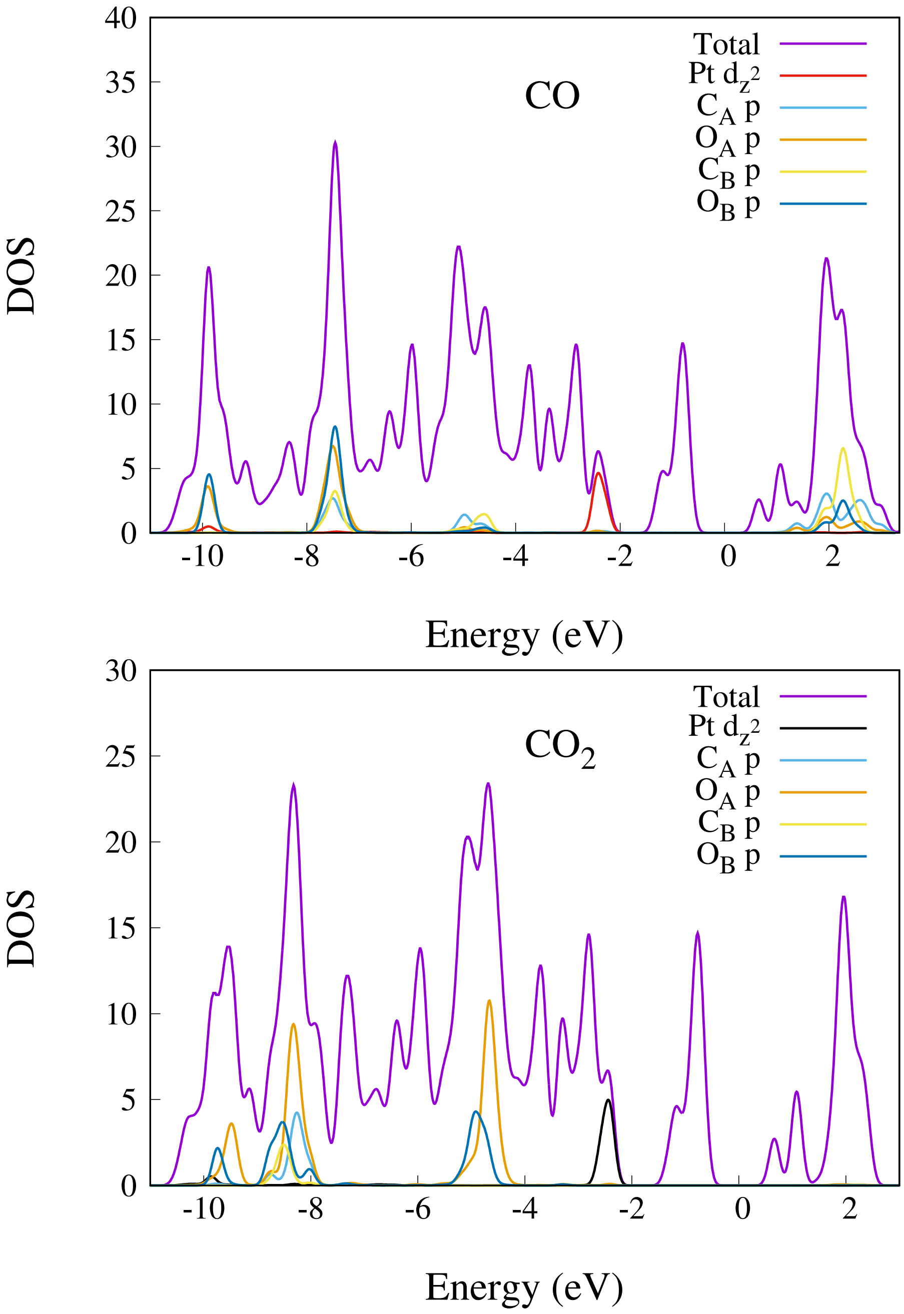

Figure 6.17: Total and projected (onto the Pt d_{z^2} and p atomic orbitals of CO and CO_2) DOS computed for the MOF+CO (2 CO/ f.u.) (upper panel) and MOF+CO_2 (1.5 CO_2/ f.u.) (lower panel). The labels A and B represent the bonding site A (platinum site) or B (pyrazine site), respectively. The Fermi level is set to 0 eV. For CO (upper panel) a bonding interaction between σ-HOMO orbital of the CO and the Pt-d_{z^2} orbital is found at -5.1 and -4.9 eV. The corresponding antibonding interaction appears at -2.3 eV.

Chapter 7

A Hubbard U-Density Corrected Scheme to Study Spin Crossover-Assisted Gas Release in Hofmann-like clathrates

Lorenzo A. Mariano[1], Ángel Fernández-Blanco[1,2], Roberta Poloni[1]

[1] *SIMaP, Grenoble-INP, University of Grenoble-Alpes, CNRS, 38042 Grenoble, France*

[2] *Institut Laue Langevin, 71 Avenue des Martyrs, CS 20156-38042, Grenoble, France*

Reproduced with permission from:

Lorenzo A. Mariano[1], Ángel Fernández-Blanco[1,2], Roberta Poloni[1], "A Hubbard U-Density Corrected Scheme to Study Spin Crossover-Assisted Gas Release in Hofmann-like clathrates".

7.1 Abstract

By employing a recently proposed Hubbard U density-corrected scheme within density functional theory we provide design principles towards the design of materials exhibiting a spin crossover-assisted gas release. Small molecular fragments are used as case study to identify two main mechanisms behind the change in binding energy upon spin transitions. The feasibility of the proposed process is assessed by correlating the change in binding energy of CO_2, CO, N_2, and H_2, upon spin crossover with the adiabatic energy difference associated with the spin state change of the square-planar metal in Hoffman-type clathrates. A few promising cases are identified and the case of H_2 adsorption stands out as the most favourable result. The intermediate ligand field splitting of H_2 yields adiabatic

energy differences that may be consistent with a temperature induced spin crossover and the strong interaction in LS as expected from a Kubas mechanism would result in a large change in uptake. The encouraging results found for the Hofmann-type clathrates are further confirmed for an already synthezied square-pyramidal Fe(II) complex.

7.2 Introduction

Metal-organic frameworks (MOF) are nanoporous materials made of metal ion centers coordinated by organic linkers to form 3D-structures [13, 202]. The wide range of possible combinations of linkers and metal ions has allowed for the design of tailor-made MOFs for different technological applications [203] like catalysis[23, 24, 25, 26], drug delivery [27], sensing [26, 16] and gas storage and separation [30]. In these materials, efficient and selective gas adsorption can be achieved due to the large internal surface area and the high affinity of the metal centers with certain gas molecules [204]. Specifically, the presence of coordinatively unsaturated metal centers[205], also called open-metal sites (OMS), has resulted in exceptional gas uptake and separation performances[206, 207] owing to the formation of selectively strong [208, 49] coordination bonds between the MOF and the guest molecules[209, 8]. Recently, Long and coworkers reported the synthesis of Fe-based OMS-MOFs[210] exhibiting a cooperative carbon monoxide adsorption mechanism via spin-transition, resulting in unprecendented large working capacities [40]. In their work, a cooperative spin-state transition occurs at the Fe centers from high spin (HS) to low spin (LS) as a function of the CO partial pressure, as a result of the strong ligand-field induced by CO upon adsorption. Once the HS→LS is triggered at all Fe centers, the uptake is shown to increase abruptly as a consequence of the significantly larger CO binding energy expected at LS compared to HS[206].

A clear limitation of the reported mechanism is its application to molecules exhibiting a quite strong ligand field so that a large ligand-field splitting, upon binding, can stabilize the LS phase. CO is located at the far right of the spectrochemical series and it exhibits one of the largest ligand-field strengths, together with CN^-. As an alternative approach to achieve large working capacities, in this work, we propose design principles for the development of MOFs that can undergo a temperature-induced spin-crossover transition once the gas has been adsorbed. As first demonstrated by some of us [49], then confirmed also by employing first-principles calculations[211, 212], and confirmed experimentally in the case of CO_2 adsorption in MOF-74 [213] and later for CO [40], large differences in the gas adsorption energy may be found between electronic configurations at the transition-metal atom involving a change in the occupation of the antibonding d_{z^2} orbital between the gas and MOF. Thus, efficient adsorption and desorption cycles could be achieved by using temperature to trigger the spin state change at the metal center resulting in a decrease in the bond order and thus allowing to release the gas. In this work, the computational proof-of-concept for this mechanism is provided by computing values of adiabatic energy differences between different spin states and by analysing them in conjunction with the associated changes in binding energies.

We employ density-functional theory calculations to predict the change in binding energy upon spin-state transitions among different spin configurations and the adiabatic energy difference associated with the spin crossover, in presence of adsorbed gas, in order to assess the feasibility of the process. We first perform a screening study by computing the change in binding energy upon spin crossover in a small molecular fragment consisting of a square planar $M(CN)_4$ molecular complex with M=Fe(II), Fe(III), and Ni(II). The results obtained for CO, CO_2, N_2, and H_2 using these fragments are exploited to pursue the quest of MOF with promising capture-and-release properties. Specifically, the calculations are performed on three MOFs: the first two belong to the Hoffman-type family [71, 78, 79] with formula $Fe(pz)[M(CN)_4]$ and $Fe(bpac)[M(CN)_4]$, where M = Fe(II), Mn(II) and Ni(II). The latter is the only one that has already been synthesized [71, 79]. These materials are built via cyanide ligands (CN) linking octahedral-coordinated Fe atoms to the open-metal site, M, of square-planar coordination. The resulting metallo-cyanide planes $Fe[M(CN)_4]_\infty$ are then pillared by organic ligands acting as bridges between the layers and occupying the axial position of the Fe(II) atoms, in this case pz = pyrazine or bpac = (bis(4-pyridyl)acetylene). The bpac ligand, being longer, results in a higher porosity in the MOF than the pz. The third MOF is $Fe_2(tpt)_2(NCS)_4$ [214] with the Fe(II) sites in a square pyramidal coordination.

A Hubbard-U density corrected scheme is employed to predict with accuracy adiabatic energy differences and binding energies in both LS and HS state. Similar to the bias in the spin splitting energies reported previously [159], here, we report and explain for the first time a bias in the binding energy introduced by the Hubbard term. Our results, rationalized using molecular orbital diagrams, show that for both $Fe(bpac)[M(CN)_4]$ and $Fe(pz)[M(CN)_4]$, overall, the ligand field splitting upon adsorption is either too weak (CO_2) or too strong (CO) to yield adiabatic energy differences consistent with a spin crossover of the OMS at RT. One exception is N_2 adsorption on $Fe(pz)[Fe(CN)_4]$ with an adiabatic energy difference of 0.326 eV and a large change in binding energy. The case of H_2 adsorption in bpac MOF also represents a promising scenario for M=Mn and M=Fe. In this case the strong adsorption in LS as expected from a Kubas mechanism results in a large uptake even at non-cryogenic conditions and the adiabatic energy difference may be consistent with a temperature-induced spin crossover. The potential of employing such a mechanism for an efficient H_2 capture and release is further confirmed for the case of $Fe_2(tpt)_2(NCS)_4$.

7.3 Computation Methods

Molecular fragments The calculations of gas adsorption are performed by employing the TPSSh functional and the aug-cc-pVTZ basis sets as implemented in ORCA [215]. The semiempirical Grimme's D3 correction [198] is employed in conjunction with the Becke-Johnson (BJ) damping scheme [216] to account for van der Waals forces which are critically important for the correct description of the adsorption mechanism[217, 211]. For each calculation we place two molecules on each side of the metal atom and perform a full geometrical optimization. The molecules are always bound in end-on configuration except for H_2 molecule for which the side-on geometry is considered [218, 219]. For the charge analysis, we employ the Bader method [220, 221, 222, 223] to extract the electrostatic charge associated with the metal cation. For the calculation of the binding energy, a geometrical counterpoise correction is applied to correct for the basis set superposition error arising from the use of localized orbitals.

Periodic calculations The calculations of the adiabatic energy difference and the binding energies are performed using Quantum Espresso [119, 117]. We employ the GBRV ultrasoft pseudopotentials [161, 224] and wavefunction and charge density cutoffs of 70 Ry and 700 Ry, respectively. The reciprocal space sampling is performed by using a 2×2×1 Monkhorst-Pack grid. A full geometrical optimization is performed for both the bare and the loaded MOF using PBE+U with U=4 on both the octahedrally coordinated Fe and the open metal center M, starting from the published structures [78]. In order to compute the spin state energetics we employ instead a Hubbard U computed self-consistently [225] using linear-response [70], called here U_{sc}. The U_{sc} is computed separately for each spin state by employing the optimized geometry. For Fe and Ni we employ a molecular fragment $M(CNH)_4$ and two N_2 adsorbed molecules. For Mn, the U_{sc} is computed using the periodic $Fe(pz)[Mn(CN)_4]$ and one CO molecule. We employ ortho-atomic projectors. These U_{sc} are then employed for all the subsequent calculations including those for the bare MOF and the other gas molecules, for both $Fe(bpac)M(CN)_4$ and $Fe(pz)M(CN)_4$. We note several convergence issues in the self-consistent cycle when using U_{sc}=8.9 eV for octahedrally-coordinated Fe. Thus, in order to avoid convergence problems we have set U=4 eV for this atom in every MOF. Similar to the molecular case, all the PBE+U calculations are performed using the Grimme-D3 correction [198] together with the BJ damping scheme [216]. As reported in previous works [211, 226], the Hubbard correction is needed in order to correctly describe the transition-metal 3d electrons in MOFs.

Corrected density scheme for adiabatic energy difference calculation The adiabatic energy differences are computed by employing the Hubbard U-corrected density scheme [159]. It consists in performing total energy calculations for each spin state using PBE+U$_{\mathrm{sc}}$ including the Grimme-D3+BJ such that

$$E_{\mathrm{PBE+D3+U}}[\rho,\{n_m^\sigma\}] = E_{\mathrm{PBE+D3}}[\rho] + \sum_{m,\sigma} \frac{U}{2}[n_m^\sigma(1-n_m^\sigma)] \tag{7.1}$$

where the second term on the right is the Hubbard energy which depends on the density through the occupations, $\{n_m^\sigma\}$, which are the eigenvalues of the 5×5 occupation matrix $n_{mm'}^\sigma = \sum_{i,k} f_{i,k}^\sigma \langle\Psi_{i,k}^\sigma|\phi_m\rangle \langle\phi_{m'}|\Psi_{i,k}^\sigma\rangle$, with $f_{i,k}^\sigma$ being Fermi-Dirac occupations. $|\Psi_{i,k}^\sigma\rangle$ are the Kohn-Sham wave functions of band index i, and the $\{|\phi_m\rangle\}$ projectors are here the 3d atomic-like functions. The density-corrected scheme consists in performing a full self consistent calculation using the self consistent U, and by keeping only the first term of the total energy of equation 7.1. By removing the Hubbard term from the adiabatic energy difference, we remove the bias of DFT+U towards HS which arises from the penalizing Hubbard term being systematically larger for LS [67].

We recently demonstrated that this method allows to compute adiabatic energy differences of Fe(II) molecular and crystalline complexes with excellent agreement with coupled cluster-corrected CASPT2 [227, 228] and with experimentally-extracted values[159]. The adiabatic energy difference between HS and LS, is thus computed as follows:

$$\Delta E_{\text{H-L}}[\rho_U] = E^{\mathrm{HS}}_{\mathrm{PBE+D3}}[\rho_U] - E^{\mathrm{LS}}_{\mathrm{PBE+D3}}[\rho_U]. \tag{7.2}$$

As discussed in detail in our previous work, the bias towards HS imposed by the Hubbard term yields negative values of all the adiabatic energy differences computed in this work, regardless of the molecule and framework choice (see SI). As expected, a larger bias is computed for stronger ligand field molecules.

Density-corrected scheme for the binding energy We employ here for the first time a density-corrected scheme to compute the binding energy in order to correct for the bias due to the difference in the Hubbard term between the bare and bound case (vide infra). The binding energy is thus computed as follows

$$E_{\mathrm{bind}}[\rho_U] = E_{\mathrm{MOF+gas}}[\rho_U] - E_{\mathrm{MOF}}[\rho_U] - E_{\mathrm{gas}}, \tag{7.3}$$

where the total energy of the MOF and the MOF with adsorbed gas are taken from the first term of equation 7.1, i.e. as $E_{PBE+D3}[\rho_U]$. We note that the calculations of the MOF and the MOF upon gas adsorption are performed using the same value of U (vide supra).

7.4 Results

7.4.1 Fragment calculations

The gas binding energies associated with each spin state are computed for the fragment model $M(CN)_4$ [with M=Fe(II), Fe(III), Ni(II)] for CO_2, CO, N_2, and H_2. The computed values, together with the gas-metal bond distance and the electrostatic charge of the metal are reported in table 7.1. For Fe(II) and Fe(III) we compute the three spin states while for Ni(II) only two spin states are possible. In order to facilitate the understanding of the results, in what follows we divide the calculations in two groups. Each group reflects a specific mechanism that we have identified as responsible for the change in binding energy upon spin-state transition. The first group represents a situation where the change in binding energy mainly results from the change in occupation of the metal-gas molecular orbital d_{z^2}. Consistent with the analysis reported in Ref. 49, the binding energies always significantly decrease (increase) upon occupation (depopulation) of the antibonding d_{z^2}, upon spin transition. The second mechanism, largely overlooked until now, involves the change in the occupation of the $d_{x^2-y^2}$ molecular orbital, which has an antibonding character between the metal and the in-plane CN^- ligands. The latter will be discussed in detail below.

Change in the occupation number of d_{z^2}

Because the d_{z^2} has an antibonding character along z, the spin crossover-induced change in the occupation of this molecular orbital yields a change in the bond order of the fragment+gas [49]. This decrease in binding energy and consequent bond elongation have been previously discussed in the case of gas adsorption in BTT-MOFs [49] and MOF-74 [49, 208] where the change in occupation of the d_{z^2} resulted from the increase in electron count of the d metal in MOFs found in high spin configuration.

This case applies to the change between S=0 (LS) and S=1 (intermediate spin, IS) for Fe(II); between S=1/2 (LS) and S=3/2 (IS) for Fe(III); and between S=0 (LS) and S=1 (HS) for Ni(II). See table 7.5 for the electronic configurations of the different molecules. The change in binding energy, ΔE_{bind} for these metal cations and the four gas molecules upon the specified spin-state transition is shown in Fig. 7.1; the associated $\Delta E_{H\text{-}L}$ are

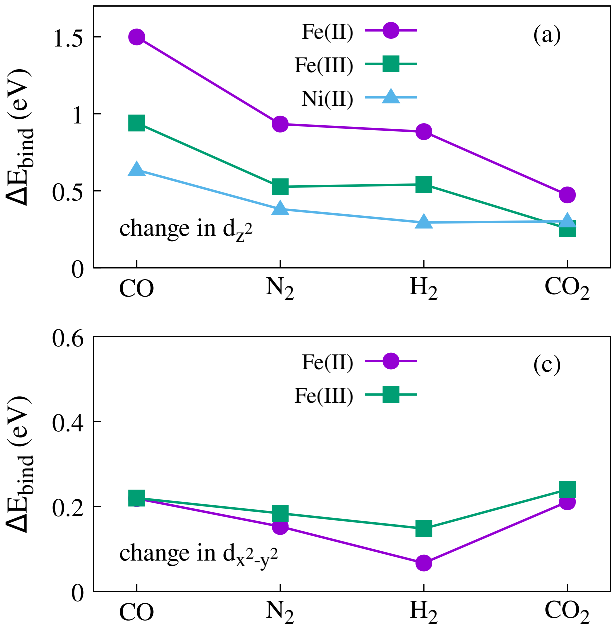

Figure 7.1: ΔE_{bind} for a spin-state transition involving a change in the occupation of the d_{z^2} (a) and the $d_{x^2-y^2}$ (c). The upper panel reports values for changes in spin state between S=0 (LS) and S=1 (IS) for Fe(II), S=1/2 (LS) and S=3/2 (IS) for Fe(III), and S=0 (LS) and S=1 (HS) for Ni(II). The lower panel reports values for spin-state changes between S=1 (IS) and S=2 (HS) for Fe(II), 3/2 (IS) and 5/2 (HS) for Fe(III). Note that the ΔE_{bind} are defined as the difference between the spin-state with the largest binding energy minus the spin-state with the lowest binding energy.

reported in table 7.6. We use the term ΔE_{bind} to refer more generally to the difference between the spin-state with the largest binding energy minus the spin-state with the lowest binding energy, while $\Delta E_{H\text{-}L}$ refers to the adiabatic energy difference between the HS or IS versus LS. Because the $\Delta E_{H\text{-}L}$ of the molecular fragments are computed using the TPSSh functional which has been shown to yield results which deviate from more accurate quantum chemistry methods[159], we report them in the SI (table 7.6) as they may serve as a reference, but we do not discuss them in detail. Ideally, in order for a spin crossover-induced gas-release process to exhibit a low energy penalty and a large working capacity the required conditions are i) a large change in binding energy upon spin transition and ii) changes in adiabatic energy difference and entropy compatible with conditions of the capture process. For example, if we assume that adsorption is performed at room temperature, the binding energy should be the largest at this temperature, and energy-efficient release could be achieved upon heating if the transition temperature is relatively close to ambient temperature. Thus, the higher the transition temperature, the

Metal center	gas	Spin	Charge (*e*)	M-L (Å)	M-gas (Å)	E_{bind} (eV)
M=**Fe(II)**	CO	0	1.62	1.91	1.87	2.159
		1	1.84	1.96	2.40	0.660
		2	2.02	2.22	2.27	0.879
	CO_2	0	1.80	1.92	2.06	0.960
		1	2.01	1.96	2.42	0.487
		2	2.22	2.19	2.24	0.698
	N_2	0	1.75	1.93	1.91	1.343
		1	1.87	1.96	2.44	0.410
		2	2.08	2.19	2.34	0.563
	H_2	0	1.49	1.92	1.67	1.131
		1	1.70	1.96	2.22	0.247
		2	1.94	2.18	2.21	0.314
Fe(III)	CO	1/2	1.82	1.97	1.93	2.270
		3/2	2.11	2.01	2.38	1.330
		5/2	2.36	2.19	2.31	1.550
	CO_2	1/2	2.11	1.98	1.98	1.599
		3/2	2.27	2.01	2.14	1.344
		5/2	2.50	2.20	2.06	1.584
	N_2	1/2	1.98	1.98	1.95	1.507
		3/2	2.15	2.01	2.30	0.981
		5/2	2.42	2.19	2.22	1.165
	H_2	1/2	1.73	1.97	1.71	1.093
		3/2	2.01	2.01	2.19	0.552
		5/2	2.27	2.17	2.12	0.700
Ni(II)	CO	0	1.19	1.87	2.91	0.318
		1	1.84	2.09	2.13	0.953
	CO_2	0	1.82	1.87	2.84	0.307
		1	2.10	2.08	2.23	0.609
	N_2	0	1.66	1.87	2.97	0.210
		1	1.94	2.09	2.19	0.591
	H_2	0	1.47	1.87	2.81	0.104
		1	1.78	2.08	2.00	0.398

Table 7.1: TPSSh-computed electrostatic charge of the metal center M, metal-cyanide ligands distance M-L, metal-gas bond distance M-gas and binding energies E_{bind} for the three molecular complexes at different spin states, spin.

larger is the energy penalty associated with the process. In this case of Ni, the LS→HS transition is accompanied by an increase in binding energy, consistent with a decrease in the occupation number of the d_{z^2}.

We note a smoother evolution of the curve for Ni(II) and a systematically larger change for Fe(II) with respect to Fe(III). The latter is due to the fact that while the binding energy is similar for the low spin case, the intermediate spin case has systematically larger binding in the case of Fe(III). For CO for example, the binding energy for LS is 2.159 eV for Fe(II) and 2.270 eV for Fe(III), and for IS we predict 0.660 eV and 1.330 eV, respectively. This results in a change of 1.5 eV for Fe(II) and 0.94 eV for Fe(III) upon spin change. We attribute this to the systematically larger electrostatic charges computed on the Fe(III) metal which may affect the binding more when weak interactions dominate.

We also note the high binding energy computed for CO_2 in the case of Fe(III). It reaches a value of approximately 1.6 eV in LS and 1.344 eV for IS, while for Fe(II) the computed values are substantially smaller (0.960 eV and 0.487 eV, for LS and IS), which is consistent with bond lengths values being significantly shorter for Fe(III). Specifically, we compute a metal-CO_2 bond length of 2.06 and 2.42 Å for LS and IS for Fe(II), and 1.98 and 2.14 Å for Fe(III).

Change in the occupation number of $d_{x^2-y^2}$.

Our calculations predict significant changes in the binding energy upon spin transition involving a change in the occupation of $d_{x^2-y^2}$. This effect becomes clear when binding energies are compared between spin states where a change in $d_{x^2-y^2}$ occurs but the occupation of d_{z^2} remains unchanged. Because $d_{x^2-y^2}$ has an antibonding character between the metal cation and the four CN^- ligands, the occupation of this molecular orbital results in a (less covalent) more ionic character of the M-L bonds. This occurs for IS→HS spin-state transition between S=1 (IS) and S=2 (HS) for Fe(II) and between S=3/2 (IS) and S=5/2 (HS) for Fe(III). See table 7.1 and Fig. 7.1 (lower panel). The occupation of the antibonding $d_{x^2-y^2}$ in HS results in longer M-L distances and an increased electrostatic positive charge at the Fe (see table 7.1). The Bader charge analysis shows a charge transfer of around 0.25 electrons from the metal to the ligands for Fe(II) and Fe(III) in absence of adsorbed molecules. We illustrate this change in Fig. 7.2 where the difference in total electronic density is computed between S=2 and S=1 of the $Fe(II)(CN)_4$ complex, bound to CO. Because the electronic configuration changes from $(d_{yz})^2(d_{x^2-y^2})^0$ for S=1 to $(d_{yz})^1(d_{x^2-y^2})^1$ for S=2, a fraction of electronic charge density migrates from the iron to the ligands consistent with a $d_{x^2-y^2}$ orbital exhibiting a molecular character with some

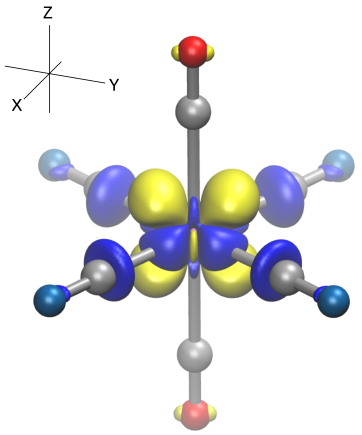

Figure 7.2: Difference of the total electron charge density between S=2 (HS) and S=1 (IS) spin for the CO@Fe(II)$(CN)_4$ complex. Yellow and blue surfaces represent negative and positive values, respectively, with an isovalue of 0.005 e/bohr^3. Iron, nitrogen, carbon, oxygen atoms are shown in purple, blue, grey and red. Hydrogen atoms are omitted for clarity.

localization on the ligand (see Fig. 7.2). This charge redistribution yields an increase in the positive charge of the metal which enhances the strength of the electrostatic component of the interaction with the guest molecule. Consistently with this analysis, we predict an increase in the MOF-gas binding energy and a decrease in bond distances (see Table 7.1). Overall, the computed ΔE_{bind} are smaller compared to the case where the spin state transition involves a change in the occupation of the d_{z^2} as shown in Fig. 7.1 (lower panel). The change in the binding mechanism upon occupation of $d_{x^2-y^2}$ and d_{z^2} is illustrated using a molecular orbital picture in Fig. 7.3 for CO_2 bound on Fe(II)$(CN)_4$. For S=0, the d_{z^2} is empty and the binding energy is the largest with E_{bind}=0.960 eV and M-CO_2 bond length of 2.06 Å. At intermediate spin, S=1, the d_{z^2} is singly occupied and the binding energy drops to 0.487 eV, with a bond length of 2.42 Å. For high spin at S=2, the d_{z^2} is singly occupied and the $d_{x^2-y^2}$ changes from empty to singly occupied. Due to the enhancement of the electrostatic contribution to the total binding mechanism, the binding energy increases with respect to S=1 and becomes E_{bind}=0.698 eV and the bond length shortens to 2.24 Å.

This analysis is consistent with previous studies reporting a change in binding energy upon change in the occupation of $d_{x^2-y^2}$ achieved by changing the metal ion in high spin configuration. Specifically, an increase in binding energy is predicted from Cr to Mn and

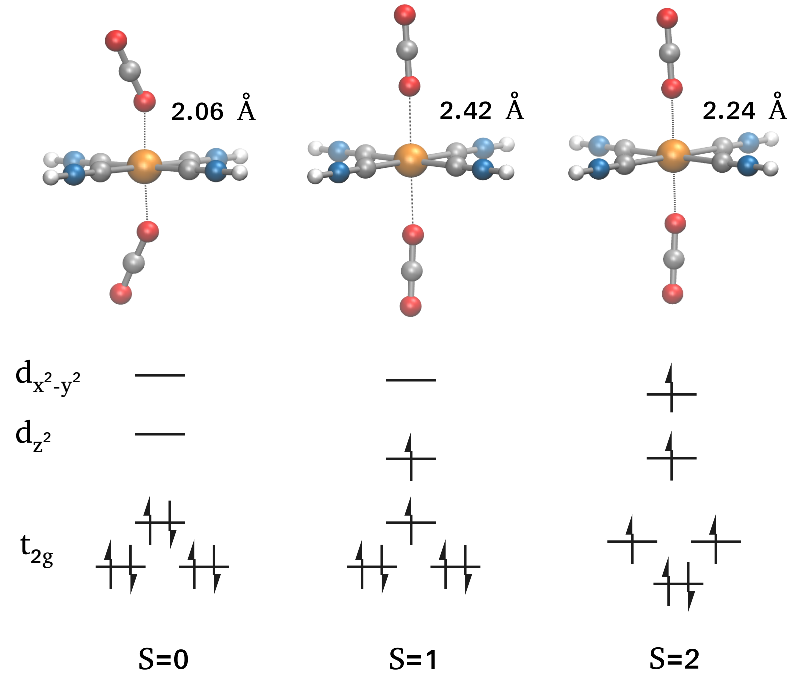

Figure 7.3: Molecular-orbital diagrams for CO_2 bound on the Fe(II)$(CN)_4$ fragment. An elongated octahedral ligand-field splitting is shown consistent with longer metal-gas bond distances as compared to the ligands. The electronic configuration at the metal results in strong (0.96 eV), weak (0.49 eV) and intermediate binding energies (0.67 eV) for low spin (S=0), intermediate spin (S=1), and high spin (S=2), respectively.

from Cu to Zn [49, 211], consistent with an increase in the electrostatic charge of the ion [49].

We want to stress that for Fe(II) and Fe(III) the ΔE_{bind} refers to energy differences between the highest possible spin state and the intermediate spin state. Thus, because the intermediate spin states are already quite high in energy (see ΔE in Table 7.6) compared to the ground state, especially for Fe(II), one should expect the transition to high spin to occur at temperatures too high for this mechanism to be feasible. These considerations, together with the relatively lower change in binding energy computed for this mechanism compared to the previous one, motivates us to further study the first scenario, i.e. a spin transition involving a change in the occupation of d$_{z^2}$.

7.4.2 MOF calculations

We compute the binding configuration and binding energy for each spin state and the corresponding adiabatic energy difference, $\Delta E_{\text{H-L}}$, in metal-organic frameworks containing the fragment molecules studied in the previous section. We have found that the predicted changes in binding energy are substantial when the occupation of the d_{z^2} changes and this may lead to efficient gas release, depending on the thermodynamics of the transition. We recall that for Ni(II), HS corresponds to a stronger interaction with gas molecules because the d_{z^2} is singly occupied while in LS it is doubly occupied. Thus, in this case gas release would be achieved upon cooling down the system (provided the ground state was the LS). As candidate MOF exhibiting the $M(CN)_4$ fragment we choose the Hoffman-like MOFs $Fe(pz)M(CN)_4$ and $Fe(bpac)M(CN)_4$. Because the open metal site contains a divalent metal, we consider M = Fe(II), Ni(II), and Mn(II). The latter is isoelectronic to (and replaces) the Fe(III) considered in the fragment calculations. We note that the Ni case has been largely studied experimentally [71, 79, 83], while the other two have no experimental realization. In each case we compute the ground state and the first accessible state. This corresponds to S=0 (LS) and S=1 (IS) for Fe(II), to S=0 (LS) and S=1 (HS) for Ni(II), and S=1/2 (LS) and S=3/2 (IS) for Mn(II).

Bias in the calculation of the binding energy

The comparison of the binding energy computed using PBE+D3+U (the total energy of equation 7.1) and the density-corrected scheme PBE+D3[U] (first term of equation 7.1) is reported in the SI for all the periodic complexes studied in this work. A large difference in binding energy between the full PBE+D3+U calculation and the density-corrected one, PBE+D3[U], is predicted. This is due to the difference in the Hubbard term between the bare MOF and the bound case and its origin is explained below. This bias yields binding energies that are lower (weaker binding) than the density-corrected scheme of equation 7.3 for Mn and Fe in LS. For Ni, the opposite behavior is found with stronger binding energies than the density-corrected scheme.

We recall that, for a given value of U, the Hubbard term is larger when the occupation numbers n are more fractional (closer to 1/2) (see second term of equation 7.1). As expected from a molecular orbital picture (see Figure 7.3), when d_{z^2} is empty (Fe and Mn in LS) the occupation number associated with the atomic projector d_{z^2} increases upon binding. This is due to the fact that in the bare MOF without any bound molecule this orbital is an atomic-like orbital which is empty and therefore its occupation number is close to zero. In the bound case, due to the hybridization between the metal and the gas molecule, the occupation number increases due to the contribution from the low lying ligand-like states to the projection onto the d_{z^2} atomic orbital[159]. To illustrate this, the values of binding energies computed using PBE+D3+U and PBE+D3[U] are reported

complex	Binding Energy (eV)				occupations n_j					$\Delta(\mathrm{E_U})$
	PBE+D3+U		PBE+D3[U]		for LS					for LS
Fe(bpac)Fe(CN)$_4$	LS	IS	LS	IS	d_{z^2}	$\mathrm{d}_{x^2-y^2}$	d_{xz}	d_{yz}	d_{xy}	(eV)
bare	/	/	/	/	0.023	0.309	0.960	0.961	0.932	zero
CO_2	0.312	0.079	0.419	0.128	0.050	0.296	0.959	0.959	0.929	0.213
H_2	0.131	0.094	1.007	0.097	0.181	0.306	0.928	0.929	0.919	1.752
N_2	0.293	0.164	1.223	0.167	0.171	0.305	0.909	0.910	0.933	1.860
CO	0.754	/	2.344	/	0.300	0.309	0.863	0.864	0.929	3.180

Table 7.2: Comparison between the binding energies computed using the PBE+D3+U and PBE+D3[U]. The stronger the binding in LS, the larger the occupation of the dz^2 and consequently the bias in the binding energy introduced by the Hubbard term.

in table 7.2 for Fe(bpac)Fe(CN)$_4$. We also report the changes in the eigenvalues of the occupation matrix for the bare MOF and for the bound cases. Because the hybridization is stronger for more strongly bound molecules, the occupation number associated with d_{z^2} increases from almost 0.050 in the case of CO_2 where the molecule's orbitals are expected to mix negligibly with the metal, to 0.300 in the case of strongly bound CO. This leads to values of the Hubbard energy term that increase as as a function of the orbital mixing between the metal and the molecules. As a consequence, the binding energies computed using the full energy expression of PBE+D3+U are always lower (weaker binding) than the density-corrected PBE+D3[U] case and the difference between the values computed using the two approaches also increases from weak to strongly bound molecules. As an example, the CO binding energy is predicted to be 0.754 eV using PBE+D3+U and 2.344 eV using the density corrected scheme. The difference in the Hubbard energy between the bare and the bound cases, $\Delta(\mathrm{E_U})$, is also reported in table 7.2. Because the occupation numbers of the octahedrally coordinated Fe barely change in the different cases, this difference corresponds to twice the difference (bias) in binding energy between the two sets of calculations (two bound molecules per unit cell).

The full list of values of binding energies computed using PBE+D3+U and PBE+D3[U] is reported in the SI.

The bias is substantially lower for Fe and Mn in HS, and for Ni in LS (see SI), as expected from a half occupied d_{z^2} orbital and substantially weaker binding between the metal and the molecules. This is consistent with previous observations on the effect of using a Hubbard U correction on the binding energy of other open-metal site-MOFs [211, 181]. The authors reported a difference of 8 kJ/mol for CO_2 adsorption onto an open square-pyramidal metal center in the M-MOF-74, in HS state. We note, however, a significantly smaller value of U employed in ref. 211 ranging from 2.0 eV for Ti and 6.4 eV for Ni.

Binding energy and binding configuration

We discuss first the case of Fe(bpac)Fe$(CN)_4$. In LS, CO_2 binds on top of the Fe site in a tilted *top on* configuration (see Fig. 7.4 d) (similar to the molecular case discussed in the previous section) with one of the O atoms of CO_2 on the two apical sites of the octahedron at a bond distance of 2.314 Å. In IS (S=1), the bond distance increases substantially (3.379 Å), as expected, and molecule orients parallel to the Fe$(CN)_4$ plane and parallel to the plane of the pyrazine rings and in between them. We note that this configuration differs from the molecular case where CO_2 binds in a top on fashion (see Fig. 7.3 and Tab. 7.1) and we attribute this difference to the dominant role of the pyrazine rings when the affinity for the metal is low. In LS, N_2 and CO adsorb on a *top on* configuration with the N-N and C-O bond perpendicular to the Fe$(CN)_4$ plane (see Fig. 7.4 b and a, respectively). At S=1, the N_2 molecule maintains its orientation while increasing the bond distance. The configuration with CO in S=1 could not be converged (*vide infra*). H_2 binds in a side on horizontal configuration (see Fig. 7.4 c) consistent with a Kubas type of binding in LS with the two H-Fe bond distances per molecule being equivalent (1.656 Å). In S=1 the bond distances increase and the molecules are found in a slightly tilted configuration. One of the molecules exhibits Fe-H distances of 2.646 Å and 2.774 Å and the other 2.684 Å and 2.791 Å. The pz case is qualitatively similar to the bpac case except that in this case CO can be converged in S=1 and that CO_2 in S=1 adopts a side on configuration perpendicular to the pyrazine rings with the Fe coordinated to the CO_2 carbon. The same configuration was predicted by Culp et *al.* for the Hofmann-like clathrate Fe(pz)[M$(CN)_4$] (M = Pt and Ni) using DFT [195]. We note a similar binding configuration of H_2, N_2, and CO in the MOF and in the molecular fragment.

Fe(bpac)Mn$(CN)_4$ adsorbs CO_2 with a side on configuration both in LS and IS with a metal-C distance of 3.611 Å and 3.663 Å, respectively. N_2 and CO adsorb on a *top on* configuration, both in LS and IS, similar to the M=Fe case. In LS H_2 binds in a Kubas mechanism with a high binding energy of 1.047 eV and an average Mn-H distance of 1.710 Å while in IS the molecule is found at an average distance as large as 3.025 Å consistent with the weak binding (0.087 eV). Similar binding configurations are found for Fe(pz)Mn$(CN)_4$.

We remind the reader that for Fe(bpac)Ni$(CN)_4$ a stronger binding is expected in HS

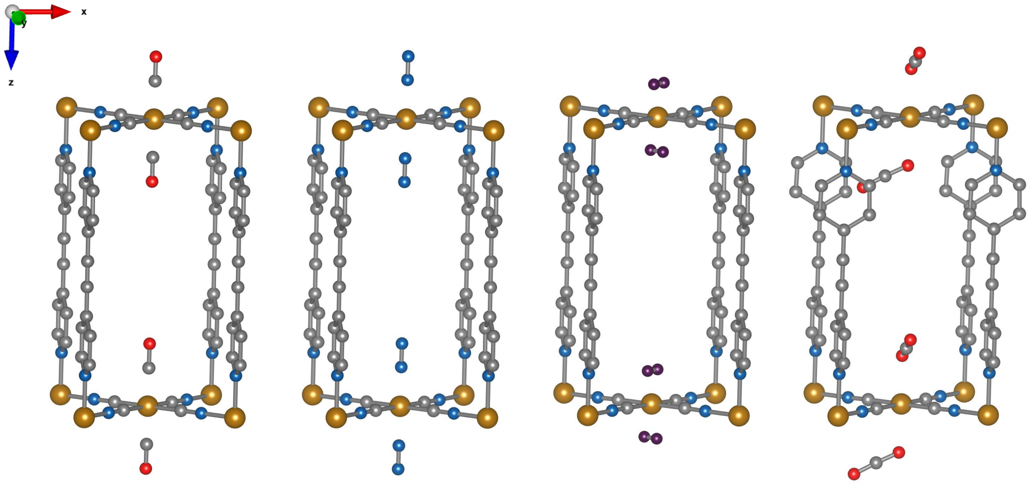

(a) (b) (c) (d)

Figure 7.4: Representation of the optimized geometry of Fe(bpac)[Fe(CN)$_4$] in LS upon adsorption of CO (a), N_2 (b), H_2 (c) and CO_2 (d). Color code: Fe (LS), C, N, O and H are orange, grey, blue, red and purple. H atoms from the MOF structure are omitted for clarity.

because consistent with a d^8 electron count and a distorted octahedral ligand field: the d_{z^2} is singly occupied while it is doubly occupied in LS. In HS, N_2 and CO bind in a top on apical configuration, while H_2 adopts a side on Kubas configuration. The CO_2 molecules are located horizontally on top of the metal and parallel to the phenyl rings with the O(CO_2)-Ni-C(CN) bond angle of 74.5°. In LS the bond distances increase for all molecules. N_2 and CO_2 maintain their orientation. H_2 adopts a tilted configuration as in the IS case of Mn and Fe, and CO also adopts a tilted configuration.

Adiabatic energy differences in Fe(bpac)M(CN)$_4$

The results are reported in Table 7.3. In this case, two molecules are adsorbed per metal site owing to the large pore volume. In the case of M=Fe, the ground state of the bare MOF is S=1 (IS). Upon coordination of CO_2 the $\Delta E_{\text{H-L}}$ becomes less negative as a result of the destabilization of d_z^2 by the interaction with the molecule but it does not yield a change of sign owing to the weak ligand field of CO_2. For the other molecules the strong interaction with the Fe center computed in S=0 (LS), i.e. 1.007 eV (H_2), 1.223 eV (N_2), and 2.344 eV (CO), allows to stabilize LS and yields positive values of $\Delta E_{\text{H-L}}$ whose values correlate well with the strength of the binding. For CO, the interaction is so strong that the high spin converges to S=2 (HS) (and not S=1, IS) thus preventing us from computing the values of adiabatic energy difference and the binding energy in the IS case. In any case this implies a configuration that is high in energy.

For Mn the ground state is S=3/2 (IS) for the bare MOF and the trend in terms of binding energies and $\Delta E_{\text{H-L}}$ is similar to the Fe case. We compute a progressive increase of the $\Delta E_{\text{H-L}}$ as the strength of the binding increases, i.e. from CO_2 to CO. The first case exhibits a binding energy of 0.550 eV and a negative adiabatic energy difference of -1.040 eV. For the strong ligand field CO molecule, we compute respectively 2.463 eV (binding) and 2.745 eV (spin splitting energy). Thus, as for Fe, due to the big energy difference, we expect the LS-HS transition not to occur as an entropy driven process for adsorbed CO.

complex **Fe(bpac)M(CN)$_4$**	$\Delta E_{\text{H-L}}$ (eV)	Binding energy (eV)		M-gas dist. (Å)	
		LS	IS	LS	IS
M=Fe, bare	-1.166	$U_{\text{Fe,LS}}$=9.23 eV, $U_{\text{Fe,IS}}$=10.11 eV			
CO_2	-0.585	0.419	0.128	2.314	3.379
H_2	0.654	1.007	0.097	1.656	2.710
N_2	0.947	1.223	0.167	1.781	2.835
CO	/	2.344	/	1.817	2.450^a
M=Mn, bare	-1.654	$U_{\text{Mn,LS}}$=6.81 eV, $U_{\text{Mn,IS}}$=7.26 eV			
CO_2	-1.040	0.550	0.243	3.611	3.663
H_2	0.267	1.047	0.087	1.710	3.025
N_2	0.825	1.412	0.173	1.908	3.013
CO	2.745	2.463	0.263	1.855	2.703
M=Ni, bare	/	$U_{\text{Ni,LS}}$=10.98 eV, $U_{\text{Ni,IS}}$=8.86 eV			
CO_2	2.888	0.258	/	3.603	3.375
H_2	2.361	0.081	/	3.273	2.179
N_2	2.302	0.132	/	3.514	2.501
CO	1.818	0.223	/	3.474	2.076

Table 7.3: Adiabatic energy difference $\Delta E_{\text{H-L}}$, change in binding energy (eV) and metal-gas distance (Å) between S=1 and S=0 for M=Fe,Ni, and between S=3/2 and S=1/2 for M=Mn, computed for Fe(bpac)M(CN)$_4$ and several gas molecules. These correspond to differences between intermediate spin and low spin. The values of U_{sc} are reported in each case. Gas-metal bond distances refer to the average value computed over the two molecules.^{a} This configuration corresponds to S=2 (see text).

complex **Fe(pz)M(CN)$_4$**	$\Delta E_{\text{H-L}}$ (eV)	Binding energy (eV)		M-gas dist. (Å)	
		LS	IS	LS	IS
M=Fe, bare	-0.973	$U_{\text{Fe,LS}}$=9.22 eV, $U_{\text{Fe,IS}}$=10.11 eV			
CO_2	-0.608	0.660	0.295	2.483	3.407
H_2	-0.030	1.023	0.081	1.641	2.502
N_2	0.326	1.439	0.140	1.840	2.868
CO	1.147	2.728	0.609	1.754	2.009
M=Mn, bare	-1.638	$U_{\text{Mn,LS}}$=6.81 eV, $U_{\text{Mn,IS}}$=7.26 eV			
CO_2	-1.518	0.502	0.381	2.563	2.880
H_2	-0.654	1.117	0.132	1.750	3.385
N_2	-0.116	1.723	0.200	1.876	2.688
CO	0.897	3.016	0.481	1.791	2.285
M=Ni, bare	/	$U_{\text{Ni,LS}}$=10.98 eV, $U_{\text{Ni,IS}}$=8.86 eV			
CO_2	2.387	0.369	/	3.409	2.797
H_2	2.356	0.088	/	3.345	2.002
N_2	2.365	0.225	/	3.510	2.363
CO	1.920	0.268	/	3.411	1.966

Table 7.4: Adiabatic energy difference $\Delta E_{\text{H-L}}$, change in binding energy (eV) and metal-gas distance (Å) between S=1 and S=0 for M=Fe,Ni, and between S=3/2 and S=1/2 for M=Mn, computed for Fe(pz)M(CN)$_4$ and several gas molecules. These correspond to differences between intermediate spin and low spin. The values of U_{sc} are reported in each case.

In the case of Ni, as discussed in the previous section, the change in Fe(bpac)Ni(CN)$_4$ from S=0 (LS) to S=1 (HS) corresponds to a change of d_{z^2} from doubly to singly occupied. Thus, larger binding energies are expected for S=1. For the bare MOF, however, the calculations could be converged only with Ni in LS, consistent with experimental findings. Thus, even though the HS could be computed for all adsorbed molecules, the binding energy can be reported only for LS. The analysis of the metal-gas bond distance, however, shows systematically stronger binding in HS, with CO possibly being the strongest among all molecules, consistent with the shortest bond length and smallest $\Delta E_{\text{H-L}}$. We note, as expected, an opposite evolution of $\Delta E_{\text{H-L}}$ for the four gas molecules between the Ni(II) MOF and the Fe(II) and Mn(II) cases. For Fe and Mn, larger values of $\Delta E_{\text{H-L}}$ are found for molecules exhibiting stronger-field ligands, i.e. for a higher destabilization of d_{z^2} with respect to the low lying non-bonding orbitals. Thus, a spin change between S=1 and S=0 in the Fe(II) MOF involving a change in occupation between the d_{z^2} and d_{xy}, results in the largest values of $\Delta E_{\text{H-L}}$ for CO for Fe and Mn and the smallest for Ni (see illustration of the molecular-orbital diagram in Fig. 7.3). For the same reason, stronger-field ligands result in the decrease of $\Delta E_{\text{H-L}}$ in the case of Ni(II). In this case, the destabilization of d_{z^2} upon a strong binding brings this molecular orbital closer to high-lying antibonding $d_{x^2-y^2}$, and because the spin transition involves these two energy levels, the associated $\Delta E_{\text{H-L}}$ decreases.

Adiabatic energy differences in Fe(pz)M(CN)$_4$

The results of the Fe(pz)M(CN)$_4$ clathrate are reported in Table 7.4. In this case, only one molecule can adsorb due to the smaller pore on the top of the coordinatively unsaturated metal.

In the case of Fe, the ground state of the bare MOF is S=1 and the $\Delta E_{\text{H-L}}$ between S=1 (IS) and S=0 (LS) is comparable to the bpac counterpart. When CO_2 is adsorbed, the $\Delta E_{\text{H-L}}$ increases only marginally, and less compared to the previous case when two molecules are adsorbed. The strong binding of CO (2.728 eV in LS) and N_2 (1.439 eV in LS) allows to change the sign of the $\Delta E_{\text{H-L}}$ as in the previous case and yields $\Delta E_{\text{H-L}}$ of 1.147 eV and 0.326 eV, respectively. For H_2, the destabilization of the d_{z^2} by one molecule is not sufficient to change the sign of $\Delta E_{\text{H-L}}$ (-0.030 eV). The metal-gas distance and the change in the binding energy are similar to the bpac case. For Mn, the $\Delta E_{\text{H-L}}$ are overall smaller than the Fe case, and the trend correlates well with the binding strength and bond distances. A positive value of $\Delta E_{\text{H-L}}$ is here predicted only for CO (0.897 eV).

The situation for Ni is similar to the bpac case. The ground state is LS, regardless of the type of molecule adsorbed. The adiabatic energy differences are still rather high even for strongly binding molecules such as CO.

Kubas interaction

Whenever the open metal site is in LS and the d_{z^2} orbital is empty, the full optimization results in a configuration with H_2 bound horizontally on top of the metal. This is the case for both MOFs with M=Fe in S=0 (LS) and for the pz case for M=Mn in S=1/2 (LS). The corresponding binding energies are rather high, above 1 eV, consistent with the short metal-gas bond lengths and a Kubas type of binding[218, 219] (see results in Tables 7.3 and 7.4). The Kubas interaction here involves the σ-donation from the H-H σ-bonding orbital into the empty d_z^2 orbital of the metal, and the simultaneous π-back-donation from a filled metal d orbital into the $\sigma*$ antibonding orbital of the molecule. It results in a lengthening of the H-H bond as found in this work. The computed H-H bond of the gas phase molecule that we found is 0.762 Å. For the bpac and pz cases and the Fe center in LS, the adsorbed H_2 molecules exhibit a H-H bond of 0.830 Å. For Mn, we compute a shorter H-H bond length of 0.823 Å in the bpac case and 0.818 Å in the pz case, and a larger H_2-metal bond for Mn as compared with Fe (see Tables 7.3 and 7.4). Also the case of partially filled d_z^2 in Ni (bpac) in HS is consistent with a Kubas interaction: a slight weakening of the H-H bond is predicted with a H-H bond length of 0.773 Å and the average H-Ni distance 2.179 Å. In IS, the interaction of H_2 is dominated by weak van der Waals forces and results in binding energies of 0.087 and 0.132 eV. The binding configurations result in significantly longer bond distances with the molecule on a semi-horizontal configuration. The large change in binding energy upon spin crossover provides a promising mechanism for an efficient hydrogen capture/storage because the use of cryogenic conditions can be bypassed[30], and storage could be performed at RT, provided the transition to IS occurs at higher temperatures. Thus, the case of bpac for M=Fe and Mn represents a promising candidate for this mechanism exploiting the strong Kubas interaction in LS because the predicted $\Delta E_{\text{H-L}}$ may be consistent with a transition occurring above RT.

7.4.3 H_2 adsorption in $Fe_2(tpt)_2(NCS)_4$

In view of the encouraging results obtained for the adsorption and release process of hydrogen molecules in $Fe(bpac)[Fe(CN)_4]$ and $Fe(bpac)[Mn(CN)_4]$, we further investigate the feasibility of the proposed spin-crossover strategy for a MOF that has already been synthesised, unlike most of the Hoffman-like clathrates discussed above. This material is the MOF $Fe_2(tpt)_2(NCS)_4$ (tpt = 2,4,6-tris(4'-pyridyl)-1,3,5-triazine) which was synthesised by C. J. Kepert and coworkers [214] and exhibit Fe(II) in a square-pyramidal coordination. In our calculations, all solvant molecules are removed from the .cif file obtained from the CoRE database [229]. This MOF consists of two interpenetrated structures in which each metal node is coordinated via three tpt ligands. The structure around the open metal center upon gas adsorption is shown in Fig. 7.5. The Fe(II) is coordinated with two tpt and two NCS ligands on the xy plane and with another tpt along the z direction. In the absence of guest molecules, the ligand field splitting induced by the ligand along z is not strong enough to stabilise the LS state and thus the ground spin state in the bare MOF is HS. Upon adsorption of H_2 on the open metal site, the ground state is LS as a result of the strong binding interacting as expected from a Kubas mechanism. The binding distances between H_2 and the Fe are 2.74 Å and 1.72 Å for HS and LS respectively. These distances and the associated binding geometries are very similar to those obtained in the case of Fe(bpac)Fe$(CN)_4$ and Fe(pz)Fe$(CN)_4$. The computed ΔE between HS and LS upon gas adsorption is 0.342 eV. Values of ΔH ranging between 0.1 and 0.3 eV have been reported for several Fe(II)-based molecular [230] and crystalline compounds [231] resulting in spin-crossover temperature near room temperature. Because of geometrical instability in the LS case of the bare MOF, it was not possible to compute the change in the binding energy associated with the change in the spin state. Nevertheless, the change in the magnetic ground state upon H_2 adsorption as well as the computed adsorption geometries clearly show that the interaction between the molecule and the MOF is significantly reduced when switching from LS to HS.

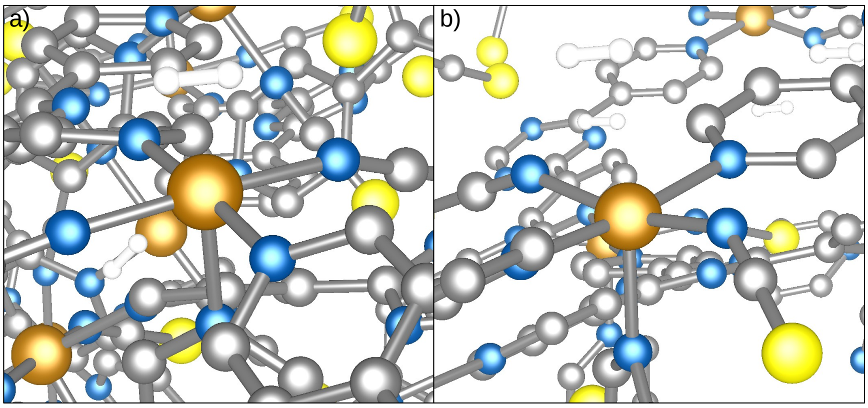

Figure 7.5: Optimized periodic $Fe_2(tpt)_2(NCS)_4$ framework upon H_2 adsorption. (a) Low-spin state. (b) High-spin state.

7.5 Discussion and conclusion

An extensive computational analysis of the relationship between the spin state of the open-metal and its affinity for guest molecules has been carried out by means of DFT. Firstly, we considered a simple square planar model $M(CN)_4$ molecular complex with M=Fe(II), Fe(III), and Ni(II), which served us as toy-model to rationalize the computed change in binding energy upon spin modification. Two different mechanisms have been identified and studied. The first, already discussed in previous works[49], involves a change in the bond order between the metal and the molecule, i.e. a change in the occupation of the d_{z^2} orbital, while the second is of electrostatic nature and is due to a change in the occupation of the planar $d_{x^2-y^2}$ bonding orbital. The latter, despite being an order of magnitude less effective in modifying binding energy than the former, has never been discussed before and its understanding may be of fundamental importance for future studies. A few experimental studies reported in recent years confirm our analysis.

In light of the possible use of the above-mentioned mechanisms for gas capture and release applications, we studied two Hofmann-like MOFs, Fe(bpac)M(CN)$_4$ and Fe(pz)M(CN)$_4$ with M=Fe(II), Ni(II), and Mn(II). The change in binding energy occurring concomitantly with the spin state change is reported for CO, CO_2, N_2, and H_2. The change in the occupation of the antibonding d_{z^2} orbital between the metal center and the host molecule yields a significant change in binding energy in all the cases. In spite of that, the main bottleneck for possible technological implementation is represented by the adiabatic energy difference between the spin states involved in the transition. Motivated by our previous studies showing an improved performance of the Hubbard U-density corrected approach compared to other good performers such as M06-L and TPSSh, we employ this method to accurately compute both. We recall that the vibrational contribution to the enthalpy change usually amounts to a few tens of meV[230, 231]. Thus, if we assume that the computed $\Delta E_{\text{H-L}}$ reported above well approximate the total ΔH of the spin-state transition, a comparison can be made with experimental values of ΔH reported for spin crossover compounds. Values of ΔH ranging between 0.2 and 0.5 eV have been reported for several Fe(II)-based molecular[230] and crystalline compounds[231] resulting in spin crossover temperature near room temperature. Thus, we consider this range of values to assess the feasibility of the proposed mechanism for the materials studied here.

The $\Delta E_{\text{H-L}}$ strongly depends on the strengths of the interaction between the metal and the molecule. The CO_2 molecule is a too weak ligand field molecules and here it never stabilizes LS thus preventing the implementation of the proposed spin-crossover mechanism in the materials studied here for an efficient CO_2 desorption. On the other hand, N_2 and CO adsorption results in a large stabilization of LS with computed $\Delta E_{\text{H-L}}$ too large in these cases, except for N_2 adsorption on Fe(pz)Fe(CN)$_4$ for which a promising value of $\Delta E_{\text{H-L}}$ =0.325 eV is predicted. The best performances are observed for H_2 molecule that induces an intermediate ligand field splitting in the metal center with a consequent computed $\Delta E_{\text{H-L}}$ of 0.654 eV and 0.267 eV in Fe(bpac)Fe(CN)$_4$ and Fe(bpac)Mn(CN)$_4$ respectively.

Finally, the proposed strategy has been applied in the already synthesised $Fe_2(tpt)_2(NCS)_4$ MOF. The adiabatic energy difference between HS and LS states upon H_2 adsorption, $\Delta E_{\text{H-L}}$=0.342 eV, shows that this compound is an excellent candidate for applications in hydrogen storage technologies. The strong interaction in LS consistent with a Kubas mechanism, may lead to an efficient adsorption and high storage capacity while the adiabatic energy difference is compatible with a temperature induced spin crossover near room temperature.

We are confident that the understanding provided here will assist future synthetic efforts towards the development of energy-efficient spin crossover-assisted separation or storage technologies.

7.6 Supplementary information

Metal center	Spin state	Electronic configuration
Fe(II)	0 (LS)	$(d_{xz})^2(d_{yz})^2(d_{xy})^2(d_{z^2})^0(d_{x^2-y^2})^0$
	1 (IS)	$(d_{xz})^2(d_{yz})^2(d_{xy})^1(d_{z^2})^1(d_{x^2-y^2})^0$
	2 (HS)	$(d_{xz})^2(d_{yz})^1(d_{xy})^1(d_{z^2})^1(d_{x^2-y^2})^1$
Fe(III)	1/2 (LS)	$(d_{xz})^2(d_{yz})^2(d_{xy})^1(d_{z^2})^0(d_{x^2-y^2})^0$
	3/2 (IS)	$(d_{xz})^2(d_{yz})^1(d_{xy})^1(d_{z^2})^1(d_{x^2-y^2})^0$
	5/2 (HS)	$(d_{xz})^1(d_{yz})^1(d_{xy})^1(d_{z^2})^1(d_{x^2-y^2})^1$
Ni(II)	0 (LS)	$(d_{xz})^2(d_{yz})^2(d_{xy})^2(d_{z^2})^2(d_{x^2-y^2})^0$
	1 (HS)	$(d_{xz})^2(d_{yz})^2(d_{xy})^2(d_{z^2})^1(d_{x^2-y^2})^1$

Table 7.5: Electronic configuration of all the spin states and metal complexes considered in this work. These occupations confirmed by looking at the Kohn-Sham orbitals are consistent with the molecular orbital diagram of an elongated octahedral field.

Metal center	gas	Spin	ΔE (eV)	Charge (e)	M-L (Å)	M-gas (Å)	$\mathrm{E}_{\mathrm{bind}}$ (eV)
Fe(II)	CO	0	0	1.62	1.91	1.87	2.159
		1	2.00	1.84	1.96	2.40	0.660
		2	2.69	2.02	2.22	2.27	0.879
	CO_2	0	0.06	1.80	1.92	2.06	0.960
		1	0	2.01	1.96	2.42	0.487
		2	0.66	2.22	2.19	2.24	0.698
	N_2	0	0	1.75	1.93	1.91	1.343
		1	0.87	1.87	1.96	2.44	0.410
		2	1.70	2.08	2.19	2.34	0.563
	H_2	0	0	1.49	1.92	1.67	1.131
		1	0.77	1.70	1.96	2.22	0.247
		2	1.77	1.94	2.18	2.21	0.314
Fe(III)	CO	1/2	0	1.82	1.97	1.93	2.270
		3/2	1.21	2.11	2.01	2.38	1.330
		5/2	1.86	2.36	2.19	2.31	1.550
	CO_2	1/2	0.16	2.11	1.98	1.98	1.599
		3/2	0	2.27	2.01	2.14	1.344
		5/2	0.45	2.50	2.20	2.06	1.584
	N_2	1/2	0	1.98	1.98	1.95	1.507
		3/2	0.40	2.15	2.01	2.30	0.981
		5/2	1.10	2.42	2.19	2.22	1.165
	H_2	1/2	0	1.73	1.97	1.71	1.093
		3/2	0.41	2.01	2.01	2.19	0.552
		5/2	1.27	2.27	2.17	2.12	0.700
Ni(II)	CO	0	0.03	1.19	1.87	2.91	0.318
		1	0	1.84	2.09	2.13	0.953
	CO_2	0	0	1.82	1.87	2.84	0.307
		1	0.64	2.10	2.08	2.23	0.609
	N_2	0	0	1.66	1.87	2.97	0.210
		1	0.48	1.94	2.09	2.19	0.591
	H_2	0	0	1.47	1.87	2.81	0.104
		1	0.66	1.78	2.08	2.00	0.398

Table 7.6: Computed adiabatic energy difference $\Delta \mathrm{E}_{\text{H-L}}$ with respect to the ground state set at 0 energy, electrostatic charge of the metal center M, metal-cyanide ligands distance M-L, metal-gas bond distance M-gas and binding energies E_{bind} for the three molecular complexes at different spin states.

complex	$\Delta E_{\text{H-L}}$ (eV)		Binding Energy (eV)			
			LS	IS	LS	IS
Fe(bpac)M(CN)$_4$	PBE+D3[U]	PBE+D3+U	PBE+D3[U]		PBE+D3+U	
M=Fe, bare	-1.166	-1.161	$U_{\text{Fe,LS}}$=9.23 eV, $U_{\text{Fe,IS}}$=10.11 eV			
CO_2	-0.585	-0.683	0.419	0.128	0.312	0.079
H_2	0.654	-1.087	1.007	0.097	0.131	0.094
N_2	0.947	-0.902	1.223	0.167	0.293	0.164
CO	/	2.457	2.344	/	0.754	/
M=Mn, bare	-1.654	-1.740	$U_{\text{Mn,LS}}$=6.81 eV, $U_{\text{Mn,IS}}$=7.26 eV			
CO_2	-1.040	-0.995	0.550	0.243	0.609	0.237
H_2	0.267	-1.136	1.047	0.087	0.386	0.084
N_2	0.825	-0.956	1.412	0.173	0.556	0.164
1CO	0.714	-0.541	3.006	0.639	1.182	-0.017
2CO	2.745	0.100	2.463	0.263	1.143	0.223
M=Ni, bare	/	/	$U_{\text{Ni,LS}}$=10.98 eV, $U_{\text{Ni,IS}}$=8.86 eV			
CO_2	2.888	0.416	0.258	/	0.261	/
H_2	2.361	-0.219	0.081	/	0.079	/
N_2	2.302	-0.327	0.132	/	0.134	/
CO	1.818	-0.296	0.223	/	0.210	/

Table 7.7: Adiabatic energy difference $\Delta E_{\text{H-L}}$ (eV) and binding energies (eV) computed for Fe(bpac)M(CN)$_4$ (M = Fe(II), Mn(II) or Ni(II)) using PBE+D3+U and PBE+D3[U].

complex	$\Delta E_{\text{H-L}}$ (eV)		Binding Energy (eV)			
Fe(pz)M(CN)$_4$			LS	IS	LS	IS
	PBE+D3[U]	PBE+D3+U	PBE+D3[U]		PBE+D3+U	
M=Fe, bare	-0.973	-0.720	$U_{\text{Fe,LS}}$=9.22 eV, $U_{\text{Fe,IS}}$=10.11 eV			
CO_2	-0.608	-0.630	0.660	0.295	0.498	0.409
H_2	-0.030	-0.878	1.023	0.081	0.062	0.220
N_2	0.326	-0.766	1.439	0.140	-5.484	-5.438
CO	1.147	-0.251	2.728	0.609	0.580	0.110
M=Mn, bare	-1.638	-1.726	$U_{\text{Mn,LS}}$=6.81 eV, $U_{\text{Mn,IS}}$=7.26 eV			
CO_2	-1.518	-1.758	0.502	0.381	0.349	0.381
H_2	-0.654	-1.383	1.117	0.132	0.474	0.131
N_2	-0.116	-1.259	1.723	0.200	0.698	0.231
CO	0.897	-0.768	3.016	0.481	1.195	0.236
M=Ni, bare	/	/	$U_{\text{Ni,LS}}$=10.98 eV, $U_{\text{Ni,IS}}$=8.86 eV			
CO_2	2.387	-0.264	0.369	/	0.373	/
H_2	2.356	-0.207	0.088	/	0.092	/
N_2	2.365	-0.253	0.225	/	0.238	/
CO	1.920	-0.252	0.268	/	0.275	/

Table 7.8: Adiabatic energy difference $\Delta E_{\text{H-L}}$ (eV) and binding energies (eV) computed for Fe(pz)M(CN)$_4$ (M = Fe(II), Mn(II) or Ni(II)) using PBE+D3+U and PBE+D3[U].

Chapter 8

Conclusions

In this thesis we have investigated the adsorption mechanism of SO_2, CO and CO_2 in the Hofmann-clathrate Fe(pz)[Pt(CN)$_4$] (pz = pyrazine) by neutron scattering techniques and density-functional theory calculations.

One of the first experimental results obtained is the discovery of an ordered structure of the bridging pyrazine ligands located in the apical positions of the octahedrally coordinated Fe(II) centers. At low temperature, these ligands adopt an ordered arrangement with the rings alternately oriented in two orthogonal posititions, resulting in a perpendicular orientation to each other. Due to this ordering, superstructure reflections are clearly observed by neutron diffraction on the deuterated homologue, whose appearance is concominant with the HS→LS transition. At low temperature the Fe(II) centers are in low-spin state and the pyrazines exhibit the perpendicular configuration, whereas, when the spin-transition temperature is reached, the Fe(II) centers switch to high-spin and the superstructure reflections disappear, indicating a disordered configuration. Although Fe(pz)[M(CN)$_4$] is one the most studied families of spin-crossover compounds, this ordered structure for the empty MOF was not reported previously. Instead, it was considered that the pyrazines were in a disordered configuration in both the low-spin and high-spin state. The energy and entropy balance between the two spin-states depend on the ordering of the pyrazines and, therefore, the order-disorder transition has direct implications in the spin-transition temperature

$$T_{1/2} = \frac{\Delta E_{ad} + \Delta E_{vib}}{\Delta S_{vib} + \Delta S_{rot} + \Delta S_{el}}. \tag{8.1}$$

The calculation of the vibrational terms and adiabatic energy difference in eq. 8.1 by DFT determines that if the configuration of the pyrazine rings in the LS state was disordered and not ordered the transition temperature would have been *ca.* 30 K higher, mostly due to the change in rotational entropy. The accurate identification of the structure is important for the understanding of the properties of these materials and also because reliable structural models are necessary for DFT calculations, for both total energy and phonon calculations.

The well-characterized structure at low-spin was used during the study of the adsorption mechanism of SO_2 via inelastic neutron scattering experiments and DFT calculations. Instruments IN1@ILL and PANTHER@ILL were used to measure the inelastic spectra in the energy transfer region [0:1500] cm^{-1} for the empty MOF and upon SO_2 adsorption. The interpretation of the spectra was assisted by the computed generalized phonon density of states, $G(\omega)$, and the experimental conditions were set up for adsorption of one SO_2 per f.u., for which DFT predicts a perpendicular pyrazine orientation. The main signature upon adsorption is the blue-shift of a peak located at *ca.* 100 cm^{-1}, which is well-reproduced by DFT in the spectral region from *ca.* 100 to 150 cm^{-1}. The main contributions of the modes involved in this signature come from librations of the pyrazine and out-of-plane movements of the cyanide ligands. We have attributed the blue-shift to the hindered rotation of the pyrazine and the out-of-plane movement of cyanide ligands.

The binding mechanism studied by molecular orbital and Bader charge analysis determined a weak backbonding from metal to ligand. However, the large binding energy predicted with DFT (PBE+D2) of 0.769 eV was found to arise from the molecular orbital interaction between the gas and the open-metal site. This was corroborated by computing the binding energy with only two $[Pt(CN)_4]$ planes. The result shows a decrease of the binding energy from 0.769 eV to 0.274 eV, demonstrating that the binding is dominated by electrostatic and dispersion interactions with the cavity of the MOF. It is, therefore, a physisorption mechanism and not a chemisorption as previously reported. The high-energy peaks in INS, which are associated with the internal vibrations of the pyrazine ligands, were negligibly affected in the presence of SO_2, consistent with the physisorption.

Because the nature of the adsorption mechanism directly influences the changes in the vibrational spectra, we expected that different gas molecules would yield different signatures. The CO and CO_2 adsorption mechanisms were then studied by neutron diffraction (D20@ILL), inelastic neutron scattering (IN1@ILL) and DFT calculations. The experimental conditions were set up to reach the saturation point for CO_2 (1.5 molecules per f.u.) and CO (2 molecules per f.u.). Neutron diffraction, assisted by DFT calculations, determined two bonding sites with disordered orientation for both CO and CO_2: on-top of the open-metal site Pt(II) (site A) and between the pyrazine rings (site B). The most stable configuration predicted by DFT is with the CO molecules in a perpendicular orientation with respect to the pyrazine ligands and parallel to the $Fe[Pt(CN)_4]_\infty$, for both site A and B. Whereas the CO_2 adopts a perpendicular orientation with respect to the pyrazine rings for site A and an almost parallel orientation for site B. For both sites, they are parallel to the $Fe[Pt(CN)_4]_\infty$. For the experimental loadings, results are consistent with a parallel orientation of the pyrazines for both CO and CO_2. The first observed signature in the inelastic spectra upon CO and CO_2 adsorption is the blue-shift of the peak around 100 cm^{-1}, resulting in a broader and less intense peak. The largest blue-shift was observed for CO (37 cm^{-1}) as compared to CO_2 (20 cm^{-1}) or SO_2 (29 cm^{-1}) (with 2, 1.5 and 1 adsorbed molecules per f.u., respectively). Additionally, a second signature was observed for CO consisting in the red-shift of a peak located at *ca.* 400 cm^{-1}. The analysis by means of the generalized phonon density of states concludes that the first signature is induced mainly by the hindered libration of the pyrazine ligands around the z axis and the out-of-plane movement of the CN ligands, similar to the case of SO_2, whereas the red-shift of the peak at *ca.* 400 cm^{-1} is caused by the steric effect and the nature of CO when the pyrazines display a torsion movement. A comparison of the shift with respect to the occupied volume upon adsorption determines that the vibrational modes at 107.9 and 403.6 cm^{-1} depend on the occupied volume and the nature of the gas, while the other modes undergo a shift only dependent on the occupied volume or a negligible change. The available experimental information allows us to conclude that if saturation points are reached, clear differences are observed for CO and CO_2, allowing a selective detection between those gases.

A significant decrease of the predicted binding energies from 0.277 (0.435) eV to 0.029 (0.002) eV for CO (CO_2) when PBE+D2 is replaced by PBE, respectively, indicates that the binding mechanism is dominated by dispersion interactions, consistent with a physisorption mechanism. A comparison of the binding energies between the whole MOF and a molecular fragment of two $Fe[Pt(CN)_4]$ planes, indicates that the main contributions are due to the interaction with the $Pt(CN)_4$. This is not the case for SO_2, where the binding is largely due to the interaction from the whole cavity.

Finally, the design of MOFs exhibiting a spin-crossover transition to efficiently adsorb and desorb the gas was studied. Firstly, we studied the change in the binding energy of CO_2, N_2, H_2 and CO upon spin modification in molecular fragments of square planar coordination $M(CN)_4$ with M = Fe(II), Fe(III) or Ni(II) which represent the site A of the Hofmann clathrate. We identify two different mechanisms responsible of this change upon spin-transition: (i) the change of the occupation of the antibonding orbital d_{z^2} responsible of the interaction with the gas molecule through the apical position of the open-metal site and (ii) the change in the occupation of the orbital $d_{x^2-y^2}$, which induces a change of the open-metal site charge. The latter is an order of magnitude less effective in modifying the binding energy than the former.

Based on these results, we decided to study the change in binding energy for the same set of gases in two Hofmann-clathrates, Fe(bpac)[M(CN)$_4$] and Fe(pz)[M(CN)$_4$] with M = Fe(II), Ni(II) and Mn(II), due to the mechanism (i). In all the cases, a significant change on binding energy was computed upon spin-transition. For M = Fe(II) and Mn(II) a decrease of the binding energy is observed when going from the LS to the HS state due to the increase of the occupation of the d_{z^2} orbital. Whereas for M = Ni(II), which already has a doubly occupied d_{z^2} in LS, an opposite trend is observed upon spin-transition to HS, where the d_{z^2} orbital is singly occupied. Apart from a large change in binding energy, in order to consider the adsorption-desorption as an effective process for technological applications, the change in the adiabatic energy ΔE_{HS-LS} must be computed and should be close to RT. In this way, the energy penalty to induce the spin-transition and, in principle, the desorption, is minimized. Typical values of ΔH_{HS-LS} between 0.2 and 0.5 eV have been reported for several Fe(II) compounds with spin-transitions near RT.

The best performances were found for the H_2 adsorption in Fe(bpac)[Mn(CN)$_4$] and Fe(bpac)[Fe(CN)$_4$]. ΔE_{HS-LS} values of 0.267 eV and 0.654 eV were predicted with a decrease in binding energy from 1.047 to 0.087 eV and from 1.007 to 0.097 eV from LS to HS for Fe(bpac)[Mn(CN)$_4$] and Fe(bpac)[Fe(CN)$_4$], respectively. For N_2 adsorption, a promising ΔE_{HS-LS} of 0.326 eV was computed for Fe(pz)[Fe(CN)$_4$] while for CO the strong interaction with the open-metal site overdestabilizes the d_{z^2} orbital resulting in a large ΔE_{HS-LS}. The ligand field of CO_2 is too weak to stabilize the LS state when M = Mn(II) and Fe(II), or the HS for M = Ni(II), therefore, the proposed mechanism is not feasible in these cases.

Finally, the feasability of the proposed strategy upon H_2 adsorption was studied in the already synthesised $Fe_2(tpt)_2(NCS)_4$ MOF, for which a value of ΔE_{HS-LS}=0.342 eV is predicted. A spin-transition from HS for the empty MOF to LS upon H_2 adsorption indicates a strong binding interaction while the adiabatic energy difference is compatible with a temperature-induced spin-transition near RT. Therefore, this compound is an excellent candidate for applications in hydrogen storage technologies.

This work is expected to assist future synthetic efforts to develop spin-crossover molecular based materials for efficient gas adsorption and desorption processes.

Chapter 9

Appendix

9.1 List of publications and engagement with the doctoral school

During my PhD thesis at SIMaP laboratory of Université Grenoble Alpes (UGA) and the Institut Laue Langevin (ILL) I published the following articles:

1. Ángel Fernández-Blanco, Lucía Piñeiro-López, Mónica Jiménez-Ruiz, Stephane Rols, José Antonio Real, J. Alberto Rodríguez-Velamazán and Roberta Poloni, "Probing the SO_2 Adsorption Mechanism in Hofmann Clathrates via Inelastic Neutron Scattering and Density Functional Theory calculations", *The Journal of Physical Chemistry C*, vol. 126, p. 8090-8099, 2022.

2. Ángel Fernández-Blanco, Lorenzo A. Mariano, Lucía Piñeiro-López, José Antonio Real, Jose Sanchez Costa, Roberta Poloni, J. Alberto Rodríguez-Velamazán, "Hidden ordered structure in the archetypical $Fe(pyrazine)[Pt(CN)_4]$ spin-crossover porous coordination compound", *CrystEngComm*, vol. 24, p. 6349-6356, 2022.

3. Ángel Fernández-Blanco, Lucía Piñeiro-López, Mónica Jiménez-Ruiz, José Antonio Real, Jose Sanchez Costa, J. Alberto Rodríguez-Velamazán and Roberta Poloni, "CO and CO_2 Adsorption Mechanism in $Fe(pz)[Pt(CN)_4]$ Probed by Neutron Scattering and Density-Functional Theory Calculations". In preparation.

4. Lorenzo A. Mariano, Ángel Fernández-Blanco and Roberta Poloni, " A Hubbard *U*-Density Correcteed Scheme to Study Spin Crossover-Assisted Gas Release in Hofmann-like clathrates". In preparation

5. J. Alberto Rodríguez-Velamazán, Kosuke Kitase, Elías Palacios, Miguel Castro,

> Ángel Fernández-Blanco, Ramón Burriel and Takafumi Kitazawa, "Structural Insights into the Two-Step Spin-Crossover Compound Fe(3,4-dimethyl-pyridine)$_2$[Ag(CN)$_2$]$_2$, *Crystals*, vol. 9, 2019.

The work published in papers 1 and 2 correspond to the chapters 4 and 5 of this thesis. Paper 3 corresponds to chapter 6, it has not yet been published and it will be submitted shortly. For these three papers (1,2 and 3) I gave the major contribution under the supervision of Roberta Poloni and J. Alberto Rodríguez-Velamazán, who also participated actively in the production of the scientific data. In paper 4 I have contributed with the calculations of the periodic MOF and the analysis of the data.

In paper 5, I participated with minor contributions. I engage to respect all the rules of I-MEP2 Ecole Doctorale for what concerns the "Thése sur articles" way of presenting the Ph.D. thesis manuscript.

Bibliography

[1] G. T. Rochelle, “Amine scrubbing for CO_2 capture,” *Science*, vol. 325, no. 5948, pp. 1652–1654, 2009.

[2] C. R. Usher, A. E. Michel, and V. H. Grassian, “Reactions on mineral dust,” *Chem. Rev.*, vol. 103, no. 12, pp. 4883–4940, 2003. PMID: 14664636.

[3] P. L. Ward, “Sulfur dioxide initiates global climate change in four ways,” *Thin Solid Films*, vol. 517, no. 11, pp. 3188–3203, 2009.

[4] F. Feyzbar-Khalkhali-Nejad, E. Hassani, A. Rashti, and T.-S. Oh, “Adsorption-based CO removal: Principles and materials,” *J. Environ. Chem. Eng.*, vol. 9, no. 4, p. 105317, 2021.

[5] “Sustainable development goals of united nations.” https://sdgs.un.org/goals. Accessed: 2023-16-02.

[6] A. Raza, R. Gholami, R. Rezaee, V. Rasouli, and M. Rabiei, “Significant aspects of carbon capture and storage a review,” *Petroleum*, vol. 5, no. 4, pp. 335–340, 2019.

[7] “Mof4Air project.” https://www.mof4air.eu. Accessed: 2023-16-02.

[8] Ü. Kökam-Demir, A. Goldman, L. Esrafili, M. Gharib, A. Morsali, O. Weingart, and C. Janiak, “Coordinatively unsaturated metal sites (open metal sites) in metalorganic frameworks: design and applications,” *Chem. Soc. Rev.*, vol. 49, pp. 2751–2798, 2020.

[9] X. Zou and G. Zhu, *CO_2 Capture with MOF Membranes*, ch. 10, pp. 323–359. John Wiley - Sons, Ltd, 2019.

[10] A. Evans, R. Luebke, and C. Petit, “The use of metal–organic frameworks for CO purification,” *J. Mater. Chem. A*, vol. 6, pp. 10570–10594, 2018.

[11] Z. Arcís-Castillo, F. J. Muñoz-Lara, M. C. Muñoz, D. Aravena, A. B. Gaspar, J. F. Sánchez-Royo, E. Ruiz, M. Ohba, R. Matsuda, S. Kitagawa, and J. A. Real, "Reversible chemisorption of sulfur dioxide in a spin crossover porous coordination polymer," *Inorg. Chem.*, vol. 52, no. 21, pp. 12777–12783, 2013. PMID: 24124923.

[12] D. Alvarado-Alvarado, J. H. González-Estefan, J. G. Flores, J. R. Álvarez, J. Aguilar-Pliego, A. Islas-Jácome, G. Chastanet, E. González-Zamora, H. A. Lara-García, B. Alcántar-Vzquez, M. Gonidec, and I. A. Ibarra, "Water adsorption properties of Fe(pz)[Pt(CN)$_4$] and the capture of CO$_2$ and CO," *Organometallics*, vol. 39, no. 7, pp. 949–955, 2020.

[13] H. Li, M. Eddaoudi, M. O'Keeffe, and O. M. Yaghi, "Design and synthesis of an exceptionally stable and highly porous metal-organic framework," *Nature*, vol. 402, pp. 276–279, Nov. 1999.

[14] B. Li, H.-T. Fan, S.-Q. Zang, H.-Y. Li, and L.-Y. Wang, "Metal-containing crystalline luminescent thermochromic materials," *Coord. Chem. Rev.*, vol. 377, pp. 307–329, 2018.

[15] M. Pan, W.-M. Liao, S.-Y. Yin, S.-S. Sun, and C.-Y. Su, "Single-phase white-light-emitting and photoluminescent color-tuning coordination assemblies," *Chem. Rev.*, vol. 118, no. 18, pp. 8889–8935, 2018. PMID: 30130099.

[16] A. Gamonal, C. Sun, A. L. Mariano, E. Fernandez-Bartolome, E. Guerrero-SanVicente, B. Vlaisavljevich, J. Castells-Gil, C. Marti-Gastaldo, R. Poloni, R. Wannemacher, J. Cabanillas-Gonzalez, and J. S. Costa, "Divergent adsorption-dependent luminescence of amino-functionalized lanthanide metal–organic frameworks for highly sensitive NO$_2$ sensors," *J. Phys. Chem. Lett.*, vol. 11, pp. 3362–3368, Mar. 2020.

[17] G. Mnguez Espallargas and E. Coronado, "Magnetic functionalities in MOFs: from the framework to the pore," *Chem. Soc. Rev.*, vol. 47, pp. 533–557, 2018.

[18] A. E. Thorarinsdottir and T. D. Harris, "Metalorganic framework magnets," *Chemical Reviews*, vol. 120, no. 16, pp. 8716–8789, 2020. PMID: 32045215.

[19] X. Xiao, L. Zou, H. Pang, and Q. Xu, "Synthesis of micro/nanoscaled metal–organic frameworks and their direct electrochemical applications," *Chem. Soc. Rev.*, vol. 49, pp. 301–331, 2020.

[20] A. A. Talin, A. Centrone, A. C. Ford, M. E. Foster, V. Stavila, P. Haney, R. A. Kinney, V. Szalai, F. E. Gabaly, H. P. Yoon, F. Léonard, and M. D. Allendorf, "Tunable electrical conductivity in metal-organic framework thin-film devices," *Science*, vol. 343, no. 6166, pp. 66–69, 2014.

[21] A. Pathak, J.-W. Shen, M. Usman, L.-F. Wei, S. Mendiratta, Y.-S. Chang, B. Sainbileg, C.-M. Ngue, R.-S. Chen, M. Hayashi, T.-T. Luo, F.-R. Chen, K.-H. Chen, T.-W. Tseng, L.-C. Chen, and K.-L. Lu, "Integration of a $(–\mathrm{Cu}–\mathrm{S}–)_n$ plane in a metalorganic framework affords high electrical conductivity," *Nat. Commun.*, vol. 10, p. 1721, 2019.

[22] W. Zhang and R.-G. Xiong, "Ferroelectric metal–organic frameworks," *Chem. Rev.*, vol. 112, no. 2, pp. 1163–1195, 2012. PMID: 21939288.

[23] J. Lee, O. K. Farha, J. Roberts, K. A. Scheidt, S. T. Nguyen, and J. T. Hupp, "Metal–organic framework materials as catalysts," *Chem. Soc. Rev.*, vol. 38, no. 5, p. 1450, 2009.

[24] Y.-B. Huang, J. Liang, X.-S. Wang, and R. Cao, "Multifunctional metal–organic framework catalysts: synergistic catalysis and tandem reactions," *Chem. Soc. Rev.*, vol. 46, no. 1, pp. 126–157, 2017.

[25] A. Herbst and C. Janiak, "MOF catalysts in biomass upgrading towards value-added fine chemicals," *CrystEngComm*, vol. 19, no. 29, pp. 4092–4117, 2017.

[26] M. Bagheri, M. Y. Masoomi, and A. Morsali, "A $\mathrm{MoO_3}$–metal–organic framework composite as a simultaneous photocatalyst and catalyst in the PODS process of light oil," *ACS Catalysis*, vol. 7, pp. 6949–6956, Sept. 2017.

[27] P. Horcajada, R. Gref, T. Baati, P. K. Allan, G. Maurin, P. Couvreur, G. Frey, R. E. Morris, and C. Serre, "Metal–organic frameworks in biomedicine," *Chem. Rev.*, vol. 112, no. 2, pp. 1232–1268, 2012. PMID: 22168547.

[28] M. Ding, R. W. Flaig, H.-L. Jiang, and O. M. Yaghi, "Carbon capture and conversion using metal–organic frameworks and mof-based materials," *Chem. Soc. Rev.*, vol. 48, pp. 2783–2828, 2019.

[29] C.-T. Yang, A. R. Kshirsagar, A. C. Eddin, L.-C. Lin, and R. Poloni, "Tuning gas adsorption by metal node blocking in photoresponsive metal-organic frameworks," *Chem. Eur. J.*, vol. 24, no. 57, pp. 15167–15172, 2018.

[30] H. Li, K. Wang, Y. Sun, C. T. Lollar, J. Li, and H.-C. Zhou, “Recent advances in gas storage and separation using metal–organic frameworks,” *Mater.*, vol. 21, pp. 108–121, Mar. 2018.

[31] J.-R. Li, R. J. Kuppler, and H.-C. Zhou, “Selective gas adsorption and separation in metal–organic frameworks,” *Chem. Soc. Rev.*, vol. 38, no. 5, p. 1477, 2009.

[32] L. He, Y. Liu, J. Liu, Y. Xiong, J. Zheng, Y. Liu, and Z. Tang, “Core-shell noble-metal@metal-organic-framework nanoparticles with highly selective sensing property,” *Angew. Chem. Int. Ed.*, vol. 52, pp. 3741–3745, Feb. 2013.

[33] H.-Y. Li, S.-N. Zhao, S.-Q. Zang, and J. Li, “Functional metal–organic frameworks as effective sensors of gases and volatile compounds,” *Chem. Soc. Rev.*, vol. 49, pp. 6364–6401, 2020.

[34] B. Li, H.-M. Wen, W. Zhou, J. Xu, and B. Chen, “Porous metal-organic frameworks: Promising materials for methane storage,” *Chem.*, vol. 1, no. 4, pp. 557–580, 2016.

[35] H. Furukawa, K. E. Cordova, M. OKeeffe, and O. M. Yaghi, “The chemistry and applications of metal-organic frameworks,” *Science*, vol. 341, no. 6149, p. 1230444, 2013.

[36] P. Z. Moghadam, A. Li, S. B. Wiggin, A. Tao, A. G. P. Maloney, P. A. Wood, S. C. Ward, and D. Fairen-Jimenez, “Development of a cambridge structural database subset: A collection of metal–organic frameworks for past, present, and future,” *Chem. Mater.*, vol. 29, pp. 2618–2625, Mar. 2017.

[37] M. A. Al-Ghouti and D. A. Da’ana, “Guidelines for the use and interpretation of adsorption isotherm models: A review,” *J. Hazard. Mater.*, vol. 393, p. 122383, 2020.

[38] J. A. Mason, M. Veenstra, and J. R. Long, “Evaluating metal–organic frameworks for natural gas storage,” *Chem. Sci.*, vol. 5, pp. 32–51, 2014.

[39] N. K. Gupta, K. Vikrant, K. S. Kim, K.-H. Kim, and D. A. Giannakoudakis, “Regeneration strategies for metal–organic frameworks post acidic gas capture,” *Coord. Chem. Rev.*, vol. 467, p. 214629, 2022.

[40] D. A. Reed, B. K. Keitz, J. Oktawiec, J. A. Mason, T. Runevski, D. J. Xiao, L. E. Darago, V. Crocell, S. Bordiga, and J. R. Long, “A spin transition mechanism for cooperative adsorption in metal–organic frameworks,” *Nature*, vol. 550, pp. 96–100, 2017.

[41] A. S. Bhown and B. C. Freeman, “Analysis and status of post-combustion carbon dioxide capture technologies,” *Environ. Sci. Technol.*, vol. 45, no. 20, pp. 8624–8632, 2011. PMID: 21905745.

[42] Z. Hu, Y. Wang, B. B. Shah, and D. Zhao, “CO_2 capture in metal–organic framework adsorbents: An engineering perspective,” *Adv. Sustain. Syst.*, vol. 3, no. 1, p. 1800080, 2019.

[43] C. A. Trickett, A. Helal, B. A. Al-Maythalony, Z. H. Yamani, K. E. Cordova, and O. M. Yaghi, “The chemistry of metal–organic frameworks for CO_2 capture, regeneration and conversion,” *Nat. Rev. Mater.*, vol. 2, no. 8, p. 17045, 2017.

[44] X. Zhang, Z. Chen, X. Liu, S. L. Hanna, X. Wang, R. Taheri-Ledari, A. Maleki, P. Li, and O. K. Farha, “A historical overview of the activation and porosity of metal–organic frameworks,” *Chem. Soc. Rev.*, vol. 49, pp. 7406–7427, 2020.

[45] Y. Jean, *Molecular Orbitals of Transition Metal Complexes.* OUP Oxford, 2005.

[46] W. Haynes, *CRC Handbook of Chemistry and Physics, 96th Edition.* 100 Key Points, CRC Press, 2015.

[47] C. Graham, D. A. Imrie, and R. E. Raab, “Measurement of the electric quadrupole moments of CO_2, CO, N_2, Cl_2 and BF_3,” *Mol. Phys.*, vol. 93, no. 1, pp. 49–56, 1998.

[48] H. Kim, M. Sohail, K. Yim, Y. C. Park, D. H. Chun, H. J. Kim, S. O. Han, and J.-H. Moon, “Effective CO_2 and CO separation using [M_2(DOBDC)] (M = Mg, Co, Ni) with unsaturated metal sites and excavation of their adsorption sites,” *ACS Appl. Mater. Interfaces*, vol. 11, no. 7, pp. 7014–7021, 2019.

[49] R. Poloni, K. Lee, R. F. Berger, B. Smit, and J. B. Neaton, “Understanding trends in CO_2 adsorption in metal–organic frameworks with open-metal sites,” *J. Phys. Chem. Lett.*, vol. 5, no. 5, pp. 861–865, 2014. PMID: 26274079.

[50] J. Li and A. Y. Rogachev, “SO_2 – yet another two-faced ligand,” *Phys. Chem. Chem. Phys.*, vol. 17, pp. 1987–2000, 2015.

[51] G. L. Miessler, P. J. Fischer, and D. A. Tarr, *Inorganic Chemistry, 5th Ed.* Pearson, 2014.

[52] J. Mascetti, F. Galan, and I. Ppai, “Carbon dioxide interaction with metal atoms: matrix isolation spectroscopic study and DFT calculations,” *Coord. Chem. Rev.*, vol. 190-192, pp. 557–576, 1999.

[53] R. Poloni, B. Smit, and J. B. Neaton, "Ligand-assisted enhancement of CO_2 capture in metal–organic frameworks," *J. Am. Chem. Soc.*, vol. 134, no. 15, pp. 6714–6719, 2012. PMID: 22463719.

[54] A. Hauser, "Ligand field theoretical considerations," in *Spin Crossover in Transition Metal Compounds I*, pp. 49–58, Springer, 2004.

[55] F. A. Cotton and G. Wilkinson, *Advanced Inorganic Chemistry: A comprehensive text, 4th Ed.* Interscience, 1980.

[56] P. Gütlich, A. B. Gaspar, and Y. Garcia, "Spin sate switching in iron coordination compounds," *Beilstein J. Org. Chem.*, vol. 9, pp. 342–391, 2013.

[57] S. Brooker, "Spin crossover with thermal hysteresis: practicalities and lessons learnt," *Chem. Soc. Rev.*, vol. 44, pp. 2880–2892, 2015.

[58] V. Ksenofontov, G. Levchenko, H. Spiering, P. Gtlich, J.-F. Ltard, Y. Bouhedja, and O. Kahn, "Spin crossover behavior under pressure of $Fe(PM\text{-}L)_2(NCS)_2$ compounds with substituted 2′-pyridylmethylene 4-anilino ligands," *Chem. Phys. Lett.*, vol. 294, no. 6, pp. 545–553, 1998.

[59] S. Cobo, D. Ostrovskii, S. Bonhommeau, L. Vendier, G. Molnár, L. Salmon, K. Tanaka, and A. Bousseksou, "Single-laser-shot-induced complete bidirectional spin transition at room temperature in single crystals of $(FeII(pyrazine)(Pt(CN)_4))$," *J. Am. Chem. Soc.*, vol. 130, no. 28, pp. 9019–9024, 2008. PMID: 18570417.

[60] S. Bonhommeau, G. Molnár, M. Goiran, K. Boukheddaden, and A. Bousseksou, "Unified dynamical description of pulsed magnetic field and pressure effects on the spin crossover phenomenon," *Phys. Rev. B*, vol. 74, p. 064424, Aug 2006.

[61] W. Nicolazzi and A. Bousseksou, "Thermodynamical aspects of the spin crossover phenomenon," *C. R. Chimie*, vol. 21, no. 12, pp. 1060–1074, 2018. Spin crossover phenomenon / Phnomne de transition de spin.

[62] D. A. McQuarie and J. D. Simon, *Molecular Thermodynamics.* University Science Books, 1999.

[63] H. Ando, Y. Nakao, H. Sato, M. Ohba, S. Kitagawa, and S. Sakaki, "Theoretical study on high-spin to low-spin transition of $Fe(pyrazine)[Pt(CN)_4]$: Guest-induced entropy decrease," *Chem. Phys. Lett.*, vol. 511, no. 4, pp. 399–404, 2011.

[64] G. G. Balint-Kurti, C. L. Ward, and C. Clay Marston, “Two computer programs for solving the schrödinger equation for bound-state eigenvalues and eigenfunctions using the fourier grid hamiltonian method,” *Comput. Phys. Commun.*, vol. 67, no. 2, pp. 285–292, 1991.

[65] G. Ganzenmüller, N. Berkaïne, A. Fouqueau, M. E. Casida, and M. Reiher, “Comparison of density functionals for differences between the high- ($^5T_{2g}$) and low- ($^1A_{1g}$) spin states of iron(ii) compounds. iv. results for the ferrous complexes [Fe(L)($'$NHS4$'$)],” *J. Chem. Phys.*, vol. 122, no. 23, p. 234321, 2005.

[66] M. Radoń, “Benchmarking quantum chemistry methods for spin-state energetics of iron complexes against quantitative experimental data,” *Phys. Chem. Chem. Phys.*, vol. 21, pp. 4854–4870, 2019.

[67] L. A. Mariano, B. Vlaisavljevich, and R. Poloni, “Biased spin-state energetics of Fe(II) molecular complexes within density-functional theory and the linear-response Hubbard U correction,” *J. Chem. Theory Comput.*, vol. 16, no. 11, pp. 6755–6762, 2020. PMID: 33108722.

[68] R. M. Dreizle and E. K. Gross, *Density Functional Theory: An approach to the quantum many-body problem.* Springer Berlin, Heidelberg, 1990.

[69] O. Salomon, M. Reiher, and B. A. Hess, “Assertion and validation of the performance of the B3LYP* functional for the first transition metal row and the G2 test set,” *J. Chem. Phys.*, vol. 117, no. 10, pp. 4729–4737, 2002.

[70] M. Cococcioni and S. de Gironcoli, “Linear response approach to the calculation of the effective interaction parameters in the LDA + U method,” *Phys. Rev. B*, vol. 71, p. 035105, Jan 2005.

[71] V. Niel, J. M. Martinez-Agudo, M. C. Muñoz, A. Gaspar, and J. Real, “Cooperative spin crossover behavior in cyanide-bridged Fe(II)-M(II) bimetallic 3d hofmann-like networks (M= Ni, Pd and Pt),” *Inorg. Chem.*, vol. 40, pp. 3838–3839, 2001.

[72] T. Kitazawa, Y. Gomi, M. Takahashi, M. Takeda, M. Enomoto, A. Miyazaki, and T. Enoki, “Spin-crossover behaviour of the coordination polymer $Fe^{II}(C_5H_5N)_2Ni^{II}(CN)_4$,” *J. Mater. Chem.*, vol. 6, pp. 119–121, 1996.

[73] R. Baur and G. Schwarzenbach, “Neue einschlussverbindungen vom typus des nickelcyanid-ammoniak-benzols,” *Helv. Chim. Acta*, vol. 43, no. 3, pp. 842–847, 1960.

[74] T. Iwamoto, T. Nakano, M. Morita, T. Miyoshi, T. Miyamoto, and Y. Sasaki, "The hofman-type clathrate: $M(NH_3)_2M'(CN)_4.2G$," *Inorganica Chim.*, vol. 2, pp. 313–316, 1968.

[75] K. A. Hofmann and F. Küspert, "Verbindungen von kohlenwasserstoffen mit metallsalzen," *Z. Anorg. Chem.*, vol. 15, no. 1, pp. 204–207, 1897.

[76] H. Powell and J. Rayner, "Clathrate compound formed by benzene with an ammonianickel cyanide complex," *Nature*, vol. 163, pp. 566–567, 1949.

[77] J. H. Rayner and H. M. Powell, "67. structure of molecular compounds. Part X. Crystal structure of the compound of benzene with an ammonia–nickel cyanide complex," *J. Chem. Soc.*, pp. 319–328, 1952.

[78] C. Bartual-Murgui, N. A. Ortega-Villar, H. J. Shepherd, M. C. Muñoz, L. Salmon, G. Molnár, A. Bousseksou, and J. A. Real, "Enhanced porosity in a new 3D Hofmann-like network exhibiting humidity sensitive cooperative spin transitions at room temperature," *J. Mater. Chem.*, vol. 21, pp. 7217–7222, 2011.

[79] C. Bartual-Murgui, L. Salmon, A. Akou, N. A. Ortega-Villar, H. J. Shepherd, M. C. Muãoz, G. Molnár, J. A. Real, and A. Bousseksou, "Synergetic effect of host–guest chemistry and spin crossover in 3D Hofmann-like metal–organic frameworks $[Fe(bpac)M(CN)_4]$ (M=Pt, Pd, Ni)," *Chem. Eur. J.*, vol. 18, no. 2, pp. 507–516, 2012.

[80] Z.-P. Ni, J.-L. Liu, M. N. Hoque, W. Liu, J.-Y. Li, Y.-C. Chen, and M.-L. Tong, "Recent advances in guest effects on spin-crossover behavior in Hofmann-type metal-organic frameworks," *Coord. Chem. Rev.*, vol. 335, pp. 28–43, 2017.

[81] M. Ohba, K. Yoneda, G. Agustí, M. Muñoz, A. Gaspar, J. Real, M. Yamasaki, H. Ando, Y. Nakao, S. Sakaki, and S. Kitagawa, "Bidirectional chemo-switching of spin state in a microporous framework," *Angew. Chem. Int. Ed.*, vol. 48, no. 26, pp. 4767–4771, 2009.

[82] D. Aravena, Z. A. Castillo, M. C. Muñoz, A. B. Gaspar, K. Yoneda, R. Ohtani, A. Mishima, S. Kitagawa, M. Ohba, J. A. Real, and E. Ruiz, "Guest modulation of spin-crossover transition temperature in a porous iron(II) metal–organic framework: Experimental and periodic DFT studies," *Eur. J. Chem.*, vol. 20, no. 40, pp. 12864–12873, 2014.

[83] P. D. Southon, L. Liu, E. A. Fellows, D. J. Price, G. J. Halder, K. W. Chapman, B. Moubaraki, K. S. Murray, J.-F. Létard, and C. J. Kepert, "Dynamic interplay between spin-crossover and host-guest function in a nanoporous metal-organic framework material," *J. Am. Chem. Soc.*, vol. 131, no. 31, pp. 10998–11009, 2009.

[84] T. Delgado, A. Tissot, C. Besnard, L. Guénée, P. Pattison, and A. Hauser, "Structural investigation of the high spin→low spin relaxation dynamics of the porous coordination network $[Fe(pz)Pt(CN)_4]\cdot 2.6H_2O$," *Chem. Eur. J.*, vol. 21, no. 9, pp. 3664–3670, 2015.

[85] X. Bao, H. J. Shepherd, L. Salmon, G. Molnár, M.-L. Tong, and A. Bousseksou, "The effect of an active guest on the spin crossover phenomenon," *Angew, Chem. Int. Ed.*, vol. 52, no. 4, pp. 1198–1202, 2013.

[86] F. J. Muñoz Lara, A. B. Gaspar, D. Aravena, E. Ruiz, M. C. Muñoz, M. Ohba, R. Ohtani, S. Kitagawa, and J. A. Real, "Enhanced bistability by guest inclusion in Fe(II) spin crossover porous coordination polymers," *Chem. Commun.*, vol. 48, pp. 4686–4688, 2012.

[87] P. Mitchell, S. Parler, A. Ramirez-Cuesta, and J. Tomkinson, *Series on Neutron Techniques and Applications. Vibrational spectroscopy with neutrons with applications in chemistry, biology, materials science and catalysis.* World scientific, 2005.

[88] G. Squires, *Introduction to the Theory of Thermal Neutron Scattering.* Dover books on physics, Dover Publications, 1996.

[89] F. Hippert, E. Geissler, J. Hodeau, E. Lelievre-Berna, and J. Regnard, *Neutron and X-ray spectroscopy.* Springer, 2006.

[90] S. Lovesey, *Theory of neutron scattering from condensed matter.* Oxford, 1984.

[91] "D20 characteristics." https://www.ill.eu/users/instruments/instruments-list/d20/description/instrument-layout. Accessed: 2022-10-09.

[92] "IN1 characteristics." https://www.ill.eu/users/instruments/instruments-list/in1-taslagrange/description/instrument-layout. Accessed: 2022-10-09.

[93] A. Ivanov, M. Jimenéz-Ruiz, and J. Kulda, "IN1-LAGRANGE – the new ILL instrument to explore vibration dynamics of complex materials," *Journal of Physics: Conference Series*, vol. 554, p. 012001, nov 2014.

[94] S. F. Parker, D. Lennon, and P. W. Albers, "Vibrational spectroscopy with neutrons: A review of new directions," *Appl. Spectrosc.*, vol. 65, no. 12, pp. 1325–1341, 2011.

[95] "PANTHER characteristics." https://www.ill.eu/users/instruments/instruments-list/panther/description/instrument-layout. Accessed: 2022-10-09.

[96] "IN5 characteristics." https://www.ill.eu/users/instruments/instruments-list/in5/description/instrument-layout. Accessed: 2022-10-09.

[97] "TOSCA characteristics." https://www.isis.stfc.ac.uk/Pages/tosca.aspx. Accessed: 2022-10-09.

[98] M. Born and R. Oppenheimer, "Zur quantentheorie der molekeln," *Ann. Phys.*, vol. 389, no. 20, pp. 457–484, 1927.

[99] P. Hohenberg and W. Kohn, "Inhomogeneous electron gas," *Phys. Rev.*, vol. 136, pp. B864–B871, Nov 1964.

[100] W. Kohn and L. J. Sham, "Self-consistent equations including exchange and correlation effects," *Phys. Rev.*, vol. 140, pp. A1133–A1138, Nov 1965.

[101] D. R. Hartree and W. Hartree, "Self-consistent field, with exchange, for beryllium," *Proceedings of the Royal Society of London. Series A - Mathematical and Physical Sciences*, vol. 150, no. 869, pp. 9–33, 1935.

[102] P. A. Dirac, "Note on exchange phenomena in the Thomas atom," in *Mathematical Proceedings of the Cambridge Philosophical Society*, vol. 26, pp. 376–385, Cambridge University Press, 1930.

[103] D. M. Ceperley and B. J. Alder, "Ground state of the electron gas by a stochastic method," *Phys. Rev. Lett.*, vol. 45, pp. 566–569, Aug. 1980.

[104] J. P. Perdew, J. A. Chevary, S. H. Vosko, K. A. Jackson, M. R. Pederson, D. J. Singh, and C. Fiolhais, "Atoms, molecules, solids, and surfaces: Applications of the generalized gradient approximation for exchange and correlation," *Phys. Rev. B*, vol. 46, pp. 6671–6687, Sept. 1992.

[105] J. P. Perdew, K. Burke, and M. Ernzerhof, "Generalized gradient approximation made simple," *Phys. Rev. Lett.*, vol. 77, pp. 3865–3868, Oct. 1996.

[106] J. P. Perdew, A. Ruzsinszky, G. I. Csonka, O. A. Vydrov, G. E. Scuseria, L. A. Constantin, X. Zhou, and K. Burke, "Restoring the density-gradient expansion for exchange in solids and surfaces," *Phys. Rev. Lett.*, vol. 100, p. 136406, Apr 2008.

[107] I. Hamada, "van der waals density functional made accurate," *Phys. Rev. B*, vol. 89, p. 121103, Mar 2014.

[108] J. Tao, J. P. Perdew, V. N. Staroverov, and G. E. Scuseria, "Climbing the density functional ladder: Nonempirical meta–generalized gradient approximation designed for molecules and solids," *Phys. Rev. Lett.*, vol. 91, Sept. 2003.

[109] Y. Zhao and D. G. Truhlar, "A new local density functional for main-group thermochemistry, transition metal bonding, thermochemical kinetics, and noncovalent interactions," *J. Chem. Phys.*, vol. 125, p. 194101, Nov. 2006.

[110] C. Lee, W. Yang, and R. G. Parr, "Development of the colle-salvetti correlation-energy formula into a functional of the electron density," *Phys. Rev. B*, vol. 37, pp. 785–789, Jan. 1988.

[111] R. H. Hertwig and W. Koch, "On the parameterization of the local correlation functional. what is Becke-3-LYP?," *Chem. Phys. Lett.*, vol. 268, pp. 345–351, Apr. 1997.

[112] S. Baroni, S. de Gironcoli, A. Dal Corso, and P. Giannozzi, "Phonons and related crystal properties from density-functional perturbation theory," *Rev. Mod. Phys.*, vol. 73, pp. 515–562, Jul 2001.

[113] X. Gonze and C. Lee, "Dynamical matrices, born effective charges, dielectric permittivity tensors, and interatomic force constants from density-functional perturbation theory," *Phys. Rev. B*, vol. 55, pp. 10355–10368, Apr 1997.

[114] W. Qian and C. Zhang, "Review of the phonon calculations for energetic crystals and their applications," *Energetic Materials Frontiers*, vol. 2, no. 2, pp. 154–164, 2021.

[115] J. M. Soler, E. Artacho, J. D. Gale, A. García, J. Junquera, P. Ordejón, and D. Sánchez-Portal, "The SIESTA method for ab initio order-n materials simulation," *J. Phys. Condens.*, vol. 14, pp. 2745–2779, mar 2002.

[116] A. García, N. Papior, A. Akhtar, E. Artacho, V. Blum, E. Bosoni, P. Brandimarte, M. Brandbyge, J. I. Cerdá, F. Corsetti, R. Cuadrado, V. Dikan, J. Ferrer, J. Gale, P. García-Fernández, V. M. García-Suárez, S. García, G. Huhs, S. Illera, R. Korytár, P. Koval, I. Lebedeva, L. Lin, P. López-Tarifa, S. G. Mayo, S. Mohr, P. Ordejón, A. Postnikov, Y. Pouillon, M. Pruneda, R. Robles, D. Sánchez-Portal, J. M. Soler,

R. Ullah, V. W.-z. Yu, and J. Junquera, “Siesta: Recent developments and applications,” *J. Chem. Phys.*, vol. 152, no. 20, p. 204108, 2020.

[117] P. Giannozzi, O. Andreussi, T. Brumme, O. Bunau, M. B. Nardelli, M. Calandra, R. Car, C. Cavazzoni, D. Ceresoli, M. Cococcioni, N. Colonna, I. Carnimeo, A. D. Corso, S. de Gironcoli, P. Delugas, R. A. DiStasio, A. Ferretti, A. Floris, G. Fratesi, G. Fugallo, R. Gebauer, U. Gerstmann, F. Giustino, T. Gorni, J. Jia, M. Kawamura, H.-Y. Ko, A. Kokalj, E. Kçkbenli, M. Lazzeri, M. Marsili, N. Marzari, F. Mauri, N. L. Nguyen, H.-V. Nguyen, A. O. de-la Roza, L. Paulatto, S. Poncé, D. Rocca, R. Sabatini, B. Santra, M. Schlipf, A. P. Seitsonen, A. Smogunov, I. Timrov, T. Thonhauser, P. Umari, N. Vast, X. Wu, and S. Baroni, “Advanced capabilities for materials modelling with quantum ESPRESSO,” *J. Phys. Condens. Matter*, vol. 29, p. 465901, oct 2017.

[118] P. Giannozzi, O. Baseggio, P. Bonfá, D. Brunato, R. Car, I. Carnimeo, C. Carvazzoni, S. de Gironcoli, P. Delugas, F. F. Ruffino, A. Ferreti, N. Mazari, I. Timrov, A. Urru, and S. Baroni, “Quantum espresso toward the exascale,” *J. Chem. Phys.*, vol. 152, pp. 154105–1 – 154105–11, 2020.

[119] P. Giannozzi, S. Baroni, N. Bonini, M. Calandra, R. Car, C. Cavazzoni, D. Ceresoli, G. L. Chiarotti, M. Cococcioni, I. Dabo, A. D. Corso, S. de Gironcoli, S. Fabris, G. Fratesi, R. Gebauer, U. Gerstmann, C. Gougoussis, A. Kokalj, M. Lazzeri, L. Martin-Samos, N. Marzari, F. Mauri, R. Mazzarello, S. Paolini, A. Pasquarello, L. Paulatto, C. Sbraccia, S. Scandolo, G. Sclauzero, A. P. Seitsonen, A. Smogunov, P. Umari, and R. M. Wentzcovitch, “QUANTUM ESPRESSO: a modular and open-source software project for quantum simulations of materials,” *J. Phys. Condens. Matter*, vol. 21, p. 395502, sep 2009.

[120] P. Gütlich and H. A. Goodwin, *Spin-Crossover in Transition Metal Compounds, Vols. I-III, in Topics in Current Chemistry.* Berlin: Springer, 2004.

[121] J. A. Real, E. Andrés, M. C. Muñoz, M. Julve, T. Granier, A. Bousseksou, and F. Varret, “Spin crossover in a catenane supramolecular system,” *Science*, vol. 268, no. 5208, pp. 265–267, 1995.

[122] G. J. Halder, C. J. Kepert, B. Moubaraki, K. S. Murray, and J. D. Cashion, “Guest-dependent spin crossover in a nanoporous molecular framework material,” *Science*, vol. 298, no. 5599, pp. 1762–1765, 2002.

[123] R. Ohtani and S. Hayami, “Guest-dependent spin-transition behavior of porous coordination polymers,” *Chem. Eur. J.*, vol. 23, no. 10, pp. 2236–2248, 2017.

[124] E. Resines-Urien, E. Burzurí, E. Fernandez-Bartolome, M. Á. García García-Tuñón, P. de la Presa, R. Poloni, S. J. Teat, and J. S. Costa, “A switchable iron-based coordination polymer toward reversible acetonitrile electro-optical readout,” *Chem. Sci.*, vol. 10, pp. 6612–6616, 2019.

[125] A. Develioglu, E. Resines-Urien, R. Poloni, L. Martín-Pérez, J. S. Costa, and E. Burzurí, “Tunable proton conductivity and color in a nonporous coordination polymer via lattice accommodation to small molecules,” *Adv. Sci.*, vol. 8, no. 22, p. 2102619, 2021.

[126] T. Tayagaki, A. Galet, G. Molnár, M. C. Muñoz, A. Zwick, K. Tanaka, J. A. Real, and A. Bousseksou, “Metal dilution effects on the spin-crossover properties of the three-dimensional coordination polymer Fe(pyrazine)[Pt$(CN)_4$],” *J. Phys. Chem. B*, vol. 109, no. 31, pp. 14859–14867, 2005. PMID: 16852882.

[127] M. C. Muñoz and J. A. Real, “Thermo-, piezo-, photo- and chemo-switchable spin crossover iron(II)-metallocyanate based coordination polymers,” *Coord. Chem. Rev.*, vol. 255, no. 17, pp. 2068–2093, 2011. Special Issue: 39th International Conference on Coordination Chemistry.

[128] G. Agustí, R. Ohtani, K. Yoneda, A. B. Gaspar, M. Ohba, J. F. Sánchez-Royo, M. C. Muñoz, S. Kitagawa, and J. A. Real, “Oxidative addition of halogens on open metal sites in a microporous spin-crossover coordination polymer,” *Angew. Chem. Int. Ed.*, vol. 48, no. 47, pp. 8944–8947, 2009.

[129] R. Ohtani, K. Yoneda, S. Furukawa, N. Horike, S. Kitagawa, A. B. Gaspar, M. C. Muñoz, J. A. Real, and M. Ohba, “Precise control and consecutive modulation of spin transition temperature using chemical migration in porous coordination polymers,” *J. Am. Chem. Soc.*, vol. 133, no. 22, pp. 8600–8605, 2011. PMID: 21526852.

[130] S. Bonhommeau, G. Molnár, A. Galet, A. Zwick, J. A. R. Real, J. J. McGarvey, and A. Bousseksou, “One shot laser pulse induced reversible spin transition in the spin-crossover complex $[Fe(C_4H_4N_2)Pt(CN)_4]$ at room temperature,” *Angew. Chem. Int. Ed.*, vol. 44, no. 26, pp. 4069–4073, 2005.

[131] M. Castro, O. Roubeau, L. Piñeiro López, J. A. Real, and J. A. Rodríguez-Velamazán, “Pulsed-laser switching in the bistability domain of a cooperative spin

crossover compound: A critical study through calorimetry," *J. Phys. Chem. C*, vol. 119, no. 30, pp. 17334–17343, 2015.

[132] J. A. Rodríguez-Velamazán, M. A. González, J. A. Real, M. Castro, M. C. Muñoz, A. B. Gaspar, R. Ohtani, M. Ohba, K. Yoneda, Y. Hijikata, N. Yanai, M. Mizuno, H. Ando, and S. Kitagawa, "A switchable molecular rotator: Neutron spectroscopy study on a polymeric spin-crossover compound," *J. Am. Chem. Soc.*, vol. 134, no. 11, pp. 5083–5089, 2012.

[133] A. Galet, A. B. Gaspar, M. C. Muñoz, G. V. Bukin, G. Levchenko, and J. A. Real, "Tunable bistability in a three-dimensional spin-crossover sensory- and memory-functional material," *Adv. Mater.*, vol. 17, no. 24, pp. 2949–2953, 2005.

[134] L. Piñeiro López, M. Seredyuk, M. C. Muñoz, and J. A. Real., "Two- and one-step cooperative spin transitions in Hofmann-like clathrates with enhanced loading capacity," *Chem. Commun.*, vol. 50, pp. 1833–1835, 2014.

[135] M. Meneses-Sánchez, R. Turo-Cortés, C. Bartual-Murgui, I. da Silva, M. C. Muñoz, and J. A. Real, "Enhanced interplay between host–guest and spin-crossover properties through the introduction of an N heteroatom in 2D Hofmann clathrates," *Inorg. Chem.*, vol. 60, no. 16, pp. 11866–11877, 2021. PMID: 34347471.

[136] T. C. Hansen, P. F. Henry, H. E. Fischer, J. Torregrossa, and P. Convert, "The D20 instrument at the ILL: a versatile high-intensity two-axis neutron diffractometer," *Meas. Sci. Technol.*, vol. 19, p. 034001, jan 2008.

[137] J. Rodríguez-Carvajal, "Recent advances in magnetic structure determination by neutron powder diffraction," *Phys. B: Condens. Matter*, vol. 192, no. 1, pp. 55–69, 1993.

[138] "Fullprof." http://www.ill.eu/sites/fullprof/. Accessed: 2022-10-20.

[139] M. I. Aroyo, J. M. Perez-Mato, C. Capillas, E. Kroumova, S. Ivantchev, G. Madariaga, A. Kirov, and H. Wondratschek, "Bilbao crystallographic server: I. databases and crystallographic computing programs," *Z. Kristallogr. Cryst. Mater.*, vol. 221, no. 1, pp. 15–27, 2006.

[140] J. Rodríguez-Hernández, A. Lemus-Santana, J. Ortiz-López, S. Jiménez-Sandoval, and E. Reguera, "Low temperature structural transformation in $\mathrm{T[Ni(CN)_4]}\cdot x\mathrm{pyz}$ with x=1,2; T=Mn,Co,Ni,Zn,Cd; pyz=pyrazine," *J. Solid State Chem.*, vol. 183, no. 1, pp. 105–113, 2010.

[141] A. Fernández-Blanco, L. Piñeiro López, M. Jiménez-Ruiz, S. Rols, J. A. Real, J. A. Rodríguez-Velamazán, and R. Poloni, “Probing the SO_2 adsorption mechanism in hofmann clathrates via inelastic neutron scattering and density functional theory calculations,” *J. Phys. Chem. C*, vol. 126, no. 18, pp. 8090–8099, 2022.

[142] S. Grimme, “Semiempirical GGA-type density functional constructed with a long-range dispersion correction,” *J. Comput. Chem.*, vol. 27, no. 15, pp. 1787–1799, 2006.

[143] S. Grimme, A. Hansen, J. G. Brandenburg, and C. Bannwarth, “Dispersion-corrected mean-field electronic structure methods,” *Chem. Rev.*, vol. 116, no. 9, pp. 5105–5154, 2016.

[144] S. J. Grabowski, *Hydrogen Bonding- New Insights.* Amsterdam: Springer, 2006.

[145] D. J. Wolstenholme and T. S. Cameron, “Comparative study of weak interactions in molecular crystals: H–H bonds vs hydrogen bonds,” *J. Phys. Chem. A*, vol. 110, no. 28, pp. 8970–8978, 2006. PMID: 16836461.

[146] S. Pillet, “Spin-crossover materials: Getting the most from x-ray crystallography,” *J. Appl. Phys.*, vol. 129, no. 18, p. 181101, 2021.

[147] A. Kashiro, K. Some, Y. Kobayashi, and T. Ishida, “Iron(II) and 1,1,1-tris(2-pyridyl)nonadecane complex showing an order–disorder-type structural transition and spin-crossover synchronized over both conformers,” *Inorg. Chem.*, vol. 58, no. 12, pp. 7672–7676, 2019.

[148] C.-F. Sheu, S. Pillet, Y.-C. Lin, S.-M. Chen, I.-J. Hsu, C. Lecomte, and Y. Wang, “Magnetostructural relationship in the spin-crossover complex t-$Fe(abpt)_2[N(CN)_2]_2$: Polymorphism and disorder phenomenon,” *Inorg. Chem.*, vol. 47, no. 23, pp. 10866–10874, 2008. PMID: 18959361.

[149] H. J. Shepherd, G. Tonge, L. E. Hatcher, M. J. Bryant, J. V. Knichal, P. R. Raithby, M. A. Halcrow, R. Kulmaczewski, K. J. Gagnon, and S. J. Teat, “A high pressure investigation of the order-disorder phase transition and accompanying spin crossover in $[FeL1_2](ClO_4)_2$ (L1 = 2,6-bis{3-methylpyrazol-1-yl}-pyrazine),” *Magnetochemistry*, vol. 2, no. 1, 2016.

[150] T. M. Ross, B. Moubaraki, K. S. Wallwork, S. R. Batten, and K. S. Murray, “A temperature-dependent order-disorder and crystallographic phase transition in a 0D

Fe^{II} spin crossover compound and its non-spin crossover Co^{III}somorph," *Dalton Trans.*, vol. 40, pp. 10147–10155, 2011.

[151] D. Rosario-Amorin, P. Dechambenoit, A. Bentaleb, M. Rouzières, C. Mathonière, and R. Clérac, "Multistability at room temperature in a bent-shaped spin-crossover complex decorated with long alkyl chains," *J. Am. Chem. Soc.*, vol. 140, no. 1, pp. 98–101, 2018. PMID: 29182269.

[152] D. Chernyshov, N. Klinduhov, K. W. Törnroos, M. Hostettler, B. Vangdal, and H.-B. Bürgi, "Coupling between spin conversion and solvent disorder in spin crossover solids," *Phys. Rev. B*, vol. 76, p. 014406, Jul 2007.

[153] R. Kulmaczewski, E. Trzop, E. Collet, S. Vela, and M. A. Halcrow, "Structure:function relationships for thermal and light-induced spin-crossover in isomorphous molecular materials," *J. Mater. Chem. C*, vol. 8, pp. 8420–8429, 2020.

[154] G. S. Matouzenko, A. Bousseksou, S. A. Borshch, M. Perrin, S. Zein, L. Salmon, G. Molnar, and S. Lecocq, "Cooperative spin crossover and order–disorder phenomena in a mononuclear compound [Fe(DAPP)(abpt)]$(ClO_4)_2$ [DAPP = [Bis(3-aminopropyl)(2-pyridylmethyl)amine], abpt = 4-Amino-3,5-bis(pyridin-2-yl)-1,2,4-triazole]," *Inorg. Chem.*, vol. 43, no. 1, pp. 227–236, 2004. PMID: 14704072.

[155] G. A. Craig, J. S. Costa, O. Roubeau, S. J. Teat, and G. Aromí, "Coupled crystallographic order–disorder and spin state in a bistable molecule: Multiple transition dynamics," *Chem. - Eur. J.*, vol. 17, no. 11, pp. 3120–3127, 2011.

[156] L. M. L. Daku, A. Vargas, A. Hauser, A. Fouqueau, and M. E. Casida, "Assessment of density functionals for the high-spin/low-spin energy difference in the low-spin iron(II) tris(2, 2'-bipyridine) complex," *ChemPhysChem*, vol. 6, no. 7, pp. 1393–1410, 2005.

[157] K. Pierloot, "Transition metals compounds: Outstanding challenges for multiconfigurational methods," *Int. J. Quantum Chem.*, vol. 111, pp. 3291–3301, Mar. 2011.

[158] A. Droghetti, D. Alfè, and S. Sanvito, "Assessment of density functional theory for iron(II) molecules across the spin-crossover transition," *J. Chem. Phys.*, vol. 137, no. 12, p. 124303, 2012.

[159] L. A. Mariano, B. Vlaisavljevich, and R. Poloni, "Improved spin-state energy differences of Fe(II) molecular and crystalline complexes via the Hubbard U-corrected density," *J. Chem. Theory Comput.*, vol. 17, no. 5, pp. 2807–2816, 2021.

[160] J. P. Perdew, M. Ernzerhof, and K. Burke, “Rationale for mixing exact exchange with density functional approximations,” *J. Chem. Phys.*, vol. 105, no. 22, pp. 9982–9985, 1996.

[161] K. F. Garrity, J. W. Bennett, K. M. Rabe, and D. Vanderbilt, “Pseudopotentials for high-throughput DFT calculations,” *Comput. Mater. Sci.*, vol. 81, pp. 446–452, 2014.

[162] J.-R. Li, R. J. Kuppler, and H.-C. Zhou, “Selective gas adsorption and separation in metal–barorganic frameworks,” *Chem. Soc. Rev.*, vol. 38, pp. 1477–1504, 2009.

[163] Z. Guo, H. Wu, G. Srinivas, Y. Zhou, S. Xiang, Z. Chen, Y. Yang, W. Zhou, M. O’Keeffe, and B. Chen, “A metal–organic framework with optimized open metal sites and pore spaces for high methane storage at room temperature,” *Angew. Chem. Int. Ed.*, vol. 50, no. 14, pp. 3178–3181, 2011.

[164] M. Albrecht and G. van Koten, “Gas sensor materials based on metallodendrimers,” *Adv. Mater.*, vol. 11, no. 2, pp. 171–174, 1999.

[165] M. Albrecht, R. A. Gossage, M. Lutz, A. L. Spek, and G. van Koten, “Diagnostic organometallic and metallodendritic materials for SO_2 gas detection: Reversible binding of sulfur dioxide to arylplatinum(II) complexes,” *Chem. Eur. J.*, vol. 6, no. 8, pp. 1431–1445, 2000.

[166] M. Albrecht, M. Lutz, A. L. Spek, and G. van Koten, “Organoplatinum crystals for gas–triggered switches,” *Nature*, vol. 406, pp. 970–974, 2000.

[167] D. Richard, M. Ferrand, and G. Kearley, “Analysis and visualization of neutron-scattering data,” *J. Neutron Res.*, pp. 33–39, 1996.

[168] A. M. Rappe, K. M. Rabe, E. Kaxiras, and J. D. Joannopoulos, “Optimized pseudopotentials,” *Phys. Rev. B*, vol. 41, pp. 1227–1230, Jan 1990.

[169] Á. Fernández-Blanco, L. A. Mariano, L. Piñeiro-López, J. A. Real, J. S. Costa, R. Poloni, and J. A. Rodríguez-Velamazán, “Hidden ordered structure in the archetypical Fe(pyrazine)[Pt$(CN)_4$] spin-crossover porous coordination compound,” *CrystEngComm*, vol. 24, pp. 6349–6356, 2022.

[170] D. Price and J. Carpenter, “Scattering function of vitreous silica,” *J. Non Cryst. Solids*, vol. 92, no. 1, pp. 153–174, 1987.

[171] S. N. Taraskin and S. R. Elliott, "Connection between the true vibrational density of states and that derived from inelastic neutron scattering," *Phys. Rev. B*, vol. 55, pp. 117–123, Jan 1997.

[172] G. Félix, M. Mikolasek, H. Peng, W. Nicolazzi, G. Molnár, A. I. Chumakov, L. Salmon, and A. Bousseksou, "Lattice dynamics in spin-crossover nanoparticles through nuclear inelastic scattering," *Phys. Rev. B*, vol. 91, p. 024422, Jan 2015.

[173] G. Molnár, V. Niel, A. B. Gaspar, J.-A. Real, A. Zwick, A. Bousseksou, and J. J. McGarvey, "Vibrational spectroscopy of cyanide-bridged, iron(ii) spin-crossover coordination polymers: Estimation of vibrational contributions to the entropy change associated with the spin transition," *J. Phys. Chem. B*, vol. 106, no. 38, pp. 9701–9707, 2002.

[174] G. Molnár, V. Niel, J.-A. Real, L. Dubrovinsky, A. Bousseksou, and J. J. McGarvey, "Raman spectroscopic study of pressure effects on the spin-crossover coordination polymers Fe(Pyrazine)[M(CN)$_4$]·2H$_2$O (M = Ni, Pd, Pt). First observation of a piezo-hysteresis loop at room temperature," *J. Phys. Chem. B*, vol. 107, no. 14, pp. 3149–3155, 2003.

[175] T. Hochdörffer, A. I. Chumakov, H.-C. Wille, V. Schönemann, and J. A. Wolny, "Vibrational properties and cooperativity of the 3D spin crossover network [Fe(pyrazine)][Pt(CN)$_4$]," *Dalton Trans.*, vol. 48, pp. 15625–15634, 2019.

[176] K. W. Muir and J. A. Ibers, "Structure of chlorocarbonyl(sulfurdioxide)bis(triphenylphosphine)rhodium, RhCl(CO)(SO$_2$)(P(C$_6$H$_5$)$_3$)$_2$," *Inorg. Chem.*, vol. 8, no. 9, pp. 1921–1928, 1969.

[177] R. Ryan, G. Kubas, D. Moody, and P. Eller, "Structure and bonding of transition metal-sulfur dioxide complexes," *Inorg. Chem.*, pp. 47–100, 1981.

[178] D. Mingos, "Sulphur dioxide complexes of the platinum metals," *Transition Met. Chem.*, pp. 1–15, 1978.

[179] D. Mingos, "Ambivalent lewis acid/bases with symmetry signatures and isolobal analogies," *Struct. Bond.*, pp. 1–52, 2014.

[180] S. L. Dudarev, G. A. Botton, S. Y. Savrasov, C. J. Humphreys, and A. P. Sutton, "Electron-energy-loss spectra and the structural stability of nickel oxide: An LSDA+U study," *Phys. Rev. B*, vol. 57, pp. 1505–1509, Jan 1998.

[181] G. W. Mann, K. Lee, M. Cococcioni, B. Smit, and J. B. Neaton, “First-principles Hubbard U approach for small molecule binding in metal-organic frameworks,” *J. Chem. Phys.*, vol. 144, no. 17, p. 174104, 2016.

[182] I. Timrov, N. Marzari, and M. Cococcioni, “Hubbard parameters from density-functional perturbation theory,” *Phys. Rev. B*, vol. 98, p. 085127, Aug 2018.

[183] M. Ito, R. Shimada, T. Kuraishi, and W. Mizushima, “Vibrational spectra of diazines,” *J. Chem. Phys.*, vol. 25, no. 3, pp. 597–598, 1956.

[184] R. Lord, A. Marston, and F. A. Miller, “Infra-red and raman spectra ot the diazines,” *Spectroc. Acta*, vol. 9, no. 2, pp. 113–125, 1957.

[185] A. R. Katritzky, “The infrared spectra of heteroaromatic compounds,” *Q. Rev. Chem. Soc.*, vol. 13, pp. 353–373, 1959.

[186] S. Califano, G. Adembri, and G. Sbrana, “Vapour and crystal spectra in polarized light of pyrazine-d0, cis pyrazine-d2 and pyrazine-d4,” *Spectrochim. Acta*, vol. 20, no. 3, pp. 385–396, 1964.

[187] J. Simmons, K. Innes, and G. Begun, “Infrared and raman spectra of pyrazine-h_4 and -d_4,” *J. Mol. Spectrosc.*, pp. 190 – 197, 1964.

[188] J. F. Arenas, J. T. Lopez-Navarrete, J. C. Otero, J. I. Marcos, and A. Cardenete, “Vibrational spectra of [$1H_4$]pyrazine and [$2H_4$]pyrazine,” *J. Chem. Soc., Faraday Trans. 2*, vol. 81, pp. 405–415, 1985.

[189] H. Endrédi, F. Billes, and S. Holly, “Vibrational spectroscopic and quantum chemical study of the chlorine substitution of pyrazine,” *J. Mol. Struct.*, vol. 633, no. 1, pp. 73–82, 2003.

[190] G. Kearley, J. Tomkinson, A. Navarro, J. López González, and M. Fernández Gómez, “Symmetrised quantum-mechanical force-fields and INS spectra: s-triazine, trichloro-s-triazine and pyrazine,” *Chem. Phys.*, vol. 216, no. 3, pp. 323–335, 1997.

[191] H. E. Toma and J. M. Malin, “Properties and reactivity of some pentacyanoferrate(II) complexes of aromatic nitrogen heterocycles,” *Inorg. Chem.*, vol. 12, no. 5, pp. 1039–1045, 1973.

[192] J. Thompson, *Infrared Spectroscopy.* Jenny Stanford Publishing, 2018.

[193] A. Koishi, A. Fernandez-Martinez, B. Ruta, M. Jimenez-Ruiz, R. Poloni, D. di Tommaso, F. Zontone, G. A. Waychunas, and G. Montes-Hernandez, "Role of impurities in the kinetic persistence of amorphous calcium carbonate: A nanoscopic dynamics view," *J. Phys. Chem. C*, vol. 122, no. 29, pp. 16983–16991, 2018.

[194] C. H. Pham and F. Paesani, "Guest-dependent stabilization of the low-spin state in spin-crossover metal-organic frameworks," *Inorg. Chem.*, vol. 57, no. 16, pp. 9839–9843, 2018. PMID: 30067340.

[195] J. T. Culp, D.-L. Chen, J. Liu, D. Chirdon, K. Kauffman, A. Goodman, and J. K. Johnson, "Effect of spin-crossover-induced pore contraction on CO_2–host interactions in the porous coordination polymers [Fe(pyrazine)$M(CN)_4$] (M = Ni, Pt)," *Eur. J. Inorg. Chem.*, vol. 2013, no. 4, pp. 511–519, 2013.

[196] M. M. Deshmukh, M. Ohba, S. Kitagawa, and S. Sakaki, "Absorption of CO_2 and CS_2 into the Hofmann-type porous coordination polymer: Electrostatic versus dispersion interactions," *J. Am. Chem. Soc.*, vol. 135, no. 12, pp. 4840–4849, 2013. PMID: 23437824.

[197] K. Momma and F. Izumi, "*VESTA3* for three-dimensional visualization of crystal, volumetric and morphology data," *J. Appl. Crystallogr.*, vol. 44, pp. 1272–1276, Dec 2011.

[198] S. Grimme, J. Antony, S. Ehrlich, and H. Krieg, "A consistent and accurate ab initio parametrization of density functional dispersion correction (DFT-D) for the 94 elements H-Pu," *J. Chem. Phys.*, vol. 132, no. 15, p. 154104, 2010.

[199] S. Grimme, S. Ehrlich, and L. Goerigk, "Effect of the damping function in dispersion corrected density functional theory," *J. Comput. Chem.*, vol. 32, no. 7, pp. 1456–1465, 2011.

[200] R. Poloni, D. Machon, M. V. Fernandez-Serra, S. Le Floch, S. Pascarelli, G. Montagnac, H. Cardon, and A. San-Miguel, "High-pressure stability of Cs_6C_{60}," *Phys. Rev. B*, vol. 77, p. 125413, Mar 2008.

[201] G. Miessler, P. Fischer, and D. Tarr, *Inorganic Chemistry 5th Ed.* Pearson Education, 2013.

[202] C. Wang, D. Liu, and W. Lin, "Metal–organic frameworks as a tunable platform for designing functional molecular materials," *J. Am. Chem. Soc.*, vol. 135, pp. 13222–13234, Aug. 2013.

[203] S. Yuan, L. Feng, K. Wang, J. Pang, M. Bosch, C. Lollar, Y. Sun, J. Qin, X. Yang, P. Zhang, Q. Wang, L. Zou, Y. Zhang, L. Zhang, Y. Fang, J. Li, and H.-C. Zhou, "Stable metal-organic frameworks: Design, synthesis, and applications," *Adv. Mater.*, vol. 30, p. 1704303, Feb. 2018.

[204] D. M. D'Alessandro, B. Smit, and J. R. Long, "Carbon dioxide capture: Prospects for new materials," *Angew. Chem. Int. Ed.*, vol. 49, pp. 6058–6082, July 2010.

[205] Y. Hwang, D.-Y. Hong, J.-S. Chang, S. Jhung, Y.-K. Seo, J. Kim, A. Vimont, M. Daturi, C. Serre, and G. Frey, "Amine grafting on coordinatively unsaturated metal centers of MOFs: Consequences for catalysis and metal encapsulation," *Angew. Chem. Int. Ed.*, vol. 47, no. 22, pp. 4144–4148, 2008.

[206] K. Sumida, S. Horike, S. S. Kaye, Z. R. Herm, W. L. Queen, C. M. Brown, F. Grandjean, G. J. Long, A. Dailly, and J. R. Long, "Hydrogen storage and carbon dioxide capture in an iron-based sodalite-type metalorganic framework (Fe-BTT) discovered via high-throughput methods," *Chem. Sci.*, vol. 1, pp. 184–191, 2010.

[207] Z. R. Herm, E. D. Bloch, and J. R. Long, "Hydrocarbon separations in metal–organic frameworks," *Chem. Mater.*, vol. 26, no. 1, pp. 323–338, 2014.

[208] K. Lee, W. C. Isley, A. L. Dzubak, P. Verma, S. J. Stoneburner, L.-C. Lin, J. D. Howe, E. D. Bloch, D. A. Reed, M. R. Hudson, C. M. Brown, J. R. Long, J. B. Neaton, B. Smit, C. J. Cramer, D. G. Truhlar, and L. Gagliardi, "Design of a metal–organic framework with enhanced back bonding for separation of N_2 and CH_4," *J. Am. Chem. Soc.*, vol. 136, no. 2, pp. 698–704, 2014. PMID: 24313689.

[209] S. S. Chui, "A chemically functionalizable nanoporous material $[Cu_3(TMA)_2(H_2O)_3]_n$," *Science*, vol. 283, pp. 1148–1150, Feb. 1999.

[210] D. A. Reed, D. J. Xiao, M. I. Gonzalez, L. E. Darago, Z. R. Herm, F. Grandjean, and J. R. Long, "Reversible CO scavenging via adsorbate-dependent spin state transitions in an iron(II)–triazolate metal–organic framework," *J. Am. Chem. Soc.*, vol. 138, pp. 5594–5602, Apr. 2016.

[211] K. Lee, J. D. Howe, L.-C. Lin, B. Smit, and J. B. Neaton, "Small-molecule adsorption in open-site metal–organic frameworks: A systematic density functional theory study for rational design," *Chem. Mater.*, vol. 27, pp. 668–678, Jan. 2015.

[212] A. Mohajeri and A. Yeganeh Jabri, “Spin crossover as an efficient strategy for controllable gas molecule capturing on open metal sites in Ni-BTC and Cu-BTC,” *J. Phys. Chem. C*, vol. 124, no. 29, pp. 15902–15912, 2020.

[213] W. L. Queen, M. R. Hudson, E. D. Bloch, J. A. Mason, M. I. Gonzalez, J. S. Lee, D. Gygi, J. D. Howe, K. Lee, T. A. Darwish, M. James, V. K. Peterson, S. J. Teat, B. Smit, J. B. Neaton, J. R. Long, and C. M. Brown, “Comprehensive study of carbon dioxide adsorption in the metalorganic frameworks M_2(dobdc) (M = Mg, Mn, Fe, Co, Ni, Cu, Zn),” *Chem. Sci.*, vol. 5, pp. 4569–4581, 2014.

[214] G. J. Halder, S. M. Neville, and C. J. Kepert, “A highly distorted (10, 3)-a coordination framework constructed from alternating T-shaped and trigonal nodes,” *CrystEngComm*, vol. 7, no. 42, p. 266, 2005.

[215] F. Neese, “The ORCA program system,” *WIREs Comput. Mol. Sci.*, vol. 2, no. 1, pp. 73–78, 2012.

[216] D. G. A. Smith, L. A. Burns, K. Patkowski, and C. D. Sherrill, “Revised damping parameters for the D3 dispersion correction to density functional theory,” *J. Phys. Chem. Lett.*, vol. 7, pp. 2197–2203, May 2016.

[217] R. Poloni, B. Smit, and J. B. Neaton, “CO_2 capture by metal–organic frameworks with van der waals density functionals,” *J. Phys. Chem. A*, vol. 116, no. 20, pp. 4957–4964, 2012. PMID: 22519821.

[218] G. J. Kubas, “Metal–dihydrogen and σ-bond coordination: the consummate extension of the Dewar–Chatt–Duncanson model for metal–olefin π bonding,” *J. Organomet. Chem.*, vol. 635, no. 1, pp. 37–68, 2001.

[219] G. J. Kubas, “Hydrogen activation on organometallic complexes and H_2 production, utilization, and storage for future energy,” *J. Organomet. Chem.*, vol. 694, no. 17, pp. 2648–2653, 2009. Organometallics for Energy Conversion.

[220] G. Henkelman, A. Arnaldsson, and H. Jónsson, “A fast and robust algorithm for Bader decomposition of charge density,” *Comput. Mater. Sci.*, vol. 36, pp. 354–360, June 2006.

[221] E. Sanville, S. D. Kenny, R. Smith, and G. Henkelman, “Improved grid-based algorithm for Bader charge allocation,” *J. Comput. Chem.*, vol. 28, no. 5, pp. 899–908, 2007.

[222] W. Tang, E. Sanville, and G. Henkelman, “A grid-based Bader analysis algorithm without lattice bias,” *J. Phys: Condens. Matter*, vol. 21, p. 084204, Jan. 2009.

[223] M. Yu and D. R. Trinkle, “Accurate and efficient algorithm for Bader charge integration,” *J. Chem. Phys.*, vol. 134, p. 064111, Feb. 2011.

[224] J. W. Bennett, B. G. Hudson, I. K. Metz, D. Liang, S. Spurgeon, Q. Cui, and S. E. Mason, “A systematic determination of Hubbard U using the GBRV ultrasoft pseudopotential set,” *Comp. Mater. Sci.*, vol. 170, p. 109137, 2019.

[225] H. J. Kulik, M. Cococcioni, D. A. Scherlis, and N. Marzari, “Density functional theory in transition-metal chemistry: A self-consistent Hubbard U approach,” *Phys. Rev. Lett.*, vol. 97, p. 103001, Sep 2006.

[226] J. A. Rodríguez-Velamazán, O. Roubeau, R. Poloni, E. Lhotel, E. Palacios, M. A. González, and J. A. Real, “Long-range magnetic order in the porous metal–organic framework Ni(pyrazine)[Pt$(CN)_4$],” *Phys. Chem. Chem. Phys.*, vol. 19, no. 43, pp. 29084–29091, 2017.

[227] K. Pierloot, Q. M. Phung, and A. Domingo, “Spin state energetics in first-row transition metal complexes: Contribution of (3s3p) correlation and its description by second-order perturbation theory,” *J. Chem. Theory Comput.*, vol. 13, no. 2, pp. 537–553, 2017.

[228] Q. M. Phung, M. Feldt, J. N. Harvey, and K. Pierloot, “Toward highly accurate spin state energetics in first-row transition metal complexes: A combined CASPT2/CC approach,” *J. Chem. Theory Comput.*, vol. 14, no. 5, pp. 2446–2455, 2018.

[229] Y. G. Chung, E. Haldoupis, B. J. Bucior, M. Haranczyk, S. Lee, H. Zhang, K. D. Vogiatzis, M. Milisavljevic, S. Ling, J. S. Camp, B. Slater, J. I. Siepmann, D. S. Sholl, and R. Q. Snurr, “Advances, updates, and analytics for the computation-ready, experimental metal–organic framework database: CoRE MOF 2019,” *J. Chem. Eng. Data*, vol. 64, pp. 5985–5998, Nov. 2019.

[230] K. P. Kepp, “Theoretical study of spin crossover in 30 iron complexes,” *Inorg. Chem.*, vol. 55, no. 6, pp. 2717–2727, 2016. PMID: 26913489.

[231] S. Vela, M. Fumanal, J. Cirera, and J. Ribas-Arino, “Thermal spin crossover in Fe(II) and Fe(III). Accurate spin state energetics at the solid state,” *Phys. Chem. Chem. Phys.*, vol. 22, pp. 4938–4945, 2020.